

Studies of volatile evolution in magmatic systems using melt inclusions

Rosario Esposito

Dissertation submitted to the faculty of the Virginia Polytechnic Institute and State University in partial fulfillment of the requirements for the degree of

**Doctor of Philosophy
In
Geosciences**

Robert J. Bodnar
Benedetto De Vivo
Annamaria Lima
J. Donald Rimstidt
Robert J. Tracy

July 2, 2012
Blacksburg, VA

Keywords: Melt Inclusion, Volatile Evolution, Magma Degassing, Melt Inclusion Assemblage, Post Entrapment Crystallization, Microscope Heating Stage

Copyright © 2012, Rosario Esposito

Studies of volatile evolution in magmatic systems using melt inclusions

Rosario Esposito

ABSTRACT

Understanding volatile evolution associated with active volcanic magmatic systems is of paramount importance because volatiles control and determine the magnitude of an eruption owing to the large change in molar volume that volatile species show depending on their physical state (volatiles dissolved in silicate melts vs. volatiles exsolved as vapor). For active volcanic systems studying the volatile evolution can help to assess the potential hazard associated to a certain locality. Also, volatile evolution in magmatic system controls the formation of certain ore deposits.

Despite the importance of understanding volatile evolution of magmatic systems, concentrations of volatiles of evolving magmas are not easily available especially for magmas originated in the deep crust. Fortunately, sample of melts can be entrapped as melt inclusion (MI) into growing igneous minerals in crystalizing magma chamber. After the entrapment, the crystal works as an insulating capsule from the external magmatic environment.

Researchers have started to use MI because they provide some advantages in respect to the classical whole rock approach to petrological studies. One of the most important advantages is that MI often represent sample of a deep and non-degassed melt (glass) available at Earth's surface.

This dissertation is a compilation of four publications produced during six years of research and is addressed to give a contribution in understanding the volatile evolution in magmatic systems and also to improve the present understanding of information that can be obtained using the melt inclusions technique.

In the first chapter, I present an alternative interpretation of H₂O-CO₂ trends obtained from MI. In this study, we demonstrate that these trends can be due to post entrapment crystallization on the wall of the MI and not to magma ascent. This alternative view is more realistic especially for cases where in the same phenocrysts MI show strongly different CO₂ concentrations.

In the second chapter, I present a study to test for the MI reliability in recording volatile concentrations. We used the approach of the melt inclusion assemblage (MIA) that consists of analyzing groups of MI presumably entrapped at the same time and, thus, at same chemical and physical conditions. The results show that most of the MIA studied show consistent volatile concentrations corroborating the reliability of the MI technique. CO₂ shows the highest degrees of variability and we have assessed this behavior mostly to C-contamination in the surface of the sample.

The third chapter is a study case (the Solchiaro eruption in Southern Italy) that shows the potential uses of MI to understanding the volatile evolution. I present a model showing the dynamic of the magma based on MI. This study also discusses the origin of anomalous MI and which MI provide the best information.

The final chapter is dedicated to test the applicability of the new Linkam TS1400XY heating stage. I was able to show how this new microthermometric tool is capable of homogenizing MI at high temperature and to quench MI to a homogeneous glass state.

Dedicated to my sister Elvira

ACKNOWLEDGEMENTS

There are a lot of people that have participated directly or indirectly to the accomplishment of this PhD, so many that it would take several pages of this document to acknowledge all of them. It would be risky to do a tentative list and forget somebody. Thus, I am going to write just a few sentences to acknowledge the two birds that last spring had built their nest few inches far from my rear door in Blacksburg. My birdy-neighbors have been so important for me because every morning listening their melody I felt so happy to wake up and be ready to go to work at the Geosciences Department.

ATTRIBUTION

I collaborated with several researchers to complete the studies presented in this dissertation. It is important to note that these collaborators work for institutions based both in the US and in other countries (Italy, Australia, Russia). A brief description of each of the collaborators is reported below.

Chapter 1: Thermodynamic model for the effect of post-entrapment crystallization on the H₂O-CO₂ systematics of vapor-saturated, silicate melt inclusions.

This chapter was published in the *Journal of Petrology*.

Matthew Steele-MacInnis, PhD candidate (Fluids Research Laboratory, Department of Geosciences, Virginia Tech), is the first author of this study because he gave the main contribution to the formulation of the numerical modeling and the discussion and interpretation of the results.

Robert J. Bodnar, University Distinguished Professors and C. C. Garvin Professor of Geochemistry (Fluids Research Laboratory, Department of Geosciences, Virginia Tech), is a coauthor of this study and he contributed in the formulation of the numerical modeling and the interpretation and discussion of the results.

Chapter 2: Do melt inclusions record the pre-eruptive volatile content of magmas?

Chapter 2 is a scientific article in preparation to be submitted to the *Earth and Planetary Science Letter*.

Jerry Hunter, Research Assistant Professor (Nanoscale Characterization and Fabrication Labs, Virginia Tech), is a coauthor of this chapter and his contribution is related to the data acquisition using the Secondary Ion Mass Spectrometer (SIMS) and to the interpretation and discussion of data.

James D. Schiffbauer, Assistant Professor (Department of Geological Sciences, University of Missouri), is a coauthor of this chapter. James has helped to obtain images using the Focused Ion Beam technique and has participated to the interpretation of data obtained in this study.

Robert J. Bodnar, University Distinguished Professors and C. C. Garvin Professor of Geochemistry (Fluids Research Laboratory, Department of Geosciences, Virginia Tech), is a coauthor of this study and has contributed to the main idea and structure of this project. Moreover he has participated to the interpretation and discussion of the results.

Chapter 3: Volatile Evolution of Magma Associated with the Solchiaro Eruption in the Phlegrean Volcanic District (Italy).

This chapter was published in the *Journal of Petrology* in 2011.

Robert J. Bodnar, University Distinguished Professors and C. C. Garvin Professor of Geochemistry (Fluids Research Laboratory, Department of Geosciences, Virginia Tech), is a coauthor of this study and provided the main contribution to the interpretation and discussion of the results.

Leonid V. Danyushevsky, Professor Leader of the Technology Research Program (CODES CoE and School of Earth Sciences, University of Tasmania, Australia), is coauthor of this study and his contribution was to provide important information about the melt inclusion technique owing his expertise in this field. Leonid contributed to data interpretation and discussion.

Benedetto De Vivo, Professor of Geochemistry (Dipartimento di Scienze della Terra, Università degli Studi di Napoli Federico II, Italy), is a coauthor of this study and his contribution is related to his profound knowledge of the Southern Italian volcanism and the fluid/melt inclusion technique. Consequently, Benedetto contributed to the interpretation and discussion of the results of this study.

Luca Fedele, Senior Research Associate (Fluids Research Laboratory, Department of Geosciences, Virginia Tech), is a coauthor of this study and his contribution was to help obtaining data using the Electron Microprobe (EMP) and the Laser Ablation-Inductively Coupled Mass Spectrometry (LA-ICPMS).

Jerry Hunter, Research Assistant Professor (Nanoscale Characterization and Fabrication Labs, Virginia Tech), is a coauthor of this chapter and his contribution is related to the data acquisition using the Secondary Ion Mass Spectrometer (SIMS) and the interpretation and discussion of the data produced by this technique.

Annamaria Lima, Associate Professor (Dipartimento di Scienze della Terra, Università degli Studi di Napoli Federico II, Italy), is a coauthor of this study and her contribution is related to her profound knowledge of the Southern Italian volcanism and the fluid/melt inclusion technique. Consequently, Annamaria contributed to the interpretation and discussion of the results of this study.

Nobumichi Shimizu, Senior Scientist (Woods Hole Oceanographic Institution, Woods Hole, MA) is a coauthor of this study and his contribution is related to sample preparation and the data acquisition using the Secondary Ion Mass Spectrometer (SIMS) and the interpretation and discussion of data.

Chapter 4: Application of the Linkam TS1400XY heating stage to melt inclusion studies.

This chapter was published in the *Central European Journal of Geosciences in 2011*.

Rita Klebesz, PhD candidate (Dipartimento di Scienze della Terra, Università degli Studi di Napoli Federico II, Italy), is a coauthor of this scientific publication. Rita participated

actively to this project performing heating experiments and producing data. Moreover, she has contributed to the interpretation of the results.

Omar Bartoli, Research Fellow (Dipartimento di Scienze della Terra, Università degli Studi di Padova, Italy), is a coauthor of this study and his contribution was to perform heating experiments and to discuss and interpret data.

Yury I. Klyukin, PhD candidate (Institute of Geology and Geochemistry of Urals Branch, Russian Academy of Sciences, Yekaterinburg, Russia), is a coauthor of this study. Yury's contribution was to help with microphotographing the heating experiments and to help with the discussion and the interpretation of data.

Daniel Moncada, PhD candidate (Fluids Research Laboratory, Department of Geosciences, Virginia Tech), is a coauthor of this study and his participation was to help with setting the heating stage for experiments and to contribute to the interpretation and discussion of data.

Angela L. Doherty, PhD candidate (Dipartimento degli Alimenti e dell'Ambiente, Università degli Studi di Messina, Italy), is a coauthor of this study. Angela contributed to this article helping with editing and with the discussion and interpretation of the result.

Robert J. Bodnar, University Distinguished Professors and C. C. Garvin Professor of Geochemistry (Fluids Research Laboratory, Department of Geosciences, Virginia Tech), is a coauthor of this study and contributed to the structure of the article and to the interpretation and discussion of the result.

Table of Contents

ABSTRACT	i
ATTRIBUTION	iv
INTRODUCTION	xiii
CHAPTER 1	1
Thermodynamic model for the effect of post-entrapment crystallization on the H₂O-CO₂ systematics of vapor-saturated, silicate melt inclusions.....	1
Abstract.....	1
1. Introduction.....	2
2. Previous Studies	4
3. Description of the Quantitative Thermodynamic Model.....	5
3.1 Numerical Representation of the NaAlSi ₃ O ₈ -H ₂ O-CO ₂ System.....	5
3.2 PTX correlations on the vapor-saturated solidus.....	6
3.3 Solubilities of H ₂ O and CO ₂ in the melt phase.....	7
3.4 Volume of the H ₂ O, CO ₂ and H ₂ O-CO ₂ fluid phase	8
3.5 Volume of the melt phase.....	8
3.6 Volume of the crystallized albite phase	8
4. Implementation of the Closed, Isochoric, Post-Entrapment Crystallization Model	8
4.1 Binary NaAlSi ₃ O ₈ -H ₂ O and NaAlSi ₃ O ₈ -CO ₂ Models	8
4.2 Ternary NaAlSi ₃ O ₈ -H ₂ O-CO ₂ System.....	9
5. Results of Simulations of the PVTX Evolution of Melt Inclusions During Post-Entrapment Crystallization	14
5.1 The system NaAlSi ₃ O ₈ -H ₂ O	15
5.2 The system NaAlSi ₃ O ₈ -CO ₂	16
5.3 The system NaAlSi ₃ O ₈ -H ₂ O-CO ₂	16
6. Application of model to other melt compositions and host phases.....	17
7. Discussion of modeling results - implications for natural MI	19
8. Summary	21
9. Acknowledgements	22
10. References.....	22
11. Tables	28
12. Figures.....	30
CHAPTER 2	40
Do melt inclusions record the pre-eruptive volatile content of magmas?	40
Abstract.....	40
1. Introduction.....	40
2. Geological background.....	42
3. Analytical methods	42
4. Results.....	44
4.1 Petrography.....	44
4.2 Volatile composition of White Island MI	45
4.3 Volatile composition of Solchiaro MI	46
4.4 White Island MIA	46
4.5 Solchiaro MIA	47
5. Discussion.....	47

6. Summary	50
7. Acknowledgement	50
8. References	50
9. Tables.....	53
10. Figures.....	55
11. Supplementary material	61
11.1 Tables	61
11.2 Figures	67
CHAPTER 3	75
 Volatile Evolution of Magma Associated with the Solchiaro Eruption in the Phlegrean Volcanic District (Italy)	75
 Abstract.....	76
 1. Introduction.....	77
 2. Geological Background.....	79
Geology and geochronology of the Phlegrean Volcanic District	79
Previous MI studies of the PVD	80
 3. Sample description	81
 4. Analytical methods	82
 5. Results.....	84
Mineral chemistry	84
Melt inclusion petrography.....	85
Major element composition	86
Trace element composition	87
Volatile Abundances	87
 6. Discussion.....	88
Variations in volatile contents of MI and their causes	89
Model for the Solchiaro magmatic system	92
Anomalous MI.....	94
 7. Summary	97
 8. Acknowledgments.....	98
 9. References	99
 10. Tables	106
 11. Figures.....	113
CHAPTER 4	122
 Application of the Linkam TS1400XY heating stage to melt inclusion studies	122
 Abstract.....	123
 1. Introduction.....	123
 2. Description of the hardware and analytical conditions.....	125
 3. Results.....	127
 4. Discussion of advantages and limitations of the Linkam TS1400XY stage.....	129
 5. Summary	130
 6. Acknowledgements	131
 7. References	131
 8. Tables.....	134
 9. Figures	135

LIST OF TABLES

Tables Chapter 1

Table 1. Calculation of total CO₂ contained in a bubble-bearing MI from Solchiaro (southern Italy).....28

Table 2. Studies that report relationships between PEC, presence or absence of shrinkage (vapor) bubbles, and dissolved volatile contents and pressure estimates from natural MI..... 29

Tables Chapter 2

Table 1. Representative analyses of volatile concentrations of MI from White Island and Solchiaro samples..... 53

Table 2. Studies that report relationships between PEC, presence or absence of shrinkage (vapor) bubbles, and dissolved volatile contents and pressure estimates from natural MI..... 54

SMTTable1. Glass standards data used to calculate calibration curves..... 61

SMTTable2. Volatile compositions of MI from White Island and Solchiaro.....62

Tables Chapter 3

Table 1. Pre-eruptive magma storage depths for PVD eruptions based on MI data..... 106

Table 2a. Petrographic information for MI from samples RESC2 and RESC3. All MI are hosted in olivine..... 107

Table 2b. Petrographic information for MI from samples RESC4 and RESC5. All MI are hosted in olivine..... 108

Table 3. Representative EMP analysis of olivine from samples RESC3, RESC4 and RESC5..... 109

Table 4a. Representative major, minor and trace element and volatile content of MI from samples RESC2 and RESC3..... 110

Table 4b. Representative major, minor and trace element and volatile content of MI from samples RESC4 and RESC5..... 111

Table 5. Parameters used to calculate total CO₂ contained in a bubble-bearing MI (RESC2-O26-M3)..... 112

Table 6. Settling times calculated for an olivine phenocryst in the Solchiaro magma... 112

Tables Chapter 4

Table 1. Heating schedule used for heating experiments on crystals from the Solchiaro, Sarno and Toba Tuff eruptions..... 134

LIST OF FIGURES

Chapter 1

Figure 1. Quartz phenocryst from the Bishop Tuff (inset) showing three large, glassy melt inclusions, with the two smaller inclusions in the lower left-center exposed on the crystal surface..... 30

Figure 2. (Top) Heating sequence for a multi-phase silicate melt inclusion in quartz from the Toba Tuff, Sumatra, showing the melting of various daughter minerals and dissolution of the vapor phase to produce a homogeneous melt (glass)..... 31

Figure 3. Raman spectrum of a shrinkage (vapor) bubble in a MI hosted in olivine (inset) from the Solchiaro volcano, Procida Island (South Italy)..... 32

Figure 4. *PTX* vapor-saturated phase relations in the $\text{NaAlSi}_3\text{O}_8\text{-H}_2\text{O}$, $\text{NaAlSi}_3\text{O}_8\text{-CO}_2$ and $\text{NaAlSi}_3\text{O}_8\text{-H}_2\text{O-CO}_2$ systems..... 33

Figure 5. Schematic flow chart outlining the steps involved in the iterative numerical model used to estimate the *PTX* evolution of volatile-bearing melt inclusions during post-entrapment crystallization..... 33

Figure 6. Isobars (solid lines, labeled in kbar) of $\text{H}_2\text{O-CO}_2$ solubility in albite melt at 900°C , based on the data of Burnham & Davis (1974), Fine & Stolper (1986) and Holloway & Blank (1994)..... 34

Figure 7. Variation in partial molar volumes of H_2O (left axis) and $\text{NaAlSi}_3\text{O}_8$ (right axis) in the melt as a function of pressure along the H_2O -saturated solidus..... 34

Figure 8. *PTX* evolution during PEC of a MI that traps an H_2O -saturated $\text{NaAlSi}_3\text{O}_8\text{-H}_2\text{O}$ melt at 2 kbar (on the H_2O -saturated solidus)..... 35

Figure 9. *PTX* evolution during PEC of a MI that traps a CO_2 -saturated $\text{NaAlSi}_3\text{O}_8\text{-CO}_2$ melt at 2 kbar (on the CO_2 -saturated solidus)..... 36

Figure 10. *PTX* evolution during PEC of a MI that traps a vapor-saturated $\text{NaAlSi}_3\text{O}_8\text{-H}_2\text{O-CO}_2$ melt at 2 kbar and 930°C 37

Figure 11. Concentrations of $\text{H}_2\text{O-CO}_2$ in melt inclusions from the Plinian fallout tuff at Pine Grove, Utah, reported by Lowenstern (1994)..... 38

Figure 12. Comparison of $\text{H}_2\text{O-CO}_2$ trends predicted by open-system degassing (dashed line) and as a result of PEC and bubble growth (solid line)..... 39

Chapter 2

Fig. 1. Reflective optical microscope photo of MIA hosted in plagioclase from White Island volcano in New Zealand..... 55

Fig. 2. Clinopyroxene from White Island scoriae showing characteristic growth zones defined by the entrapment of inclusions (MI, mixed MI and solid inclusions).....	55
Fig. 3. Variability diagrams for H ₂ O, F, and Cl concentrations of MIA hosted in clinopyroxene, orthopyroxene, and plagioclase from White Island.....	56
Fig. 4. H ₂ O contents variability associated to different working sessions.....	57
Fig. 5. Variability diagrams of CO ₂ and S concentrations of MIA hosted in clinopyroxene, orthopyroxene, and plagioclase from White Island.....	58
Fig. 6. Variability diagrams of H ₂ O, F, Cl, CO ₂ and S concentrations of MIA hosted in olivine and clinopyroxene from Solchiaro Sample.....	59
Fig. 7. CO ₂ depth profiles of exposed and unexposed MI from both White Island and Solchiaro samples.....	60
Fig. SM1. Calibration curves of CO ₂ . Known standard CO ₂ concentrations are plotted versus ¹² C/ ³⁰ Si isotope ratios measured by SIMS.....	67
Fig. SM2. Calibration curves of H ₂ O. Known standard H ₂ O concentrations are plotted versus ¹⁶ O ¹ H/ ³⁰ Si isotope ratios measured by the SIMS.....	68
Fig. SM3. Calibration curves of F. Known standard F concentrations are plotted versus ¹⁹ F/ ³⁰ Si isotope ratios measured by SIMS.....	69
Fig. SM4. Calibration curves of F. Known standard F concentrations are plotted versus ³² S/ ³⁰ Si isotope ratios measured by SIMS.....	70
Fig. SM5. Calibration curves of Cl. Known standard Cl concentrations are plotted versus ³⁵ Cl/ ³⁰ Si isotope ratios measured by SIMS.....	71
Fig. SM6. FIB image of a MI hosted in plagioclase of White Island.....	72
Fig. SM7. Microphotograph of a “pseudosecondary MIA” hosted in pyroxene.....	73
Fig. SM8. FIB image of a MI hosted in olivine from Solchiaro.....	73
Fig. SM9. Variability diagrams of CO ₂ concentration of single MIs.....	74
Chapter 3	
Fig. 1. a) Location of the Campi Flegrei area showing the distribution of volcanism in central-southern Italy (after Tonarini et al., 2004).....	113
Fig. 2. Back-scattered electron images of olivine phenocrysts from the Solchiaro eruption.....	114
Fig. 3. Compositions of MI from Solchiaro.....	115

Fig. 4. Compositions of corrected MI.....	116
Fig. 5. Primitive mantle-normalized incompatible trace element abundances (Sun & McDonough, 1989) of MI from Solchiaro obtained in this study.....	117
Fig. 6. Abundances of CO ₂ vs. Al ₂ O ₃ /CaO and CO ₂ vs. H ₂ O of all studied MI, shown according to sample.....	118
Fig. 7. Compositions of anomalous MI hosted in olivine from Solchiaro compared to volatile abundances of normal MI.....	119
Fig. 8. a) Variation in CO ₂ abundances with eruptive time in normal MI. b) Relative stratigraphic position of the Solchiaro samples.....	120
Fig. 9. Schematic representation of the dynamic evolution of the Solchiaro magmatic system showing where (when) in the overall evolution different MI were trapped and erupted to the surface.....	121
Chapter 4	
Fig. 1. The Linkam TS1400XY heating stage.....	135
Fig. 2. Heating experiment performed on quartz phenocryst from the Toba Tuff eruption in Sumatra.....	136
Fig. 3. Heating experiment performed on MI in an olivine phenocryst from scoriae of the Solchiaro eruption of the Phlegrean Volcanic District (PVD) in Southern Italy.....	137
Fig. 4. Heating experiment performed on MI contained in an olivine phenocryst from scoriae of the Solchiaro eruption of the Phlegrean Volcanic District (PVD) in Southern Italy.....	138
Fig. 5. Heating experiment performed on a melt inclusion in clinopyroxene from a nodule from the Sarno eruption at Mt Somma-Vesuvius in Southern Italy.....	139

INTRODUCTION

“The Earth is alive, and like humans, needs to breathe”. In a very general way, the Earth functions somewhat like the human body: we must provide fluids (water, oxygen, etc.) to our body in order to live. Our Earth does the same through its dynamic geochemical cycles. Broadly, the subducting lithosphere provides fluids to the interior, and volcanoes transfer out volatile species. Moreover, as water is integral to human cells, volatiles are integrated into minerals (e.g., as fluid or melt inclusions). This conceptual framework illustrates the paramount importance of understanding volatiles in magmatic systems. In fact, magmatic systems are the most crucial means by which fluids can be transported from the “deep” Earth to the surface, and even out of the atmosphere.

One of the problems to understanding volatile evolution in volcanic system is that volatiles dissolved in melt are difficult to measure directly with exception of degassed melts at the Earth’s surface. Melt inclusions (MI) are small samples of silicate melt that are trapped during magma crystallization. Once MI are entrapped, the host crystal isolate the MI from the external magmatic environment. For this reason, MI can provide direct information of volatile content dissolved in the entrapped melt. If the relative entrapment time of MI is known the evolution of volatiles can be studied. However, MI may undergo through important modifications due to post entrapment processes such as crystallization on the wall. In the last decade, researchers have studied how these processes can affect the reliability of MI.

Recently several authors have studied MI to understand the magma dynamic of active volcanic system based on MI. In fact under volatile saturated conditions, MI can provide depths of formation of phenocrysts. Most researchers have been able to track the magma ascent from deep in the crust to shallow depth.

The dissertation presented here represents six years of work from July 2006 to June 2012. The first three years, the PhD was carried out through an international fellowship sponsored by the *Ministero dell’Istruzione Università e Ricerca* (MIUR). The international research has been developed between the Department of Geosciences, Virginia Tech (PI, R.J. Bodnar) and the *Dipartimento di Scienze della Terra, Università di Napoli Federico II* (PI, B. De Vivo).

During these years, the results of the PhD program have been partially published in three different articles issued in international scientific journals with recognized impact factor. Other results produced during the PhD program have not yet been published in international scientific journal, but are currently submitted to the *Earth and Planetary Science Letters* for review or in preparation for other journals. In this thesis, I include the three scientific published papers plus the submitted work. Each study is here presented in four different chapters. The four works presented below show a defined scientific path I have developed during the six years of research. On the one hand, the works presented here focus on understanding the evolution of volatiles in magmatic system using melt inclusions (MI). On the other hand, the PhD research focuses on the reliability of the MI technique in understanding magmatic processes. Moreover, part of the research has consisted of testing the application of a newly designed heating stage by Linkam to MI studies. The publications carried out through these research directions show that critical approach to scientific research is necessary to achieve correct answers especially for methods or technique that have recently progressed such as the MI technique.

The first two chapters of this document are focused on testing the reliability of the MI technique especially in recording the pre-eruptive volatile content. The first chapter is a work that has been published in the *Journal of Petrology* and my contribution has been as second author. The work is a rigorous thermodynamic model predicting the H₂O-CO₂ variations of MI as crystallization occurs at the host/MI interface. In this study, the hypothetical MI is trapped in an albite crystal that grows from an H₂O-CO₂ saturated albitic melt. The study has important implications regarding the interpretation of H₂O-CO₂ systematic recorded by MI. In fact, trends obtained in this study closely resemble trends commonly interpreted as representing degassing of ascending magma.

The topic of the second chapter is the assessment of the reliability of MI technique and, in particular, is focused on the reliability of volatile abundance recorded by MI. In this study we have used groups of MI that were presumably entrapped all at the same time and, thus, at the same chemical and physical conditions, to test for variations of volatile contents. Groups of MI trapped at the same time are known in the literature as a Melt Inclusion Assemblages. In most of the cases, our results indicate that MI within a single MIA show consistent volatile concentrations, suggesting that MI are reliable tool to investigate pre-eruptive volatile content in volcanic system. The CO₂ content is not consistent in several cases, and the interpretation of the results is problematic. Like the first chapter, the results of this work have important implications on the interpretation of H₂O-CO₂ systematic recorded by MI.

The third chapter is a case study showing the application of MI for understanding magmatic processes. In this study, we have investigated the volatile evolution during the Solchiaro eruption in the Phlegrean Volcanic District. The paper contains an extensive dataset and in depth discussion of the data. First of all we have found a good correlation between the time of the eruption and the CO₂ and Cl contents of MI indicating that magma has ascended the crust from a deep reservoir and ponded at shallow depth before the eruption. In this dynamic model, the olivine phenocrysts that ascended from great depth were not ejected to the surface in later eruptive event because they sank or dissolved into the magma chamber. In this work also we have demonstrated that bubble-free MI better fit geochemical trends (which may relate to the results of the first chapter). Finally, we have reported anomalous MI compositions indicating mixing reactions between the ascending hot melt and stagnant mush zone.

The fourth chapter is a short paper illustrating the use of a new microscope heating stage developed by Linkam. The work consists of demonstrating the applicability of the Linkam TS1400XY to homogenize the MI and to quench the MI in a homogeneous glass state. The work focuses on the reheating experiments of MI of mafic composition hosted in olivine and pyroxene. These MI homogenize at high temperature and we tested for the optical quality at these high temperatures.

A more detailed introduction for each of the discussed topics is provided at the start of each chapter.

CHAPTER 1

Steele-MacInnis, M. J., *Esposito, R.* & Bodnar, R. J. (2011). Thermodynamic model for the effect of post-entrapment crystallization on the H₂O-CO₂ systematics of volatile saturated silicate melt inclusions. *Journal of Petrology*. 52, 12, 2461-2482.

Thermodynamic model for the effect of post-entrapment crystallization on the H₂O-CO₂ systematics of vapor-saturated, silicate melt inclusions

M. Steele-MacInnis, R. Esposito & R. J. Bodnar
Fluids Research Laboratory, Department of Geosciences, Virginia Tech
Blacksburg, VA 24061 USA

Abstract

Melt inclusions (MI) represent the best source of information concerning pre-eruptive volatile contents of magmas. If the trapped melt is enriched in volatile species, following trapping the MI may generate a vapor bubble containing volatiles that have exsolved from the melt. Thermodynamic modeling of vapor-saturated albitic composition (NaAlSi₃O₈) MI shows that the CO₂ content of the melt phase in the MI is sensitive to small amounts of post-entrapment crystallization (PEC), whereas the H₂O content of the melt is less sensitive to PEC. During PEC, CO₂ is transferred from the melt to the vapor phase and the vapor bubble may contain a significant amount, if not most, of the CO₂ in the MI. The contrasting behaviors of H₂O and CO₂ during PEC lead to H₂O-CO₂ trends that are similar to those predicted for open-system degassing during magma ascent and decompression. Thus, similar H₂O-CO₂ trends may be produced if 1) vapor-saturated MI are trapped at various depths along a magmatic ascent path, or 2) MI having the same volatile content are all trapped at the same depth, but undergo different amounts of PEC following trapping. It is not possible to distinguish between these two contrasting interpretations based on MI volatile data alone. However, by examining the volatile trends within the context of other geochemical monitors of crystallization or magma evolution progress, it may be possible to determine whether the volatile trends were generated along a degassing path or if they reflect various amounts of PEC in an originally homogeneous melt inclusion assemblage. The volatile trends resulting from PEC of MI described in this study are directly applicable to silica-rich (granitic) MI trapped in non-ferromagnesian host phases, and are only qualitatively applicable to more mafic melt compositions and/or host phases owing to modifications resulting from Fe exchange with the host and to post-entrapment reequilibration processes.

Keywords: melt inclusions; volatiles; post-entrapment crystallization; magmatic degassing; H₂O-CO₂

1. Introduction

Silicate melt inclusions (MI) represent samples of melt that are trapped during growth of igneous phenocrysts in a crystallizing magma body, and today MI are one of the major tools used to study igneous petrogenesis (Roedder, 1979; Lowenstern, 1995, 2003; Sobolev, 1996; Frezzotti, 2001; Danyushevsky *et al.*, 2002; Kent, 2008; Métrich & Wallace, 2008). Once the melt inclusion has become completely enclosed by the host phenocryst and isolated from the surrounding bulk melt from which the phenocryst is continuing to precipitate, the MI may continue to evolve physically and chemically, independent of the evolution of the melt outside of the phenocryst. At the moment that the MI is isolated from the bulk melt, it is unlikely to have a morphology that represents the minimum surface free energy of the system (sphere or negative-crystal shape). As a result, the MI will continue to mature through dissolution of material from the walls and re-precipitation elsewhere on the walls to achieve the lowest energy state, in a manner similar to the evolution in morphology that fluid inclusions undergo after trapping (*cf.*, Roedder, 1984, Fig. 2-15; Bodnar *et al.*, 1989). If dissolution and re-precipitation on the walls occurs in a closed system at essentially constant *PT* conditions, little or no net mass may be transferred from the melt phase into the host and the composition of the MI will not be affected by this morphological maturation process (Manley, 1996). If the host rock is subsequently erupted to the surface and cools rapidly, (preventing significant crystallization on the walls), the MI may be preserved as a homogeneous, single-phase glass (Fig. 1). In such cases, the MI are usually studied "*as found*", and the assumption that the glass composition represents the composition of melt in equilibrium with the host phase at the time of trapping is probably valid.

If, following trapping, the phenocryst containing MI cools relatively slowly, the MI may be modified in one of several ways. In the simplest case, some material from the melt may crystallize on the inclusion walls during cooling, resulting in a single-phase, homogeneous glass MI that has had some material removed and precipitated as host crystal. This post-entrapment crystallization (PEC) can occur while the phenocryst still resides in the magma chamber, or during ascent to the surface, or at the earth's surface, perhaps at the bottom of a volcanic pile or the base of a lava flow (where cooling rates are slower compared to the lava-air interface). If PEC occurs in any of these environments, the composition of the remaining melt (glass) phase in the MI may be significantly modified. Danyushevsky (2001) has developed a methodology to account for PEC-induced changes in composition for MI in olivine.

Larger MI and those that cooled somewhat more slowly often contain multiple phases when observed at room temperature, and may consist of any combination of glass, daughter crystals that grew from the melt during cooling, and one or more vapor bubbles (Roedder, 1984). Ideally, one would heat these MI in the laboratory to return the inclusion contents to a single, homogeneous melt state and then quench the MI to a glass before conducting microanalysis to determine the composition (Fig. 2; top). However, heating MI to homogenization can be problematic in some cases. First, many MI decrepitate during heating at one atmosphere, owing to the large internal pressures that are generated in volatile-rich MI (Fedele *et al.*, 2003; Student & Bodnar, 1996). In some cases, decrepitation of volatile-rich MI during heating may be eliminated or minimized by heating the MI in a hydrothermal vessel under a high confining pressure (Skirius *et al.*, 1990; Webster & Duffield, 1991; Anderson *et al.*, 2000; Thomas *et al.*, 2002; Student

& Bodnar, 2004; Bodnar & Student, 2006). Other workers have attempted to reconstruct the bulk composition without the necessity to homogenize the MI by determining the compositions of the various phases contained in the MI and then using their volumetric proportions to estimate the original melt composition (Szabo *et al.*, 1996), and Anderson (2010) recently described a technique involving focused ion beam (FIB) milling and SEM analysis to identify daughter phases and determine compositions of crystal-rich MI.

A second problem associated with heating MI to return them to their original melt (glass) state is the possibility of diffusive reequilibration of the inclusion during laboratory heating (Lu *et al.*, 1995; Zajacz *et al.*, 2009). Danyushevsky *et al.* (2000) have documented this behavior for MI in olivine, and Severs *et al.* (2007) have experimentally investigated H₂O loss from MI in quartz during laboratory heating, and Gaetani *et al.* (2011) described the effect of post-entrapment diffusion on the H₂O-CO₂ systematics of glassy MI in olivine.

Owing to the problems associated with heating MI to homogenization described above, some workers choose to study the inclusions "*as found*". Depending on the nature of the MI, the host phase, the analytical techniques used, and the problem being studied, this approach may not introduce serious errors. For example, single phase, glassy MI in quartz, such as those that are common in the Bishop Tuff (Anderson *et al.*, 2000) (Fig. 1), have likely only experienced some small amount of post-entrapment crystallization (PEC) of quartz on the inclusion walls. Thus, while the silica content of the melt may be reduced by a few percent at most if the MI are not heated before analysis, ratios of all other elements in the melt should be relatively unaffected. Additionally, if the study does not involve determination of the pre-eruptive volatile (especially H₂O and/or CO₂) content of the melt, the presence of a vapor bubble is unlikely to significantly affect abundances of major and trace elements in the glass (melt) phase. Finally, if the MI are analyzed by laser ablation ICPMS to determine only the major and trace element (non-volatile) content of the melt, homogenization of the MI is not necessary because all phases in the MI are sampled quantitatively during the analysis and the analytical results are easily corrected for contributions from the host phase (Halter *et al.*, 2002).

A potentially more serious problem occurs when the MI contains a vapor bubble and the goal of the study is to determine the pre-eruptive volatile content of the melt. The presence of a vapor bubble is especially problematic if the MI trapped a vapor-saturated melt, or if the melt became vapor-saturated as a result of post-entrapment crystallization following entrapment. In this study, we investigate the effect of post-entrapment crystallization and vapor bubble growth on the volatile content of the melt (glass) in MI. This quantitative model is based on rigorous thermodynamic and experimental data for volatile solubilities in melts and the volumetric properties of the MI system. We emphasize that the model assumes that equilibrium between the melt and volatile and host phases is maintained during cooling, but we also recognize that equilibrium is not always maintained in MI following trapping. We also document that at least in some cases the vapor bubble in MI contains sufficient CO₂ to be detectable by Raman spectroscopy, supporting the interpretation that the vapor bubble may contain a significant portion of the total volatiles in the MI. Finally, we document that H₂O-CO₂ trends that are often interpreted to represent trapping of vapor-saturated melt at various depths during continuous degassing and trapping of MI in an ascending magma can also be produced if a group of MI all trap a melt with the same composition (H₂O and CO₂

content), but undergo varying degrees of post-entrapment crystallization on the walls, such as might occur if the host phenocrysts are collected from different locations within a volcanic unit.

2. Previous Studies

Various workers have previously considered the effect of post-entrapment crystallization (PEC) and/or the presence of vapor bubbles on the measured volatile content of the glass phase in MI. Kress & Ghiorso (2004) considered the effect of PEC on compositions of MI based on thermodynamic modeling using the MELTS software. In the examples presented by these authors, the MI did not contain a vapor bubble and the MI did not become saturated in volatiles as a result of PEC. Based on their model, Kress & Ghiorso (2004) estimated that olivine-hosted MI from the June 30, 1997, Popocatepetl andesite pumice experienced 7.3% PEC that resulted in an increase in the H₂O content from the original 1.3 wt% to the measured 1.4 wt% following PEC. Similarly, orthopyroxene-hosted MI from a more siliceous portion of this same eruption experienced 3% PEC that raised the H₂O content from 2.7 wt% to 2.8 wt%. Finally, Kress & Ghiorso (2004) reported that a MI in plagioclase from Satsuma-Iwojima, Japan, underwent 29% PEC that increased the H₂O content from the original 2.88 wt% to the measured 3.99 wt% following PEC. While this amount of PEC is significant, similar amounts of PEC are common in MI from deeper volcanic or plutonic environments (Student & Bodnar, 1996; Bodnar & Student, 2006) (Fig. 2, bottom).

The MI considered by Kress & Ghiorso (2004) did not contain vapor bubbles, but many natural MI do contain one or more vapor bubbles, which are often referred to as “shrinkage” bubbles. Vapor bubbles in MI may form in various ways, depending on the melt composition and crystallization processes that occur inside of the MI after trapping. It is generally accepted that a shrinkage bubble should form as a natural consequence of cooling after MI entrapment, because thermal contraction (shrinkage) of the melt phase is significantly greater than that of the host phenocryst (Roedder, 1979; Lowenstern, 1995, 2003; Schiano, 2003; Métrich & Wallace, 2008). If the trapped MI is volatile-free, then the bubble is essentially a vacuum, since the vapor pressures of dry silicate melts are low.

In contrast, if the entrapped melt contains volatiles, the vapor bubble may contain some of the volatiles that were originally dissolved in the melt phase, as has been recognized by previous workers (c.f., Roedder, 1979; Anderson & Brown, 1993; Cervantes *et al.*, 2002). Skirius *et al.* (1990) noted that CO₂ and H₂O originally dissolved in the melt may be redistributed into vapor bubbles (and hydrous minerals) that form during cooling, and Anderson & Brown (1993) noted a wide range in CO₂ contents of MI in olivine from the 1959 Kilauea Iki eruption and attributed the variation to the transfer of CO₂ from the melt to the vapor bubbles that were found in some MI. Similarly, Cervantes *et al.* (2002) noted that MI in olivine from Puu Wahi at Mauna Loa, Hawaii, all contain vapor bubbles and showed CO₂ contents ranging from 60-180 ppm. When MI from this same sample were heated in the laboratory to homogenize the vapor back into the melt, followed by quenching, the glass contained 300-600 ppm CO₂. These workers related the difference in CO₂ contents of naturally quenched versus laboratory homogenized MI to the loss of CO₂ to the vapor bubble during cooling in nature.

In some MI, the vapor bubble may contain a relatively dense fluid phase at room temperature. For example, Raman analysis of a vapor bubble in an olivine-hosted MI

from the Solchiaro volcano, Procida Island (Italy) shows peaks characteristic of CO₂ (Fig. 3). The distance between the two peaks of the Fermi diad (Fig. 3) indicates that the density of the fluid in the bubble is $\sim 0.17 \text{ g/cm}^3$ (using the equation of Kawakami *et al.*, 2003, as modified by Fall *et al.*, 2011). Assuming that the fluid is pure CO₂, the internal pressure in the bubble is estimated to be 50 bars. Mass balance calculations indicate that the CO₂ contained in the vapor bubble represents $\approx 2/3$ of the total CO₂ in the MI (Table 1).

An important implication of the presence of vapor bubbles in volatile-bearing MI is related to pressures of trapping that are inferred from measured volatile contents of the glass phase, as has been emphasized by Anderson & Brown (1993) and Cervantes *et al.* (2002). Table 2 lists of some recent studies in which pressures of formation have been estimated based on data from MI that contain vapor bubbles and/or have experienced various degrees of PEC. Most of the MI are hosted in olivine. Because olivine-silicate melt equilibrium is well characterized, it is possible to accurately estimate the percentage of PEC that has occurred in olivine-hosted MI (Danyushevsky, 2001). The volume percent of the MI occupied by the bubble for studies listed in Table 2 ranged up to 20% (Spilliaert *et al.*, 2006), although most of the bubble-bearing MI showed $< 10\%$ PEC. All of the studies listed in Table 2 report a wide range of CO₂ concentrations in the glass, and thus a wide range in the estimated pressures of entrapment. This wide range in CO₂ contents and calculated trapping pressures for MI containing vapor bubbles and which have experienced PEC is consistent with results of the present study described below.

3. Description of the Quantitative Thermodynamic Model

3.1 Numerical Representation of the NaAlSi₃O₈-H₂O-CO₂ System

In order to quantitatively investigate the *PVTX* evolution in a MI during post-entrapment crystallization, numerical formulations are required to represent phase equilibria, volatile solubilities and volumetric properties of all phases. In this study, we apply a system of theoretical and empirical thermodynamic expressions to model the systems NaAlSi₃O₈-H₂O, NaAlSi₃O₈-CO₂, and NaAlSi₃O₈-H₂O-CO₂. The NaAlSi₃O₈-H₂O-CO₂ system is chosen because

- (1) it is a relatively “simple” system (relatively few components, compared to natural rhyolitic or basaltic compositions);
- (2) abundant experimental and theoretical data exist for this system (e.g, Burnham & Davis, 1971, 1974; Egglar & Kadik, 1979; Hamilton & Oxtoby, 1986; Stolper *et al.*, 1987; Bohlen *et al.*, 1982);
- (3) the topology of the NaAlSi₃O₈-H₂O-CO₂ system (along with SiO₂-H₂O-CO₂) forms the basis of our current understanding of phase relations in crystallizing melt-volatile systems (Hack *et al.*, 2007);
- (4) the *PVTX* thermodynamic relations derived from this system can be extended with confidence to other melt-volatile systems (Burnham & Davis, 1974; Burnham, 1997) and;
- (5) numerical expressions describing the *PVTX* properties and phase relations in this system are available, or can be developed from existing experimental data.

In the following sections we describe the numerical models used to characterize the *PTX* phase relations on the H₂O-, CO₂- and H₂O-CO₂-saturated albite solidi, the *PTX* dependence of H₂O and CO₂ solubility in the melt phase, and the *PTX* dependence of the molar volumes of melt, vapor and albite.

3.2 *PTX* correlations on the vapor-saturated solidus

For the binary systems NaAlSi₃O₈-H₂O and NaAlSi₃O₈-CO₂, the Gibbs Phase Rule ($f = c - p + 2$) specifies a single degree of freedom if three phases are present, indicating that the system is univariant. Therefore, the 3-phase coexistence is described by a *line* or *curve* in *PTX* space. We may thus describe *T* as a function of *P* (or vice-versa) along the three-phase albite + melt + vapor curve. A consequence of this geometry is that if the temperature of a two-component NaAlSi₃O₈-H₂O or NaAlSi₃O₈-CO₂ MI containing albite + melt + vapor changes, the internal pressure must change accordingly to maintain all three phases (as discussed in the previous section).

In this study, data for the H₂O-saturated albite solidus from Burnham & Davis (1974) are used. We performed a regression of data for the H₂O-saturated solidus, and used the regression equation to numerically describe *T* on the 3-phase curve as a function of *P*. The CO₂-saturated solidus is approximately equal to the dry (H₂O-absent) solidus up to 10 kbar, as shown by Burnham & Davis (1974) and Bohlen *et al.* (1982). We thus represent the CO₂-saturated solidus based on a linear regression of data for the NaAlSi₃O₈-H₂O system from Burnham & Davis (1974) where $a_{H_2O} = 0$. The regression equation for the H₂O-saturated solidus is given by:

$$T = 888 - 76 \ln(P) \quad (6)$$

and that for the CO₂-saturated solidus as:

$$T = 1121 + 20P \quad (7)$$

In both equations, *T* is in degrees Celsius and *P* is in kbar. Equations (6) and (7) reproduce temperature along the solidus curves to within $\pm 1\%$, over the range 50 bar to 8 kbar for H₂O (Eqn. 6), and over the range 1 bar to 9 kbar for CO₂ (Eqn. 7). The H₂O- and CO₂-saturated solidus curves calculated using Eqns. (6) and (7) are shown in Fig. 4.

For the ternary system NaAlSi₃O₈-H₂O-CO₂, the Gibbs' Phase Rule specifies two degrees of freedom if three phases are present, and the system is therefore divariant. Thus, in the ternary system the 3-phase coexistence is described by a *surface* in *PTX* space. In this case, we may describe *T* as a function of *P* & *X*.

In the numerical model, we incorporated the a_{H_2O} -dependent vapor-saturated albite solidus reported by Burnham & Davis (1974, their Fig. 19) to represent the H₂O-CO₂ saturated solidus and fitted a regression equation to describe *T* as a function of *P* and a_{H_2O} . Note that a_{H_2O} refers to the activity of H₂O in both the melt and vapor phases because we use the same standard state, which is pure H₂O at *P* & *T*, for both phases. The Burnham & Davis model was chosen to maintain internal consistency between the *PTX* position of the solidus and the H₂O solubility calculations, which are based on data from Burnham & Davis (1971, 1974). Although significant discrepancy exists between the *PTX* location of the solidus surface from Burnham & Davis compared to the solidus locations reported by Egger & Kadik (1979) and Bohlen *et al.* (1982), the three models show a similar topology, such that *PTX trends* describing the change in location of the solidus as a function of a_{H_2O} are the same for each of these models. Furthermore, to

verify that the *PVTX* evolution predicted in this study is independent of the exact *PTX* coordinates of the solidus surface, reconnaissance modeling using the Bohlen *et al.* (1982) solidus data was conducted and found to yield the same trends as described here based on the Burnham & Davis data.

The regression equation describing the *PTX* location of the NaAlSi₃O₈-H₂O-CO₂ solidus is given by:

$$T = \exp(7.011 - 4.768 \times 10^{-3} P + 4.187 \times 10^{-4} \tilde{P}^3 + 1.116 \times 10^{-4} \tilde{P}^4 - 7.184 \times 10^{-5} \tilde{P}^5 + 7.414 \times 10^{-6} \tilde{P}^6 - 0.3019 a_{H_2O} + 2.652 \times 10^{-2} \tilde{a}_{H_2O}^2 - 0.3884 \tilde{a}_{H_2O}^3 - 3.394 \times 10^{-2} \tilde{P} \tilde{a}_{H_2O} + 1.895 \times 10^{-4} \tilde{P}^4 \tilde{a}_{H_2O} - 6.057 \times 10^{-5} \tilde{P}^5 \tilde{a}_{H_2O} + 5.185 \times 10^{-6} \tilde{P}^6 \tilde{a}_{H_2O}) \quad (8)$$

where T is in degrees Celsius, P is in kbar, and $\tilde{P} = P - 4.255$ and $\tilde{a}_{H_2O} = a_{H_2O} - 0.575$.

Equation (8) reproduces the Burnham & Davis (1974) albite solidus temperature to within $\pm 3\%$, over the range 50 bar to 10 kbar and from $a_{H_2O} = 1$ to $a_{H_2O} = 0.1$. Equation (8) does not reproduce the most CO₂-rich part of the solidus ($a_{H_2O} < 0.1$) because of the pronounced change in the slope and curvature of the solidus that occurs between approximately $a_{H_2O} = 0.1$ and $a_{H_2O} = 0$. Iso-activity lines for H₂O calculated from Equation (8) are shown in Fig. 4.

3.3 Solubilities of H₂O and CO₂ in the melt phase

The solubility of H₂O in the melt phase is described as a function of P , T & the activity of H₂O (a_{H_2O}) by the model of Burnham & Davis (1974, their equations 20 and 21) and Burnham (1997; his equation 3.6). When the volatile component is pure H₂O, the melt is saturated in H₂O when $a_{H_2O} = 1$. When the volatile component is a mixture of H₂O and CO₂, a_{H_2O} is calculated from the equation of state (EOS) for the vapor phase (Holloway, 1977, 1987; Flowers, 1979). Only relatively small differences between $X_{H_2O}^{vapor}$ and a_{H_2O} occur at the *PT* conditions investigated here, which is consistent with the near ideal mixing of H₂O and CO₂ at these conditions (Holloway, 1977; Flowers, 1979).

The solubility of CO₂ in the melt phase is calculated from the model of Fine & Stolper (1986) as implemented by Holloway & Blank (1994, their equations 13, 22 and 23) using their parameters for rhyolite melts. Equation 13 of Holloway & Blank (1994) is equivalent to equation 4 of Stolper *et al.* (1987), which is specifically for albitic melts. However, here we use the parameters from Holloway & Blank (1994) for rhyolitic melts, rather than the albite melt parameters from Stolper *et al.* (1987), because the model of Stolper *et al.* was fitted to data between 15 and 30 kbar, whereas the parameters of Holloway & Blank (1994) were fitted to data covering a wider range of pressures, including the lower pressure region considered here ($P < 5$ kbar). We note, however, that the *PTX trends* in CO₂ solubility predicted using parameters from Stolper *et al.* (1987) are identical to those predicted using the parameters from Holloway & Blank (1994).

The CO₂ solubility model requires knowledge of the fugacity of CO₂ (f_{CO_2}) at the given *PTX* conditions. In our implementation, f_{CO_2} is calculated using the EOS for H₂O-CO₂ (Holloway, 1977, 1987; Flowers, 1979).

The solubility of H₂O in the melt is a function of a_{H_2O} while the solubility of CO₂ is a function of f_{CO_2} . Thus, as the proportion of CO₂ in the system is increased, a_{H_2O} and H₂O solubility in the melt decrease, whereas f_{CO_2} and CO₂ solubility in the melt increase. Isobars of H₂O and CO₂ solubility in the melt and vapor-phase composition isopleths calculated as described above are shown in Fig. 6. While there is some difference in absolute values, the magnitudes and trends of the solubility and vapor-phase composition estimates are consistent with values predicted in other studies (Newman & Lowenstern, 2002; Papale, 1999).

3.4 Volume of the H₂O, CO₂ and H₂O-CO₂ fluid phase

The EOS of Haar *et al.* (1984) is used to describe the molar volume of pure H₂O as a function of P & T . At magmatic PT conditions, H₂O is in the supercritical state and L-V immiscibility is not encountered.

The modified Redlich-Kwong EOS of Holloway (1977, 1987) is used to describe the molar volume of the fluid as a function of P , T & X for pure CO₂ and for H₂O-CO₂ mixtures. The activities and fugacities of the components are also calculated using the EOS (Holloway, 1977, 1987) with the correction reported by Flowers (1979). At magmatic PT conditions, pure CO₂ is always in the supercritical state so L-V immiscibility does not occur, and H₂O and CO₂ are completely miscible at all temperature above 374.1°C, the critical temperature of H₂O (Sterner & Bodnar, 1991). Thus, volatile-phase immiscibility does not occur at magmatic PT conditions for any of the volatile phases considered here. We note, however, that in more complex natural systems containing various salts in addition to H₂O and CO₂, volatile (vapor)-phase immiscibility is common (De Vivo *et al.*, 1995; Frezzotti, 2001).

3.5 Volume of the melt phase

The molar volume of the melt phase is calculated from the partial molar volumes of each component in the melt as:

$$V^{melt} = X_{NaAlSi_3O_8}^{melt} \bar{V}_{NaAlSi_3O_8}^{melt} + X_{H_2O}^{melt} \bar{V}_{H_2O}^{melt} + X_{CO_2}^{melt} \bar{V}_{CO_2}^{melt} \quad (9)$$

The partial molar volume of the NaAlSi₃O₈ and H₂O components are from Burnham & Davis (1971, their equations 8 and 9). The partial molar volume of CO₂ in the melt phase is assigned a constant value of 28.6 cm³/mol from Lange (1994) after Stolper *et al.* (1987). The variations in partial molar volume of NaAlSi₃O₈ and H₂O in the melt along the vapor-saturated solidus at $P \leq 4$ kbar are shown on Fig. 7.

3.6 Volume of the crystallized albite phase

The molar volume of the albite phase is described as a function of P & T by the regression EOS of Burnham & Davis (1971, their equation 6).

4. Implementation of the Closed, Isochoric, Post-Entrapment Crystallization Model

4.1 Binary NaAlSi₃O₈-H₂O and NaAlSi₃O₈-CO₂ Models

The first step in the numerical model is to define the initial conditions (Fig. 5). A fixed mass of the NaAlSi₃O₈ component is selected (because the $PVTX$ evolution path at equilibrium is scale-independent, the actual mass chosen is not important). An initial

pressure, or pressure of entrapment of the MI, is specified, and the system is represented by a single-phase vapor-saturated melt. Thus, the initial temperature (the temperature on the vapor-saturated solidus at the initial pressure) is calculated from either Equation (6) or (7), depending on which binary system is being considered.

At the initial PT conditions (the trapping conditions), the solubility of H_2O or CO_2 is determined from the solubility model, and that amount of H_2O or CO_2 is added to the melt. The total mass of the MI is the mass of $NaAlSi_3O_8$ plus the mass of the volatile component, either H_2O or CO_2 . The molar volume of the melt is calculated from the composition and partial molar volumes of the various components using Equation (9). The total MI volume is equal to the initial vapor-saturated melt volume. The total mass and volume of the inclusion (represented by crystals + vapor + melt) remains constant in all subsequent steps as PEC proceeds, to maintain a closed, isochoric system.

PEC is simulated by crystallizing albite from the melt in fixed increments (one percent of initial melt mass crystallized at each step). The PEC mass is subtracted from the mass of $NaAlSi_3O_8$ in the melt, and is added to the mass of crystallized albite (which is initially zero before PEC begins). The mass of H_2O or CO_2 dissolved in the remaining melt is determined from the solubility model, and the remainder (the total mass of H_2O or CO_2 in the MI minus the mass in the melt) is added to the vapor (which is initially zero, before PEC and vapor exsolution begin). The net inclusion volume is calculated as the sum of the volumes of melt *plus* albite *plus* vapor.

If the calculated net volume is any value other than the initial volume (\pm the acceptable tolerance), the pressure is incremented and the temperature, volatile solubility and phase volumes are recalculated. Note that during the pressure iteration, the vapor density and the solubility of H_2O and/or CO_2 in the melt change in response to pressure (and temperature) changes, so these parameters must be recalculated for each pressure iteration. The pressure iteration continues until the net inclusion volume equals the initial volume, and the $PVTX$ conditions are recorded, representing the $PVTX$ conditions consistent with closed system, isochoric equilibrium in the MI for the given amount of PEC. The calculation process is repeated as additional increments of albite melt are crystallized.

4.2 Ternary $NaAlSi_3O_8$ - H_2O - CO_2 System

The calculation method described above for the binary systems applies to the ternary system as well. However, because of the added degree of freedom on the vapor-saturated solidus in the three-component $NaAlSi_3O_8$ - H_2O - CO_2 system compared to the binary systems, the iterative procedure used in the ternary model is modified.

To establish the initial conditions, an initial mass of $NaAlSi_3O_8$ is chosen and the initial pressure *and* temperature in the system are specified. The initial a_{H_2O} is estimated from Equation (8) and the solubility of H_2O in the melt phase is calculated as a function of P , T & a_{H_2O} . The composition of the vapor phase that is in equilibrium with a melt having the specified a_{H_2O} is calculated from the EOS of Holloway (1977, 1987) (note that although the vapor composition in equilibrium with the initial melt is calculated, zero grams of vapor are present initially). The solubility of CO_2 in the melt phase is determined as a function of P , T & f_{CO_2} and the masses of H_2O and CO_2 necessary to achieve vapor saturation are added to the melt. The total mass of melt is the sum of the

masses of NaAlSi₃O₈ plus H₂O plus CO₂. As with the binary models, the total mass, the masses of the individual components and the total volume are held constant in all subsequent steps.

As in the binaries, a fixed mass of albite is crystallized during each step. However, because the solidus in the ternary system is divariant, pressure and a_{H_2O} can vary independently (with T fixed for any P- a_{H_2O} combination). Therefore, in order to uniquely determine the PTX point representing closed system, isochoric equilibrium for each albite crystallization increment, an additional constraint is required. This constraint is provided by the number of moles of CO₂ in the vapor phase ($n_{CO_2}^{vapor}$), which can be computed by two independent methods, and the values calculated by the two methods are only equal at a single PTX point. The iterative procedure therefore involves cycling through values of a_{H_2O} at each pressure increment to find the P- a_{H_2O} combination that satisfies the closed system isochoric condition as well as the conservation of CO₂ requirement as described below.

First, the mass of H₂O dissolved in the melt phase is determined from the solubility of H₂O at the P & T . The remaining amount of H₂O that cannot be accommodated by the melt is partitioned into the vapor phase. The total mass of H₂O in the vapor phase is converted to moles using the molar mass of H₂O. The mole fraction of CO₂ in the vapor phase is calculated from the a_{H_2O} of the vapor phase using the EOS of Holloway (1977, 1987) for H₂O-CO₂. The number of moles of CO₂ in the vapor is calculated from the number of moles of H₂O in the vapor and the mole fraction of CO₂ in the vapor phase according to:

$$n_{CO_2}^{vapor} = \left(\frac{1}{X_{CO_2}^{vapor}} - 1 \right)^{-1} n_{H_2O}^{vapor} \quad (10)$$

where $n_{H_2O}^{vapor}$ is the number of moles of H₂O in the vapor phase and $X_{CO_2}^{vapor}$ is the mole fraction CO₂ in the vapor phase.

The number of moles of CO₂ in the vapor phase, $n_{CO_2}^{vapor}$, may also be calculated starting from the melt composition. The number of moles of CO₂ in the melt, $n_{CO_2}^{melt}$, is computed from the solubility of CO₂ in the melt (calculated as a function of P , T & f_{CO_2} using the solubility model) and the number of moles of NaAlSi₃O₈ in the melt, according to

$$n_{CO_2}^{melt} = \left(\frac{1}{X_{CO_2}^{melt}} - 1 \right)^{-1} n_{NaAlSi_3O_8}^{melt} \quad (11)$$

The number of moles of CO₂ in the vapor phase equals the number of moles of CO₂ remaining after the amount of CO₂ in the melt phase is subtracted from the total (or bulk) amount of CO₂,

$$n_{CO_2}^{vapor} = n_{CO_2}^{total} - n_{CO_2}^{melt} \quad (12)$$

where $n_{CO_2}^{total}$ is the total number of moles of CO₂ in the MI. The amount of CO₂ in the vapor phase calculated from Equations (10) and (12) must be equal to satisfy the requirement of conservation of mass, and this only occurs at a single PT condition.

The iterative procedure employed to determine the closed system, isochoric, equilibrium *PTX* point corresponding to each increment of albite crystallization is represented by a pair of nested iteration loops, in which a_{H_2O} is first incremented at constant *P* to determine the *TX* point satisfying conservation of CO₂ from Equations (10) and (12), followed by *P* iteration to constrain the *PTX* condition that satisfies the isochoric conditions that requires constant MI volume. After the *PVTX* condition that satisfies the closed system, isochoric equilibrium requirement is determined for a given amount of albite crystallization, the conditions are recorded (output) and the model proceeds to crystallize the next increment of albite. The simulated albite crystallization procedure may be continued to predict the *PVTX* evolution of the MI to crystallization of 100% of the silicate component if desired.

Our conceptual model for the *PVTX* evolution in volatile-bearing MI during post-entrapment crystallization is constrained by Roedder's Rules as applied to MI by Bodnar & Student (2006), and assuming chemical equilibrium is maintained at each step. Therefore, in our conceptual model:

1. The MI is entrapped as a homogeneous, single-phase silicate melt;
2. The total mass and bulk composition of the MI, represented by melt + vapor + crystal formed during PEC, do not change after entrapment;
3. The system is isochoric and the total volume of the MI, represented by melt + vapor + crystal formed during PEC, is constant after entrapment; and
4. Phase changes (crystallization, vapor exsolution) occur at the equilibrium phase boundaries.

Conditions (1) to (3) represent Roedder's Rules, while condition (4) assumes chemical equilibrium. In addition to these four constraints, we specify

5. The melt phase is saturated in volatiles (H₂O, CO₂ or H₂O-CO₂) at the time of entrapment.

Condition (5) is added because any interpretation of volatile contents in natural MI in the context of magmatic degassing ("degassing paths") requires that MI trap a vapor-saturated melt. It follows from condition (5) that the MI is trapped at *PTX* conditions that are on the vapor-saturated solidus (Fig. 4), as discussed in detail later. Our model may be easily modified to accommodate trapping of a melt that is originally volatile-undersaturated, but which later becomes saturated as a result of PEC (see Student & Bodnar, 1996; their Fig. 4E, F).

We acknowledge that some or all of conditions (1) to (5) may be violated in some natural MI. However, the assumed conditions represent a reasonable approximation for many natural MI. Bodnar & Student (2006) described the petrographic procedures necessary to identify melt inclusion assemblages (MIA), combined with microthermometry and microanalysis to demonstrate that MI adhere to Roedder's Rules (conditions 1 to 3). The isochoric condition (condition 3) is a reasonable approximation for MI because the compressibility and thermal expansion of the host phase are small in comparison to the melt (\pm vapor). In our model, as in that of Student & Bodnar (1996), the volume of the MI includes the volume of host phase precipitated on the inclusion walls during PEC. The equilibrium condition (condition 4) is certainly violated in many natural MI because they contain a silicate glass, which is a metastable phase. However, evidence of nucleation and growth of crystals and bubbles in natural MI is commonly observed, and can be approximated by equilibrium behavior down to the glass transition

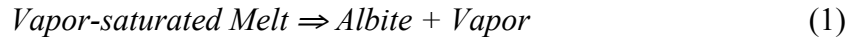
temperature (which can occur after significant post-entrapment crystallization and bubble growth have occurred).

Within the framework of conditions (1) to (5), we investigate the effects of post-entrapment crystallization on the internal pressure in the inclusion and the volatile composition of the melt phase. Starting with trapping of a single-phase, vapor-saturated melt of known mass, composition and volume, we model the effect of crystallization on the *PVTX* evolution of the MI.

A flow chart outlining the calculation procedure used in the numerical model is shown in Fig. 5. Initial conditions are represented by a fixed mass of melt of known composition trapped as a MI at a known temperature and pressure. Using available *PVTX* data for volatile-bearing melts, the volume of the MI is calculated, then the silicate melt component is allowed to crystallize in 1% increments. The solubilities of H₂O and CO₂ in the melt at the *P* & *T* are used to calculate the amounts of these volatiles that may be dissolved in the melt – any difference between this value and the total amount in the original melt is assumed to be contained in the vapor bubble. The total volume of the MI after each increment of crystallization, represented by the sum of the volume of remaining melt *plus* the volume of material that crystallized from the melt *plus* the volume of the vapor bubble, represents the new volume of the MI. If this new volume equals the original volume, this step in the model is completed and the calculations can be stopped or another increment of crystallization may be examined.

In general, after each stage of crystallization the new volume will not equal the original volume because the sum of the volumes occupied by the crystallized phase and the vapor bubble are not equal to their partial molar volumes in the melt. As a result, because of the requirement of constant volume, the pressure in the inclusion must be adjusted to find a new pressure at which the density of the volatile phase (and, therefore, its volume) and the solubility of the volatile phase in the melt are such that the sum of the volumes (crystals + vapor-saturated melt + vapor bubble) equals the original MI volume. Thus, the model incrementally increases or decreases the pressure, depending on whether the new volume is greater than or less than the original volume, until a pressure is obtained that satisfies the requirement of constant volume and mass of the MI.

Consider a melt inclusion with a composition represented by the system NaAlSi₃O₈-H₂O-CO₂. Crystallization of some portion of the vapor-saturated melt may be described by the relationship



and the volume change (ΔV_r) of reaction (1) can be expressed as:

$$\Delta V_r = X_{\text{NaAlSi}_3\text{O}_8} \Delta V_{\text{NaAlSi}_3\text{O}_8}^{\text{melt} \Rightarrow \text{xl}} + X_{\text{H}_2\text{O}} \Delta V_{\text{H}_2\text{O}}^{\text{melt} \Rightarrow \text{vapor}} + X_{\text{CO}_2} \Delta V_{\text{CO}_2}^{\text{melt} \Rightarrow \text{vapor}} \quad (2)$$

where X_i represents the mole fraction of component “*i*”, and $\Delta V_i^{\alpha \Rightarrow \beta}$ represents the change in volume of component “*i*” as it moves from phase α to phase β . The volume terms in Equation (2) are further given by

$$\Delta V_{\text{NaAlSi}_3\text{O}_8}^{\text{melt} \Rightarrow \text{xl}} = V_{\text{NaAlSi}_3\text{O}_8}^{o,\text{xl}} - \bar{V}_{\text{NaAlSi}_3\text{O}_8}^{\text{melt}} \quad (3)$$

$$\Delta V_{\text{H}_2\text{O}}^{\text{melt} \Rightarrow \text{vapor}} = \bar{V}_{\text{H}_2\text{O}}^{\text{vapor}} - \bar{V}_{\text{H}_2\text{O}}^{\text{melt}} \quad (4)$$

$$\Delta V_{\text{CO}_2}^{\text{melt} \Rightarrow \text{vapor}} = \bar{V}_{\text{CO}_2}^{\text{vapor}} - \bar{V}_{\text{CO}_2}^{\text{melt}} \quad (5)$$

where \bar{V}_i^α is partial molar volume of component *i* in phase α , and $V_{\text{NaAlSi}_3\text{O}_8}^{o,\text{xl}}$ is the molar volume of crystalline albite at the *P* & *T* of the MI. The net ΔV_r of crystallization of a

mole of vapor-saturated melt of a given composition is thus a function of the partial molar volumes of NaAlSi₃O₈, H₂O and CO₂ in the melt, the partial molar volumes of H₂O and CO₂ in the vapor, and the molar volume of albite. For models involving only a pure (one-component) vapor phase, the partial molar volumes of H₂O and CO₂ in the vapor phase are equal to the molar volumes, and these were calculated using the algorithms of Haar *et al.* (1984) and Holloway (1977, 1987), respectively.

Each of the parameters contributing to the net ΔV_r in Equations (1) to (4) vary as functions of P & T , and the partial molar volumes of H₂O and CO₂ in the vapor also vary as functions of the vapor composition (Sterner & Bodnar, 1991). The molar volume of albite ($V_{NaAlSi_3O_8}^{o,xl}$) at PT conditions considered here is approximately 102 ± 1 cm³/mol, while $\bar{V}_{NaAlSi_3O_8}^{melt}$ is usually ~ 10 cm³/mol greater than the molar volume of albite at the same P & T (Burnham & Davis, 1974), yielding a $\Delta V_{NaAlSi_3O_8}^{melt \Rightarrow xl}$ of about -10 cm³/mol. In other words, the volume occupied by the crystalline albite is smaller than the volume occupied by albite melt at the same P & T conditions. The partial molar volume of H₂O in the vapor phase, $\bar{V}_{H_2O}^{vapor}$, varies over the range of about 50-150 cm³/mol (Holloway, 1977, 1987), whereas the partial molar volume of H₂O in the melt, $\bar{V}_{H_2O}^{melt}$, varies between ≈ 14 -22 cm³/mol (Lange, 1994; Burnham & Davis, 1971), such that $\Delta V_{H_2O}^{melt \Rightarrow vapor}$ varies from about $+36$ to $+128$ cm³/mol. Note that the large difference between the partial molar volume of H₂O in the melt and the molar volume of H₂O vapor at the same temperature and pressure is the main driver for the large pressure increase associated with exsolution of H₂O from a hydrous melt (Burnham, 1979, 1997; Student & Bodnar, 1996). The partial molar volume of CO₂ in the vapor, $\bar{V}_{CO_2}^{vapor}$, varies over the range 25-115 cm³/mol (Holloway, 1977; 1987), whereas the partial molar volume of CO₂ in the melt, $\bar{V}_{CO_2}^{melt}$, is about 28.6 cm³/mol (Stolper *et al.*, 1987; Lange, 1994). Thus, $\Delta V_{CO_2}^{melt \Rightarrow vapor}$ varies between -3 and $+86$ cm³/mol. Given the ranges in values presented above, the volume change associated with vapor-saturated crystallization can thus be negative or positive, depending on the PT conditions and the proportions of NaAlSi₃O₈, H₂O and CO₂ in the melt. Because the system is isochoric, the direction of volume change associated with volatile exsolution from the melt thus determines whether the pressure in the MI increases or decreases during PEC and this, in turn, determines whether the volatile content of the remaining melt (glass) in the MI increases or decreases during PEC.

In the isochoric MI model, the net volume change is always zero and we invoke the principle that pressure and volume are inversely related. If PEC predicts an increase in volume (positive ΔV_r), which is not permitted in our constant volume model, then the internal pressure in the MI is increased incrementally to determine the pressure that results in a constant volume. Thus, for an NaAlSi₃O₈-H₂O MI, the NaAlSi₃O₈ crystallization term [$\Delta V_{NaAlSi_3O_8}^{melt \Rightarrow xl}$; Eqn. (3)] predicts a decrease in pressure because the volume change is negative, whereas the H₂O term [$\Delta V_{H_2O}^{melt \Rightarrow vapor}$; Eqn. (4)] predicts an increase in pressure during PEC because the volume change is positive. A consequence of the relatively high solubility of H₂O in silicate melt is that the pressure evolution of an H₂O-rich MI during post-entrapment crystallization is controlled by the difference

between the partial molar volume of the H₂O component in the melt and the molar volume of H₂O in the vapor, which results in an increase in internal pressure during post-entrapment crystallization (Student & Bodnar, 1996). In contrast, because of the relatively low solubility of CO₂ in silicate melts, the *PVTX* evolution of a CO₂-rich MI is dominated by the difference between the partial molar volume of the NaAlSi₃O₈ component in the melt and the molar volume of crystalline albite, resulting in a decrease in internal pressure during PEC.

The solubilities of H₂O and CO₂ both increase with increasing pressure (Burnham & Davis, 1971; Mysen *et al.*, 1976; Egglar & Kadik, 1979; Hamilton & Oxtoby, 1986; Stolper *et al.*, 1987; Blank *et al.*, 1993). Thus, for an H₂O-rich MI, the internal pressure increases as H₂O exsolves from the melt during crystallization. The increase in pressure increases H₂O solubility in the melt, and H₂O continues to exsolve until a pressure is achieved that satisfies mass and volume balance in the isochoric system (Student & Bodnar, 1996). The net result is that the mass and volume of the H₂O vapor bubble are less than would be expected under isobaric conditions. For the CO₂-rich MI, the decrease in internal pressure caused by post-entrapment crystallization results in decreased CO₂ solubility, and the CO₂ concentration of the melt decreases during PEC. The mass and volume of exsolved CO₂ in the isochoric model are thus greater than they would be if crystallization occurred isobarically.

The evolution of internal pressure in the MI must be accompanied by a systematically related evolution in temperature. The correlation between *P* & *T* must be consistent with the Gibbs' Phase Rule and with known phase equilibria in the melt-volatile system (Fig. 4). Because the system under consideration consists of melt plus crystals plus vapor, *PT* conditions during PEC are constrained to lie on the vapor-saturated solidus. Therefore, as the internal pressure changes in response to crystallization and volatile exsolution, the temperature must change accordingly to remain on the vapor-saturated solidus. Furthermore, for an H₂O-saturated MI, temperature decrease is accompanied by an *increase* in pressure, while for a CO₂-saturated MI, decrease in temperature is accompanied by a *decrease* in pressure. This behavior is consistent with the above discussion contrasting the evolution of internal *P* during post-entrapment crystallization in H₂O-rich versus CO₂-rich MI. We note that the direction of pressure change during PEC is controlled by the relative change in solubility combined with the difference between the partial molar volumes of the volatiles in the melt compared to their molar volumes, within the constraint that the entire system remains isochoric. The methodology followed in our numerical model is to incrementally crystallize aliquots of the melt and monitor the bubble growth and evolution of *P* & *T* based on known phase equilibrium and thermodynamic properties of the melt-volatile system. This is accomplished by iterating in pressure to find the *PT* conditions that satisfy mass balance under the restriction that the system must remain isochoric.

5. Results of Simulations of the *PVTX* Evolution of Melt Inclusions During Post-Entrapment Crystallization

For each of the NaAlSi₃O₈-H₂O, NaAlSi₃O₈-CO₂ and NaAlSi₃O₈-H₂O-CO₂ systems described above, several PEC simulations were conducted, ranging from zero to 100% crystallization and starting at various *PTX* conditions. However, because the amount of

PEC reported in studies of natural MI rarely exceeds about 20% (Johnson *et al.*, 2008), we limit the discussion to MI that have experienced $\leq 25\%$ PEC.

As described in the conceptual model above, the *PVTX* trend for the NaAlSi₃O₈-H₂O system differs significantly from that for NaAlSi₃O₈-CO₂, reflecting the significant differences in volumetric properties and solubilities of H₂O and CO₂, as well as differences in the *PTX* topologies of the NaAlSi₃O₈-H₂O and NaAlSi₃O₈-CO₂ systems. The ternary system combines features of each of the two end-member systems, and *PVTX* trends for the ternary system may mimic either of the binaries, depending on the bulk volatile composition of the MI and the amount of PEC.

Below we present examples of the *PVTX* evolution of MI for the two binary systems and the ternary NaAlSi₃O₈-H₂O-CO₂ system. The discussion emphasizes general trends observed in the simulations, which are mainly independent of the specific starting conditions. For each example below, the MI is assumed to be trapped at 2 kbar under vapor-saturated conditions. The *PTX* evolution trends of the MI up to 25% PEC are summarized in Figs 8-10.

5.1 The system NaAlSi₃O₈-H₂O

As albite is progressively crystallized from an NaAlSi₃O₈-H₂O melt and H₂O vapor is exsolved, the internal pressure in the inclusion increases and the temperature decreases accordingly to maintain *PT* conditions on the H₂O-saturated solidus (i.e., to maintain the coexistence of three phases, as described above). In the example shown in Fig. 8, an H₂O-saturated MI trapped at 2 kbar shows an increase in internal pressure of approximately 500 bar (from 2 to ≈ 2.5 kbar) during 25% PEC. This result is consistent with results of Student & Bodnar (1996) for MI in the system H₂O-haplogranite.

As H₂O vapor is exsolved from the melt during PEC, the internal pressure increases and this results in an increase in H₂O solubility in the melt phase. Therefore, the melt phase becomes enriched in H₂O (relative to the H₂O content of the melt that was originally trapped in the MI) with increasing crystallization, despite the fact that H₂O is being exsolved from the melt during PEC (Fig. 8). The H₂O content of the melt (glass) phase increases by about 10% during 25% PEC.

The vapor bubble occupies about 6.5 volume percent of the MI after 25% PEC, which corresponds to a spherical bubble with a diameter of about 20 μm in a spherical MI with a diameter of 50 μm (Fig. 8). To calculate the volume percent occupied by the bubble, we use the expression:

$$\text{volume \% bubble} = \frac{\text{volume of vapor}}{\text{volume of vapor} + \text{melt}} \times 100\% \quad (13)$$

which neglects the volume of albite precipitated on the inclusion walls. The albite volume is not included in this calculation because the albite that crystallized during PEC would likely not be recognized during routine petrography - only the melt (glass) phase and the vapor bubble would be recognized. [Note that 25% PEC for a spherical MI that was originally 50 μm in diameter would result in a rim of albite on the walls that is about 2-3 μm thick, and 10% PEC would produce an albite rim $\approx 1\mu\text{m}$ thick]. Neglecting the volume of albite that crystallized on the walls during PEC in the computation of the volume percent bubble means that the volume percent vapor shown on Figs 8-10 is slightly greater than the volume percent of vapor that would be estimated if the MI is considered to include melt (glass) + vapor + crystallized albite. Note, however, that the

volume of albite crystallized on the walls was included in the iterative calculation to determine the isochoric solution to the PEC model.

5.2 The system $\text{NaAlSi}_3\text{O}_8\text{-CO}_2$

In contrast to the MI that traps an H_2O -saturated melt, the internal pressure for a CO_2 -saturated MI *decreases* during PEC. For example, a MI trapped at 2 kbar experiences a pressure decrease of 1.5 kbar (from 2 to 0.5 kbar) during 25% PEC (Fig. 9). As the pressure decreases during PEC, the temperature also decreases, as is required for the *PTX* conditions to remain on the CO_2 -saturated solidus in the $\text{NaAlSi}_3\text{O}_8\text{-CO}_2$ system (Fig. 9).

As the internal pressure in the MI decreases during PEC, the solubility of CO_2 in the melt also decreases, resulting in a lowering of the CO_2 content in the melt phase. In the example shown in Fig. 9, the CO_2 content in the melt phase decreases from about 1350 ppm in the original trapped melt to < 400 ppm CO_2 after 25% PEC, representing a decrease of more than 70%. The reduction in CO_2 content in the melt is accompanied by growth of a vapor bubble that occupies about two volume percent of the inclusion after 25% PEC. The relatively small volume occupied by the bubble, coupled with the relatively large change in CO_2 content of the melt, illustrates the significant effect that even a small amount of PEC can have on the CO_2 content in the melt. The density of the vapor bubble after 25% PEC is 0.16 g/cm^3 . According to Rosso & Bodnar (1995), CO_2 vapor with density greater than about 0.1 g/cm^3 is readily detectable in inclusions using Raman spectroscopy. Thus the CO_2 in this vapor bubble could be detected by Raman spectroscopic analysis, as was done for the MI in olivine from Procida Island (Fig. 3) (Esposito *et al.*, in press).

5.3 The system $\text{NaAlSi}_3\text{O}_8\text{-H}_2\text{O-CO}_2$

In general, the *PTX* evolution of MI that are saturated in an $\text{H}_2\text{O-CO}_2$ vapor phase (Fig. 10) follows a path during the early stage of PEC that is more similar to the CO_2 -saturated end-member (see Fig. 9), evolving with continued PEC towards a path that is similar to that of an H_2O -saturated end-member (see Fig. 8). Whereas the mole fraction of H_2O in the melt and that in the vapor in equilibrium with the melt are generally of the same order of magnitude (Fig. 6), the mole fraction of CO_2 in the melt can be several orders of magnitude less than the mole fraction of CO_2 in the vapor because CO_2 partitions preferentially into the vapor phase. Meanwhile, because the activity of H_2O in the system increases with decreasing temperature (Fig. 4), the vapor and melt become increasingly enriched in H_2O as the temperature decreases during continued PEC. The tendency towards increased H_2O in the melt and in the vapor (relative to CO_2) drives the system towards a *PTX* evolution path that is more similar to the path for $\text{NaAlSi}_3\text{O}_8\text{-H}_2\text{O}$ as PEC continues.

Any H_2O -bearing MI in which $a_{\text{H}_2\text{O}}$ is less than about 0.95 will follow a *PT* path characterized by an initial decrease in the internal pressure with decreasing temperature during PEC. As the internal pressure decreases, $a_{\text{H}_2\text{O}}$ increases, and the *PT* evolution undergoes a transition from decreasing pressure to increasing pressure as PEC continues and the *PT* conditions approach the H_2O -saturated solidus. Because the activity of CO_2 in the system is finite (albeit low, at lower temperature), the MI cannot intersect the H_2O -saturated solidus but, rather, approaches it asymptotically (Fig. 10). If crystallization were to continue to > 25% PEC (or if the initial trapped melt composition were more

H₂O-rich), the internal pressure in the inclusion would continue to increase, and might eventually exceed the trapping pressure (Fig. 10), similar to the trend shown by the H₂O-saturated MI described above (Fig. 8). This dramatic increase in pressure for MI that experience large amounts of PEC provides a likely explanation for the large number of MI in plutonic rocks that appear to have decrepitated during PEC (Student & Bodnar, 2004).

The change in concentrations of H₂O and CO₂ in an NaAlSi₃O₈-H₂O-CO₂ MI during $\leq 25\%$ PEC are shown in Fig. 10c. The concentration of CO₂ in the original trapped melt is ~ 520 ppm, and after 25% PEC the CO₂ content of the melt has been reduced to ~ 60 ppm. Whereas the CO₂ content of the melt phase *decreases* by an order of magnitude during PEC, the H₂O content *increases* from ~ 3.8 to ~ 4.7 wt %, or to about 25% above its initial value. These results are similar to those reported by Blundy & Cashman (2008) for crystallization of a vapor-saturated melt under isobaric conditions. The similarity between the H₂O-CO₂ evolution of melts in a magma body during isobaric crystallization predicted by Blundy & Cashman (2008) and that occurring during isochoric crystallization in a MI reported in this study highlights the importance of careful petrography to identify melt inclusion assemblages (MIA; Bodnar & Student, 2006) and the need to combine volatile data with other geochemical monitors of magma evolution to distinguish between processes that are occurring at the scale of a magma chamber and those that are occurring within individual MI.

The reduction in CO₂ content of the melt by an order of magnitude (from ~ 520 ppm to ~ 60 ppm) is associated with a vapor bubble that occupies < 2.5 volume % of the MI. As a result, in MI studies the presence of a vapor bubble in the MI should be noted, even if it appears to occupy only a very small proportion of the total MI volume. And, if possible, the MI should be heated in an attempt to dissolve the volatile phase back into the melt before analysis, and/or the bubbles should be analyzed by Raman spectroscopy to test for presence of volatiles (especially CO₂). Failure to do so could result in misleading and incorrect interpretations of the MI volatile systematics.

6. Application of model to other melt compositions and host phases

The quantitative model described here was developed for the system NaAlSi₃O₈-H₂O-CO₂ because detailed phase equilibrium and thermodynamic data are available for this system. An important question then is: *To what extent do the results presented here apply to melts of other compositions and trapped in host phases other than albite?* Data are not available to permit a rigorous quantitative evaluation for the wide range in natural melt compositions and host minerals for MI reported in the literature. However, it is possible to identify natural melt compositions for which the pressure and volatile evolution paths estimated here for the albite-H₂O-CO₂ system might be applicable.

The volatile evolution path that an MI follows during post-entrapment crystallization is mainly a function of four factors. The first factor, and the one that has the largest effect on the *PT* path, is the absolute solubilities of H₂O and CO₂ in the melt phase. The higher the solubility, the greater the amount of H₂O and/or CO₂ that will be released during crystallization of an aliquot of melt. At 3 kbar and 900°C, the solubility of H₂O in albite melt is 7.6 wt %, compared to a solubility of 7.7 wt % in rhyolite melt at these same conditions, calculated using the VolatileCalc model of Newman & Lowenstern (2002). Moreover, the rate of change in H₂O solubility with changing pressure for albite and

rhyolite melts is similar in this *PT* range. As a result, the amount of H₂O that would be exsolved from each increment of rhyolite melt that crystallizes would be essentially the same as the amount exsolved during crystallization of albite melt. Thus, the contribution of H₂O exsolution during PEC to the pressure increase in the MI for rhyolitic melt would be essentially the same as for albite melts, and we may assume that the results for the albite-H₂O system may be applied to H₂O-rich rhyolitic MI. Moreover, because arc dacites and rhyolites are typically very depleted in CO₂ relative to H₂O (Wallace, 2005; his Fig. 8), we may further assume that results for the albite-H₂O system are generally applicable to silica-rich (dacitic to rhyolitic) MI based on H₂O solubility data.

A second factor that affects the pressure-volatile content path followed by MI during PEC is the relative volume change of the melt phase as the *PT* conditions in the MI change during PEC. This factor (along with the volume of fusion discussed below) constrains the volume available for the exsolved volatiles to occupy, which in turn affects the density of the volatile phase and the pressure in the MI. Because the volume changes associated with thermal expansion are about an order of magnitude larger than those predicted from the compressibility data, we will focus our discussion on the thermal expansion. Few data are available for the thermal expansion and compressibility of real melts, but Lange & Carmichael (1990) summarized the relative volume changes of silicate melts as a function of the oxide components in the melt. The ratios (on a molar basis) of the oxide components Na₂O:Al₂O₃:K₂O:CaO:FeO:Fe₂O₃:MgO in a typical rhyolite melt are 1.0:2.27:0.80:0.35:0.27:0.16:0.17. Using these ratios to approximate the composition of a rhyolite melt and thermal expansion data for these components from Lange & Carmichael (1990; their Table 3), the average coefficient of thermal expansion for a rhyolite melt is $5.30 \times 10^{-3} \text{ cm}^3/\text{mol}\cdot\text{K}$. This compares to a coefficient of thermal expansion for albitic melt (Na₂O) of $7.41 \times 10^{-3} \text{ cm}^3/\text{mol}\cdot\text{K}$. This means that, compared to albite melt, a rhyolitic melt will "shrink" by about 30% less as a result of cooling during PEC. This, in turn, indicates that there will be less volume available to accommodate the exsolved vapor phase, and its density and the internal pressure in the MI will therefore be higher compared to an albitic melt. The net result is that the effect on the H₂O content of the melt during PEC will be enhanced relative to the effect predicted for the pure albite MI.

A third factor that affects the pressure-volatile content path followed by the MI during PEC is the volume change of the host phase during cooling. As with the melt phase above, the change in molar volume of the host phase as a result of pressure changes is considerably smaller than that resulting from temperature changes over the limited pressure range investigated here, and we will limit our discussion to the thermal expansion of the host phase. Skinner (1966) summarized thermal expansion data for a wide range of materials, including many common hosts to MI. Over the temperature range 1000°C → 600°C, the molar volume of albite (Ab₉₉An₁) decreases by 1.31 %. For comparison, over this same temperature range the volume of intermediate (Or₆₇Ab₃₃) and K-rich (Or_{83.5}Ab_{16.5}) alkali feldspar change by 1.43% and 0.96%, respectively. Thus, the change in volume available for the melt to occupy as a result of cooling for MI in intermediate composition feldspars is essentially the same as for MI in albite, whereas the volume change is slightly smaller for K-rich feldspar. For K-rich feldspar hosts, the density of the vapor phase and the internal pressure will be slightly greater compared to MI in albite owing to the smaller volume available for the vapor phase.

The mineral quartz is unlike most other hosts for MI in the sense that the molar volume of β -quartz *increases* by 0.23% during cooling from 1000°C to 600°C (Skinner, 1966). At temperatures below the quartz α/β transition at approximately 573°C (at one bar pressure), α -quartz shows the more typical behavior of decreasing volume with decreasing temperature. Many MI in volcanic settings are likely trapped in β -quartz (see Student & Bodnar, 1999; their Fig. 3q). As the MI cools, the volume available for the MI to occupy *increases* as the molar volume of quartz increases. For all other common mineral hosts for MI, the decrease in volume of the host phase during cooling is to a large extent balanced by the increase in volume available for the bubble owing to shrinkage of the melt during cooling. However, for MI trapped in β -quartz, the volume changes associated with the host phase molar volume change and the change in volume associated with melt phase shrinkage are additive. The net result is that the volume available for the vapor bubble to occupy is considerably larger for MI in quartz, compared to other common host phases, and this in turn will lead to lower densities for the volatile phase in the bubble, and concomitantly lower pressures in the MI and lower volatile solubilities in the remaining melt phase.

The fourth factor that influences the *PT* volatile path is the volume change associated with crystallization of the melt on the inclusion walls, i.e., the volume of fusion. Lange & Carmichael (1990) summarized volumes of fusion for 12 common minerals, including albite. The volume of fusion of albite is 8.64 cm³/mol. Other reported values are sanidine (9.75 cm³/mol), anorthite (5.48 cm³/mol), diopside (12.62 cm³/mol), fayalite (5.49 cm³/mol) and forsterite (5.53 cm³/mol). Bourova & Richet (1998) report a volume of fusion for quartz of 3.85 cm³/mol. Comparing these values, the contribution of crystallization to the volume available for the vapor bubble would be larger for MI in diopside and sanidine (compared to albite-hosted MI), and would be smaller for MI in anorthite and olivine. The result is that the density of the vapor phase and the pressure in MI in diopside and sanidine would be lower compared to MI in albite, and higher in MI in anorthite and olivine.

Based on the results presented above we conclude that the quantitative model developed for the system albite-H₂O-CO₂ is generally applicable to intermediate composition silicate MI trapped in non-ferromagnesian host minerals. This interpretation is consistent with results predicted for a haplogranite melt by Student & Bodnar (1996). The anomalous thermal expansion of β -quartz suggests that the predicted "degassing" of the melt in a quartz-hosted MI would be enhanced as the host volume increases while the melt density increases (and its volume decreases). This further suggests that volatile contents of the melt (glass) phase in quartz-hosted MI are even more sensitive to PEC compared to those hosted in albite and other common MI host phases.

7. Discussion of modeling results – implications for natural MI

The model described here assumes that equilibrium is maintained between the melt, volatile and host phase during cooling and PEC, while recognizing that such is not always the case for natural MI. It is likely that in nature a rapidly cooled MI may nucleate a vapor bubble without experiencing PEC – in this case the results described here are not applicable.

One of the most striking results of this study is the observation that relatively small amounts of PEC can have a large influence on CO₂ contents of MI that trap CO₂-bearing

or H₂O-CO₂-bearing melts. Moreover, a relatively small vapor bubble may contain a significant portion, if not most, of the CO₂ in the MI. In contrast, the concentration of H₂O in the melt phase is relatively less sensitive to PEC and bubble formation. This result is consistent with the observations of Cervantes *et al.* (2002), who found that CO₂ contents in homogenized MI from picrites from Puu Wahi, Mauna Loa were generally significantly higher (by several hundred ppm) than those in “naturally-quenched,” bubble-bearing MI from the same site, whereas the H₂O contents of homogenized and non-homogenized MI showed little difference. Anderson & Brown (1993) corrected for the amount of CO₂ contained in the vapor bubble in natural MI from the 1959 Kilauea Iki picrite by adding to each measured CO₂ content of the melt (glass) an amount of CO₂ that would be contained in a bubble occupying 0.5 volume percent of the inclusion at the vapor pressure of CO₂ in the melt at 1200°C. This correction resulted in an increase in the estimated pressure of trapping by up to a few hundred bar for most MI, and in some cases increased the pressure by more than a kbar.

Perhaps the most significant observation of this study is that H₂O-CO₂ trends produced during closed system PEC and bubble growth in MI (Fig. 10c) are similar to open-system degassing paths. Owing to the lower solubility of CO₂ in the melt compared to H₂O, relatively more CO₂ is lost from the melt phase during ascent and degassing, resulting in a trend in H₂O-CO₂ contents characterized by a wide range in CO₂ contents with relatively small variation in H₂O (Fig. 11a). In Fig. 11a, H₂O-CO₂ data from Lowenstern (1994) are plotted using the same axis scaling as in that study. However, if both axes are scaled to the respective ranges in the data (Fig. 11b), no trend in H₂O vs. CO₂ is apparent. In other words, there is no correlation between H₂O and CO₂ contents in this data set. As such, H₂O-CO₂ data from natural MI rarely show *statistically significant* trends consistent with open-system degassing paths. Instead, when trends similar to those shown in Fig. 11a are observed, workers often assume that the MI were trapped along a degassing path, with the most CO₂-rich MI being trapped at the greatest depth. Often, no petrographic or other geochemical evidence is offered to support the interpretation that the H₂O-CO₂ trends represent a degassing path.

Open-system degassing is one explanation for the apparent vertical or sub-vertical trends in H₂O-CO₂ contents often observed in studies of MI. The results of this study show that similar H₂O-CO₂ trends may be generated as a result of PEC in vapor-saturated MI. To demonstrate the significance of this point, Fig. 12 shows the H₂O-CO₂ data from Lowenstern (1994), along with an H₂O-CO₂ path that would be produced as a result of PEC, calculated as described above. The calculated trend assumes trapping of an H₂O-CO₂-saturated melt at 4.5 kbar and 895°C, followed by various amounts of PEC. As seen in Fig. 12, the H₂O-CO₂ trend resulting from bubble growth during PEC provides an alternative explanation for the trend in the H₂O-CO₂ data. It should be noted that Lowenstern (1994) analyzed only MI with ≤ 0.5 volume percent vapor, in an effort to eliminate (or minimize) possible errors associated with loss of some of the volatiles to the vapor bubble. However, even if the bubble occupies only one volume percent of the MI, the CO₂ content of the melt is reduced by nearly an order of magnitude. Thus, the CO₂ content of the melt can show wide variability as a result of PEC, even if inclusions with only relatively small bubbles are analyzed. We emphasize that we agree with the interpretation of Lowenstern (1994) that the trend shown by MI from Pine Grove is a result of degassing. That is precisely why this is a good example to use for this

comparison – the Pine Grove MI define a *real* degassing path that *looks just like* a path that would result from PEC, which highlights the difficulty in distinguishing between these phenomena based solely on the H₂O-CO₂ systematics of the MI.

Lowenstern (personal communication, 2010) noted that the H₂O-CO₂ trends resulting from PEC resemble most closely those for open-system degassing, whereas the model presented here assumes a closed system. The reason for this difference is that calculated closed-system degassing paths are normally isothermal, not isochoric, whereas the PEC calculation in the model is isochoric rather than isothermal. This is an important difference because, in the NaAlSi₃O₈-H₂O-CO₂ system, decreasing temperature in the presence of melt + albite + vapor results in an increase in the equilibrium activity of H₂O, and H₂O is thus “retained” in the melt, and does not exsolve as readily as in the closed-system degassing path. This results in a near-vertical trend in H₂O versus CO₂ concentration, which looks more like a typical open-system degassing path than a typical closed-system degassing path. The important point here is that, if an H₂O-CO₂ trend is the result of PEC but is not recognized as such, the trend would likely be interpreted to represent trapping of MI along an open-system degassing path.

Pseudo-degassing paths can also be produced by processes other than PEC. Recently, Gaetani *et al.* (2011) performed reequilibration experiments to assess the effect of diffusion on H₂O-CO₂ concentrations of glassy MI hosted in olivine. These workers showed that CO₂ concentrations are unaffected by diffusion, whereas H₂O concentrations are reset on timescales of a few hours. MI with initially different H₂O concentrations, when reequilibrated with the same magma at the same conditions, attain similar H₂O concentrations. If several MI with a range in volatile concentrations reequilibrated together, then the MI would consequently have a range of CO₂ concentrations but similar H₂O concentrations. Thus, a suite of MI with a random distribution of H₂O and CO₂ concentrations may develop an apparent H₂O-CO₂ trend resembling an open-system degassing path owing to hydrogen diffusion (Gaetani *et al.*, 2011).

8. Summary

A rigorous thermodynamic model has been developed to estimate the evolution in volatile contents of melt inclusions during post-entrapment crystallization (PEC) of a vapor-saturated melt under isochoric conditions. Owing to the relatively high solubility of H₂O in silicate melts, combined with the fact that the partial molar volume of H₂O dissolved in the melt is generally much smaller than the molar volume of H₂O in the vapor phase, the internal pressure in an NaAlSi₃O₈-H₂O MI increases during PEC and the amount of H₂O in the melt phase increases slightly. Conversely, the internal pressure in an NaAlSi₃O₈-CO₂ MI and the CO₂ concentration in the melt phase both decrease during PEC, owing to the lower solubility of CO₂ in the melt and the relatively small difference between the partial molar volume of CO₂ in the melt and the molar volume of CO₂ in the vapor. For MI that trap an NaAlSi₃O₈-H₂O-CO₂ melt, the internal pressure first decreases during PEC as mostly CO₂ exsolves from the melt, and later increases as the exsolving vapor phase becomes more H₂O-rich. The quantitative model described here is directly applicable to intermediate to silica-rich (dacitic to rhyolitic) MI trapped in host phases that do not contain iron as a major component. For MI trapped in Fe-bearing hosts, trends similar to those described here may be produced through diffusive reequilibration (Gaetani *et al.*, 2011).

The trends in H₂O-CO₂ contents of MI during PEC and vapor bubble formation are similar to trends expected for open-system degassing of an ascending magma. Without additional supporting data, it may not be possible to determine which process is responsible for producing the observed H₂O-CO₂ trends. Given the potential for PEC and associated bubble formation to affect the volatile concentrations in the melt (glass) phase in MI, we recommend that MI with vapor bubbles be heated to dissolve the volatiles back into the melt, followed by quenching to produce a homogeneous, glassy MI, and/or that the vapor bubbles be analyzed by Raman spectroscopy to test for the presence of CO₂. In addition, the presence or absence of vapor bubbles and the relative bubble size should be recorded and accompany all interpretations of volatile contents of MI.

9. Acknowledgements

The authors thank Leonid Danyushevsky for discussions concerning the use of Petrolog software and implications of post-entrapment crystallization on melt inclusion composition. Discussions with Jim Webster, Luca Fedele and Bob Lowell improved our understanding of the role and behavior of volatiles in melts. Thorough reviews by Jake Lowenstern, Leonid Danyushevsky, Paul Wallace and Wendy Bohrsen helped to clarify our thinking and significantly improved an earlier version of the manuscript. This work was supported by funding from the Institute for Critical Technology and Applied Science at Virginia Tech (MJS-M), the U. S. National Science Foundation (RJB), and through a project coordinated by Benedetto De Vivo from the Italian Ministry of University Research (RE).

10. References

- Anderson, A. J. (2010). Accurate phase volume ratio determination of crystal-rich inclusions by focused ion beam milling and microanalysis. *Geochimica et Cosmochimica Acta* 74S, A19.
- Anderson, A. T., Davis, A. M. & Lu, F. (2000). Evolution of Bishop Tuff rhyolitic magma based on melt and magnetite inclusions and zoned phenocrysts. *Journal of Petrology* 41, 449-473.
- Anderson, A. T., Jr. & Brown, G. G. (1993). CO₂ contents and formation pressures of some Kilauean melt inclusions. *American Mineralogist* 78, 794-803.
- Blank, J. G., Stolper, E. M. & Carroll, M. R. (1993). Solubilities of carbon dioxide and water in rhyolitic melt at 850 degrees C and 750 bars. *Earth and Planetary Science Letters* 119, 27-36.
- Blundy, J., & Cashman, K. (2008). Petrologic reconstruction of magmatic system variables and processes. *Reviews in Mineralogy and Geochemistry* 69, 179-239.
- Bodnar RJ, Binns PR & Hall DL (1989). Synthetic fluid inclusions. VI. Quantitative evaluation of the decrepitation behavior of fluid inclusions in quartz at one atmosphere confining pressure. *Journal of Metamorphic Geology*, 7, 229-242.
- Bodnar, R. J. & Student, J. J. (2006). Melt inclusions in plutonic rocks: Petrography and microthermometry. In: Webster, J. D. (ed.) *Melt Inclusions in Plutonic Rocks: Mineralogical Association of Canada, Short Course 36*, 1-26.

- Bohlen, S. R., Boettcher, A. L. & Wall, V. J. (1982). The system albite-H₂O-CO₂; a model for melting and activities of water at high pressures. *American Mineralogist* 67, 451-462.
- Bourova, E. & Richet, P. (1998). Quartz and cristobalite: High-temperature cell parameters and volumes of fusion. *Geophysical Research Letters* 25, 2333-2336.
- Burnham, C. W. (1979). Magmas and hydrothermal fluids. In: Barnes, H. L. (ed.) *Geochemistry of Hydrothermal Ore Deposits*. New York: John Wiley & Sons, 71-136.
- Burnham, C. W. (1997). Magmas and hydrothermal fluids. In: Barnes, H. L. (ed.) *Geochemistry of Hydrothermal Ore Deposits*. New York: John Wiley & Sons, 63-125.
- Burnham, C. W. & Davis, N. F. (1971). The role of H₂O in silicate melts: I. P-V-T relations in the system NaAlSi₃O₈-H₂O to 10 kbar and 1000 degrees C. *American Journal of Science* 270, 54-79.
- Burnham, C. W. & Davis, N. F. (1974). The role of H₂O in silicate melts: II. Thermodynamic and phase relations in the system NaAlSi₃O₈-H₂O to 10 kbar, 700 degrees to 1100 degrees C. *American Journal of Science* 274, 902-940.
- Cervantes, P., Kamenetsky, V. & Wallace, P. (2002). Melt inclusion volatile contents, pressures of crystallization for Hawaiian picrites, and the problem of shrinkage bubbles. *Eos, Transactions, American Geophysical Union* 83, F1495-F1496.
- Cervantes, P. & Wallace, P. (2003). Magma degassing and basaltic eruption styles; a case study of approximately 2000 year BP Xitle Volcano in central Mexico. *Journal of Volcanology and Geothermal Research* 120, 249-270.
- Collins, S. J., Pyle, D. M. & Maclennan, J. (2009). Melt inclusions track pre-eruption storage and dehydration of magmas at Etna. *Geology* 37, 571-574.
- Danyushevsky, L. V. (2001). The effect of small amounts of H₂O on crystallisation of mid-ocean ridge and backarc basin magmas. *Journal of Volcanology and Geothermal Research* 110, 265-280.
- Danyushevsky, L. V., Della Pasqua, F. N. & Sokolov, S. (2000). Re-equilibration of melt inclusions trapped by magnesian olivine phenocrysts from subduction-related magmas: petrological implications. *Contributions to Mineralogy and Petrology* 138, 68-83.
- Danyushevsky, L. V., McNeill, A. W. & Sobolev, A. V. (2002). Experimental and petrological studies of melt inclusions in phenocrysts from mantle-derived magmas: an overview of techniques, advantages and complications. *Chemical Geology* 183, 5-24.
- De Vivo, B., Torok, K., Ayuso, R.A., Lima, A. & Lirer, L. (1995). Fluid inclusion evidence for magmatic silicate/saline/CO₂ immiscibility and geochemistry of alkaline xenoliths from Ventotene island, Italy. *Geochimica et Cosmochimica Acta*, 59, 2941-2953.
- Eggler, D. H. & Kadik, A. A. (1979). The system NaAlSi₃O₈-H₂O-CO₂ to 20 kbar pressure: I. Compositional and thermodynamic relations of liquids and vapors coexisting with albite. *American Mineralogist* 64, 1036-1048.
- Esposito, R., Bodnar, R. J., Danyushevsky, L. V., De Vivo, B., Fedele, L., Hunter, J., Lima, A. & Shimizu, N. (2011). Volatile evolution of magma associated with the

- Solchiaro eruption in the Phlegrean Volcanic District (Italy). *Journal of Petrology*, in press.
- Fall, A., Tattitch, B. & Bodnar, R. J. (2011). Combined microthermometric and Raman spectroscopic technique to determine the salinity of H₂O-CO₂-NaCl fluid inclusions based on clathrate melting. *Geochimica et Cosmochimica Acta* 75, 951-964.
- Fedele, L., Bodnar, R. J., DeVivo, B. & Tracy, R. (2003). Melt inclusion geochemistry and computer modeling of trachyte petrogenesis at Ponza, Italy. *Chemical Geology* 194, 81-104.
- Fine, G. & Stolper, E. (1986). Dissolved carbon dioxide in basaltic glasses; concentrations and speciation. *Earth and Planetary Science Letters* 76, 263-278.
- Flowers, G. C. (1979). Correction of Holloway's (1977) adaptation of the modified Redlich-Kwong equation of state for calculation of the fugacities of molecular species in supercritical fluids of geologic interest. *Contributions to Mineralogy and Petrology* 69, 315-318.
- Frezzotti, M. L. (2001). Silicate-melt inclusions in magmatic rocks; applications to petrology. *Lithos* 55, 273-299.
- Gaetani, G., O'Leary, J. & Shimizu, N. (2011). Post-entrapment changes to H₂O and CO₂ in olivine-hosted melt inclusions. *Mineralogical Magazine* 75, 879.
- Haar, L., Gallagher, J. S. & Kell, G. S. (1984). NBS/NRC steam tables: thermodynamic and transport properties and computer programs for vapor and liquid states of water in SI units. Washington, D.C.: Hemisphere Publishing Corporation.
- Hack, A. C., Thompson, A. B. & Aerts, M. (2007). Phase relations involving hydrous silicate melts, aqueous fluids, and minerals. *Reviews in Mineralogy and Geochemistry* 65, 129-185.
- Halter, W. E., Pettke, T., Heinrich, C. A. & Rothen-Rutishauser, B. (2002). Major to trace element analysis of melt inclusions by laser-ablation ICP-MS; methods of quantification. *Chemical Geology* 183, 63-86.
- Hamilton, D. L. & Oxtoby, S. (1986). Solubility of water in albite-melt determined by the weight-loss method. *Journal of Geology* 94, 626-630.
- Hauri, E. H. (2002). SIMS analysis of volatiles in silicate glasses 2: Isotopes and abundances in Hawaiian melt inclusions. *Chemical Geology* 183, 115-141.
- Holloway, J. R. (1977). Fugacity and activity of molecular species in supercritical fluids. In: Fraser, D. (ed.) *Thermodynamics in Geology*. Boston, MA: Reidel, 161-181.
- Holloway, J. R. (1987). Igneous fluids. *Reviews in Mineralogy* 17, 211-233.
- Holloway, J. R. & Blank, J. G. (1994). Application of experimental results to C-O-H species in natural melts. *Reviews in Mineralogy* 30, 187-230.
- Johnson, E. R., Wallace, P. J., Cashman, K. V., Granados, H. D. & Kent, A. J. R. (2008). Magmatic volatile contents and degassing-induced crystallization at Volcan Jorullo, Mexico; implications for melt evolution and the plumbing systems of monogenetic volcanoes. *Earth and Planetary Science Letters* 269, 477-486.
- Kamenetsky, V. S., Pompilio, M., Métrich, N., Sobolev, A. V., Kuzmin, D. V. & Thomas, R. (2007). Arrival of extremely volatile-rich high-Mg magmas changes explosivity of Mount Etna. *Geology* 35, 255-258.
- Kawakami, Y., Yamamoto, J. & Kagi, H. (2003). Micro-Raman Densimeter for CO₂ Inclusions in Mantle-Derived Minerals. *Applied Spectroscopy* 57, 1333-1339.

- Kent, A. J. R. (2008). Melt inclusions in basaltic and related volcanic rocks. *Reviews in Mineralogy and Geochemistry* 69, 273-331.
- Kress, V. C. & Ghiorso, M. S. (2004). Thermodynamic modeling of post-entrapment crystallization in igneous phases. *Journal of Volcanology and Geothermal Research* 137, 247-260.
- Lange, R. A. (1994). The effect of H₂O, CO₂ and F on the density and viscosity of silicate melts. *Reviews in Mineralogy* 30, 331-369.
- Lange, R. A. & Carmichael, I. S. E. (1990). Thermodynamic properties of silicate liquids with emphasis on density, thermal expansion and compressibility. In: Nicholls, J. & Russell, J. K. (eds.) *Modern Methods of Igneous Petrology: Understanding Magmatic Processes: Mineralogical Society of America, Reviews in Mineralogy* 24, 25-64.
- Lowenstern, J. B. (1994). Dissolved volatile concentrations in an ore-forming magma. *Geology* 22, 893-896.
- Lowenstern, J. B. (1995). Applications of silicate-melt inclusions to the study of magmatic volatiles. In: Thompson, J. F. H. (ed.) *Magmas, fluids and ore deposition: Mineralogical Association of Canada, Short Course* 23, 71-99.
- Lowenstern, J. B. (2003). Melt inclusions come of age; volatiles, volcanoes, and Sorby's legacy. In: De Vivo, B. & Bodnar, R. J. (eds.) *Melt Inclusions in Volcanic Systems: Methods, Applications and Problems*. Amsterdam: Elsevier.
- Lu, F., Anderson, A. T. & Davis, A. M. (1995). Diffusional gradients at the crystal/melt interface and their effect on the composition of melt inclusions. *Journal of Geology* 103, 591-597.
- Mangiaccapra, A., Moretti, R., Rutherford, M., Civetta, L., Orsi, G. & Papale, P. (2008). The deep magmatic system of the Campi Flegrei Caldera (Italy). *Geophysical Research Letters* 35, L21304.
- Manley, C. R. (1996). Morphology and maturation of melt inclusions in quartz phenocrysts from the Badlands rhyolite lava flow, southwestern Idaho. *American Mineralogist* 81, 158-168.
- Métrich, N. & Wallace, P. J. (2008). Volatile abundances in basaltic magmas and their degassing paths tracked by melt inclusions. *Reviews in Mineralogy and Geochemistry* 69, 363-402.
- Mysen, B. O., Eggler, D. H., Seitz, M. G. & Holloway, J. R. (1976). Carbon dioxide in silicate melts and crystals; Part I, Solubility measurements. *American Journal of Science* 276, 455-479.
- Newman, S. & Lowenstern, J. B. (2002). VolatileCalc; a silicate melt-H₂O-CO₂ solution model written in Visual Basic for Excel. *Computers & Geosciences* 28, 597-604.
- Papale, P. (1999). Modeling of the solubility of a two-component H₂O+CO₂ fluid in silicate liquids. *American Mineralogist* 84, 477-492.
- Papale, P., Moretti, R. & Barbato, D. (2006). The compositional dependence of the saturation surface of H₂O+CO₂ fluids in silicate melts. *Chemical Geology* 229, 78-95.
- Roedder, E. (1979). Origin and significance of magmatic inclusions. *Bulletin de Mineralogie* 102, 487-510.
- Roedder, E. (1984). Fluid inclusions. *Reviews in Mineralogy* 12, 644.

- Rosso, K. M. & Bodnar, R. J. (1995). Microthermometric and Raman spectroscopic detection limits of CO₂ in fluid inclusions and the Raman spectroscopic characterization of CO₂. *Geochimica et Cosmochimica Acta* 59, 3961-3975.
- Saito, G., Kazahaya, K., Shinohara, H., Stimac, J. & Kawanabe, Y. (2001). Variation of volatile concentration in a magma system of Satsuma-Iwojima volcano deduced from melt inclusion analysis. *Journal of Volcanology and Geothermal Research* 108, 11-31.
- Schiano, P. (2003). Primitive mantle magmas recorded as silicate melt inclusions in igneous minerals. *Earth-Science Reviews* 63, 121-144.
- Severs, M. J., Azbej, T., Thomas, J. B., Mandeville, C. W. & Bodnar, R. J. (2007). Experimental determination of H₂O loss from melt inclusions during laboratory heating: Evidence from Raman spectroscopy. *Chemical Geology* 237, 3-4.
- Sisson, T. W. & Layne, G. D. (1993). H₂O in basalt and basaltic andesite glass inclusions from four subduction-related volcanoes. *Earth and Planetary Science Letters* 117, 619-635.
- Skinner, B. F. (1966). Thermal Expansion. In: Clark, S. P., Jr. (ed.), *Handbook of Physical Constants: Geological Society of America Memoir* 97, 75-96.
- Skirius, C. M., Peterson, J. W. & Anderson, A. T., Jr. (1990). Homogenizing rhyolitic glass inclusions from the Bishop Tuff. *American Mineralogist* 75, 1381-1398.
- Sobolev, A. V. (1996). Melt inclusions in minerals as a source of principal petrological information. *Petrology* 4, 209-220.
- Spilliaert, N., Allard, P., Métrich, N. & Sobolev, A. V. (2006). Melt inclusion record of the conditions of ascent, degassing, and extrusion of volatile-rich alkali basalt during the powerful 2002 flank eruption of Mount Etna (Italy). *Journal of Geophysical Research* 111, B40203.
- Sterner, S. M. & Bodnar, R. J. (1991). Synthetic fluid inclusions: X. Experimental determination of P-V-T-X properties in the CO₂-H₂O system to 6 kb and 700 degrees C. *American Journal of Science* 291, 1-54.
- Stolper, E., Fine, G., Johnson, T. & Newman, S. (1987). Solubility of carbon dioxide in albitic melt. *American Mineralogist* 72, 1071-1085.
- Student, J. J. & Bodnar, R. J. (1996). Melt inclusion microthermometry; petrologic constraints from the H₂O-saturated haplogranite system. *Petrology* 4, 291-306.
- Student, J. J. & Bodnar, R. J. (1999). Synthetic fluid inclusions XIV: Coexisting silicate melt and aqueous fluid inclusions in the haplogranite-H₂O-NaCl-KCl system. *Journal of Petrology* 40, 1509-1525.
- Student, J. J. & Bodnar, R. J. (2004). Silicate melt inclusions in porphyry copper deposits; identification and homogenization behavior. *The Canadian Mineralogist*, 42, 1583-1599.
- Szabo, C., Bodnar, R. J., Sobolev, A. V. & Ayora, C. (1996). Metasomatism associated with subduction-related, volatile-rich silicate melt in the upper mantle beneath the Nograd-Gomor volcanic field, northern Hungary/southern Slovakia: evidence from silicate melt inclusions. *European Journal of Mineralogy* 8, 881-899.
- Thomas, J. B., Bodnar, R. J., Shimizu, N. & Sinha, A. K. (2002). Determination of zircon/melt trace element partition coefficients from SIMS analysis of melt inclusions in zircon. *Geochimica et Cosmochimica Acta* 66, 2887-2901.

- Vigouroux, N., Wallace, P. J. & Kent, A. J. R. (2008). Volatiles in high-K magmas from the western Trans-Mexican volcanic belt; evidence for fluid fluxing and extreme enrichment of the mantle wedge by subduction processes. *Journal of Petrology* 49, 1589-1618
- Walker, J. A., Roggensack, K., Patino, L. C., Cameron, B. I. & Matias, O. (2003). The water and trace element contents of melt inclusions across an active subduction zone. *Contributions to Mineralogy and Petrology* 146, 62-77.
- Wallace, P. J. (2005). Volatiles in subduction zone magmas: concentrations and fluxes based on melt inclusion and volcanic gas data. *Journal of Volcanology and Geothermal Research*, 140, 217-240.
- Webster, J. D. & Duffield, W. A. (1991). Volatiles and lithophile elements in Taylor Creek Rhyolite: constraints from glass inclusion analysis. *American Mineralogist* 76, 1628-1645.
- Zajacz, Z., Hanley, J. J., Heinrich, C. A., Halter, W. E. & Guillong, M. (2009). Diffusive reequilibration of quartz-hosted silicate melt and fluid inclusions; are all metal concentrations unmodified? *Geochimica et Cosmochimica Acta* 73, 3013-3027.

11. Tables

Table 1. Calculation of total CO₂ contained in a bubble-bearing MI from Solchiaro (southern Italy).

	<i>parameter</i>	<i>measured value</i>
Raman spectrum	Peak 1 (cm ⁻¹)	1284.33
	Peak 2 (cm ⁻¹)	1387.21
	Δ (cm ⁻¹)	102.88
Vapor bubble	Vapor density (g/cm ³) ¹	1.67 x 10 ⁻¹
	Bubble diameter (cm)	4.00 x 10 ⁻³
	Vapor volume. (cm ³) ²	3.35 x 10 ⁻⁸
	CO ₂ mass (g)	5.60 x 10 ⁻⁹
Melt/Glass	Inclusion. diameter (cm)	1.50 x 10 ⁻²
	Inclusion volume (cm ³) ²	1.77 x 10 ⁻⁶
	Melt/Glass volume (cm ³) ³	1.73 x 10 ⁻⁶
	Melt/Glass density (g/cm ³)	2.75
	Melt/Glass mass (g)	4.77 x 10 ⁻⁶
	Inclusion mass ⁴ (g)	4.77 x 10 ⁻⁶
CO ₂ contents	Bubble volume percent	1.90%
	CO₂ melt (ppm)⁵	650
	CO₂ in the MI (melt + vapor) (ppm)	1822

CO₂ content of the glass phase was determined using secondary ionization mass spectrometry (SIMS). The CO₂ density in the vapor bubble was determined by Raman spectroscopy. It should be noted that the CO₂ concentration dissolved in the melt (glass) is only 36% of the total CO₂ in the MI, and that the bubble accounts for 64% of the total CO₂ in the MI.

¹ Estimated using the equation of Kawakami et al. (2003).

² Volumes estimated from the MI/bubble diameters assuming spherical geometry.

³ Melt/glass volume = inclusion volume – vapor volume

⁴ Inclusion mass = melt/glass mass + vapor mass

⁵ Measured using SIMS.

Table 2. Studies that report relationships between PEC, presence or absence of shrinkage (vapor) bubbles, and dissolved volatile contents and pressure estimates from natural MI.

Reference	Locality	MI host ¹	MI petrography	V_w/V_{MI}^2	PEC ²	CO ₂ in glass (ppm)	CO ₂ in bubble ²	Pressure (kbar)	Notes
Spilliaert et al. (2006)	Etna (Italy)	ol	40 to 200 μm , bubble-bearing	4-8%, (few 10-20%)	<6%	150-3145	Detected ⁵	0.25-4.25 ⁴	MI in same crystal have >1000 ppm range in CO ₂
Collins et al. (2009)	Etna (Italy)	ol	>35 μm .	NR	<10%	60-4000	NR	0-3.20 ⁴	
Hauri (2002)	Hawaii	ol	Some bubble-bearing	NR	<12%	5-862	NR		CO ₂ varies widely for MI within same crystal
Mangiacapra et al. (2008)	Campi Eleggri (Italy)	ol cpx	Glassy, some bubble-bearing	NR	NR	200-1200	NR	0.50-2.0 ³	Volatile-poor MI are not included in this study
Vigouroux et al. (2008)	Trans-Mexican volcanic belt	ol	Detailed (see their Table 2)	wide range (see their Table 2)	<16%	bdl-5300	Indicated	$\leq 7.5^4$	Bubbles may be trapped along with melt
Walker et al. (2003)	Southeastern Guatemala	ol	Most 45-85 μm , all bubble-bearing	NR	<7%	Mostly between 300-2000	NR	0.50-5.0 ⁴	
Johnson et al. (2008)	Central Mexico	ol	Fully enclosed, glassy, some bubble-bearing	NR	<20.6	bdl-2500 (1 site ≤ 6000)	Indicated	$\leq 3.0^4$	
Anderson and Brown (1993)	Kilauea Iki (Hawaii)	ol	2 types: bubble-free and bubble-bearing	16 MI 2.1-3.0% 6 MI 4.1-7.0%	NR	bdl(<400) (1 MI ~800)	Calculated ⁶	41 MI < 1 9 > 1 ⁴	MI within same aggregates show wide range in CO ₂
Cervantes and Wallace (2003)	Xitle (Mexico)	ol	2 types: bubble-free and bubble-bearing	<6.2%	<13%	bdl (2 MI 312-338)	NR	< 8 ⁴	
Kamenetsky et al. (2007)	Etna (Italy)	ol	Negative crystal shaped, bubble-bearing		NR		Indicated		Ca-Mg carbonates detected in bubble using Raman
Sisson and Layne (1993)	Various backarc	ol	Spherical to elliptical 5 to 150 μm .	<1 to 20%	0 to 11%	NR	NR	NR	
Saito et al. (2001)	Satsuma-Iwojima	plg cpx opx	Assumed spherical	0.1 to 9%	NR	bdl to 300	NR	0.20-<1.50 ⁴	

¹ ol = olivine; opx = orthopyroxene; plg = plagioclase; cpx = clinopyroxene; opx = orthopyroxene. ² NR = not reported. ³ Calculated from H₂O-CO₂ contents using the model of Papale et al. (2006). ⁴ Calculated from H₂O-CO₂ contents using the model of Newman and Lowenstern (2002). ⁵ CO₂ detected using nuclear microprobe. ⁶ Calculated from the CO₂ vapor pressure determined from the glass analysis, at 1200°C.

12. Figures

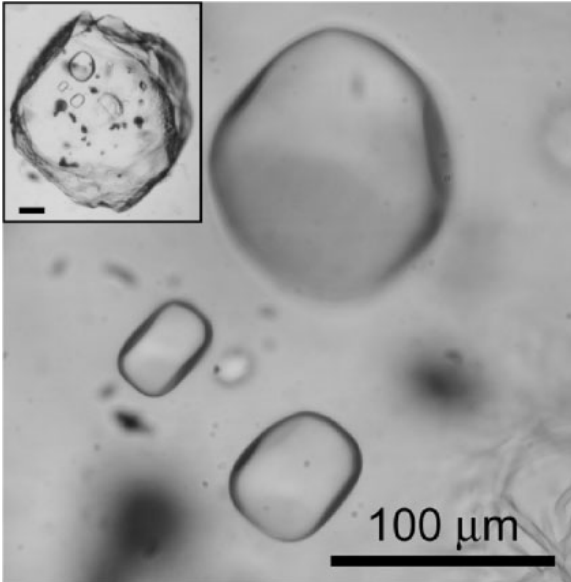


Figure 1. Quartz phenocryst from the Bishop Tuff (inset) showing three large, glassy melt inclusions, with the two smaller inclusions in the lower left-center exposed on the crystal surface.

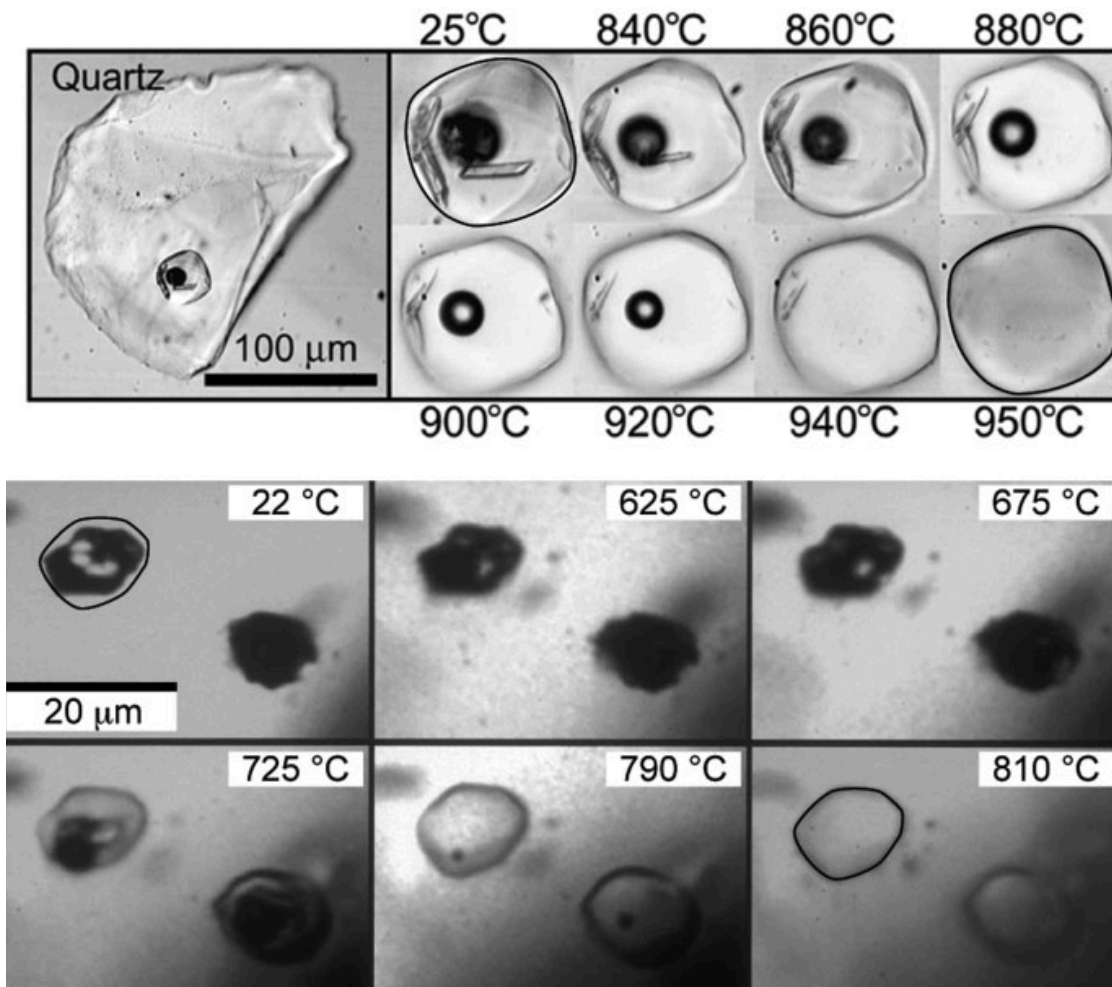


Figure 2. (Top) Heating sequence for a multi-phase silicate melt inclusion in quartz from the Toba Tuff, Sumatra, showing the melting of various daughter minerals and dissolution of the vapor phase to produce a homogeneous melt (glass). The boundary between the melt and host quartz has been highlighted by a solid black line in the image taken at 950°C, and this same line has been copied onto the image taken at 25°C to show the amount of quartz host dissolved during heating from 25° to 950°C. Note that little of the quartz host was dissolved during heating. (Bottom) Heating sequence on two completely crystallized MI in a quartz phenocryst from Red Mountain, Arizona, showing the homogenization behavior. The boundary between the melt and host quartz has been outlined by a solid black line in the MI on the left in the image taken at 810°C, and this is interpreted to represent the size (volume) of the original MI at trapping. The same outline (representing the size of the original trapped MI) has been copied onto the image taken at 25°C to show the amount of quartz host dissolved during heating from 25° to 810°C. The lighter area between the outline and the dark, crystallized MI represents quartz that precipitated on the walls following entrapment. Note that this quartz host on the walls dissolved into the melt during heating from 25° to 810°C (modified from Student & Bodnar, 2004).

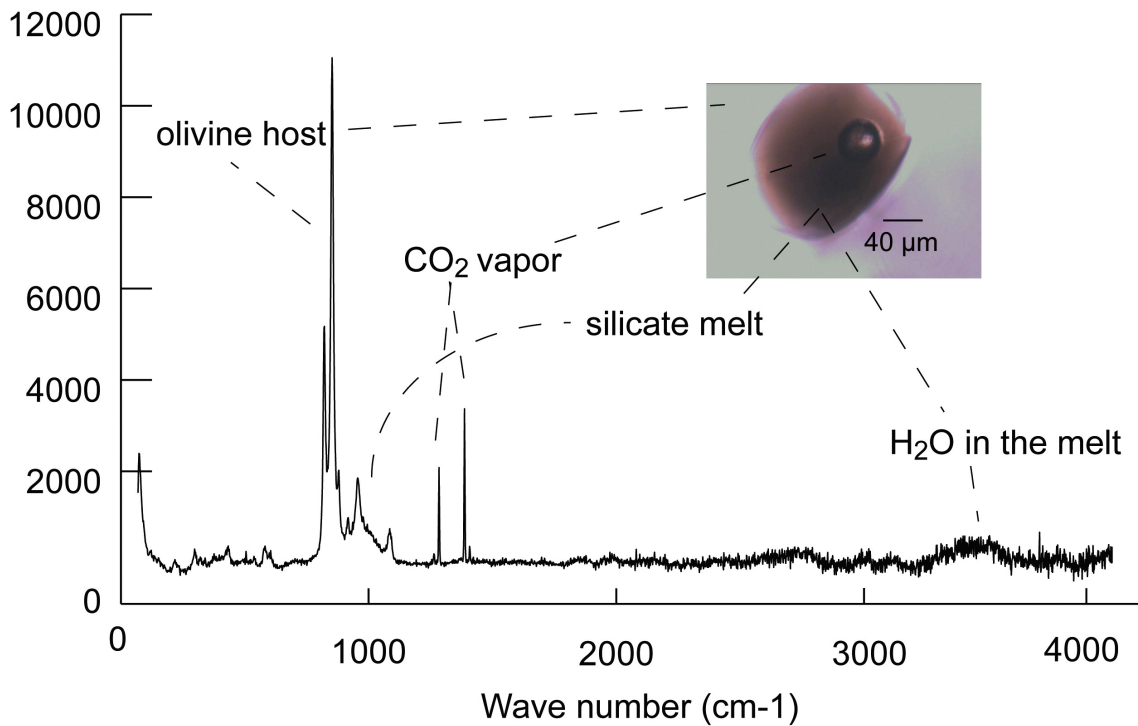


Figure. 3. Raman spectrum of a shrinkage (vapor) bubble in a MI hosted in olivine (inset) from the Solchiaro volcano, Procida Island (South Italy). Peaks labeled “CO₂ vapor” correspond to the Fermi diad for CO₂, and the distance between these peaks varies as a function of the density of the CO₂ phase (Kawakami *et al.*, 2003). Also shown on the spectrum are peaks corresponding to the host (Fo-rich olivine), the silicate glass, and H₂O dissolved in the glass (melt).

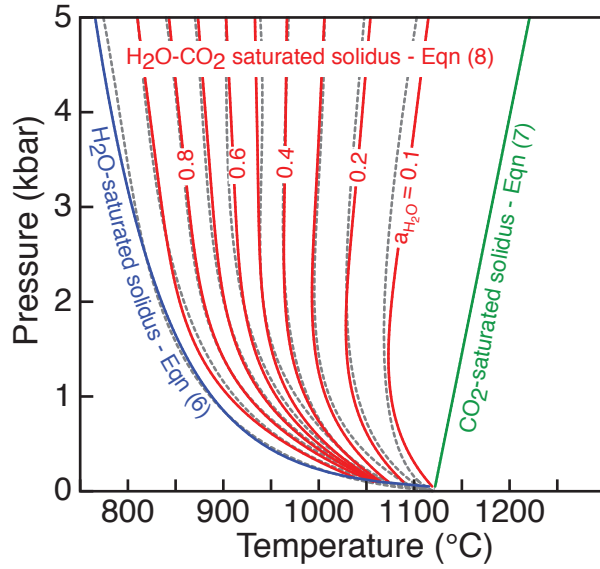


Figure 4. *PTX* vapor-saturated phase relations in the $\text{NaAlSi}_3\text{O}_8\text{-H}_2\text{O}$, $\text{NaAlSi}_3\text{O}_8\text{-CO}_2$ and $\text{NaAlSi}_3\text{O}_8\text{-H}_2\text{O-CO}_2$ systems. The *PT* coordinates for the $\text{NaAlSi}_3\text{O}_8\text{-H}_2\text{O}$ vapor-saturated solidus were calculated using Eqn. 6, the *PT* coordinates for the $\text{NaAlSi}_3\text{O}_8\text{-CO}_2$ vapor-saturated solidus were calculated using Eqn. 7, and the *PT* coordinates for the $\text{NaAlSi}_3\text{O}_8\text{-H}_2\text{O-CO}_2$ vapor-saturated solidus were calculated using Eqn. 8. Sections through the vapor-saturated solidus for the ternary system are labeled in $a_{\text{H}_2\text{O}}^{\text{melt}}$. The grey dashed curves represent the vapor-saturated solidus as a function of $a_{\text{H}_2\text{O}}^{\text{melt}}$ from Burnham & Davis (1974).

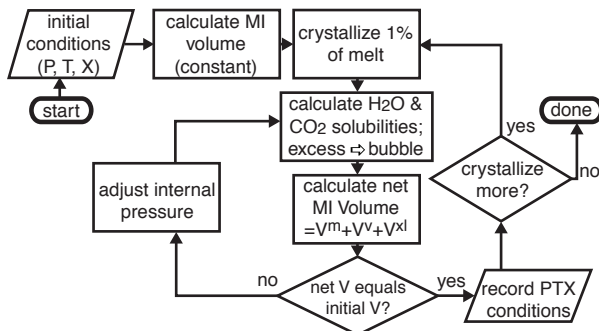


Figure 5. Schematic flow chart outlining the steps involved in the iterative numerical model used to estimate the *PTX* evolution of volatile-bearing melt inclusions during post-entrapment crystallization.

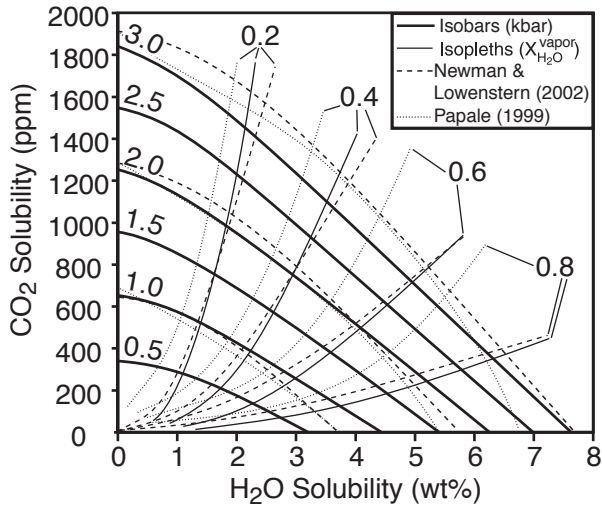


Figure 6. Isobars (solid lines, labeled in kbar) of H₂O-CO₂ solubility in albite melt at 900°C, based on the data of Burnham & Davis (1974), Fine & Stolper (1986) and Holloway & Blank (1994). Also shown for comparison are solubilities of H₂O-CO₂ in rhyolite melt at 900°C calculated from the models of Newman & Lowenstern (2002; dashed lines) and Papale (1999; dotted lines). Isopleths of the composition of the vapor phase that is in equilibrium with the melt calculated using the three different models are also shown and are labeled in mole fraction of H₂O in the vapor.

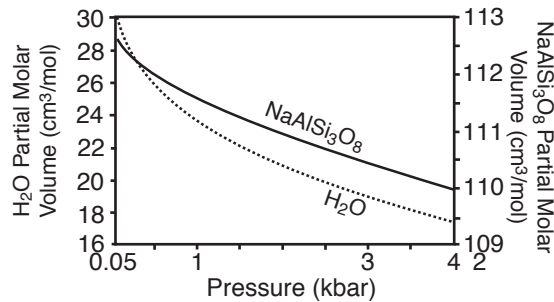


Figure 7. Variation in partial molar volumes of H₂O (left axis) and NaAlSi₃O₈ (right axis) in the melt as a function of pressure along the H₂O-saturated solidus.

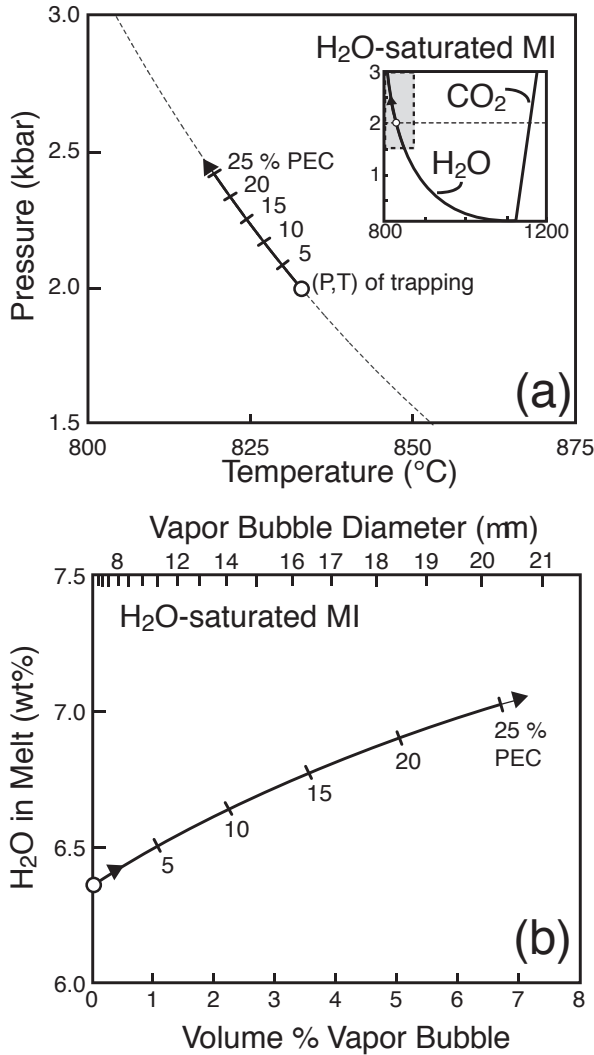


Figure 8. *PTX* evolution during PEC of a MI that traps an H₂O-saturated NaAlSi₃O₈-H₂O melt at 2 kbar (on the H₂O-saturated solidus). Tick marks on both graphs show the mass percent of albite removed from the melt during PEC, and the arrows on the curves show the *PT* trend with increasing amount of PEC.

(a) Evolution of the temperature and internal pressure of the MI during PEC. Inset shows expanded *PT* axes, showing the locations of the H₂O-saturated and CO₂-saturated (\approx dry) solidus curves (labeled "H₂O" and "CO₂", respectively) with the shaded box representing the *PT* area included in the larger diagram.

(b) Evolution of H₂O content in the melt (glass) phase as a function of the vapor bubble size. The vapor bubble size shown as volume percent of the MI (bottom axis) and vapor bubble diameter (top axis), assuming a spherical vapor bubble and a spherical 50 μ m diameter MI.

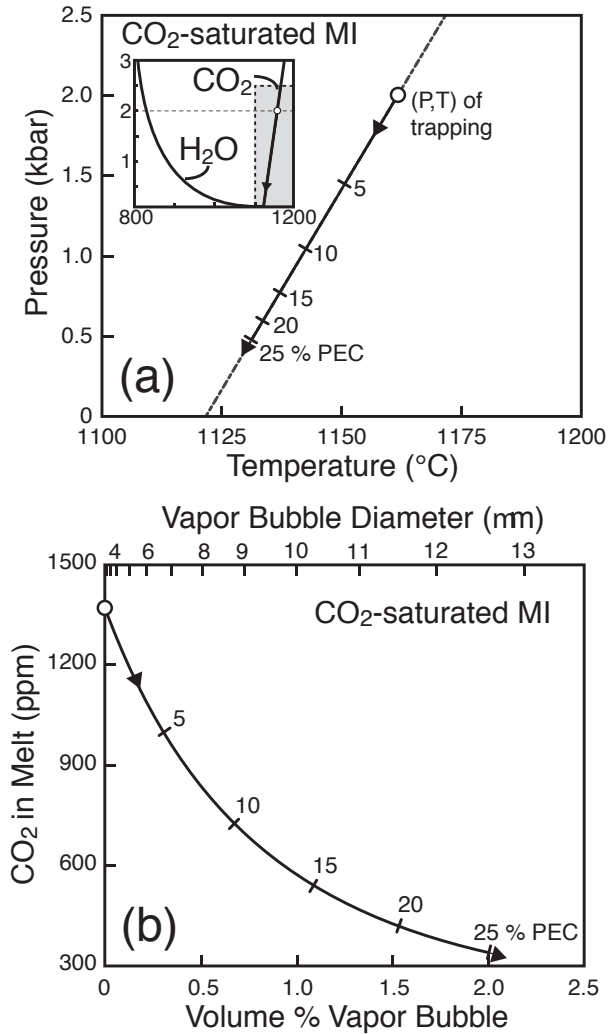


Figure 9. *PTX* evolution during PEC of a MI that traps a CO₂-saturated NaAlSi₃O₈-CO₂ melt at 2 kbar (on the CO₂-saturated solidus). Tick marks on both graphs show the mass percent of albite removed from the melt during PEC, and the arrows on the curves show the *PT* trend with increasing amount of PEC.

(a) Evolution of the temperature and internal pressure of the MI during PEC. Inset shows expanded *PT* axes, showing the locations of the H₂O-saturated and CO₂-saturated (\approx dry) solidus curves (labeled “H₂O” and “CO₂”, respectively), with the shaded box representing the *PT* area included in the larger diagram.

(b) Evolution of CO₂ content in the melt (glass) phase as a function of the vapor bubble size. The vapor bubble size shown as volume percent of the MI (bottom axis) and vapor bubble diameter (top axis), assuming a spherical vapor bubble and a spherical 50 μ m diameter MI.

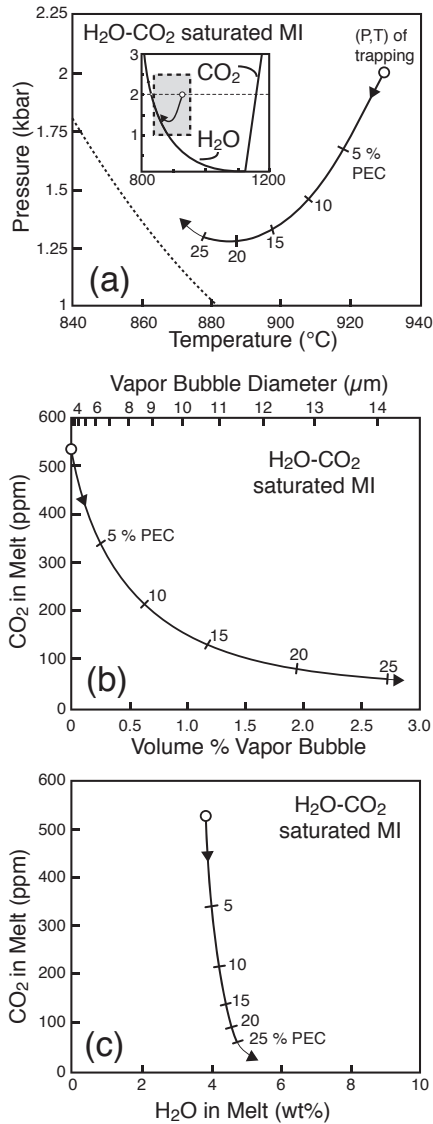


Figure 10. PTX evolution during PEC of a MI that traps a vapor-saturated $\text{NaAlSi}_3\text{O}_8$ - H_2O - CO_2 melt at 2 kbar and 930°C. Tick marks on all graphs show the mass percent of albite removed from the melt during PEC, and the arrows on the curves show the PT trend with increasing amount of PEC.

(a) Evolution of the temperature and internal pressure of the MI during PEC. Inset shows expanded PT axes, showing the topologies of the H_2O -saturated and CO_2 -saturated (≈ dry) solidus curves (labeled “ H_2O ” and “ CO_2 ”, respectively), with the shaded box representing the PT area included in the larger diagram. The dashed line shows a portion of the H_2O -saturated solidus.

(b) Evolution of CO_2 content in the melt (glass) phase as a function of the vapor bubble size. The vapor bubble size shown as volume percent of the MI (bottom axis) and vapor bubble diameter (top axis), assuming a spherical vapor bubble and a spherical 50 μm diameter MI.

(c) Evolution in the H_2O - CO_2 concentration of the melt (glass) during PEC and vapor bubble growth.

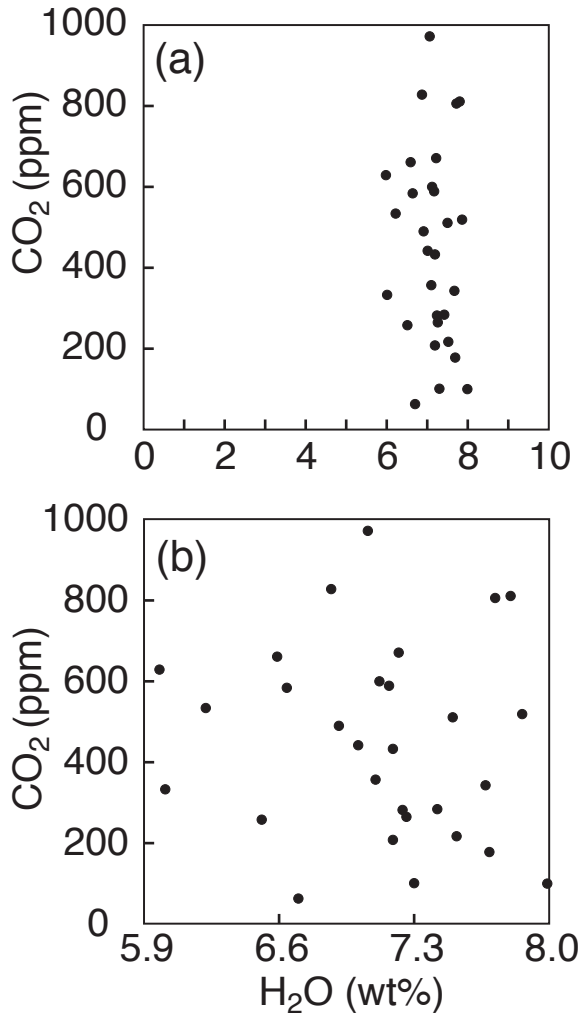


Figure 11. Concentrations of H₂O-CO₂ in melt inclusions from the Plinian fallout tuff at Pine Grove, Utah, reported by Lowenstern (1994).
 (a) Pine Grove data with CO₂ axis scaled to the range of the data, and H₂O axis scaled to 5x the range of the data, as originally published by Lowenstern (1994).
 (b) Same data as plotted in (a), with CO₂ and H₂O axes scaled to the range of the data. When viewed in this manner, it can be seen that there is no statistical correlation between CO₂ and H₂O contents of the MI.

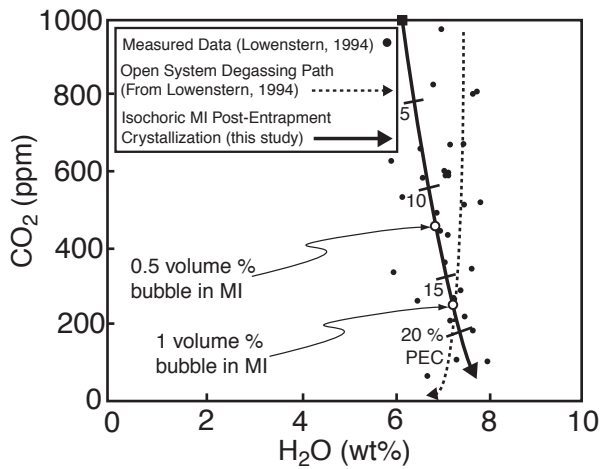


Figure 12. Comparison of H₂O-CO₂ trends predicted by open-system degassing (dashed line) and as a result of PEC and bubble growth (solid line). The data points represent the H₂O-CO₂ data of Lowenstern (1994), and the open circles show the points along the PEC path corresponding to 0.5 and 1 volume percent vapor in the MI. Lowenstern (1994) calculated an open-system degassing path for rhyolite using the data and assuming an initial condition of 4.3 kbar and 675°C. The PEC/bubble growth trend was calculated assuming MI trapping at 4.5 kbar and 895°C (the solid square). Either the open-system degassing trend or the PEC trend can be a reasonable interpretation of the data.

CHAPTER 2

Do melt inclusions record the pre-eruptive volatile content of magmas?

R. Esposito^a, J. Hunter^b, J. Schiffbauer^b and R. J. Bodnar^a

^aVirginia Polytechnic Institute & State University, Department of Geosciences, 4044 Derring Hall, 24061, Blacksburg, VA, USA

^bNanoscale Characterization and Fabrication Labs, Virginia Tech, Blacksburg, VA 24061, USA

Abstract

In most MI studies, the volatile contents of the MI vary widely even for MI hosted in the same phenocryst. In this study, we have analyzed groups of MI presumably trapped at the same time [Melt Inclusion Assemblage (MIA)] to test the reliability of volatile contents of MI.

MIAs hosted in phenocrysts from White Island (WI) (New Zealand) and from Solchiaro (Italy) were analyzed by Secondary Ion Mass Spectrometry (SIMS). In most MIA, H₂O, F, and Cl abundances were consistent in all MI indicating that analysis of MI is a reliable technique to characterize representative concentrations of these three volatile species. CO₂ and S abundances were consistent in some MIA, but especially CO₂ showed wide variation in others. The wide range in CO₂ content and the approximately constant H₂O of several MI within a MIA would suggest degassing paths. However, the degassing paths cannot be real for MI entrapped at the same time (same MIA). The inconsistent behavior of CO₂ may be due to C-contamination during sample preparation on the surface of MI.

Keywords:

melt inclusion technique

melt inclusion assemblage

pre-eruptive volatile contents

volcanic degassing

1. Introduction

In the last several decades the number of publications describing the use of melt inclusions (MI) to determine the pre-eruptive volatile contents of magmas has increased significantly (Introductory Fig. in De Vivo and Bodnar, 2003; Métrich and Wallace, 2008). In fact, MI provide the only potential means of determining the volatile content of a magma before this magma is erupted. However, in most MI studies, the volatile contents of the MI from the same sample vary widely (Métrich and Wallace, 2008 and references therein). The volatile concentration variability in MI may depend on (i) crystals forming in a volatile-zoned magmatic reservoir, (ii) crystals growing in a magma ascending through the uppermost mantle or crust, (iii) post-entrapment processes and (iv) boundary layer effects at the moment of the entrapment. Among all the volatile species, CO₂ has been reported to span a wider range relative to other volatiles (e.g., H₂O) and these results have been commonly interpreted as degassing of a carbon-dioxide rich

magmatic vapor from an ascending and crystallizing magma. This interpretation suggests that the crystallizing magma was volatile-saturated, and MI entrapped at great depth may be CO₂-rich while MI entrapped at shallow depth are CO₂-poor owing the lower solubility of CO₂ relative to other volatile species in silicate melt. Importantly, MI may not only show large variation of CO₂ concentration in the same sample, but also in the same phenocryst. Esposito et al. (2011, included in this thesis) reported that some bubble-bearing MI entrapped in a single olivine phenocryst show relatively high range in CO₂ (as much as 650 ppm) and that all the other volatiles do not show significant variations considering the analytical errors. In contrast, in the same study, bubble-free MI, entrapped in the same phenocryst, show range in CO₂ as low as 250 ppm. Recently, Steele-Macinnis et al. (2011) demonstrated that the glass contents of CO₂ from MI can be affected by post entrapment crystallization on the wall of the MI by up to an order of magnitude. Another process that can cause variation in MI from the same phenocryst is diffusion of volatiles through the host after trapping. Gaetani et al. (2011) have shown that H can completely diffuse from the MI through olivine in relatively short time and, thus, depending on where the MI occurs relative to core and rim of the host, diffusion may act in a different manner for different MI.

In order for MI to provide reliable information concerning the pre-eruptive volatile content, the MI must obey Roedder's (Sorby's) Rules (Roedder, 1984; Sorby, 1858). Namely, (i) the MI must have trapped a single homogeneous melt phase, (ii) the volume of the MI must remain constant after trapping, and (iii) nothing can be added or lost from the MI after trapping. In fluid inclusion studies, the adherence to Roedder's Rules is tested by examining two or more fluid inclusions (FI) from a Fluid Inclusion Assemblage (FIA), representing a group of FI that were all trapped at the same time (Goldstein and Reynolds, 1994). If all of the FI in the assemblage show the same room temperature phase relations and behavior during microthermometry, then it is highly likely that the FI in the assemblage obey Roedder's Rules. If the FI are primary in origin and obey Roedder's Rules, the FI are representative of the fluid from which the host had originated. As reported by Bodnar and Student (2006), a similar approach should be used to study MI, and for this reason they proposed the term *Melt Inclusion Assemblages* (MIA). In contrast to FIA, MIA are rarely studied because they are more difficult to recognize and less commonly found than FIAs. In addition, it is challenging to simultaneously expose more than one MI of the same MIA, and volatile concentrations in the MI can be obtained only if the inclusion is exposed, since analysis of volatile requires surface exposure of the MI. Moreover, volatiles in MI are often determined by Fourier transform infrared spectroscopy (FTIR), which requires that the MI be exposed on both surfaces of the host phenocryst. That requires the removal of most of the phenocryst (and its contained MI) during polishing and reduces the likelihood that more than one MI of the same MIA (or even of the same phenocryst) will be available for analysis in each crystal.

In this study, we will report and discuss the variability of volatile compositions (CO₂, H₂O, F, S, and Cl) of groups of MI belonging to several MIA to test for the fidelity of the MI technique applied to magma dynamics and evolution. The examined MIA are hosted in phenocrysts erupted from the White Island (WI) volcano in New Zealand and from the Solchiaro volcano in southern Italy. Major and trace element concentrations of MI from WI samples have been extensively studied (Rapien et al., 2003; Severs et al., 2009;

Wardell et al., 2001). In particular, Rapien et al. (2003) and Severs et al. (2009) reported that within an MIA major and trace elements are consistent.

2. Geological background

Samples analyzed in this study are from two recent eruptions (1986 and 1988; Rapien et al., 2003) at White Island, New Zealand and from the eruption of Solchiaro at Procida Island, Italy, that occurred between 19.6 and 14.3 ka (Alessio et al., 1989; Lirer et al., 1991).

These two magmatic systems are completely different in origin. White Island is an active volcano and is part of the active margin between the Australian plate and the Pacific plate (Isacks et al., 1968). The WI volcano is located at the northern end of the Taupo Volcanic Zone (TVZ) and temporally ranges in composition between andesite and dacite. The two most recent cycles of eruptions are the 1976–1982 and 1986–1992 in which the eruptive style alternated between phreatomagmatic and strombolian. On July 27th, 2000 the most recent eruption blanketed the island with scoriae. The 1976–1982 and 1986–1992 activity has been associated with a large magma body (approximately 10^6 m³) ponding at shallow depth in the crust at around 0.5 km depth (Clark and Cole, 1989). The samples are ejected scoriae and were collected by Dr. C. Peter Wood of the Institute of Geological and Nuclear Sciences, Wairakei, New Zealand. These same samples were described in more detail by Rapien et al. (2003) and Severs et al. (2009).

Solchiaro is not an active volcano and several authors have studied its volcanic history (Di Girolamo et al., 1984; D'Antonio et al., 1999; Cecchetti et al., 2001; De Astis et al., 2004; Esposito et al., 2011; Mormone et al., 2011). The Solchiaro vulcanites are part of the potassic rock series that crops out in the Phlegrean Volcanic District (Campanian magmatic province). De Astis et al. (2004) have subdivided the Solchiaro deposits into three units. The eruptive style has changed during the eruption from prevalently phreatomagmatic in unit I to increasingly strombolian in units II and III. The composition of Solchiaro products varies from trachybasalt (unit I) to shoshonite (unit II and III). The two samples we have studied in this work (RESC2 and RESC5) are gray tuffs from the Solchiaro unit I and have been described in detail by Esposito et al. (2011).

3. Analytical methods

Samples from White Island and Solchiaro were treated and prepared as described by Esposito et al. (2011) with the exception of one set of MI from WI which was mounted and polished simultaneously in a one-inch epoxy mount (Shimizu personal communication). Selection of MIA was based on whether or not MI contained only glass and if they were > 20 μ m, owing to the minimum spot size suggested for Secondary Ion Mass Spectroscopy (SIMS) analyses.

When a MIA was selected and petrographically studied, crystals were remounted on glass bars or in a one-inch epoxy mount in an attempt to expose as many MI as possible in a single MIA. After several MI were exposed, phenocrysts were removed from the glass rod/epoxy mount and mounted in an indium ion probe mount one inch in diameter. The indium mount was used because at high vacuum of the SIMS chamber the epoxy can outgas and contaminate the sample with H₂O and CO₂ (Shimizu, personal

communication). If only one MI of an MIA was analyzed, the same crystal hosting the MI was removed from the indium mount and polished again to expose other MI of the same MIA. The same crystal was remounted in indium and the new exposed MI were analyzed.

Petrography using the SEM was performed as described in Esposito et al. (2011) to test for the homogeneity of the exposed MI. We did not analyze major elements of MI because other workers have extensively studied this aspect (Esposito et al., 2011; Rapien et al., 2003; Severs et al., 2009).

Before SIMS analysis, we used the laser of the laser ablation inductively coupled plasma mass spectrometry (LA-ICP-MS) lab at Virginia Tech to drill holes (ablation pits) around MI hosted in plagioclase (Fig. 1). These holes around the MI were necessary because the reflectance of glass and host plagioclase is similar and was not possible to locate MI hosted in plagioclase with the optical microscope mounted on the SIMS. After this operation, the indium mounts were cleaned in deionized water in an ultrasonic bath. All samples were gold-coated (sputter coating) for the SIMS analysis. In addition, we used the Focused Ion Beam Electron Microscope (FIB-EM) at Virginia Tech to study the morphology of MI. We used current between 0.043 and 1.4 nA and voltage of 5 kv for the imaging of MI. The sample was tilted 52° before the images were captured as described by Schiffbauer and Xiao (2011).

Volatile concentrations (CO₂, H₂O, F, S, and Cl) of MI were obtained by two different ion probes: the IMS 7f-GEO at Virginia Tech (Blacksburg VA, US) and the Cameca IMS 1280 at the Woods Hole Oceanographic Institution (Woods Hole, MA, USA). Results were collected during eight working sessions: May 2008, December 2008, March 2010, December 2010, February 2011, October 2011, March 2012, and May 2012. The Cameca IMS 1280 at the Woods Hole Oceanographic Institution was used only for the February 2011 working session. The analytical conditions were the same as described in Esposito et al. (2011). Details on glass standards and calibration curves are reported on Supplementary Material. The 2-sigma errors based on the slope of each calibration are 17% relative for CO₂, 18% for H₂O, 10% for F, 5% for S, and 13% for Cl.

During SIMS analysis, each MI was monitored through the time-resolved response “ion response screen” to test for anomalous ion distribution. In fact, we noted that sometimes the ion distribution on the probe screen showed C-heterogeneity. We noted that these anomalous screen responses may result in drastically high concentrations (e.g. up to 5 wt % of CO₂). Often we observed that MI showing this behavior also shows fractures that apparently originated during the polishing. We further noted that the same behavior is observed sometimes when the probe spot is not well centered in the MI (spot touching the wall of the MI). Therefore, we excluded all the MI showing heterogeneity in the ion-response screen during the SIMS analysis because we interpreted this behavior as being due to contamination. This interpretation has to be treated with caution because there is the possibility that CO₂-rich concentration might be real and represent actual anomalous concentrations in MI.

For this reason we have performed deep profiling in some of the MI to test for the homogeneity of CO₂ during the March 2012 and May 2012 working sessions. During these two working sessions the setting of the instrument was changed to optimize the depth resolution for C ion. At the conditions used, we calculated that sputtering rate of the SIMS is roughly 1 μm each 1000 sec, or 1nm per second.

For the sessions March 2010 and October 2011, after SIMS analysis the samples were studied under the optical microscope to check if the beam spot was centered on the MI. If the beam was not centered in the MI, the data was discarded.

4. Results

4.1 Petrography

The petrography of the White Island sample analyzed in this study has been extensively described by Rapien et al. (2003). Phenocrysts are from vesicular porphyritic andesitic scoria. Phenocrysts present in these samples are clinopyroxene, plagioclase, and orthopyroxene in decreasing order of abundance. The size of phenocrysts ranges from 0.5 to 3 mm and the habit of phenocrysts is predominantly euhedral (Fig. 2). The SEM images of the phenocrysts examined do not show any apparent chemical zoning, but Rapien et al. (2003) reported that etching in fluoboric acid reveals that plagioclase phenocrysts are zoned. Most of the polished phenocrysts show inclusions of various types. These inclusions are commonly trapped along growth zones in all of the phenocrysts (Fig. 1 and 2). Clinopyroxene, plagioclase and orthopyroxene inclusions are hosted by all three of these types of phenocrysts, with the exception of orthopyroxene inclusions in plagioclase. This suggests that the clinopyroxene, plagioclase and orthopyroxene were likely in equilibrium during the crystallization of the White Island magma, as also noted by Rapien et al. (2003) and by Severs et al. (2009). Apatite inclusions are common in all the three phenocryst types. Magnetite was observed occasionally as inclusions in clinopyroxene, as also reported by Rapien et al. (2003). MI are ubiquitous in clinopyroxene, plagioclase and orthopyroxene phenocrysts. We have recognized four main types of MI: (1) MI containing only glass, (2) MI containing glass plus mineral inclusion (also referred as mixed MI), (3) mixed MI containing a vapor bubble, (4) MI containing a sulfide globule (originally a sulfur-rich immiscible melt) or a sulfide globule plus a vapor bubble. In type-2 MI (mixed MI), the mineral inclusions are never considered to be daughter crystals because the ratios between the mineral volume and the glass volume change from approximately 1 to < 0.1 . Crystallized MI or partially crystallized MI were not observed in the sample studied. In most of the cases, vapor bubbles are observed in mixed MI indicating that those bubbles were entrapped along with the mineral and the melt. Alternatively, during quenching the likelihood that a bubble nucleates increases owing to the irregularity of interface between the melt and the mineral inclusion. In fact, glassy MI (type-1) rarely contain a vapor bubble. Type-4 MI (MI containing sulfide globules) are observed in clinopyroxene and orthopyroxene but not in plagioclase, and they are found only in the core of these phenocrysts.

In order to estimate the geometry of MI we have used the Focused Ion Beam Electron Microscope (FIB-EM) to excavate vertical sections through or adjacent to the MI. The sections range from ~ 5 to ~ 15 μm deep and MI shape was observed to vary from ovoid to prismatic (Supplementary material, SMFig.6). The MI shape can only be approximated because of the unknown variation in the third dimension. Two FI were observed in two different clinopyroxene phenocrysts suggesting that clinopyroxene crystallized under volatile-saturated conditions. In most cases, MI of all types were entrapped along growth zones or in the core of phenocrysts (Fig. 1 and 2). MI entrapped along growth zone were

called *zonal* MI and were interpreted as primary MI by Sobolev and Kostyuk (1976). MI clustered in the cores of phenocrysts were defined as *azonal* MI and were also interpreted to be primary by the same authors.

In this study, groups of MI trapped along the same growth zone or clustered in the core are interpreted to be part of the same MIA. In two cases, we noted trails of MI with elongated shape and assume that these were entrapped when two phenocrysts of the same mineral connected together during growth (pseudo-secondary MI, Supplementary Material, SMFig.7). In the White Island phenocrysts, we have recognized three types of MIA: (I) MIA composed only of type-1 MI, (II) MIA composed only by type-2 MI, and (III) MIA composed by mixing of all four types of MI. It is important to note that the three types of MIA can alternate in the same phenocryst as is commonly observed in plagioclase (Fig. 1). MIA identified as the group of MI clustered in the core of phenocrysts are often of type-III. Most of the MIA studied are type I, but in three cases also the other two types were analyzed as well.

MI studied from the Solchiaro samples are naturally quenched glass and were initially described by Esposito et al. (2011). Five of the phenocrysts, already analyzed by Esposito et al. (2011), were selected for analysis of additional MI in the same MIAs. The MI shape of the Solchiaro sample is sometimes irregular, sometimes negative-crystal shaped and sometimes other shapes, including ovoid to spherical. FIB-EM examination of MI hosted in olivine show that the MI/host interface is irregular (Supplementary Material SMFig.8). In most cases, MIAs are defined by MI which range from 3 to 10 μm and are thus too small to be analyzed with the SIMS. We identified and analyzed six MIAs. In most cases only two MI were analyzed for the same MIA because MI are less abundant relative to the White Island samples. MIA hosted in olivine are composed of type-1 MI, and type-2 MI which were trapped along growth zones or clustered in the core as in the WI phenocrysts.

4.2 Volatile composition of White Island MI

In this study, we analyzed the volatile compositions of 124 MI (Table 1 and Supplementary Material SMTable2). H_2O contents range from 0.20 to 0.59 wt% (average = 0.37 wt%). One MI contains only 0.05 wt% of H_2O and this is interpreted as a degassed MI (decrepitate?) or that the SIMS analyzed MI plus mineral inclusion. H_2O concentrations from this study are comparable to those obtained by other authors. Rapien et al. (2003) reported H_2O contents of 5 MI (1988 and 1989 eruptions) ranging from 0.27 to 0.89 wt%. Wardell et al. (2001) reported that H_2O concentration of 9 MI (1986-1989 eruptions) ranges from 0.4 to 0.8 wt%. Importantly, no correlation exists between the types of the host of the MI and the H_2O concentration range.

Fluorine concentrations range from 163 to 619 ppm (average = 323 ppm). Fluorine content of MI does not show any correlation with MI host mineral (Fig. 3). Average F content reported by Rapien et al. (2003) is ~1300 ppm.

Chlorine concentrations range from 416 to 2010 ppm (average = 1027 ppm) much wider than that obtained by Rapien et al. (2003) (600-1000 ppm) and comparable with the range reported by Wardell et al. (2001) (1010–1770 ppm). MI hosted in clinopyroxene show the highest Cl content (Fig. 3).

Sulfur contents range from 30 to 384 ppm (average = 92 ppm). In contrast to our results, Rapien et al. (2003) and Wardell et al. (2001) reported S abundance ≤ 100 . MI

hosted in plagioclase show S concentrations always < 100 ppm consistent with the absence of sulfide globules in MI hosted in plagioclase. In contrast to MI S concentration, SO₂ emission rates during recent volcanic activity were relatively high (Rose et al., 1986; Wardell et al., 2001).

CO₂ contents show a wide range (from 15 to 3508 ppm) as has been reported in other studies (Helo et al., 2011; Métrich and Wallace, 2008). Most of the MI show CO₂ concentration <200 ppm. High CO₂ concentrations are consistent with the high CO₂ flux from the WI crater during the 1982-1998 activity Wardell et al. (2001 and references therein).

We have compared the results from different working sessions to check if variability in volatile concentrations was due to significant variation among the calibration curves (Fig 4). This evaluation is important in order to interpret the variability of volatile contents among MIAs. As shown in Fig. 4, the October, 2011, working session shows slightly higher contents of H₂O relative to all the other sessions.

4.3 Volatile composition of Solchiaro MI

In this study, we have analyzed 11 MI from the Solchiaro and we have integrated the data set with 6 MI analyses already published by Esposito et al. (2011) (Table 1 and SMTTable2). Interestingly, two MI from this sample were analyzed several times during different working sessions (Table 1). If a MI is homogeneous in volatiles, the volatile compositions of the same glass obtained at different times and with different SIMS instruments should not be significantly different. As shown in Table 1, the relative standard deviations (1- σ) of volatile contents of the MI that was measured four times is 28% for CO₂, 29% for H₂O, 14% for F, 19% for S, 32% for Cl. The other MI that was measured three times shows CO₂, H₂O, F, S, and Cl relative 1- σ errors of 19%, 24%, 5%, 10%, and 22% respectively. Thus, relative errors are < 20% for F and S, while are < 30% for CO₂ and H₂O, and 32% for Cl.

Volatile compositions of MI from Solchiaro obtained in this study are comparable to with data already published in previous studies (Esposito et al., 2011; Mormone et al., 2011). H₂O contents range from 0.52 to 1.82 wt%, F contents range from 650 to 1472 ppm, Cl contents range from 763 to 2794 ppm, S contents range from 639 to 1621 ppm, and CO₂ contents range from 168 to 1189 ppm.

4.4 White Island MIA

We analyzed in total 34 MIA hosted in phenocrysts from White Island: 14 MIA are hosted in clinopyroxene, 14 MIA are hosted in plagioclase, and 6 are hosted in orthopyroxene.

In most of the cases, H₂O contents of single MIA do not show significant variability suggesting that H₂O content of MI are representative of the melt at time of the trapping (Fig. 3). MIA hosted in orthopyroxene and plagioclase show narrower range of H₂O relative to those hosted in clinopyroxene. Only in a MIA hosted in plagioclase, one MI shows H₂O concentration inconsistent with the other MI in the same MIA.

Fluorine shows behavior similar to H₂O, but it is slightly more consistent within the same MIA (see Table 1 and SMTTable2). Therefore, we infer that F concentrations likely represent the concentration of the melt at the moment of MI trapping.

Chlorine shows the same behavior as F, suggesting that Cl contents of MI are representative of the melt from which the hosted phenocrysts were crystallizing.

In summary, 28 out of 29 MIA (~97%) show consistent behavior for H₂O, F, and Cl. One MIA (MIA-27) shows inconsistent results and is hosted in plagioclase. For MIA-27 (Fig. 3), only one MI (RE-WI-29-E) is significantly different from the rest of MI. This MI has been probably degassed before or during entrapment because all the five volatiles analyzed are lower relative to the other MI.

Carbon dioxide concentrations are consistent in 11 out of 29 MIA (5 hosted in clinopyroxene, 4 hosted in orthopyroxene, and 2 hosted in plagioclase), and when CO₂ is consistent the average concentrations are ≤200 ppm (Fig. 5). Relative standard deviation of CO₂ contents of MI in a single MIA can be > 100%, and these significant variations suggest that for CO₂, either the MI do not follow Roedder's rules or the variability originated from contamination on the surface of the sample.

Twenty-four out of 29 MIA show consistent S concentrations, and of the 5 MIA showing inconsistency, four are hosted in clinopyroxene. Sulfur concentrations are < 100 ppm for MIA hosted in plagioclase. In one MIA hosted in clinopyroxene, one type-4 MI (sulfide-bearing MI) shows 367 ppm S and other type-1 MI show S concentration as low as 49 ppm.

4.5 Solchiaro MIA

In addition to the 34 MIA hosted in White Island phenocrysts, we have studied five MIA hosted in olivine and one MIA hosted in clinopyroxene from Solchiaro. As was the case for White Island MIA, H₂O, F and Cl are consistent with the contemporaneous entrapment of a representative melt and thus represent the same physical and chemical conditions (Fig. 6). In addition, three out of six MIA show consistent behavior of CO₂ that is a similar ratio relative to that of the White Island MIA. In contrast to the White Island MIA, MIA from Solchiaro show more consistent results for S. Only one of the MIA from Solchiaro shows inconsistent results (Fig. 6).

5. Discussion

In this section we discuss the volatile concentration variability of MI presumably trapped at the *same* time, that is, under the same physical and chemical conditions. In fact, most of the MI we analyzed here were trapped along growth zones and are defined as MIAs (Bodnar and Student, 2006). The MIAs thus consist of MI which should have trapped the same silicate melt (same chemical composition) if the MI follow the Roedder's Rules. Establishing the time frame at which a MI is trapped along a growth zone or in the core of a phenocryst is crucial for the interpretation of the data presented here. Bodnar and Student (2006) reported that entrapment of a 10-μm MI may take from a fraction of second to around 3000 years based on growth rates determined by Dowty (1980), Bacon (1989), and Tomiya and Takahashi (2005). However, it is also important to note that MI are generally thought to have kinetic implications, that is to be trapped during periods of extremely rapid growth rates caused by abrupt changes in temperature, pressure and volatile exsolution rate (Roedder, 1979). In other words, if a melt becomes super-saturated in volatiles, how long does it take for volatiles to exsolve from the melt? In a related question, are the growth rates of silicate minerals comparable to exsolution

rates of volatiles in a super-saturated silicate melt? In the following discussion, we assume that the exsolution rates of volatiles from melt are lower than any possible crystal growth rate (instantaneous exsolution).

In this study, we showed that concentrations of H₂O, F and Cl are consistent within a single MIA. In addition, S is consistent in most of the MIAs and CO₂ in only half of the MIAs. In other words, the volatile concentrations from most of the MI analyzed in this study likely are representative of the melt from which White Island and Solchiaro phenocrysts had originated. In most of the cases, Roedder's rules are satisfied and the volatile concentrations we obtained from these MI are reliable.

Lately, it has been shown that volatiles can diffuse out of the MI into the surrounding host-crystal environment. For instance, Gaetani et al. (2011) reported that H re-equilibrated entirely with the surrounding environment of MI hosted in olivine in matter of minutes owing to the high diffusive rates of H. Thus, another possible explanation for the consistent H₂O concentration within single MIAs is that H₂O of MI in the White Island phenocrysts have re-equilibrated with the outer silicate melt. However, major and trace element compositions of MIA from White Island show a narrow range (Rapien et al., 2003; Severs et al., 2009). This suggests either that all elements had been re-equilibrated with the surrounding melt or that these MI were entrapped from a homogeneous melt. Assuming that this uniformity of major/trace element is caused by diffusion, phenocrysts should have resided in a certain magmatic homogeneous environment for relatively long time. The consistency of concentration of slow-diffusing elements (e.g. LILE) in MIAs suggests that the consistency of volatile elements as well is not due to diffusion. Therefore, we argue that most of the MIAs analyzed in this study are reliable for volatile analyses and that volatile concentrations are not due to diffusive processes. We emphasize that the MI are either 1) representative of the melt at the moment of the trapping or 2) the MI are representative of a later magmatic stage that leads MI to record a particular moment of the magmatic evolution. If we had assumed volatile saturation, the calculated pressures of consistent MIAs are ≤ 320 bars, calculated using the H₂O-CO₂-silicate melt solubility model by Papale et al. (2006), assuming FeO = 0.8 x FeO_{tot}, 1100 °C, and assuming the average MI composition by (Rapien et al., 2003) for major elements. Calculated pressures are in agreement with geophysical data (Clark and Cole, 1989). In the case of MI being representative of melt at the trapping time, MI may represent a melt still undersaturated in volatiles and residing at greater depth.

Sulfur variability in some MIAs suggests that some of the sulfur concentrations may not be representative. That is, either the melt from which some crystals were growing was heterogeneous, or after entrapment of a homogeneous melt some process modified the original composition. As reported above, sulfide globules correlate with sulfur variability in a single MIA. Interestingly, the glass composition of one sulfide-globule-bearing MI shows 367 ppm S, which is one order of magnitude higher than other MI from the same MIA (REWI-15-I in Table 1). Sulfide globule volume ratios within an MIA do not vary, suggesting that an immiscible sulfur-rich melt form after trapping (Roedder, 1979) and that the trapped melt was originally homogeneous. Phenocrysts do not show sulfide mineral inclusions, suggesting that originally the melt was not saturated with sulfide. MIAs hosted in plagioclase does not show significant sulfur variability, and MI show < 100 ppm of S, suggesting that plagioclase crystallized from a Sulfur-degassed melt. In

contrast, clinopyroxene, orthopyroxene and plagioclase are in equilibrium with each other as suggested by petrographic observations (mineral inclusions of these three phases are observed in all the three phenocrysts). One possible interpretation is that S diffused from the MI through the plagioclase host and re-equilibrated with an S-poor melt. A test of this interpretation would involve constrain of S diffusivity in pyroxene vs. plagioclase, but the authors know of no experimental study on this. Assuming that S diffused through the host, S-rich MI hosted in pyroxene are the most representative of non-degassed melt that in turn may represent melt composition deeper in the system. We have calculated the mass of S that has degassed in the White Island system. The highest S content in MI is 384 ppm while the lowest S content is 29 ppm (Table 1). Therefore, 355 ppm of S has been exsolved from the melt. Clark and Cole (1989) estimated that in mid-1973 approximately 10^6 m³ of magma had ponded at shallow depth under the White Island volcano. Assuming a density of 2700 kg/m³, the mass of magma is 2.7×10^9 kg. Therefore, 355 ppm of 2.7×10^9 kg corresponds to 9.7×10^8 g of S or approximately 2×10^9 g of SO₂ has been exsolved and may have discharged from the main vent during eruption or during fumarole activity at White Island. Considering 15 years of activity (5475 days), S degassing calculated from MI is around 3.65×10^5 g/day of SO₂. During the 1984 and 1999 eruptions, the flux of SO₂ from the WI crater was in average 4.33×10^8 g/day. This rate is of three orders of magnitude more than the flux recorded MI at WI. This inconsistency may be due either to an erroneous estimation of melt volume or to the lack of recording of the initial S concentration by MI.

Half of the MIAs show inconsistent CO₂ concentration, which are the least reliable of the five volatile components analyzed. The CO₂ variability is more exaggerated for MIAs hosted in plagioclase. CO₂ variability may be due to sample contamination, as indicated by the high standard deviation of some glasses analyzed. In fact, in some cases, CO₂ concentration significantly decreases from the beginning to the end of the analysis (see also the analytical methods section). To test this hypothesis we have checked the variability of CO₂ contents analyzed more than one time on the same MI (Supplementary Material SMFig.9). The CO₂ concentrations are all consistent with the exception of one MI (3% of all the MI), suggesting that only a few % of analyses may be affected by C-contamination. However, we have performed some CO₂ and F depth profiles to test for homogeneity of CO₂ with depth in an MI. As can be observed from Fig.7, the initial (shallow) part of the CO₂ profiles shows unpredictable behavior, and is mainly characterized by CO₂ enrichment. It is important to note that this anomalous behavior is more significant for MI hosted in plagioclase, which is consistent with the more exaggerated variability of CO₂ in MIA hosted in plagioclase. CO₂ depth profiling in MI hosted in pyroxene or olivine is not characterized by such strong enrichment of CO₂ in the initial part, and similarly profiles in the glass standard (Fig. 7).

We interpreted this anomalous CO₂ enrichment of the shallow part of the profile of plagioclase-hosted MI to be due to C-contamination on the surface of the sample. We have noticed that this contamination effect may reach as deep as 2 μm from the sample surface at these analytical conditions. If the C-contamination is mainly due to sample preparation, it is remarkable that plagioclase crystals are more affected by this issue than other host minerals. In fact, plagioclase, clinopyroxene, orthopyroxene, and olivine have all been mounted in the same indium mounts and the sample preparation procedures were the same for each of these host phases. Also, glass standards have been mounted,

prepared, and cleaned using the same method as for the last mount analyzed for this study. At this point, we do not have any interpretation regarding why MI in plagioclases are more affected by the C-contamination.

For other workers using similar SIMS working conditions to those we have used in this study, we suggest prolonging the pre-sputtering time of each analysis for up to 1500-2000 seconds before recording ion counts from the surface of the sample, especially for MI hosted in plagioclase, to avoid a possible C-contamination issue.

6. Summary

In this study, we have addressed the question of whether or not the measured volatile contents of MI are reliable enough to obtain dependable information that constrains magmatic evolution or magma dynamics in active systems. We have addressed this question using the fluid (melt) inclusion assemblage (MIA) approach.

Volatile-concentration variability of MIAs indicates that H₂O, F, and Cl contents from MI are reliable for the White Island and the Solchiaro volcanic systems. Sulfur is consistent in several MIAs. CO₂ is inconsistent in half of the MIAs, likely because of poorly understood C-contamination on the surface of the sample.

7. Acknowledgement

This study has been supported by the National Science Foundation under grant no. EAR-1019770. The authors would like to thank Nobumichi Schimizu for comments and suggestions on sample preparation and support with SIMS analysis.

8. References

- Alessio, M., Allegri, L., Azzi, C., Calderoni, G., Cortesi, C., Improta, S. & Petrone, V. (1989). ¹⁴C tephrochronology with different fractions of Paleosol humic matter at Procida Island, Italy. *Radiocarbon* 31, 664-671.
- Bacon, C. R. (1989). Crystallization of accessory phases in magmas by local saturation adjacent to phenocrysts. *Geochimica Et Cosmochimica Acta* 53, 1055-1066.
- Bodnar, R. J. & Student, J. J. (2006). Melt inclusions in plutonic rocks: Petrography and microthermometry. *Melt Inclusions in Plutonic Rocks* 36, 1-25.
- Clark, R. H. & Cole, J. W. (1989). Volcanic monitoring and surveillance at White Island before the 1976-82 eruption sequence. In: Houghton, B. F. & Nairn, I. A. (eds.). Wellington: New Zealand Geological Survey.
- De Astis, G., Piochi, M., Pappalardo, L. (2004). Procida Volcanic History: new insights in the evolution of the Phlegraean Volcanic District (Campania, Italy). *Bulletin of Volcanology* 66, 622-641.
- De Vivo, B. & Bodnar, R. J. (2003). *Melt inclusions in volcanic systems*. Amsterdam: Elsevier Sciences.
- Dowty, E. (1980). Crystal growth and nucleation theory and the numerical simulation of igneous crystallization. In: Hargraves, R. B. (ed.). Princeton: Princeton Univ. Press.

- Esposito, R., Bodnar, R. J., Danyushevsky, L., De Vivo, B., Fedele, L., Hunter, J., Lima, A. & Shimizu, N. (2011). Volatile Evolution of Magma Associated with the Solchiaro Eruption in the Phlegrean Volcanic District (Italy). *Journal of Petrology* 52, 2431-2460.
- Gaetani, G., O'Leary, J., Shimizu, N. & Anonymous. (2011). Post-entrapment changes to H₂O and CO₂ in olivine-hosted melt inclusions. *Mineralogical Magazine* 75, 879.
- Goldstein, R. H. & Reynolds, T. J. (1994). Systematics of fluid inclusions in diagenetic minerals. *SEPM Short Course Notes* 31, 199.
- Helo, C., Longpre, M.-A., Shimizu, N., Clague, D. A. & Stix, J. (2011). Explosive eruptions at mid-ocean ridges driven by CO₂-rich magmas. *Nature Geosci* 4, 260-263.
- Isacks, B., Oliver, J. & Sykes, L. R. (1968). Seismology and the new global tectonics. *Journal of Geophysical Research* 73, 5855-5899.
- Lirer, L., Rolandi, G. & Rubin, M. (1991). ¹⁴C age of the "Museum Breccia" (Campi Flegrei) and its relevance for the origin of the Campanian Ignimbrite. *Journal of Volcanology and Geothermal Research* 48, 223-227.
- Métrich, N. & Wallace, P. J. (2008). Volatile abundances in basaltic magmas and their degassing paths tracked by melt inclusions. In: Putirka, K. D. & Tepley, F. J., III (eds.) *Minerals, Inclusions and Volcanic Processes: The Mineralogical Society of America*, 363-402.
- Mormone, A., Piochi, M., Bellatreccia, F., De Astis, G., Moretti, R., Della Ventura, G., Cavallo, A. & Mangiacapra, A. (2011). A CO₂-rich magma source beneath the Phlegraean Volcanic District (Southern Italy): Evidence from a melt inclusion study. *Chemical Geology* 287, 66-80.
- Papale, P., Moretti, R. & Barbato, D. (2006). The compositional dependence of the saturation surface of H₂O + CO₂ fluids in silicate melts. *Chemical Geology* 229, 78-95.
- Rapien, M. H., Bodnar, R. J., Simmons, S. F., Szabo, C. & Sutton, S. R. (2003). The embryonic porphyry copper system at White Island, New Zealand. *Geochimica Et Cosmochimica Acta* 67, A391-A391.
- Roedder, E. (1979). Origin and significance of magmatic inclusions. *Bulletin de Mineralogie* 102, 487-510.
- Roedder, E. (1984). Fluid Inclusions. *Reviews in Mineralogy* 12.
- Rose, W. I., Chuan, R. L., Giggenbach, W. F. & Symonds, R. B. (1986). Rates of sulphur dioxide and particle emissions from White Island volcano, New Zealand, and an estimate of the total flux of major gaseous species. *Bulletin of Volcanology* 48, 181-188.
- Schiffbauer, J. D. & Xiao, S. (2011). Paleobiological Applications of Focused Ion Beam Electron Microscopy (FIB-EM): An Ultrastructural Approach to the (Micro)Fossil Record
- Quantifying the Evolution of Early Life. In: Laflamme, M., Schiffbauer, J. D. & Dornbos, S. Q. (eds.): Springer Netherlands, 321-354.
- Severs, M. J., Beard, J. S., Fedele, L., Hanchar, J. M., Mutchler, S. R. & Bodnar, R. J. (2009). Partitioning behavior of trace elements between dacitic melt and plagioclase, orthopyroxene, and clinopyroxene based on laser ablation ICPMS

- analysis of silicate melt inclusions. *Geochimica Et Cosmochimica Acta* 73, 2123-2141.
- Sobolev, A. V. & Kostyuk, V. P. (1976). Magmatic crystallization based on study of melt inclusions. *Fluid inclusion research* 9, 182-253.
- Sorby, H. C. (1858). On the microscopic structures of crystals, indicating the origin of minerals and rocks. *The Quarterly journal of the Geological Society of London* 14, 453-500.
- Steele-MacInnis, M. J., Esposito, R. & Bodnar, R. J. (2011). Thermodynamic model for the effect of post-entrapment crystallization on the H₂O-CO₂ systematics of volatile saturated silicate melt inclusions. *Journal of Petrology* 52, 2461-2482.
- Tomiyama, A. & Takahashi, E. (2005). Evolution of the magma chamber beneath Usu Volcano since 1663; a natural laboratory for observing changing phenocryst compositions and textures. *Journal of Petrology* 46, 2395-2426.
- Wardell, L. J., Kyle, P. R., Dunbar, N. & Christenson, B. (2001). White Island Volcano, New Zealand; carbon dioxide and sulfur dioxide emission rates and melt inclusion studies. In: Bergfeld, D., Goff, F. & Allard, P. (eds.) *Chemical Geology*. Amsterdam: Elsevier, 187-200.

9. Tables

Table 1. Representative analyses of volatile concentrations of MI from White Island and Solchiaro samples.

MI ID	MIA ID	CO ₂ (ppm)	H ₂ O (wt%)	F (ppm)	S (ppm)	Cl (ppm)	host	working session
REWI_15_A	MIA-10	172	0.40	401	60	903	cpx	March_2010
REWI_15_D	MIA-10	126	0.38	382	50	876	cpx	March_2010
REWI_15_H	MIA-10	106	0.40	415	131	975	cpx	March_2010
REWI_15_I	MIA-10	179	0.38	384	375	964	cpx	March_2010
WI_36_A	MIA-23	98	0.33	333	71	1380	opx	December_2010
WI_36_B	MIA-23	122	0.24	220	50	1339	opx	December_2010
WI_36_D	MIA-23	69	0.30	303	65	1266	opx	December_2010
WI_36_E	MIA-23	89	0.31	314	69	1302	opx	December_2010
RE-WI-29-A	MIA-27	15	0.43	307	46	969	plg	February_2011
RE-WI-29-C	MIA-27	21	0.45	348	60	1085	plg	February_2011
RE-WI-29-D	MIA-27	259	0.44	317	57	1011	plg	February_2011
RE-WI-29-E	MIA-27	61	0.05	230	42	726	plg	February_2011
RE-WI-29-F	MIA-27	105	0.44	326	62	1031	plg	February_2011
WI_25_A	MIA-19	87	0.33	254	45	1010	plg	December_2010
WI_25_C	MIA-19	192	0.30	229	33	748	plg	December_2010
WI_25_D	MIA-19	271	0.33	248	39	840	plg	December_2010
WI_25_F	MIA-19	na	0.34	261	44	837	plg	December_2010
WI_25_G	MIA-19	484	0.28	218	38	682	plg	December_2010
WI_25_I	MIA-19	270	0.30	229	41	769	plg	December_2010
WI_25_B	MIA-19	61	0.35	265	44	1019	plg	December_2010
WI_25_E ^a	MIA-19	1418	0.34	251	41	827	plg	December_2010
RESC5_O27_F1	MIA-35	447	1.80	1471	1600	2732	oli	VT_Oct_2011
RESC5_O27_F2	MIA-35	448	1.82	1472	1621	2794	oli	VT_Oct_2011
RESC5_O27_C	MIA-35	361	1.45	1000	1305	2572	oli	VT_Oct_2011
RESC5-O27-G	MIA-35	694	1.47	1354	1304	1969	oli	WHOI Feb_2011
RESC5-O27-F	MIA-35	742	1.07	1042	1025	1328	oli	WHOI Feb_2011
RESC5-O27-F	MIA-35	552	1.24	1259	1571	2818	oli	VT Dec_2010
RESC5-O27_F1	MIA-35	507	1.24	1238	1563	2796	oli	VT Dec_2010
RESC5-O27_G	MIA-35	490	1.20	1285	1532	2734	oli	VT Dec_2010
RESC5-O27_E	MIA-35	450	1.23	1286	1134	2916	oli	VT Dec_2010
RESC5_O27_F	MIA-35	509	1.19	1365	1418	2042	oli	VT Mar_2010
RESC5_O27_F1	MIA-35	493	1.17	1350	1411	2019	oli	VT Mar_2010
RESC5_O27_G	MIA-35	645	1.08	1266	1299	1892	oli	VT Mar_2010

^aMI measured more than one time; na = not available; cpx = clinopyroxene; opx = orthopyroxene; plg = plagioclase; oli = olivine.

Table 2. Volatile compositions of MI from the Solchiaro volcano measured multiple times during different working sessions.

MI-ID	CO ₂	H ₂ O	F	S	Cl
RESC5-O27-MF-WHOI-Feb-2011	742	1.07	1042	1025	1328
RESC5-O27-MF-VT-Dec-2010	529	1.24	1248	1567	2807
RESC5-O27-MF-VT-Mar-2010	501	1.18	1358	1415	2031
RESC5-O27-MF-VT-Oct-2011	447	1.81	1471	1610	2763
average	555	1.33	1280	1404	2232
stdev	129	0.33	183	266	700
relative stdev	23.32%	24.81%	14.29%	18.96%	31.37%
RESC5-O27-MG-WHOI-Feb-2011	694	1.47	1354	1304	1969
RESC5-O27-MG-VT-Dec-2010	490	1.20	1285	1532	2734
RESC5-O27-MG-VT-Mar-2010	645	1.08	1266	1299	1892
average	610	1.25	1302	1378	2198
stdev	106	0.20	46	133	466
relative stdev	17.42%	15.76%	3.55%	9.66%	21.18%

10. Figures

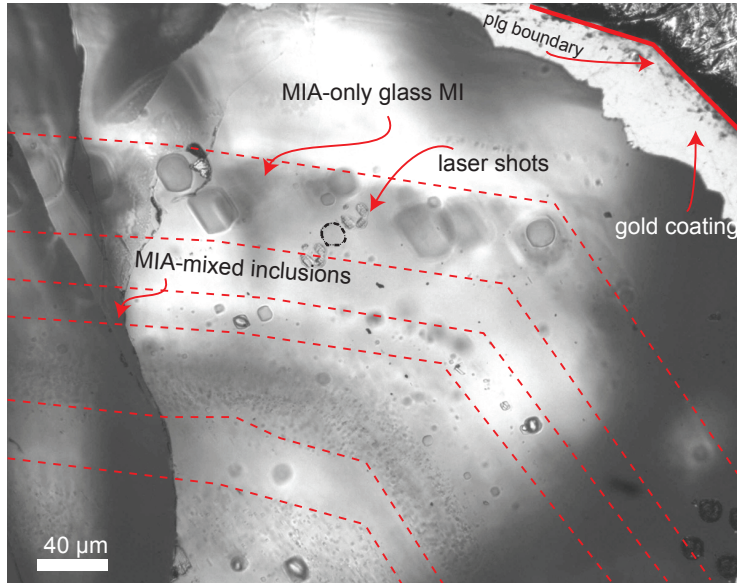


Fig. 1. Reflective optical microscope photo of MIAs hosted in plagioclase from White Island volcano in New Zealand. In this microphotograph is shown laser-drilled holes around exposed MI. MIAs are marked by the red dashed lines and are parallel to the euhedral boundaries of the phenocryst. Different types of MI and MIA can be observed in this plagioclase phenocryst (see text for more details).

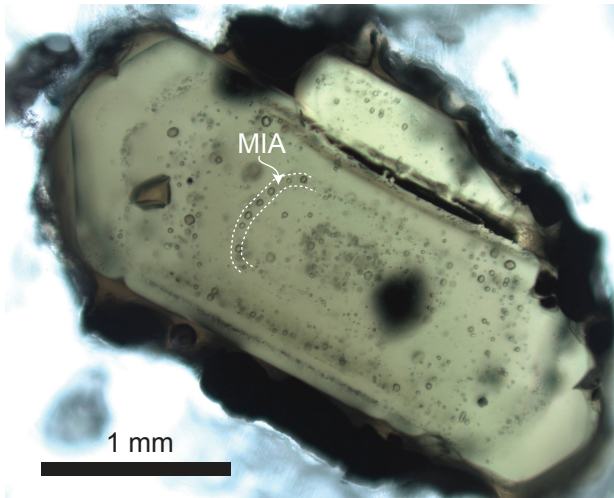


Fig. 2. Clinopyroxene of White Island scoriae showing characteristic growth zones defined by the entrapment of inclusions (MI, mixed MI and solid inclusions). The white dashed lines highlight a MIA.

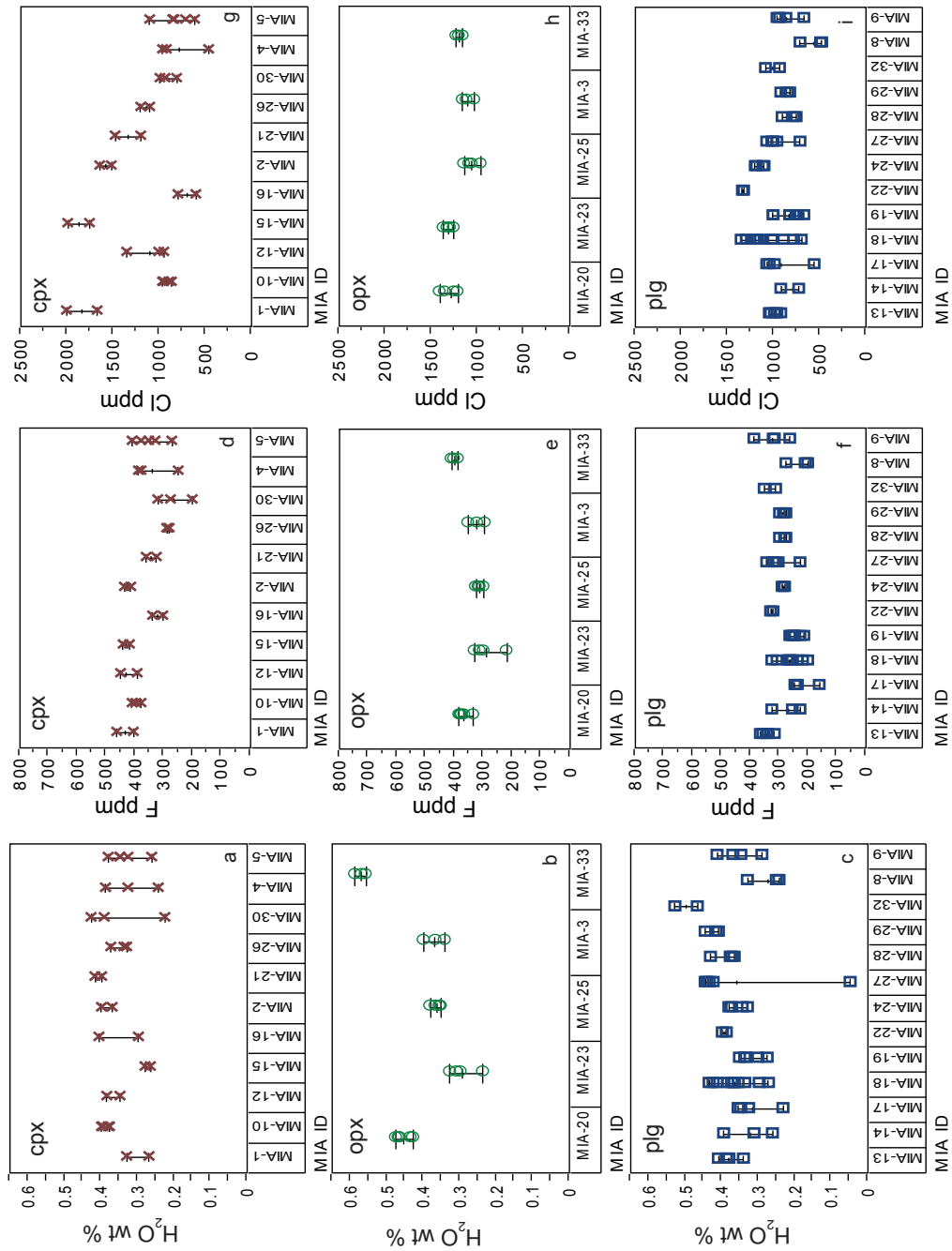


Fig. 3. Variability diagrams for H₂O, F, and Cl concentrations of MIA hosted in clinopyroxene, orthopyroxene, and plagioclase from White Island. It is important to note the consistency of MI within a single MIA.

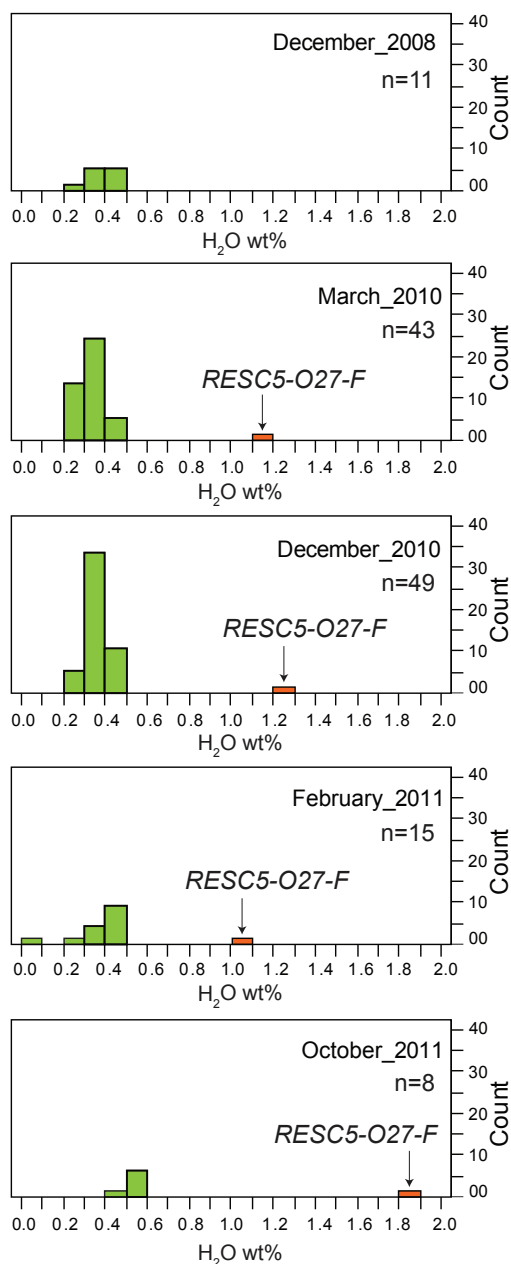


Fig. 4. H₂O contents variability associated to different working sessions. Note that contents from October-2011 were slightly higher than the other working sessions and that on March-2011 H₂O contents are slightly lower. It is important to note that the same MI (RESC5-O27-MF from Solchiaro sample) was measured in different working sessions. The concentration variability likely reflects the different slopes of the calibration curves calculated for each working session (see Supplementary Material for more details).

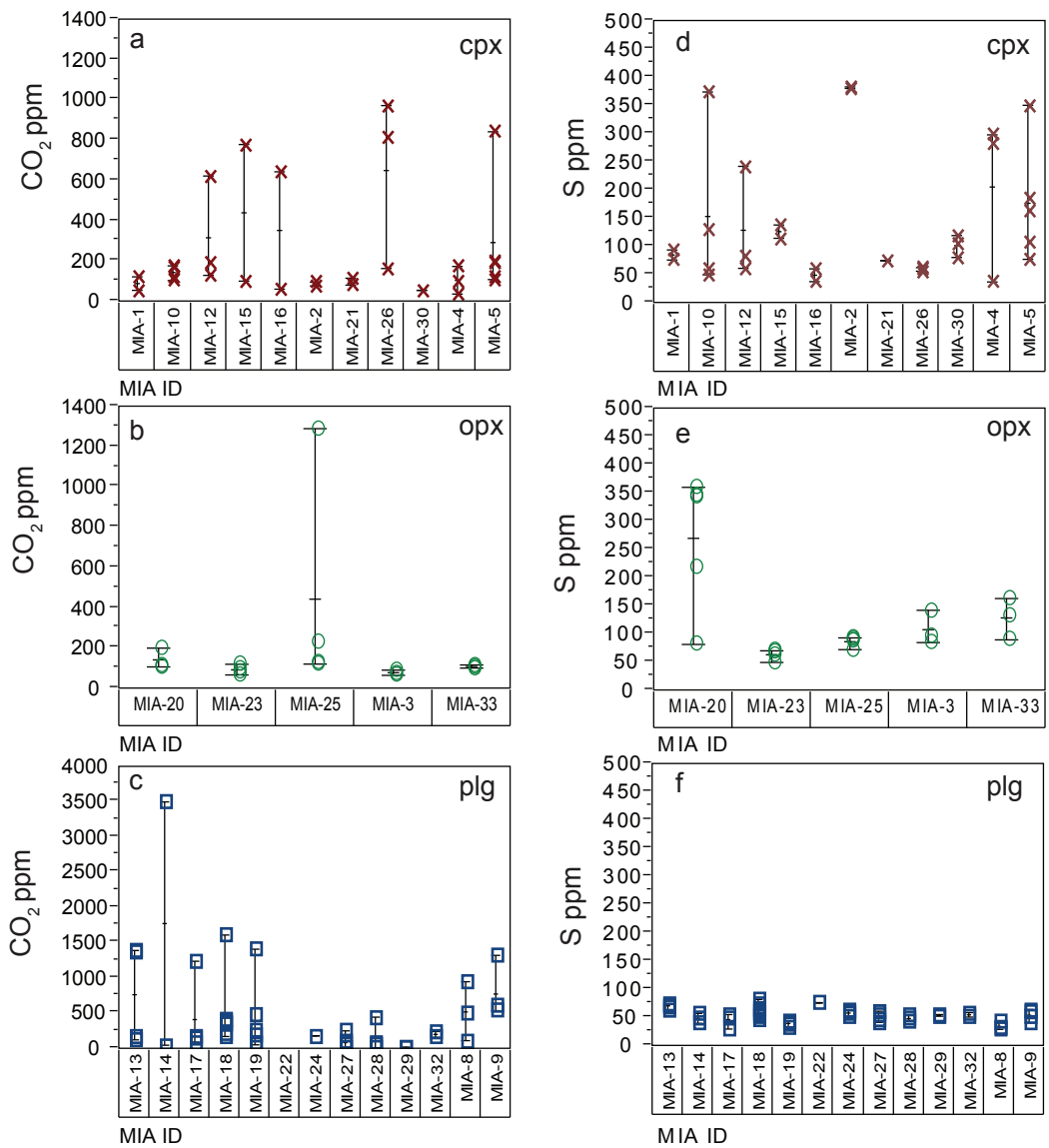


Fig. 5. Variability diagrams of CO₂ and S concentrations of MIA hosted in clinopyroxene, orthopyroxene, and plagioclase from White Island. It is important to note the high CO₂ variability within a single MIA for half of the all MIA. Also, it is important to note that S concentrations are consistent in MIA hosted in plagioclase, and that concentration of CO₂ is <200 ppm for consistent MIA.

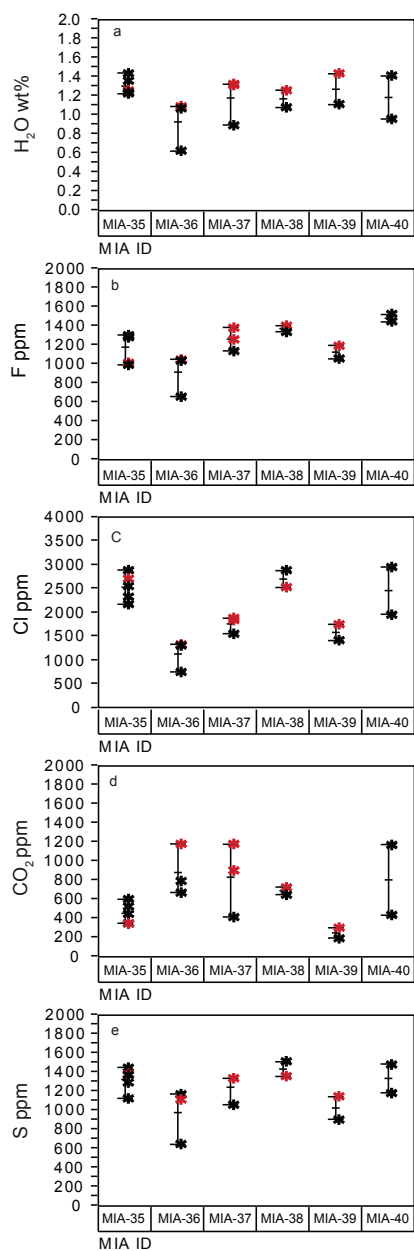


Fig. 6. Variability diagrams of H₂O, F, Cl, CO₂ and S concentrations of MIA hosted in olivine and clinopyroxene from Solchiaro Sample. It is important to note that the CO₂ variability of MIA from Solchiaro is less exaggerated than that of the White Island.

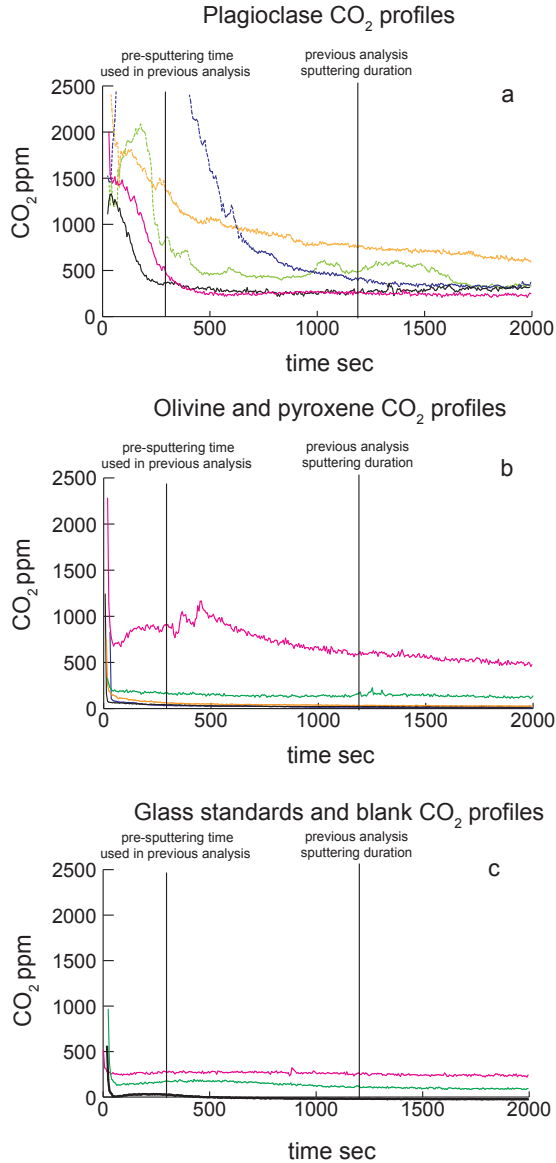


Fig. 7. CO₂ depth profiles of exposed and unexposed MI from White Island and Solchiaro samples. a) CO₂ depth profiles for MI hosted in plagioclase. It is important to note the unpredictable CO₂ behavior in the shallowest part of the MI; b) CO₂ depth profiles for MI hosted in mafic phenocrysts. The shallowest part of the profiles does not show the same unpredictable behavior of CO₂ of MI hosted in plagioclase; c) CO₂ depth profiles for glass standards and blank used to calculate the calibration curves. It is important to note that CO₂ concentration does not behave anomalously in the glass standards. The solid lines indicate the duration of the pre-sputtering and the analysis. It is important to note, however, that these lines represent times relative to different analytical conditions.

11. Supplementary material

11.1 Tables

SMTTable1. Glass standards data used to calculate calibration curves. Glass standards information is reported by Helo et al. (2011).

work-session	$^{12}\text{C}/^{30}\text{Si}$	CO_2 ppm	$^{16}\text{O}1\text{H}/^{30}\text{Si}$	H_2O wt%	$^{19}\text{F}/^{30}\text{Si}$	F ppm	$^{32}\text{S}/^{30}\text{Si}$	S ppm	$^{35}\text{Cl}/^{30}\text{Si}$	Cl ppm	Glass standard ID
May-08	1.31E-02	161	1.92E+00	0.61	1.55E+00	445	3.00E+00	1640	2.24E+00	1433	ALV-1649-3
May-08	1.24E-02	165	5.75E-01	0.17	3.32E-01	90	1.47E+00	950	8.02E-02	45	ALV-519-4-1
May-08	9.53E-03	159	2.53E+00	1.00	2.48E+00	997	2.26E+00	1562	4.21E+00	2914	ALV-1654-3
Dec-08	2.19E-02	237	5.70E-01	0.11	3.92E-01	124	1.34E+00	877	2.18E-02	45	EN-113-46D
Dec-08	1.64E-02	161	1.89E+00	0.61	1.35E+00	445	2.61E+00	1640	1.75E+00	1433	ALV-1649-3
Dec-08	8.83E-03	88	2.70E+00	1.00	1.29E+00	431	1.72E+00	1183	4.30E-01	322	GL07-D52-5
Dec-08	1.12E-02	159	3.04E+00	1.00	2.54E+00	997	2.22E+00	997	4.04E+00	2914	ALV-1654-3
Mar-10	n.a.	237	1.33E+00	0.11	3.47E-01	124	3.47E-01	877	3.18E-02	45	EN-113-46D
Mar-10	1.25E-02	161	2.49E+00	0.61	1.16E+00	445	1.16E+00	1640	2.15E+00	1433	ALV-1649-3
Mar-10	1.22E-02	88	3.60E+00	1.00	1.12E+00	431	1.12E+00	1183	5.23E-01	322	GL07-D52-5
Mar-10	n.a.	159	3.51E+00	1.00	2.28E+00	997	2.28E+00	1562	4.69E+00	2914	ALV-1654-3
Dec-10	9.59E-03	88	2.74E+00	1.00	1.03E+00	431	1.80E+00	1183	5.29E-01	322	GL07-D52-5
Dec-10	1.86E-02	237	6.25E-01	0.11	3.24E-01	124	1.42E+00	877	3.25E-02	45	EN-113-46D
Dec-10	1.48E-02	159	2.04E+00	1.00	1.96E+00	997	1.98E+00	1562	3.41E+00	2914	ALV-1654-3
Dec-10	1.30E-02	165	5.18E-01	0.17	2.41E-01	90	1.23E+00	950	7.10E-02	45	ALV-519-4-1
Oct-11	2.04E-02	237	3.60E-01	0.11	3.45E-01	124	1.51E+00	877	3.32E-02	45	EN-113-46D
Oct-11	1.60E-02	165	4.41E-01	0.17	2.51E-01	90	1.23E+00	950	7.42E-02	45	ALV-519-4-1
Oct-11	1.68E-02	159	2.20E+00	1.00	2.15E+00	997	2.09E+00	1562	4.09E+00	2914	ALV-1654-3
Oct-11	9.47E-03	88	2.13E+00	1.00	1.03E+00	431	1.67E+00	1183	4.36E-01	322	GL07-D52-5
Mar-12	1.71E-02	237	n.a.	n.a.	3.81E-04	124	n.a.	n.a.	n.a.	n.a.	EN-113-46D
Mar-12	7.61E-03	88	n.a.	n.a.	1.86E-03	431	n.a.	n.a.	n.a.	n.a.	GL07-D52-5

n.a. = not available

SMTTable2. Volatile compositions of MI from White Island and Solchiaro.

MI ID	MIA ID	CO ₂ ppm	H ₂ O wt%	F ppm	S ppm	Cl ppm	host	working session
<i>White Island</i>								
WI-3-beta	MIA-01	124	0.33	467	77	1681	cpx	December_2008
WI-3-gamma	MIA-01	57	0.27	407	95	2010	cpx	December_2008
WI-7-1	MIA-02	79	0.37	419	384	1524	cpx	December_2008
WI-7-3	MIA-02	97	0.40	439	381	1650	cpx	December_2008
WI-5-C	MIA-03	93	0.40	356	143	1173	opx	December_2008
WI-5-D	MIA-03	81	0.37	324	97	1127	opx	December_2008
WI-5-E	MIA-03	67	0.34	300	86	1042	opx	December_2008
REWI_8_1	MIA-04	39	0.25	254	38	470	cpx	March_2010
REWI_8_4	MIA-04	176	0.33	384	299	977	cpx	March_2010
REWI_8_5	MIA-04	120	0.38	389	274	889	cpx	March_2010
REWI_8_5bis	MIA-04	88	0.40	396	290	965	cpx	March_2010
REWI_8_5-av	MIA-04	104	0.39	392	282	927	cpx	March_2010
REWI_8_alfa	MIA-05	191	0.35	356	108	847	cpx	March_2010
REWI_8_beta	MIA-05	127	0.35	413	351	1116	cpx	March_2010
REWI_8_gamma	MIA-05	845	0.33	333	163	723	cpx	March_2010
REWI_8_teta	MIA-05	199	0.26	274	186	623	cpx	March_2010
REWI_8_omega	MIA-05	130	0.39	382	79	873	cpx	March_2010
REWI_8_omega_bis	MIA-05	91	0.38	379	77	857	cpx	March_2010
REWI_8_omega_av	MIA-05	111	0.38	381	78	865	cpx	March_2010
REWI_21_A	MIA-08	503	0.33	280	43	726	plg	March_2010
REWI_21_B	MIA-08	956	0.24	203	32	490	plg	March_2010
REWI_21_D	MIA-08	121	0.25	212	30	500	plg	March_2010
REWI_4b_B	MIA-09	545	0.29	267	42	679	plg	March_2010
REWI_4b_D	MIA-09	629	0.41	391	65	972	plg	March_2010
REWI_4b_E	MIA-09	1330	0.35	322	60	881	plg	March_2010
REWI_4b_F	MIA-09	621	0.37	325	53	945	plg	March_2010
REWI_15_A	MIA-10	172	0.40	401	60	903	cpx	March_2010
REWI_15_D	MIA-10	126	0.38	382	50	876	cpx	March_2010
REWI_15_H	MIA-10	106	0.40	415	131	975	cpx	March_2010
REWI_15_I	MIA-10	179	0.38	384	375	964	cpx	March_2010
REWI_7_A	MIA-12	625	0.39	454	84	1011	cpx	March_2010
REWI_7_D	MIA-12	132	0.35	395	62	955	cpx	March_2010
REWI_7_C	MIA-12	280	0.40	465	251	1397	cpx	March_2010
REWI_7_Cbis	MIA-12	115	0.37	443	234	1324	cpx	March_2010
REWI_7_C_av	MIA-12	198	0.39	454	243	1361	cpx	March_2010
REWI_19_A	MIA-13	170	0.34	321	64	926	plg	March_2010
REWI_19_D	MIA-13	dishom	0.38	348	70	1005	plg	March_2010
REWI_19_G	MIA-13	132	0.39	359	75	1056	plg	March_2010
REWI_19_I	MIA-13	1400	0.39	342	73	975	plg	March_2010
REWI_19_L	MIA-13	1384	0.41	368	75	1040	plg	March_2010
REWI_20_D	MIA-14	3508	0.26	256	41	740	plg	March_2010

REWI_20_E	MIA-14	54	0.40	328	58	925	plg	March_2010
REWI_20_F	MIA-14	dishom	0.31	230	49	737	plg	March_2010
REWI_17_A	MIA-15	781	0.27	446	115	1761	cpx	March_2010
REWI_17_B	MIA-15	103	0.28	422	139	1994	cpx	March_2010
REWI_12a_A	MIA-16	63	0.30	344	38	803	cpx	March_2010
REWI_12a_B	MIA-16	646	0.41	306	61	608	cpx	March_2010
WI_26_A	MIA-17	1246	0.35	243	56	1078	plg	December_2010
WI_26_B	MIA-17	176	0.36	251	51	1053	plg	December_2010
WI_26_D	MIA-17	97	0.23	163	31	570	plg	December_2010
WI_26_E	MIA-17	153	0.33	239	51	1004	plg	December_2010
WI_27_A	MIA-18	na	0.36	260	64	1186	plg	December_2010
WI_27_B	MIA-18	415	0.37	265	62	1157	plg	December_2010
WI_27_C	MIA-18	na	0.37	265	65	1205	plg	December_2010
WI_27_D	MIA-18	na	0.38	275	67	1198	plg	December_2010
WI_27_E	MIA-18	1618	0.41	311	83	1355	plg	December_2010
WI_27_H	MIA-18	405	0.30	220	54	796	plg	December_2010
WI_27_I	MIA-18	372	0.34	239	57	906	plg	December_2010
WI_27_k	MIA-18	348	0.38	268	58	1031	plg	December_2010
WI_27_L	MIA-18	340	0.28	204	48	702	plg	December_2010
WI_27_F	MIA-18	152	0.44	329	73	1300	plg	December_2010
WI_27_F_1	MIA-18	204	0.44	328	75	1315	plg	December_2010
WI_27_F_av	MIA-18	178	0.44	328	74	1307	plg	December_2010
WI_27_G	MIA-18	391	0.36	258	56	1018	plg	December_2010
WI_27_J	MIA-18	288	0.40	291	64	1068	plg	December_2010
WI_27_J_a	MIA-18	270	0.44	329	73	1300	plg	December_2010
WI_27_J_3	MIA-18	76	0.45	308	63	1278	plg	December_2010
WI_27_J_av	MIA-18	211	0.43	309	67	1216	plg	December_2010
WI_25_A	MIA-19	87	0.33	254	45	1010	plg	December_2010
WI_25_C	MIA-19	192	0.30	229	33	748	plg	December_2010
WI_25_D	MIA-19	271	0.33	248	39	840	plg	December_2010
WI_25_F	MIA-19	na	0.34	261	44	837	plg	December_2010
WI_25_G	MIA-19	484	0.28	218	38	682	plg	December_2010
WI_25_I	MIA-19	270	0.30	229	41	769	plg	December_2010
WI_25_B	MIA-19	79	0.34	253	45	1016	plg	December_2010
WI_25_B_a	MIA-19	42	0.37	277	42	1022	plg	December_2010
WI_25_B_av	MIA-19	61	0.35	265	44	1019	plg	December_2010
WI_25_E	MIA-19	na	0.39	294	48	1028	plg	December_2010
WI_25_E_a	MIA-19	1418	0.28	208	33	625	plg	December_2010
WI_25_E_av	MIA-19	1418	0.34	251	41	827	plg	December_2010
WI_30_A	MIA-20	na	0.47	389	219	1219	opx	December_2010
WI_30_B	MIA-20	na	0.47	383	361	1355	opx	December_2010
WI_30_C	MIA-20	203	0.48	376	343	1215	opx	December_2010
WI_30_E	MIA-20	120	0.44	370	346	1412	opx	December_2010
WI_30_D	MIA-20	na	0.43	338	86	1278	opx	December_2010
WI_30_D_2	MIA-20	109	0.43	339	79	1252	opx	December_2010

WI_30_D-av	MIA-20	109	0.43	339	82	1265	opx	December_2010
WI_31_A	MIA-21	117	0.40	331	75	1208	cpx	December_2010
WI_25_B	MIA-21	79	0.34	253	45	1016	cpx	December_2010
WI_25_B_a	MIA-21	42	0.37	277	42	1022	cpx	December_2010
WI_31_B-av	MIA-21	69	0.35	265	44	1019	cpx	December_2010
WI_33_A	MIA-22	na	0.40	325	77	1353	plg	December_2010
WI_33_B	MIA-22	na	0.39	332	77	1330	plg	December_2010
WI_36_A	MIA-23	98	0.33	333	71	1380	opx	December_2010
WI_36_B	MIA-23	122	0.24	220	50	1339	opx	December_2010
WI_36_D	MIA-23	69	0.30	303	65	1266	opx	December_2010
WI_36_E	MIA-23	89	0.31	314	69	1302	opx	December_2010
WI_37_A	MIA-24	na	0.33	289	63	1115	plg	December_2010
WI_37_B	MIA-24	na	0.35	293	57	1128	plg	December_2010
WI_37_C	MIA-24	na	0.38	292	62	1215	plg	December_2010
WI_37_D	MIA-24	188	0.38	283	53	1201	plg	December_2010
WI_38_A	MIA-25	131	0.35	327	94	1096	opx	December_2010
WI_38_B	MIA-25	235	0.37	320	90	1147	opx	December_2010
WI_38_E	MIA-25	1292	0.36	302	91	970	opx	December_2010
WI_38_G	MIA-25	123	0.38	315	73	1073	opx	December_2010
WI_39_A	MIA-26	816	0.33	289	63	1115	cpx	December_2010
WI_39_B	MIA-26	975	0.34	285	57	1112	cpx	December_2010
WI_39_C	MIA-26	165	0.38	292	62	1215	cpx	December_2010
RE-WI-29-A	MIA-27	15	0.43	307	46	969	plg	February_2011
RE-WI-29-C	MIA-27	21	0.45	348	60	1085	plg	February_2011
RE-WI-29-D	MIA-27	259	0.44	317	57	1011	plg	February_2011
RE-WI-29-E	MIA-27	61	0.05	230	42	726	plg	February_2011
RE-WI-29-F	MIA-27	105	0.44	326	62	1031	plg	February_2011
RE-WI-32-A	MIA-28	453	0.37	278	49	762	plg	February_2011
RE-WI-32-B	MIA-28	78	0.38	278	47	787	plg	February_2011
RE-WI-32-C	MIA-28	59	0.43	304	54	913	plg	February_2011
RE-WI-32-E	MIA-28	20	0.40	288	47	825	plg	February_2011
RE-WI-32-E-1	MIA-28	19	0.37	279	44	740	plg	February_2011
RE-WI-32-E-av	MIA-28	19	0.38	283	46	783	plg	February_2011
RE-WI-40-A	MIA-29	16	0.42	279	53	863	plg	February_2011
RE-WI-40-B	MIA-29	na	0.45	303	56	935	plg	February_2011
RE-WI-40-C	MIA-29	28	0.41	289	54	832	plg	February_2011
RE-WI-41-A	MIA-30	na	0.43	323	105	950	cpx	February_2011
RE-WI-41-C	MIA-30	na	0.23	204	81	1003	cpx	February_2011
RE-WI-41-D	MIA-30	57	0.39	282	120	814	cpx	February_2011
WI_Dec_7_B	MIA-32	249	0.53	355	60	1093	plg	October_2011
WI_Dec_7_D	MIA-32	167	0.47	317	52	943	plg	October_2011
WI-Dec-5_A	MIA-33	103	0.56	391	90	1170	opx	October_2011
WI-Dec-5_B	MIA-33	111	0.59	412	134	1241	opx	October_2011
WI-Dec-5_C	MIA-33	119	0.57	404	164	1205	opx	October_2011
WI-Prev-2-5-B	single MI	113	0.57	619	70	1216	plg	October_2011

REWI_86_A1	single MI	101	0.56	621	101	1433	cpx	October_2011
REWI_86_A2	single MI	73	0.56	617	101	1450	cpx	October_2011
REWI_86_A_av	single MI	87	0.56	619	101	1441	cpx	October_2011
REWI_11_C	single MI	46	0.20	216	32	416	cpx	March_2010
REWI_13_A	single MI	321	0.34	400	65	704	cpx	March_2010
REWI_20_2	single MI	197	0.24	249	38	710	plg	March_2010
REWI_22_1	single MI	934	0.26	327	34	532	cpx	March_2010
REWI_23_A	single MI	150	0.27	336	53	849	cpx	March_2010
REWI_9_I	single MI	82	0.27	269	72	471	cpx	March_2010
WI-5-2	single MI	86	0.42	373	91	1258	opx	December_2008
REWI_10_G	single MI	47	0.41	380	85	925	opx	December_2008
REWI_10_G_bis	single MI	130	0.40	375	87	902	opx	December_2008
REWI_10_G_tris	single MI	35	0.41	378	84	913	opx	December_2008
REWI_10_G_av	single MI	71	0.41	378	85	914	cpx	March_2010
WI-6-1	single MI	59	0.44	332	60	930	cpx	December_2008
REWI_3_I	single MI	84	0.40	346	192	892	cpx	May_2008
WI-6-A	single MI	309	0.47	346	60	1226	cpx	December_2008
WI-7-III	single MI	246	0.39	387	126	1279	cpx	December_2008
REWI_8_D Average WI MI composition	single MI	179	0.39	396	56	872	cpx	March_2010
<i>Solchiaro</i>								
RESC5_O27_F1	MIA-35	447	1.80	1471	1600	2732	olivi ne	VT_Oct_2011
RESC5_O27_F2	MIA-35	448	1.82	1472	1621	2794	olivi ne	VT_Oct_2011
RESC5_O27_F_a v_Oct_2011	MIA-35	448	1.81	1471	1610	2763	olivi ne	VT_Oct_2011
RESC5_O27_C	MIA-35	361	1.45	1000	1305	2572	olivi ne	VT_Oct_2011
RESC5-O27-MG	MIA-35	694	1.47	1354	1304	1969	olivi ne	WHOI Feb_2011
RESC5-O27-MF	MIA-35	742	1.07	1042	1025	1328	olivi ne	WHOI Feb_2011
RESC5-O27-MF	MIA-35	552	1.24	1259	1571	2818	olivi ne	VT Dec_2010
RESC5-O27_F1	MIA-35	507	1.24	1238	1563	2796	olivi ne	VT Dec_2010
RESC5_O27_F_a v_Dec_2010	MIA-35	530	1.24	1248	1567	2807	olivi ne	VT Dec_2010
RESC5-O27_G	MIA-35	490	1.20	1285	1532	2734	olivi ne	VT Dec_2010
RESC5-O27_E	MIA-35	450	1.23	1286	1134	2916	olivi ne	VT Dec_2010
RESC5_O27_F	MIA-35	509	1.19	1365	1418	2042	olivi ne	VT Mar_2010
RESC5_O27_F1	MIA-35	493	1.17	1350	1411	2019	olivi ne	VT Mar_2010
RESC5_O27_F_a v_Mar_2010	MIA-35	501	1	1358	1415	2031	olivi ne	VT Dec_2010

RESC5_O27_G	MIA-35	645	1.08	1266	1299	1892	olivi ne	VT Mar_2010
RESC5-O27_B*	MIA-35	358	1.27	1026	1384	2730	olivi ne	VT Jul_2009
RESC5_O6_C	MIA-36	680	0.63	668	652	780	olivi ne	VT Mar_2010
RESC5_O6_D	MIA-36	799	1.08	1045	1180	1332	olivi ne	VT Mar_2010
RESC5_O6_B*	MIA-36	1189	1.10	1059	1122	1358	olivi ne	VT Jul_2009
RESC5_O21_F	MIA-37	424	0.90	1147	1068	1582	olivi ne	VT Mar_2010
RESC5-O21-A*	MIA-37	1185	1.33	1393	1344	1905	olivi ne	VT july_2009
RESC5-O21-E*	MIA-37	914	1.33	1272	1342	1870	olivi ne	VT July_2009
RESC5_O30_B	MIA-38	658	1.09	1348	1518	2902	olivi ne	VT Mar_2010
RESC5-O30-A*	MIA-38	737	1.27	1411	1364	2550	olivi ne	VT July_2009
RESC5_O22_B	MIA-39	203	1.12	1063	915	1437	olivi ne	VT Mar_2010
RESC5-O22-A*	MIA-39	310	1.44	1204	1151	1777	olivi ne	VT July_2009
RESC_C53_C	MIA-40	1182	0.97	1528	1192	1989	cpx	VT Mar_2010
RESC2-C53-A	MIA-40	442	1.42	1450	1494	2978	cpx	VT Dec_2008
RESC5_O6_EM1	single MI	857	1.20	1532	1311	1743	oli	VT Mar_2010
Average composition of Solchiaro MI		612	1.25	1262	1325	2177		

* = data by Esposito et al. (2011)

na = not available

11.2 Figures

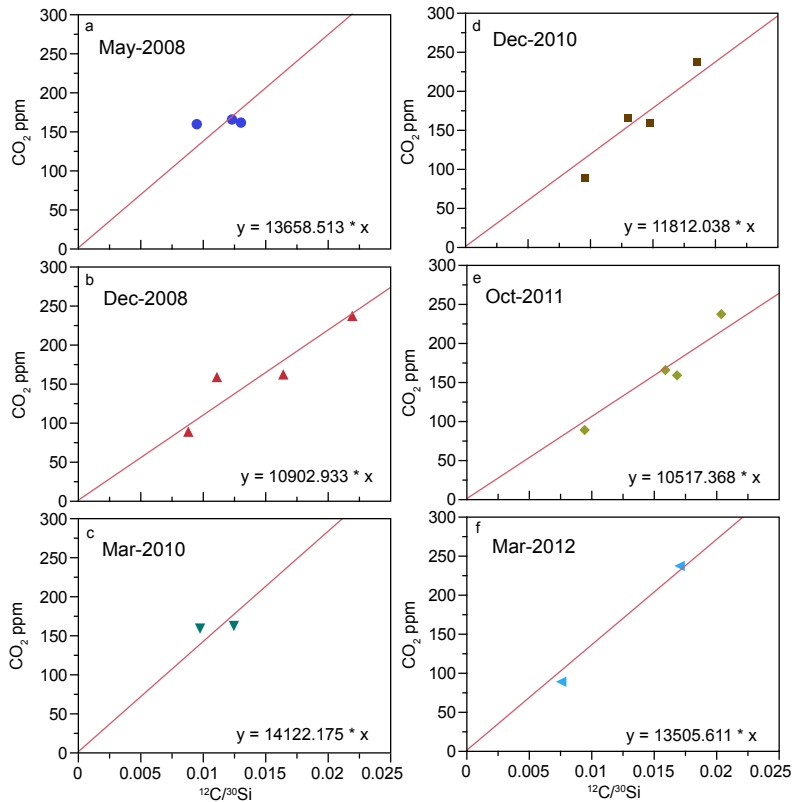


Fig. SM1. Calibration curves of CO₂. Known standard CO₂ concentrations are plotted versus ¹²C/³⁰Si isotope ratios measured by SIMS. The ratio is expressed as the ion count per second of ¹²C divided by the ion counts per second of ³⁰Si. In the diagrams we have reported the linear regressions forced to the origin. Data used for the calibration are reported in SM Table1. Panels a, b, c, d, e, and f show calibration curves representative of each working session performed by SIMS at Virginia Tech in May 2008, December 2008, March 2010, December 2010, October 2011, and March 2012 respectively. Note that CO₂ calibration curves calculated for this study are consistent with that reported by Helo et al. (2011).

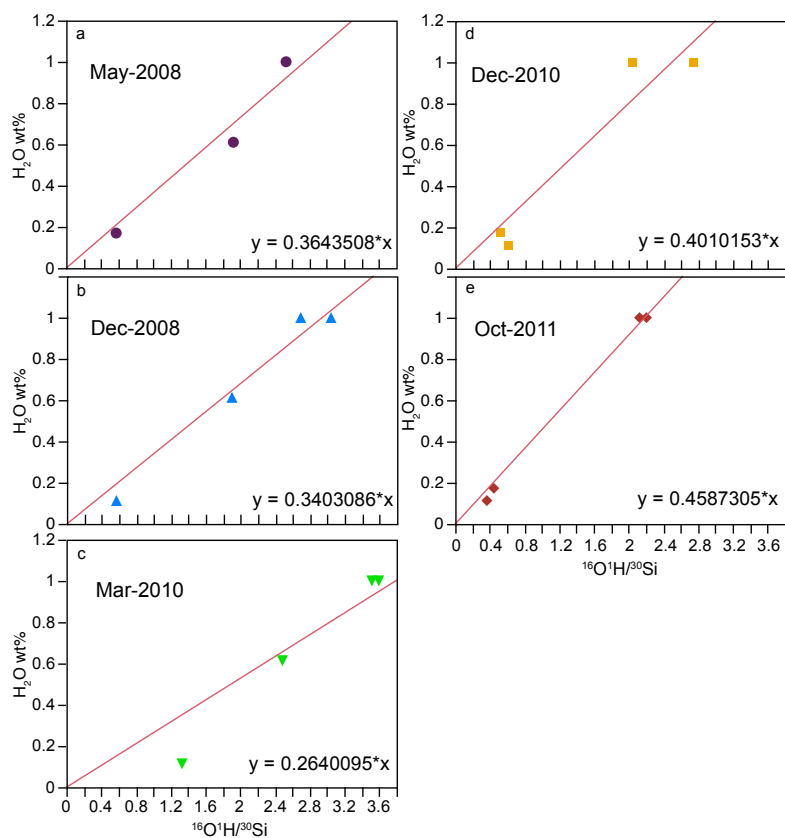


Fig. SM2. Calibration curves of H₂O. Known standard H₂O concentrations are plotted versus ¹⁶O¹H/³⁰Si isotope ratios measured by the SIMS. The ratio is expressed as the ion count per second of ¹⁶O¹H divided by the ion counts per second of ³⁰Si. In the diagrams we have reported the linear regressions forced to the origin. Data used for the calibration are reported in SM Table1. Panels a, b, c, d, and e show calibration curves representative of each working session performed by SIMS at Virginia Tech in May 2008, December 2008, March 2010, December 2010, October 2011, and March 2012 respectively. Note that H₂O calibration curves calculated for this study are consistent with that reported by Helo et al. (2011).

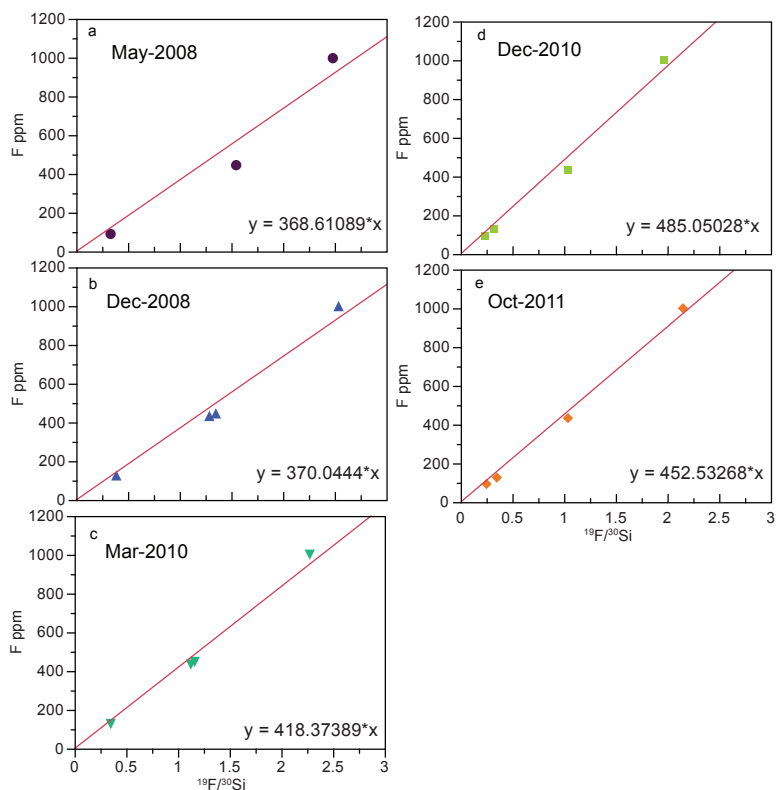


Fig. SM3. Calibration curves of F. Known standard F concentrations are plotted versus $^{19}\text{F}/^{30}\text{Si}$ isotope ratios measured by SIMS. The ratio is expressed as the ion count per second of ^{19}F divided by the ion counts per second of ^{30}Si . In the diagrams we have reported the linear regressions forced to the origin. Data used for the calibration are reported in SM Table1. Panels a, b, c, d, and e show calibration curves representative of each working session performed by SIMS at Virginia Tech in May 2008, December 2008, March 2010, December 2010, October 2011, and March 2012 respectively. Note that the F calibration curves calculated for this study are consistent with that reported by Helo et al. (2011).

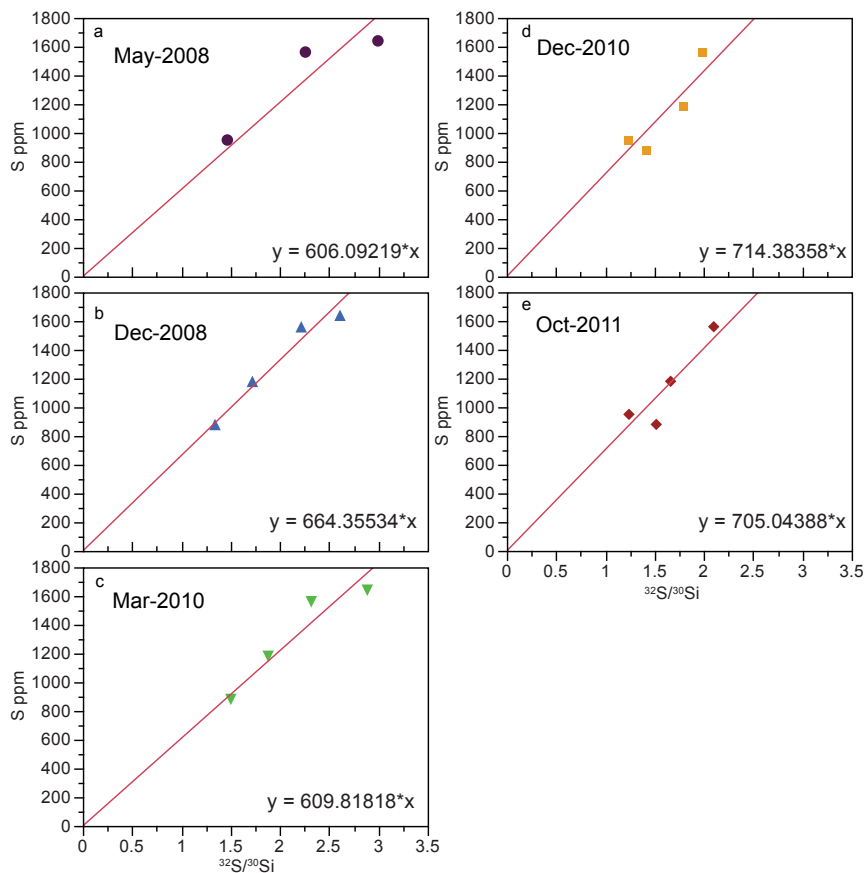


Fig. SM4. Calibration curves of F. Known standard F concentrations are plotted versus $^{32}\text{S}/^{30}\text{Si}$ isotope ratios measured by SIMS. The ratio is expressed as the ion count per second of ^{32}S divided by the ion counts per second of ^{30}Si . In the diagrams we have reported the linear regressions forced to the origin. Data used for the calibration are reported in SM Table1. Panels a, b, c, d, and e show calibration curves representative of each working session performed with the SIMS at Virginia Tech in May 2008, December 2008, March 2010, December 2010, October 2011, and March 2012 respectively. Note that the S calibration curves calculated for this study are consistent with that reported by Helo et al. (2011).

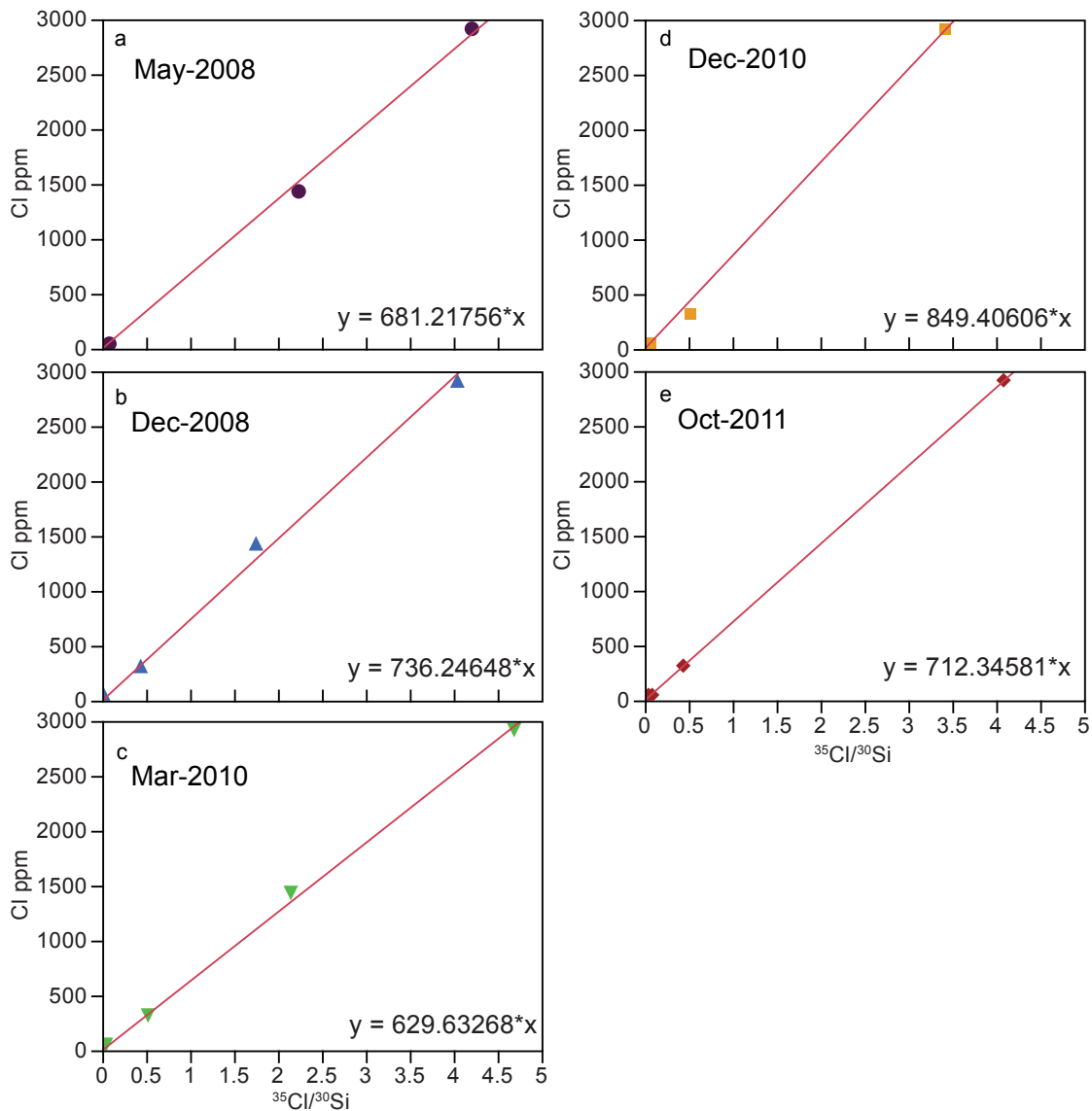


Fig. SM5. Calibration curves of Cl. Known standard Cl concentrations are plotted versus $^{35}\text{Cl}/^{30}\text{Si}$ isotope ratios measured by SIMS. The ratio is expressed as the ion count per second of ^{35}Cl divided by the ion counts per second of ^{30}Si . In the diagrams we have reported the linear regressions forced to the origin. Data used for the calibration are reported in SM Table1. Panels a, b, c, d, and e show calibration curves representative of each working session performed by SIMS at Virginia Tech in May 2008, December 2008, March 2010, December 2010, October 2011, and March 2012 respectively. Note that the Cl calibration curves calculated for this study are consistent with that reported by Helo et al. (2011).

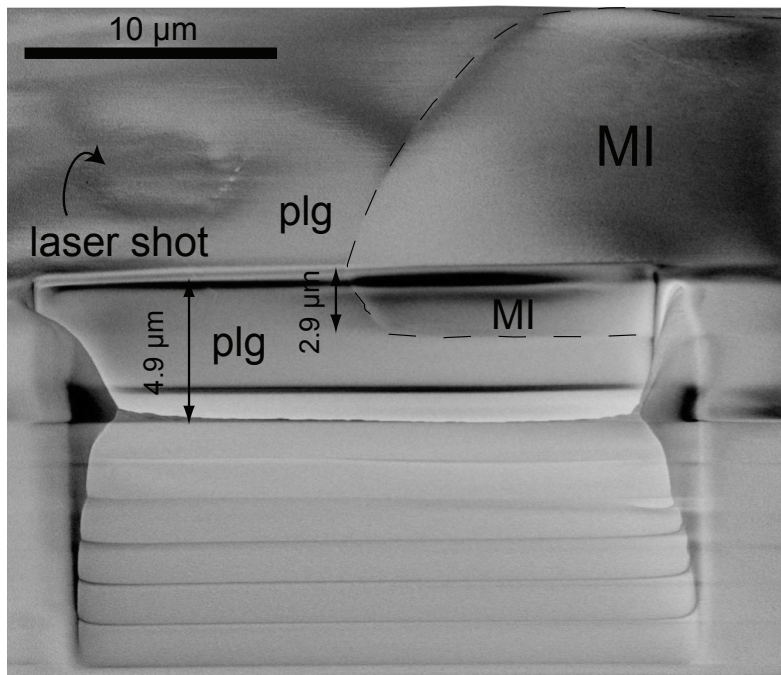


Fig. SM6. FIB image of a MI hosted in plagioclase of White Island. It is important to note the regularity of the MI/Host interface.

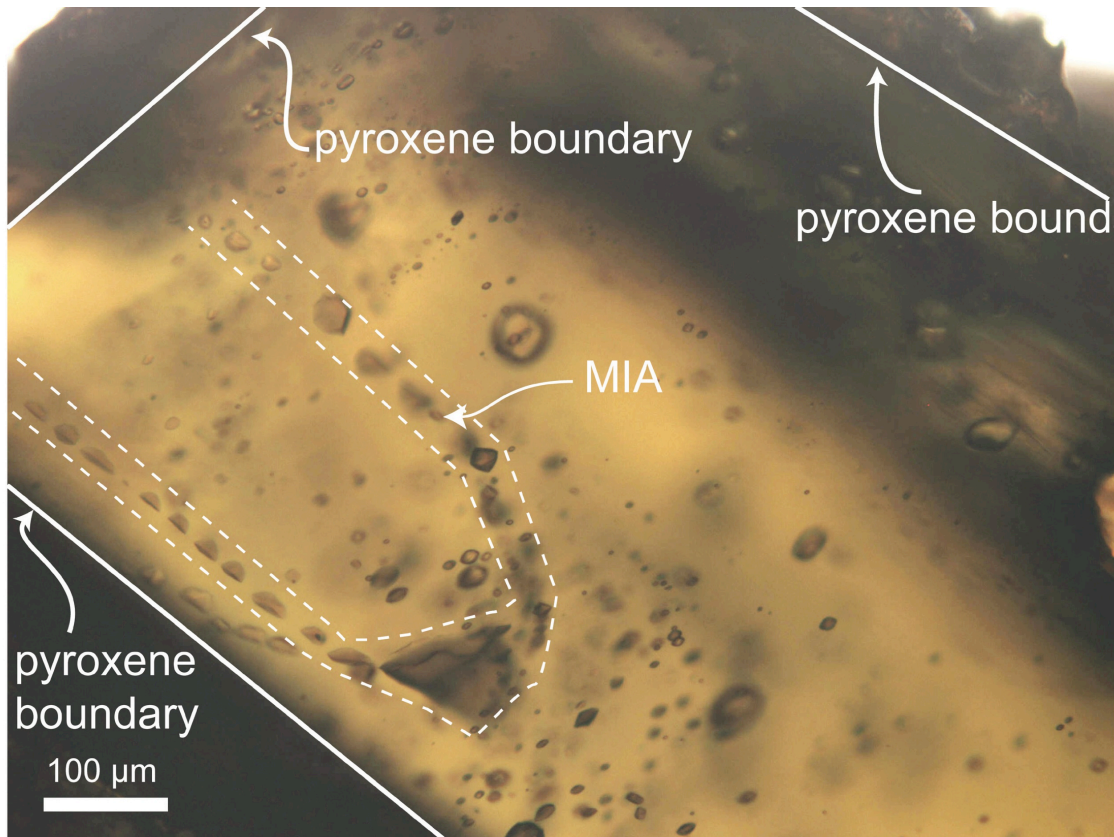


Fig. SM7. Microphotograph of a “pseudosecondary MIA” hosted in pyroxene.

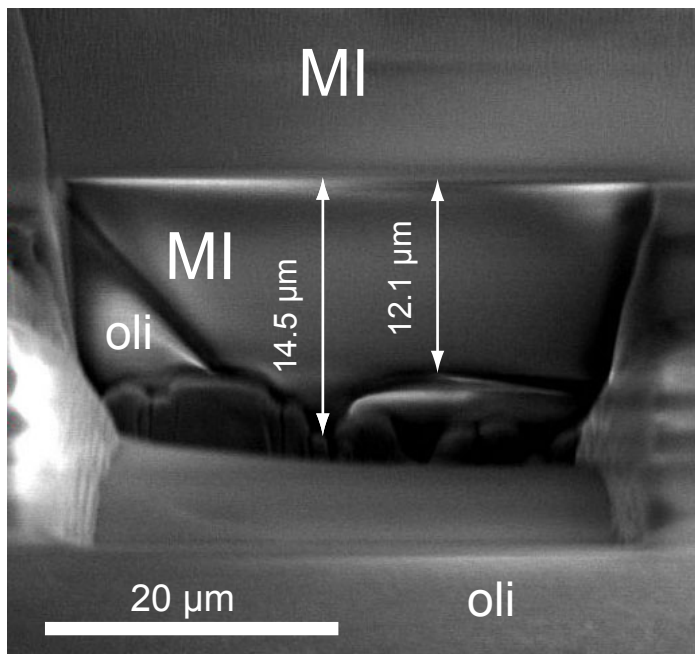


Fig. SM8. FIB image of a MI hosted in olivine from Solchiaro. Note the irregularity of the MI/host interface.

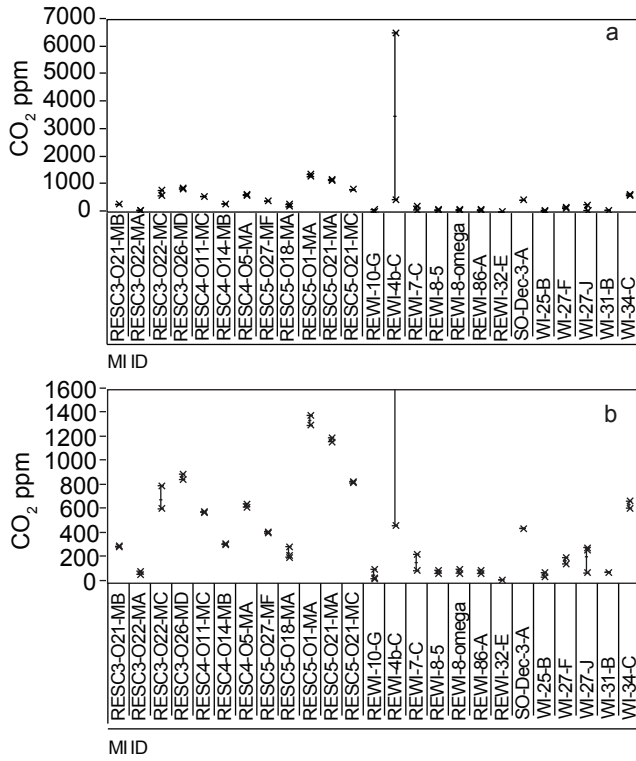


Fig. SM9. Variability diagrams of CO₂ concentration of single MIs. Data includes MI from Esposito et al. (2011).

CHAPTER 3

Esposito, R., Bodnar, R. J., Danyushevsky, L., De Vivo, B., Fedele, L., Hunter, J., Lima, A. & Shimizu, N. (2011). Volatile Evolution of Magma Associated with the Solchiaro Eruption in the Phlegrean Volcanic District (Italy). *Journal of Petrology*. 52, 12, pg 2431-2460.

Volatile Evolution of Magma Associated with the Solchiaro Eruption in the Phlegrean Volcanic District (Italy)

R. Esposito^a, R. J. Bodnar^a, L. V. Danyushevsky^b, B. De Vivo^c, L. Fedele^a, J. Hunter^d, A. Lima^c, N. Shimizu^e

^a Fluids Research Laboratory, Department of Geosciences, Virginia Tech, Blacksburg VA, 24061 USA

^b CODES CoE and School of Earth Sciences, University of Tasmania, Private Bag 79, Hobart, TAS 7001 Australia

^c Dipartimento di Scienze della Terra, Università degli Studi di Napoli Federico II, Via Mezzocannone 8, Napoli, 80134 Italy

^d Nanoscale Characterization and Fabrication Labs, Virginia Tech, Blacksburg, VA 24061 USA

^e Woods Hole Oceanographic Institution, Woods Hole MA, USA

Abstract

More than 1.5 million people live in or near the Phlegrean Volcanic District (PVD) in southern Italy. The PVD represents one of the most carefully studied volcanic hazard areas in the world. Throughout its history, the style of volcanic activity has varied greatly, from relatively quiescent lava flows to explosive phreatomagmatic eruptions. The goal of this study is to develop a more detailed understanding of the physical and chemical processes associated with the Solchiaro eruption in the PVD.

The PVD includes three volcanic fields: the Campi Flegrei (CF) caldera and the volcanic islands of Ischia and Procida. The Solchiaro eruption on the island of Procida is one of the few primitive (less evolved) eruptions in the PVD and can provide information on the source of more evolved magmas associated with this volcanic system. One of the more important chemical parameters that determines the style of volcanic eruptions is the volatile budget of the magma before and during eruption, and melt inclusions (MI) provide the most direct information on the volatile contents of the pre-eruptive melt in the source region for the PVD. The composition of the melt phase before eruption was determined by analyzing major, minor and trace element and volatile contents of 109 MI in olivine from 4 samples of the Solchiaro eruption, representing different stratigraphic heights and, therefore, different relative times of eruption. Olivine compositions vary from F_{O82} to F_{O88} with one maximum value of F_{O90} . Compositions of MI in olivine were corrected for post entrapment crystallization (PEC) and for Fe-loss by diffusion.

Most (97 out of 109) of the MI studied are classified as “normal” MI because they show chemical evolution trends consistent with that of bulk rock from the PVD. Two types of anomalous MI were also recognized based on their major and trace element compositions: 1) Sr-rich MI and 2) enriched MI that are variably enriched in TiO_2 , K_2O , P_2O_5 , LILE, HFSE and REE relative to “normal” MI. These MI likely originated from dissolution-reaction-mixing processes in the mush zone of the magma body.

“Normal” MI include both bubble-bearing and bubble-free (containing only glass \pm trapped chromite) types. Bubble-free MI most closely record the pre-eruptive volatile content of the melt over a range of temporal and spatial conditions. The observed trends in CO_2 contents of MI versus crystallization indicators (e. g., Al_2O_3/CaO) support the interpretation that variations in volatile contents of bubble-free MI reflect real variations in the volatile budget of the melt during evolution of the magma.

The correlation between CO_2 contents of MI and the relative stratigraphic position of each sample is consistent with eruption of a volatile-saturated magma that initially ascended through the crust from an original depth of at least 8 km. The magma ponded at 4 to 2 km prior to eruption and crystallization and the concomitant volatile exsolution from the saturated melt in the shallow chamber triggered the Solchiaro eruption. As the eruption proceeded, the Solchiaro magma continued to ascend through the crust to a final storage depth of about 1 km.

1. Introduction

The Phlegrean Volcanic District (PVD) in southern Italy is comprised of three volcanic fields: the Campi Flegrei (CF) caldera and the volcanic islands of Ischia and Procida (Fig. 1a). The PVD includes numerous volcanic centers (cinder cones, tuff rings, calderas) and has experienced intermittent volcanic activity for approximately 150 ka, with the most recent eruption being the Monte Nuovo eruption in 1538 AD. Some of these eruptions have been highly explosive, but a wide range in eruptive styles is suggested by the volcanic deposits (Di Girolamo *et al.*, 1984). Because of its location near Naples (≈ 1 million inhabitants), many workers have studied these deposits over the years to develop a better understanding of the volcanic history of the PVD system to help predict the nature of potential future volcanic hazards associated with this active volcanic system.

In this study, the pre-eruptive volatile evolution of the Solchiaro magma was investigated using melt inclusions in phenocrysts. Melt inclusions (MI) are small samples of silicate melt that are trapped during magma crystallization. In the last few decades, the MI technique has proven to be a valid tool to study magmatic evolution (Roedder, 1979; Sobolev & Shimizu, 1993; Kamenetsky *et al.*, 1995; Frezzotti, 2001; Danyushevsky *et al.*, 2002b; Schiano, 2003; De Vivo & Bodnar, 2003; Student & Bodnar, 2004; Kent, 2008), especially concerning the pre-eruptive volatile content of the magma (e.g. Anderson, 1976; Lowenstern, 1995; Sobolev, 1996; Wallace *et al.*, 1999; Kent, 2008; Métrich & Wallace, 2008). As such, MI are an important source of information concerning minimum depths at which the magmas were generated or evolved, and if the magma was saturated in volatiles prior to an eruption (Lowenstern, 1995).

Burnham (1979) was one of the first workers to develop rigorous quantitative models describing the solubility of H₂O in silicate melts and the effect of volatiles on magma dynamics and chemical evolution of the melt. In a recent review, Moore (2008) describes the application of volatile solubility models for interpreting H₂O and CO₂ contents in MI, and Métrich & Wallace (2008) report that exsolution of major volatile constituents exerts a strong control on ascent, dynamics and eruption of magmas. It is noteworthy that MI often record evidence for volatile degassing during ascent of a crystallizing magma (Danyushevsky *et al.*, 1995; Anderson *et al.*, 2000; Saito *et al.*, 2001; Wade *et al.*, 2006; Benjamin *et al.*, 2007; Johnson *et al.*, 2008).

In addition to the more common "normal" MI contained in Solchiaro samples (as described below), a few MI with anomalous compositions similar to those reported in mafic volcanic products from various geodynamic settings have also been observed. One type of anomalous MI is referred to as Sr-rich MI - their origin is controversial but some workers have suggested that Sr-rich compositions reflect interaction with plagioclase in the source region (Sobolev *et al.*, 2000; Gurenko & Chaussidon, 1995; Schiano *et al.*, 2000; Danyushevsky *et al.*, 2004). Another type of anomalous MI is characterized by variable degrees of trace element enrichment relative to other "normal" MI whose trace element compositions are consistent with the bulk rock compositions. The composition of these MI suggests interaction of the melt with a complex mineral assemblage in the mush zone of a magma body, but their origin is still debated (Gurenko & Chaussidon, 1995; Kent *et al.*, 2002; Danyushevsky *et al.*, 2004).

In this study, we report the geochemical evolution of the magma associated with the Solchiaro eruption in the Procida volcanic field based on data obtained from MI. This work follows on previous studies of the Solchiaro eruption and Procida Island by other workers (Di Girolamo *et al.*, 1984; D'Antonio *et al.*, 1999; Cecchetti *et al.*, 2001; De Astis *et al.*, 2004). MI were studied in olivine phenocrysts from four samples representing different stratigraphic levels of the Solchiaro eruption. Solchiaro products were collected to test for geochemical variations as a function of stratigraphic height, representing a proxy for relative time of eruption from the magma chamber and, possibly, the depth from which the material was erupted. This study is focused mainly on correlations among pre-eruptive volatile concentrations, major and trace elements, and eruptive history to develop a better understanding of the evolution of the magma body associated with the Solchiaro eruption.

2. Geological Background

Geology and geochronology of the Phlegrean Volcanic District

The Phlegrean Volcanic District (PVD) is located near the margin of the Campanian Plain and is part of the Campanian Province (CP) that includes the Mt. Somma-Vesuvius volcanic edifice. The CP, in turn, is part of a more widespread Plio-Quaternary volcanic magmatic event that occurred in the circum-Tyrrhenian area (Peccerillo, 1999, 2005). The Campanian Margin is located in the hinge zone between the eastern Tyrrhenian Sea and the southern Apennines. Campanian magmatism is associated with NW-SE and NE-SW trending normal faults (Ippolito *et al.*, 1973; D'Argenio *et al.*, 1973; Finetti & Morelli, 1974; Bartole, 1984; Turco *et al.*, 2006). The PVD includes three volcanic fields that are thought to be part of the same magmatic system: the Campi Flegrei (CF) caldera and the nearby volcanic islands of Ischia and Procida (Fig. 1a and 1b). The various volcanic districts of the CP include rocks representing a wide variety of magma types (Peccerillo, 2005, and references therein). In general, rocks of the PVD range from slightly silica-undersaturated to oversaturated potassic rocks, while Somma-Vesuvius products are silica undersaturated and ultrapotassic. On the island of Procida, a scoria and some lava lithics (De Astis *et al.*, 2004; D'Antonio *et al.*, 1999) show low potassium contents comparable to calc-alkaline basaltic rocks. All rocks of the CP exhibit OIB and arc signatures, indicating that they likely originated from an OIB-type mantle contaminated by subduction-related fluids or melts.

At Procida, volcanic activity began as early as 55 ka, with the emplacement of the Vivara tuff (Rosi *et al.*, 1988), and terminated with the Solchiaro eruption. Paleosols underlying the Solchiaro deposits have been dated at 19.6 ka (Alessio *et al.*, 1989) and 17.3 ka (Lirer *et al.*, 1991), and a paleosol above the Solchiaro deposits has been dated at 14.3 ka (Alessio *et al.*, 1989). Thus, the Solchiaro eruption occurred at some time between 19.6 and 14.3 ka, and De Astis *et al.* (2004) assumed an age younger than about 18 ka for the Solchiaro eruption. Following the Solchiaro eruption, no volcanic activity has been recorded on Procida, and the island contains no fumaroles and shows little seismic activity. Procida is covered by the products of later eruptions from nearby CF and Ischia (Di Girolamo & Stanzione, 1973; Rosi *et al.*, 1988), and products of Procida eruptions are exposed along the mainland coast, interbedded with CF and Ischia products.

Recent stratigraphic studies on Procida volcanic rocks have been carried out by De Astis *et al.* (2004) and by Perrotta *et al.* (2010). Five volcanic vents that are considered to be monogenetic (De Astis *et al.*, 2004) have been recognized on the island: Vivara, Terra Murata, Pozzo Vecchio, Fiumicello and Solchiaro (from the oldest to the youngest; Fig. 1c). The eruptions related to these vents provided the material to form Procida Island. Solchiaro and the other four volcanoes of Procida Island formed along a volcano-tectonic belt oriented NE-SW and extending from Ischia to the Monte di Procida in CF (De Astis *et al.*, 2004). The volcanic rocks erupted along this volcano-tectonic belt show a bimodal composition - trachybasalts originated from a single magma batch rising from a deeper reservoir whereas trachyte originated from a shallower reservoir (De Astis *et al.*, 2004). The magmas produced during the Solchiaro, Fiumicello, and Vivara eruptions are the most primitive in composition of all of the eruptions in the PVD. The Solchiaro eruption built a tuff ring, and the maximum height of Solchiaro deposits is 60 m with a basal

diameter of 2.4 km (see Table 5 in Perrotta *et al.*, 2010). Solchiaro is one of the most voluminous eruptions in CF and Procida (see Fig. 37 in Di Girolamo *et al.*, 1984).

Solchiaro outcrops are abundant along most of the coast of Procida Island. Proximal Solchiaro deposits are stratified and lithified yellow tuffs with bomb sags and deep erosive channels, while distal deposits are gray and range from partially lithified to unlithified tuffs (Perrotta *et al.*, 2010; Di Girolamo *et al.*, 1984). De Astis *et al.* (2004) recognized three different units for the Solchiaro tuff ring. According to De Astis *et al.* (2004), the basal Solchiaro unit I consists of lithified and stratified yellow tuffs which contain bombs and blocks. These yellow tuffs grade into grey tuffs with increasing stratigraphic height. Products at the base of Solchiaro unit I are characteristic of a phreatomagmatic eruptive style. The increase in well-sorted lapilli layers and impact sags at the top of the sequence suggests that the eruptive style became more magmatic with time. The distal deposits of the Solchiaro unit I are layered and partially lithified gray tuffs. The deposits show sub-parallel and cross stratification facies (see Fig. 14 and 15 in Di Girolamo *et al.*, 2004) with traction structures indicating dry surge activity. The Solchiaro unit II (the middle unit) is generally < 1m thick and consists of sub-parallel cm to dm-thick layers containing ash, scoriae and scoriaceous bombs. The eruptive style of this unit is mostly strombolian and lapilli and scoria are commonly well sorted and vesiculated. The Solchiaro unit III (the upper unit) is <4 m thick and is also related to strombolian activity. The basal part of unit III is characterized by thin layers of ash and lapilli which show sub-parallel, small-scale sandwave and weak cross-lamination structures. The top part of Solchiaro unit III consists of dm-thick layers with slightly agglutinated scoriae and dm-size bombs. Thin layers of fine ash to lapilli alternate with the scoriaceous layers.

The most primitive sample studied by De Astis *et al.* (2004) is a scoria from Solchiaro unit I (their sample PRO 7/11). This scoria plots in the basaltic field on a TAS diagram, and the high Mg # and the high concentrations of Ni and Cr suggest that this sample represents a primary or near-primary magma that has experienced little or no crystallization (De Astis *et al.*, 2004). For comparison, Solchiaro units II and III have more shoshonitic compositions, indicating a more evolved composition relative to unit I. As described below, based on similar volcanic textures and compositions, samples collected for this study are interpreted to be correlative with Solchiaro unit I of De Astis *et al.* (2004).

Previous MI studies of the PVD

In recent years, numerous MI studies have been conducted to constrain the pre-eruptive history of the PVD and many of these studies have focused on the volatile content of the MI and estimated pressures (and depths) of trapping of the MI (Table 1). The Campanian Ignimbrite (CI) (39 ka; De Vivo *et al.*, 2001) is a trachy-phonolite and represents the largest volume eruption in the PVD (estimated at 150 km³ DRE by Civetta *et al.*, 1997, and 200 km³ DRE by Rolandi *et al.*, 2003; Fig. 1b). Chlorine contents of MI from the CI indicate pressures of crystallization between 50 and 100 MPa (Signorelli *et al.*, 2001). For the same volcanic products, Marianelli *et al.* (2006) estimate pressures of crystallization between 40 and 150 MPa based on H₂O contents of MI, which is in agreement with the results of Signorelli *et al.* (2001). Webster *et al.* (2003) studied MI

hosted in clinopyroxene from various ignimbrites in the Campanian Plain, ranging in age from 205.6 to 23-18 ka (De Vivo *et al.*, 2001). They recognized two different populations of MI: one containing high-Mg compositions and the other low-Mg composition melts. The high-Mg MI also show a high H₂O content. The same two populations are observed in the Giugliano Ignimbrites (23-18 ka; De Vivo *et al.*, 2001) and are considered to share a similar origin with MI from the CI (Webster *et al.*, 2003).

Several MI studies in the PVD have focused on the more primitive magmas (from trachybasalt to latite) having compositions similar to the MI of the present study (Cannatelli *et al.*, 2007; Cecchetti *et al.*, 2001 and 2005; Mangiacapra *et al.*, 2008). Cecchetti *et al.* (2001) report MI from the Solchiaro eruption that have trachybasaltic compositions, H₂O contents up to 3 wt%, and CO₂ up to 4000 ppm. These workers calculated minimum pressures of crystallization of ~ 200 to ~ 800 MPa, which corresponds to minimum depths of formation of 7 to 27 km, assuming a 30 MPa/km pressure gradient. Cecchetti *et al.* (2005) reported pressures of formation of MI from Minopoli 2, Somma-Vesuvius, and Solchiaro (assuming volatile-saturation conditions) between 200 and 400 MPa. These consistently high trapping pressures obtained from MI indicate that the PVD magmas were generated at considerable depth beneath the PVD.

MI from Fondo Riccio (latite) and from Minopoli 1 (shoshonite) have H₂O contents that range from 3.3 to 7 wt% and from 2 to 5.3 wt %, respectively (Cannatelli *et al.*, 2007). In a more recent study, pre-eruptive volatile contents of MI from Fondo Riccio and from Minopoli 2 (shoshonite) suggest minimum pressures of formation mostly between 100 and 200 MPa (Mangiacapra *et al.*, 2008). Roach (2005) estimated pressures of crystallization of CO₂-poor (20-50 MPa) and CO₂-rich (250 MPa) MI from the Agnano-Monte Spina trachytic volcanic eruption, suggesting the presence of both a shallower and a deeper magma reservoir. Arienzo *et al.* (2010) report entrapment pressures ranging from 107 to 211 MPa for this same eruption based on the H₂O and CO₂ contents of MI hosted in clinopyroxene, corresponding to depths of 4 to 8 km.

In summary, magma storage depths in the PVD based on volatile contents of MI span a wide range that extends from the base of the crust to within ≈1 km (or even less) of the surface (Table 1). The range in calculated depths likely reflects the complex relationship between magmatism and the regional tectonic setting of the Campanian Plain.

3. Sample description

Solchiaro products outcrop along the coast of Procida Island and reach up to several meters in height (Di Girolamo & Stanzione, 1973; Pescatore & Rolandi, 1981; De Astis *et al.*, 2004; Perrotta *et al.*, 2010). Four samples (RESC2, RESC3, RESC4, RESC5) of the Solchiaro eruption were collected at different locations and at different stratigraphic heights (Figs 1c and 1d), representing proxies for relative time of eruption from the magma chamber and, possibly, depth from which the eruption originated. It is not straightforward to correlate the samples collected in this study and those described by De Astis *et al.* (2004) because the sample locations were not the same. However, we believe that all samples collected for this study are representative of Solchiaro unit I described by De Astis *et al.* (2004). Our correlation is based on the absence in outcrops of well sorted lapilli and scoria layers that are characteristic of strombolian activity and which are observed in Solchiaro units II and III.

A simplified chronostratigraphic correlation among samples is illustrated in Fig. 1d. Sample RESC2 was collected from the base of the southeast cliff between Punta Pizzaco and Corricella (Figs 1c and 1d), ~ 2 km from the vent (assumed to be the center of Solchiaro Bay; De Astis *et al.*, 2004). In the outcrop, the volcanic deposits show a sand-wave facies. Sample RESC3 was collected 6 m upslope from RESC2 and ~ 500 m closer to the vent. Sample RESC4 was collected at the same distance from the vent as sample RESC3 but 15 m higher in the section. Samples RESC3 and RESC4 were collected where the base surge deposits show a characteristic plano-parallel stratification. Sample RESC5 is a lithified yellow tuff, characteristic of lower and proximal products of the Solchiaro eruption (Pescatore & Rolandi, 1981; Di Girolamo *et al.*, 1984) or the basal section of Solchiaro unit I of De Astis *et al.* (2004). Lithification processes obliterated the stratigraphic elements and complicate the chronostratigraphic correlation between sample RESC5 and the others.

Samples RESC2, RESC3 and RESC4 consist mainly of gray ash, dark brown lapilli (<4 mm) and phenocrysts of clinopyroxene (50%) and olivine (45%) that are always coated by glass. The samples also contain 1 to 0.5 mm sanidine (5%) crystals that show euhedral morphology. Pale green glass shards that are not vesiculated are rarely found in the samples. Lithic fragments make up less than ca. 3 % of RESC2 and RESC3 and are rare in RESC4. Some of the lithic fragments are angular and poorly vesiculated lava lithics while others are non-vesiculated lithic clasts. Olivine varies from 1.5 to 3 mm in maximum dimension and clinopyroxenes range from 1 to 2 mm. Sample RESC5 shows a high proportion in lithic material, suggesting a more phreatomagmatic eruptive style. Phenocrysts from this sample are the same size as in the samples previously described, but perfectly euhedral olivine phenocrysts are more common in RESC5. The olivine phenocrysts are isolated in the tuff and rarely show an altered glass coating.

4. Analytical methods

Olivine phenocrysts were hand picked from the poorly consolidated samples (RESC2, RESC3 and RESC4) under a binocular microscope and then cleaned in deionized water in an ultrasonic cleaner. Sample RESC5 was more lithified and required gentle crushing to release crystals - olivine phenocrysts from this sample were hand picked and cleaned as described above. Selected crystals were mounted on glass rods (2.5 mm in diameter) generally with the *c* axes ca. parallel to the long dimension of the glass rod, and polished using alumina powder as described in Thomas & Bodnar (2002). The crystals were removed from the glass rods and MI were studied petrographically (Table 2) using a transmitted light microscope to select MI for further study. [Note that petrographic information was not obtained for the first group of MI from sample RESC2, representing 6 MI]. The selection of MI was based mainly on size (> 20 μm) to assure that the MI were large enough for Secondary Ion Mass Spectrometric (SIMS) analyses. MI containing only glass were preferred to those containing one or more bubbles or associated crystals.

After the MI was exposed at the crystal surface and polished, the crystal was removed from the glass rod. Approximately 20-30 polished crystals with one or more MI exposed at the surface were mounted in a one-inch round indium microprobe mount, to prevent contamination from H and C in epoxy at high vacuum conditions in the SIMS. Indium mounts were coated with gold rather than carbon to avoid contamination with C. After

preparing the probe mounts, the MI and host phase were analyzed using a variety of techniques. MI were first imaged at Virginia Tech (Blacksburg VA, USA) with a Camscan Series II scanning electron microscope (SEM) equipped with energy-dispersive X-ray (EDX) and backscatter electron (BSE) detectors to test for homogeneity of the glass in the MI, to look for evidence of crystallization on the inclusion walls, and zoning of the host phase (Fig. 2). Next, the MI and adjacent olivine were analyzed using an electron microprobe to determine the major element composition. The first set of olivine phenocrysts was analyzed by a JEOL JXA 8900 electron microprobe (EMP) for major elements at the USGS (Reston VA, USA). An accelerating voltage of 15 kV was used with a beam current of 10 nA. Analyses were conducted with a defocused beam of 10 μm . For each MI, the host phase was analyzed at about 15 μm from the glass/host interface. It should be noted that only the indium mount prepared for the first group of olivine crystals was carbon coated (6 olivines from sample RESC2), all other MI mounts were gold coated. Then, the carbon coating was removed and the MI were analyzed for volatiles by SIMS (Cameca IMS 1280) at the Woods Hole Oceanographic Institution (Woods Hole, MA, USA). Analyses were performed using $^{133}\text{Cs}^+$ as the source, with a current between 1 and 1.6 nA. A 30 μm x 30 μm spot was rastered within the glass for 240 seconds to clean the surface before analysis. Then, a 15 μm x 15 μm spot within the rastered area was analyzed ten times in depth profile mode. One large MI was analyzed in two different spots to test for homogeneity of volatile abundances. Volatile contents were related to the ratio of the element (mass) of interest ($^{16}\text{O}^1\text{H}$, ^{12}C , ^{19}F , ^{32}S , or ^{35}Cl) to ^{30}Si .

A second set of phenocrysts was analyzed by EMP (Cameca SX-50 electron probe) and SIMS (IMS 7f ion probe) at Virginia Tech. Instrumental conditions for EMP included an accelerating potential of 15 kV and a regulated beam current of 20 nA. A defocused spatial resolution (spot size) of approximately 2 μm was achieved with the above analytical conditions. Two or three spots were analyzed in each MI to test for homogeneity. SIMS instrumental conditions at Virginia Tech were the same as for the first series of analyses at Woods Hole. When large enough, two or three spots in each MI were analyzed by SIMS. The four standard glasses we used to calibrate the SIMS are natural glasses EN11346D-2, ALV1649-3, GL07D52-5, and ALV1654-3. Information about the compositions and provenience of these standard glasses are reported by Helo *et al.* (2011). The calibration curves for $^{12}\text{C}/^{30}\text{Si}$ versus the respective standard glass CO_2 concentrations are given in Electronic Appendix 1.

For EMP analysis, relative precision is always better than 5% one-sigma when the oxide concentration was >1 wt%. Minor elements in MI show relative precision of $<10\%$ one-sigma. Relative precision for volatiles by SIMS is considered to be $<10\%$ relative for all the volatiles analyzed, based on repeated analysis on glass standards. In addition, all MI and some olivine crystals were analyzed by Laser Ablation Inductively Coupled Plasma Mass Spectrometry (LA ICP-MS) at the Department of Geosciences, Virginia Tech. The facility consists of a GeolasTM Pro ArF 193 nm excimer laser coupled with an Agilent 7500ce ICPMS quadrupole mass spectrometer equipped with a reaction cell. Analytical conditions for the analyses of the NIST glass, MIs, and host analyses were 27 kV, 150 mJ, with a pulse rate of 5 Hz. Precision is estimated at $<10\%$ on the analyzed elements based on repeated analysis of NIST612 (SRM). For LA ICP-MS analyses, NIST 610 glass was used as the standard for data reduction. Background signal was collected for 60 seconds before the laser was turned on. Only MI exposed at the crystal surface

were analyzed. During the analysis, the transition from the MI into the underlying host crystal was determined by monitoring elements with extremely low or high partition coefficients in the melt-olivine system i.e., those elements that occur either only in the melt (Ba, K, Na) or mostly in the host olivine (Mg). Then, during data reduction, only the signal from the MI was included. The analytical software AMS (Mutchler *et al.*, 2008) was used to reduce the data from the LA ICP-MS analyses. All element concentrations were calculated using Si as an internal standard based on the concentration obtained from EMP analysis. Because Cs is the source of ions for SIMS analysis, we noted that Cs abundances are anomalously high for some of the analyzed MI. The Cs contamination results in a continuous decrease in Cs concentration with depth during the analysis.

5. Results

Mineral chemistry

Olivine compositions for all 4 samples from the Solchiaro eruption range from Fo₇₇ to Fo₉₀, with Fo mol% calculated including the Mn and Ca components (Table 3 and Electronic Appendix 2). Ten olivine phenocrysts from sample RESC2 were studied and their compositions vary from Fo₈₂ to Fo₈₈. Most of the olivines show euhedral to sub-euhedral shape and 3 of them present a characteristic hollow shape. Olivines RESC2-O22 and RESC2-O12 are strongly reverse zoned with the former showing Fo₈₂ at the core and Fo₈₆ at the rim (see Fig. 2a). Chromite is a common solid inclusion in forsterite-rich olivine. Often, chromite inclusions show a film of glass at the inclusion/olivine interface.

Twenty-five olivines selected from sample RESC3 range in composition from Fo₇₇ to Fo₈₉. Some of these phenocrysts are zoned while others are unzoned. Generally, olivines from this sample show an unzoned core and a 10-200 µm rim showing oscillatory, normal and reverse zoning, indicating crystallization under open system conditions or a variation in the oxidation state of the system during magmatic evolution (Streck, 2008). In one case, olivine shows a patchy zoning coupled with glass channels and embayments suggestive of dissolution/recrystallization processes (Fig. 2f). Most of the olivines have a euhedral to sub-euhedral habit (Fig. 2c) that indicates a slow growth rate (Faure & Schiano, 2005) and glass reentrants are less frequent compared to sample RESC2.

Seventeen olivines from sample RESC4 also show zoning and range in composition from Fo₇₉ to Fo₈₈. Most of the olivines show the same type of oscillatory zonation described for RESC3 but simple reverse zoning was not observed, and only a few olivine phenocrysts are not zoned.

Sample RESC5 shows the highest proportion of euhedral crystals (Fig. 2b) among the Solchiaro samples, and 28 olivines analyzed from this sample range from Fo₈₁ to Fo₉₀. These phenocrysts rarely show glass coatings and are slightly larger than olivines from other samples (up to 3 mm). Generally, olivines from RESC5 also show an unzoned core and a 10-200 µm rim showing oscillatory, normal and reverse zoning. Rarely, olivine phenocrysts show textures suggesting dissolution/recrystallization processes (Fig. 2e). An approximately 1 µm thick Fe-rich rim is found in all olivines (Fig. 2). An Fe-rich olivine band with the same width is observed at the interface between MI and host, reflecting crystallization on the walls during quenching (e.g., Sobolev & Shimizu, 1993). In

addition to chromite inclusions, diopside and plagioclase inclusions were also found in few olivines.

Melt inclusion petrography

Studied MI always contain a homogeneous glass phase. Some contain one or more bubbles (hereafter referred to as bubble-bearing MI) while others contain no bubbles (hereafter referred to as bubble-free MI) (Table 2). None of the MI studied contain daughter minerals. Size (1 up to 400 μm in diameter) and color (colorless to brownish) are both variable with larger (thicker) inclusions being more brownish than smaller (thinner) ones. The correlation of MI color with size suggests that all MI are brownish but that the thinner ones appear to be colorless owing to their thinness. Note, however, that the Sr-rich MI always appear to be clear, even when the MI are relatively large. The proportion of bubble-free MI increases from earlier to later volcanic products (from RESC2 to RESC4).

MI shape is variable, ranging from perfectly elliptical/spherical to faceted (negative shape of olivine) to irregular (Table 2). In some crystals, MI show constant $V_{\text{melt}}/V_{\text{bubble}}$ ratio (e.g. RESC3-O6) whereas in other crystals the ratio is highly variable (e.g. RESC4-O10). We observed that in some olivines MI below a certain size do not contain bubbles, whereas larger MI in the same sample contain one or more bubbles. However, the size that separates bubble-free from bubble-bearing MI varies from one olivine to another in the same sample. For instance, MI $<50 \mu\text{m}$ in olivine RESC3-O9 do not contain bubbles, but in other olivines from the same sample bubble-free MI never exceed 20 μm . Other olivine phenocrysts show bubble-free MI in one area while in another area MI of comparable size contain bubbles with consistent $V_{\text{melt}}/V_{\text{bubble}}$. In only one case, the $V_{\text{melt}}/V_{\text{bubble}}$ ratio is less than ca. 0.7, suggesting either trapping of a vapor bubble along with the melt or necking of the MI after the vapor bubble had nucleated. The host/inclusion interface is usually smooth at the micron scale, but in a few cases this interface shows a wrinkled texture that is also found in some laboratory-heated MI and may indicate natural reheating of the MI after trapping (Cervantes *et al.*, 2003). MI from all the Solchiaro samples are often entrapped along with chromite solid inclusions. In fact, the $V_{\text{melt}}/V_{\text{chromite}}$ ratio shows large variability, with some MI containing mostly chromite and very little melt, indicating that chromite is not a daughter crystal but, rather, is a trapped solid. In some cases the MI appear to have nucleated on chromite crystals, as has also been reported by Roedder (1979; Fig. 11). Bubbles in mixed MI are always attached to the chromite crystal. Embayment and hourglass inclusions are often observed in the studied phenocrysts but are not considered in this study.

Groups of MI all trapped at the same time (thus at the same physical and chemical conditions) within a single phenocryst are defined as Melt Inclusion Assemblages (MIA) (Bodnar & Student, 2006). While some MIA were observed in olivine phenocrysts from Solchiaro, the MI were always $<3 \mu\text{m}$ and therefore too small to analyze, with the exception of one MIA in olivine (RESC5-O21) in which two bubble-free MI in the same growth zone were exposed and analyzed (Fig. 2B).

Major element composition

The low Fe-Mg exchange coefficient, K_D , calculated based on the composition of the MI and the adjacent host phase, combined with the general depletion of FeO_{tot} in the MI relative to bulk rocks, both suggest disequilibrium between the MI and the adjacent host phase. This suggests that the MI composition was modified by post-entrapment crystallization (PEC) during cooling (Kent, 2008, references therein). Thus, compositions of MI were corrected for chemical modification by PEC. We calculated the Fo content of olivines that would be in equilibrium with Solchiaro bulk rocks. For this calculation, we used the olivine-silicate melt model of Ford *et al.* (1983) assuming NNO buffer and f_{O_2} calculated using the equation of Borisov & Shapkin (1990). Errors associated with the calculated Fo content of bulk rocks may be large owing to the assumptions involved in the calculation. Thus, the comparison between bulk rock composition and MI composition has to be taken with caution. Over the entire range of Fo contents predicted (e.g., from 70 to 92) based on the bulk rock composition, MI compositions still show a general depletion in FeO relative to bulk rock compositions (Fig. 3a), suggesting Fe-loss from MI by diffusion (Danyushevsky *et al.*, 2000; 2002a). Therefore, we corrected our MI compositions using software FEO_EQ2 (Danyushevsky *et al.*, 2000; 2002a). In order to correct the MI composition for PEC and Fe-loss, the oxidation fugacity was fixed using the NNO buffer as was previously suggested for the nearby Roman magmatic province by Métrich & Clocchiatti (1996). The $\text{Fe}^{2+}/\text{Fe}^{3+}$ ratio in the melt was calculated based on data of Borisov & Shapkin (1990). Olivine-silicate melt equilibrium was based on thermobarometric equations of Ford *et al.* (1983). All calculations assumed an anhydrous system and were normalized to 100%, and both uncorrected and corrected compositions are listed in Table 4 (see also Electronic Appendices 3 and 4). The percentage of PEC predicted from the correction is $\leq 15\%$ and for 90% of the studied MI PEC is $< 10\%$. Trace element and volatile abundances in the melt were corrected assuming they are not incorporated into the crystallizing olivine. The olivine composition plus the strong reverse and oscillatory zoning of some olivine phenocrysts indicate magma mixing and possible preservation of xenocrysts. Thus, in addition to PEC, magma mixing likely affected MI compositions.

Corrected MI compositions plot in the basalt through trachy-basalt to basaltic trachy-andesite fields, with a few compositions in the phono-tephrite field on the TAS diagram (Le Bas *et al.*, 1986) (Fig. 3b). It is important to note that, after correcting the MI compositions, the ratios between olivine incompatible elements are unchanged. Corrected and uncorrected MI compositions are essentially the same on the TAS diagram (Fig. 3b) indicating that MI composition was not strongly modified by PEC. In addition, most of the corrected MI compositions overlap with scorias and lava lithic bulk rock compositions from the literature (Di Girolamo *et al.*, 1984; D'Antonio *et al.*, 1999; De Astis *et al.*, 2004). As shown on Figure 4a, $\text{CaO}/\text{Al}_2\text{O}_3$ from MI decreases during magmatic evolution. This suggests that diopsidic clinopyroxene was crystallizing along with olivine, in agreement with hand specimen observations.

The major element that shows the largest variation in concentration in corrected, normal MI is K_2O (ranging from 1.25 to 4.87 wt %; Figs 4b and c). This range cannot be explained by fractional crystallization alone. K_2O concentrations in Solchiaro whole rock

samples also span a wide range (De Astis *et al.*, 2004). Corrected MI compositions also show a wide range in P₂O₅ concentrations (Fig. 4b).

As shown in most other studies, MI compositions span a wider range in major/trace element and volatile contents and isotopic composition compared to the bulk rock and matrix glass (Kent, 2008, and references therein). MI from our study similarly show wider compositional variation than the bulk rocks, in agreement with many previous studies (Figs 3, 4 and 5).

As in other mafic volcanic systems located in various geodynamical settings, MI with anomalous compositions were found in Solchiaro tephra samples. We define “anomalous” MI as those showing 4 or more elements with concentrations that do not follow the main trend outlined by the corrected MI compositions. Two types of anomalous MI were observed in the 4 samples from Solchiaro. One type has been previously described in the literature and referred to as *Sr-rich MI* and the other type is here referred to as “*enriched*” MI. As shown in Fig. 5b, the Sr-rich MI always show a positive Eu anomaly along with a negative Zr anomaly and a general depletion of most of the other trace elements (Gurenko & Chaussidon, 1995; Sobolev *et al.*, 2000; Schiano *et al.*, 2000; Kent *et al.*, 2002; Lassiter *et al.*, 2002; Danyushevsky *et al.*, 2004). In contrast to the Sr-rich MI, the enriched MI show relative enrichment/depletion trends that are similar to “normal” MI and the bulk rock, but show relatively greater enrichment relative to primitive mantle (see Nb, Ta, Ce, P, Nd, Zr, Eu and Ti in Fig. 5b).

Trace element composition

Normal MI show trace element concentrations comparable to bulk rock compositions reported in other studies of the Solchiaro eruption (Di Girolamo *et al.*, 1984; D’Antonio *et al.*, 1999; De Astis *et al.*, 2004). In agreement with these studies, normal MI hosted in Fo-rich olivine show REE trends characteristic of weak fractionation, with no Eu anomaly, while those hosted in Fo-poor olivine show higher HREE in agreement with a higher degree of crystallization. As has been observed for mafic rocks from the entire PVD, normal MI (especially those hosted in olivine with Fo < 84) are strongly enriched in most of the LILE, especially Ba, K, and Pb, and show negative anomalies for HFSE. This pattern is characteristic of rocks erupted along a subduction zone (Pearce & Peat, 1995). Normal MI hosted in olivine with Fo > 86 show Dy, Y, Yb, and Lu compositions comparable to those of primitive mantle (Sun & McDonough, 1989). However, HFSE in most MI show compositions similar to those reported for intraplate-like basalts (Sun, 1980 and references therein). As reported by De Astis *et al.* (2004), HFSE and HFSE/LILE compositions from this study are more characteristic of intraplate magmas. Based on trace element data, De Astis *et al.* (2004) suggested that the source of the PVD magmas was an OIB-type mantle that had previously been metasomatized by subduction-related fluids.

Volatile Abundances

Volatile abundances of “normal” MI from Solchiaro show systematic variations. H₂O concentrations of MI span a narrow range from 0.8 to 1.6 wt% (Fig. 6), with most values between about 1.0 and 1.3 wt %, and are significantly lower than those reported for other

MI in the PVD (Cannatelli *et al.*, 2007; Cecchetti *et al.*, 2001; Mangiacapra *et al.*, 2008). The CO₂ contents of Solchiaro MI show a wide variation, both within individual samples and between samples (Fig. 6), and the CO₂ content of the MI correlates with stratigraphic position. The minimum CO₂ content varies from about 300 ppm in the earliest sample (RESC2) to about 100 ppm in the latest erupted sample (RESC4) (Figs 6 and 7). The maximum CO₂ content varies systematically from about 1700 ppm in earliest sample RESC2, to about 600 ppm in latest sample RESC4. Note that even though only a single MI with the highest CO₂ content was found in RESC2 (\approx 1700 ppm), there was no indication from the SIMS analysis that would lead to rejection of this data point. That is, the distribution of C within the analytical volume was uniform and homogeneous during the analysis. Additionally, CO₂ was detected in the vapor bubble of another MI in this same sample using Raman spectroscopy (see also Fig. 3 in Steele-MacInnis *et al.*, in press). When the CO₂ in the bubble is added back into the melt, the corrected CO₂ content of the melt is 1822 ppm (Table 5). To summarize, the CO₂ content of Solchiaro MI shows a wide variation, and the maximum and minimum CO₂ contents, as well as the total range in CO₂ content, decrease with time (Fig. 8). Assuming that the trapped melts were volatile saturated, H₂O-CO₂ concentrations of normal MI from all studied samples indicate pressures of trapping from 210 to 20 MPa (Electronic Appendix 3 and Fig. 6), calculated using the model of Papale *et al.* (2006). A temperature of 1200°C and oxidation state equal to the NNO buffer were used for the calculations. Most of the pressures range from 100 to 30 MPa, and assuming 27 MPa/km pressure gradient, these pressures correspond to depths of 4 to 1 km. Sulfur ranges from 1780 ppm to 755 ppm (only considering normal MI, see Fig. 7a and c) and does not show any systematic variation with other volatiles, other than perhaps Cl. In normal MI, Cl concentration varies the most of all volatiles measured, with concentrations ranging from 864 to 4432 ppm (Fig. 7b and c). In normal MI, F contents span a range from 518 to 2116 ppm (Figure 7a). Sr-rich MI are characterized by depletion in CO₂, S, and Cl, but not in H₂O and F. In general, enriched MI show volatile compositions similar to “normal” MI, with the exception of one enriched MI showing the highest concentration of all volatiles (Fig. 7). Among volatiles in normal MI, good correlations are shown by S vs. Cl and H₂O vs. F.

6. Discussion

In the following discussion, we focus on three topics: (1) variations in volatile contents of MI and their causes, (2) anomalous MI, and (3) model to explain the temporal and spatial variations in volatile contents of the Solchiaro system. We discuss each sample separately because the volatile contents appear to be sample specific and related to stratigraphic position, and we compare data from samples representing different stratigraphic position. Anomalous MI are excluded from discussion of topics (1) and (3) and are considered separately for reasons outlined below.

Variations in volatile contents of MI and their causes

As observed in this study and often reported in other MI studies, volatile concentrations of MI show large variability (especially CO₂, Cl, and S). The first issue that we consider is whether these observed variations reflect real variability in the volatile content of the melt beneath Procida before and during the Solchiaro eruption, or if these variations might reflect post-entrapment modifications to the MI.

Generally, the much larger variation in CO₂ content of MI relative to H₂O has been interpreted to indicate trapping of MI in an ascending and degassing magma body. Thus, if a crystallizing volatile-saturated magma ascends through the crust, volatile concentrations of MI are dependent on the pressure at which they are trapped (Métrich & Wallace, 2008, and references therein), and the different volatile concentrations correspond to different depths of entrapment. Variation in the volatile content of MI may thus occur if the crystals are growing in different locations within the magmatic system during ascent from depth. For example, some phenocrysts may form and trap MI in the source region, whereas other MI may be trapped in a shallower reservoir where the magma resides immediately before eruption. Other MI may be formed in feeder dikes connecting the deeper source region with more shallow magma bodies, and some may even be trapped in the magma conduit connecting the magma body to the surface. Blundy & Cashman (2008) note that the volatile content of the melt within a single magma chamber may vary depending on where and when the melt is sampled within the magma body. Other workers suggest that the volatile content of the melt may vary as a result of gas fluxing from a deeper reservoir (Métrich & Wallace, 2008, and references therein). Moreover, volatile contents in the melt are affected by crystallization, and volatile abundances in MI may be expected to vary as a function of the time of entrapment.

We have examined each sample in order of increasing stratigraphic height, from the bottom of the section (RESC2) and proceeding upwards through samples RESC5, RESC3 and RESC4 (top). For each sample we have discussed different aspects that we believe are important to interpret H₂O-CO₂ systematic of MI.

In general, the major and trace element contents of MI entrapped in the same olivine phenocryst show little variation. In contrast, concentrations of CO₂ in MI within the same olivine vary greatly, especially between bubble-free MI and bubble-bearing MI. Some studies show that volatile concentrations of MI may be modified by post entrapment processes such as crystallization on the inclusion walls (Kress & Ghiorso, 2004), formation of a shrinkage bubble (Anderson & Brown, 1993; Steele-MacInnis *et al.*, in press), leakage of volatiles from the MI and diffusion of volatile components through the host phenocryst (Danyushevsky *et al.*, 2002b; Severs *et al.*, 2007; Portnyagin *et al.*, 2008). In this study, one possible explanation for the CO₂ variation is that some proportion of the CO₂ that was originally dissolved in the melt when it was trapped as an MI now resides in the vapor bubble, as has been recognized by other workers (e.g., Anderson & Brown, 1993; Cervantes *et al.*, 2002). Indeed, we detected CO₂ in some MI bubbles using Raman spectroscopy. For one sub-spherical MI in sample RESC2 (RESC2-O26-M3 in Electronic Appendix 3 and 4) we estimated that 64% of the total amount of CO₂ in the MI is stored in the bubble (Table 5). The density of the CO₂ vapor was obtained by measuring the splitting of the CO₂ Raman Fermi diad and using the equation of Kawakami *et al.* (2003) to calculate the CO₂ density, which is equal to 0.167 g/cm³.

The dry liquidus temperature of this MI is 1138°C as calculated from the glass composition using the olivine-melt equilibrium model of Ford *et al.* (1983) assuming NNO buffer and the model of Borisov & Shapkin (1990) and 0.1 MPa. Note that the liquidus temperature of this same melt at 100 MPa is 1143°C, or only 5°C higher. The dry liquidus temperature of the same MI using the K_D value obtained from the equation of Toplis (2005) is 1139°C that is essentially equal to the temperature obtained using the model of Ford *et al.* (1983). The hydrous liquidus temperature is 1063°C based on the model of Falloon & Danyushevsky (2000). Because the Solchiaro melt contains H₂O, its effect on lowering the liquidus temperature should be taken into account (Falloon & Danyushevsky, 2000; Almeev *et al.*, 2007; Medard & Grove, 2008). According to these studies, the liquidus temperature of this MI is between 1060-1100°C. Therefore, the H₂O and CO₂ contents of the glass indicate a pressure of ~ 80 MPa, based on the model of Papale *et al.* (2006). Assuming that no additional CO₂ was added to the vapor phase during quenching, the density of the CO₂ in the bubble would continue to decrease as the vapor bubble volume increased, owing to the larger expansion coefficient of the glass, compared to the host. Thus, the isochore corresponding to the density in the bubble measured at room temperature should intersect the quenching temperature (1060-1100°C) at a pressure lower than that predicted by the H₂O and CO₂ contents of the glass. Extrapolation of the isochore for a density of 0.167 g/cm³ indicates a pressure of 47 MPa (Bottinga & Richet, 1981), which is considerably lower than the pressure of 80 MPa indicated by the H₂O and CO₂ contents of the glass, indicating that the volume of the bubble has doubled during quenching. Note that if we consider the liquidus temperature of the dry olivine of 1138°C, the pressure calculated from the equation of Bottinga & Richet (1981) is 50 MPa. The pressure calculated by the extrapolation of the isochore of the CO₂ fluid in the MI is considerably lower than the pressure calculated by the solubility model for H₂O-CO₂ in silicate melt. This result is consistent with our interpretation that the CO₂ in the vapor bubble was originally dissolved in the trapped melt, and that the CO₂ content measured in the glass phase in this and similar inclusions represents a minimum CO₂ content of the original melt.

In sample RESC2, bubble-free MI are uncommon and none were analyzed in this study. However, when compared to all the other samples, the glass in MI from sample RESC2 shows higher CO₂ concentrations, and these likely represent minimum values because some of the CO₂ that was originally in the melt is now in the bubble. Both H₂O and CO₂ concentrations show a good correlation with crystallization indicators (Fig. 6g). The trend in CO₂ versus Al₂O₃/CaO of MI from sample RESC2 is similar to that of MI from RESC5, and suggests that the MI in RESC2 were entrapped at different depths (pressures) within the Solchiaro plumbing system.

One of the more difficult questions to answer in MI studies is whether the observed ranges in volatile contents of MI are the result of natural temporal and spatial variations in the volatile content of the melt, or whether these variations reflect post-entrapment modifications. One approach to address this issue is to analyze a group of MI that were all trapped at the same time within a single phenocryst and represent a Melt Inclusion Assemblage (MIA) (Esposito *et al.*, 2010a). If the MI were all trapped at the same time (and place), they would all presumably trap a melt of the same composition. Thus, any variations in chemistry among the group of MI within the MIA would likely be the result of post-entrapment processes. Sample RESC5 offers a good opportunity to check the

fidelity of MI. One olivine phenocryst (RESC5-O21) contains two bubble-free MI in the same MIA that were exposed and analyzed (Fig. 2b). For each element analyzed, the concentration in each MI was the same within analytical uncertainty. The greatest variation between the two MI was for C. These two MI support the hypothesis that the volatile contents of the bubble-free MI are more representative (compared to the bubble-bearing MI) of the volatile content of the Solchiaro melt during the formation of olivine RESC5-O21.

In sample RESC5, if only bubble-free MI are considered, H₂O contents show less variation (compared to bubble-bearing MI) (Fig. 6f), suggesting that H₂O concentrations in MI may be related to the presence of bubbles in MI (Esposito *et al.*, 2010b; Steele-MacInnis *et al.*, in press). Enrichment of the melt in H₂O may also indicate an advanced stage of crystallization in the magma chamber at isobaric conditions (before the MI is trapped, Blundy & Cashman, 2008). It is noteworthy that isobaric conditions are only applicable to crystallizing magma bodies in which the volume can change. Isobaric conditions are generally not applicable to MI systems where the volume is constrained by the host crystal and the system is essentially isochoric. As also observed in sample RESC2, the highest H₂O concentration is observed in a bubble-bearing MI, suggesting that the H₂O enrichment observed in bubble-bearing MI is the consequence of either PEC processes or entrapment of a vapor phase along with the melt phase. After the data were filtered for anomalous MI and bubble-bearing MI, CO₂ concentrations in sample RESC5 show a negative correlation with Al₂O₃/CaO ratios (Fig. 6e). Importantly, the same correlation is observed between CO₂ and most of the olivine/diopside incompatible elements (i.e., Na and LILE). Consistently, abundances of olivine/diopside compatible elements (e.g. Sr and CaO) increase with increasing CO₂ content. Since ratios between olivine/diopside incompatible elements and olivine/diopside compatible elements are indicators of crystallization, a negative correlation between these ratios and CO₂ is evidence of vapor saturation in the magma even in the absence of vapor fluid inclusions (Wallace *et al.*, 1999). The CO₂-H₂O systematics for sample RESC5 (Fig. 6f) can be interpreted to indicate that MI are trapped along a degassing path driven by decompression as suggested by the correlation between CO₂ and Al₂O₃/CaO ratios (Fig. 6e). The highest pressure recorded by the CO₂-H₂O systematics in MI in sample RESC5 is 159 MPa (Papale *et al.*, 2006), corresponding to ≈6 km depth, assuming a 27 MPa/km pressure gradient. The lowest pressure recorded by MI in sample RESC5 is 36 MPa, which is equivalent to about 1 km depth. For MI with CO₂ < 500 ppm there is no clear correlation with crystallization indicator (Fig. 6e), but there is a correlation between CO₂ and crystallization indicator for higher CO₂ contents. Therefore, we interpret the correlation between crystallization indicators and CO₂-H₂O systematics observed in MI from RESC5 to indicate that the volatile contents reflect natural variations in the magmatic system during entrapment of the MI in this sample.

In sample RESC3, bubble-free and bubble-bearing MI show essentially the same distribution in H₂O and CO₂ contents, but bubble-bearing MI extend to slightly higher H₂O (Fig. 6d), similar to sample RESC5. As discussed above, the higher H₂O content of bubble-bearing MI is likely due to crystallization on the MI wall, which, in turn, will lead to enrichment in dissolved H₂O relative to CO₂. In sample RESC3, bubble-free MI with CO₂ < 500 ppm span a wider range of H₂O concentrations compared to bubble-free MI in sample RESC5 (Figs. 6d, f). Our interpretation is that the H₂O-CO₂ distribution is due to crystallization at different locations and/or at different times in an evolving magmatic

system, in agreement with Blundy & Cashman (2008). In contrast to sample RESC5, CO₂ in sample RESC3 does not correlate with the crystallization indicator Al₂O₃/CaO (Fig. 6c). The lack of correlation between volatile contents and crystallization monitors indicates that MI were trapped from a magma that was crystallizing not because of decompression, but, rather, as a result of nearly isobaric crystallization. Thus, we interpret the observed variations in volatile contents of normal MI from sample RESC3 to reflect natural variations in the volatile content of the trapped melt.

In sample RESC4, which represents the last erupted of the 5 samples based on stratigraphic position, CO₂-rich MI (>≈ 500 ppm) are not present (Fig. 6a, 6b and 8), indicating that none of the olivine from this sample formed deep in the system. This sample is the only one of the four studied samples that also shows a positive correlation between H₂O and Al₂O₃/CaO for bubble-free MI. The positive correlation between H₂O and Al₂O₃/CaO is consistent with an interpretation that the MI were trapped over a range of depths (pressures) within a magma body undergoing crystallization. In addition to H₂O, CO₂ shows a weak negative correlation with crystallization indicators, in agreement with the above interpretation, suggesting that the observed volatile contents reflect natural variations in the Solchiaro system.

In summary, the volatile contents of most bubble-free MI from Solchiaro show trends in CO₂ versus Al₂O₃/CaO that suggest that the variations in volatile contents observed reflect real variations in the volatile content of the melt that was trapped as MI. This further suggests that the MI were trapped over a range of temporal and spatial conditions (depths) within the Solchiaro magmatic system as has been reported for other volcanic systems (Métrich & Wallace, 2008, and references therein).

Model for the Solchiaro magmatic system

Previous workers have examined the volatile content of MI as a function of stratigraphic position within an eruptive sequence in order to assess variations in volatile content of MI erupted from different depths within a magmatic plumbing system. For example, Johnson *et al.* (2008) reported that MI from the early tephra layer of the Volcan Jorullo eruption in Mexico record greater depths of entrapment compared to MI from the middle and late tephra layers. The Jorullo eruption was estimated to have lasted 15 years – the duration of the Solchiaro eruption is unknown. Based on the similarity to the Capelinhos eruption, Azores, (Pescatore & Rolandi, 1981) a volume of magma comparable to the Solchiaro eruptive products could have been erupted in about one year. In agreement with Johnson *et al.* (2008), we also noted a correlation between maximum CO₂ content of the MI and the stratigraphic position of the sample (Fig. 8). Based on this correlation, earlier eruptive events ejected olivine phenocrysts that trapped MI over a wider range of depths (from ≥8 km to 2 km; sample RESC2), compared to olivine phenocrysts ejected during intermediate (from 6 km to 1 km; sample RESC3), and later stages (from 4 km to 1 km; sample RESC4). Olivine phenocrysts from sample RESC5 trapped MI over a range of depths (from ≤6 km to 1 km) more similar to sample RESC3, suggesting that RESC5 may have been erupted at a time intermediate between eruptions RESC2 and RESC3.

In addition to CO₂, Cl also shows a correlation with the stratigraphic height. However, in contrast to CO₂, the highest Cl concentrations are found in the latest sample RESC4, while the lowest concentrations are observed in the early-erupted sample RESC2. This correlation suggests that Cl was retained in the melt during the eruption.

As reported above, the correlation between CO₂ content of MI and crystallization indicators reveals that most of the MI studied were trapped over a limited range of depths (1 to 4 km), indicating that most MI entrapment likely occurred within a shallow magma body. However, some MI were trapped over a wider range of depths (4 to ≥ 8 km), perhaps during ascent of the magma body from deep in the crust. Considering the relationship between the CO₂ abundance of MI and the stratigraphic position, and the correlation between CO₂ content of MI and Al₂O₃/CaO crystallization indicator, lead to the following model for the evolution of the Solchiaro system.

Initially, the Solchiaro magma body formed in the deep crust and started to crystallize at ≥ 8 km depth (time t_0 in Fig. 9), and at this depth the magma was saturated in volatiles (in equilibrium with a CO₂-rich fluid). At this depth, olivine phenocrysts trapped MI (MI 1-3, Fig. 9; time t_0) containing approximately 1800 ppm CO₂ and about 1 wt % H₂O. Subsequently, the magma body ascended to shallower levels of the crust and continued to crystallize due to ongoing degassing, and also trap MI (MI 4, time t_1 in Fig. 9) along the way. MI 4 (Fig. 9) would contain between about 1800 and 500 ppm CO₂ (depending on when, or where, along the ascending path the MI was trapped) and about 1 wt % H₂O. Owing to the nearly constant Al₂O₃/CaO ratio of MI that show a range in CO₂ from about 1800 to 500 ppm (Figs. 6e and 6g), only a few percent of crystallization could have occurred during the amount of time it took the magma to rise from about 8 km depth (time t_0) to 4 km (time t_2). The Solchiaro magma ponded at depths between 4 and 2 km (t_2 in Fig. 9), where extensive crystallization (Al₂O₃/CaO from 1.3 to 2.3) occurred over a limited depth (pressure) range. The extensive crystallization that occurred in the shallow magma chamber trapped many MI (MI 5-11; Fig. 9) containing about 500-300 ppm CO₂ and about 1 wt % H₂O, and the resultant volatile exsolution from the melt likely triggered the eruption (t_2 in Fig. 9). Sample RESC2 containing MI trapped at depths ranging from ≥ 8 to 2 km (for example, MI 1 and 6; Fig. 9) was ejected during this phase. The Solchiaro magma continuously ascended the crust to more shallow levels during the eruption (time t_2 to t_3 in Fig. 9). During this time, sample RESC3, containing MI trapped at intermediate (MI 4; Fig. 9) to shallow (MI 5; Fig. 9) depths, was ejected. MI that were trapped as the magma continued to rise to about 1 km depth (MI 11; Fig. 9) were also ejected during RESC3 time. As the eruption proceeded, the magma body continued to rise through the crust to even shallower depths (<1 km). At this time (t_4 in Fig. 9), the latest erupted sample (RESC4), containing MI trapped from 3 km (MI 7, 10; Fig. 9) to <1 km (MI 12; Fig. 9), was ejected.

One question related to the magma evolution model described above is why olivine phenocrysts that formed at the greatest depths are not found in later eruptions? One possibility is that over time olivine phenocrysts formed at higher pressure and temperature settled to form a cumulate. Earlier formed phenocrysts are more likely to sink and become part of the cumulate compared to later-formed phenocrysts (MI 2 and 3, Fig. 9) as has also been suggested by Johnson *et al.* (2008). These authors interpret the lack of MI with high volatile contents indicative of trapping at great depth in later products of the Jurullo volcano to be the result of olivine fractionating (settling) out of

the melt. To test this hypothesis in our study, we calculated the olivine settling time using a simple Stoke's equation (Table 6). For this calculation, we assumed a 2 km thick magma chamber (Fig. 9), and temperature, density and viscosity were based on the average MI composition (Electronic Appendix 1). The olivine wet liquidus temperature was calculated using the model of Ford *et al.* (1983) and Falloon & Danyushevsky (2000) assuming 100 MPa, the NNO buffer, and melt composition equal to the average MI composition. Viscosity and density were calculated using the models of Giordano *et al.* (2008) and Lange & Carmichael (1987), respectively. Our calculations suggest that a 2.5 mm olivine crystal will settle from the top to the bottom of the magma chamber in about 262 days (Table 6). If the amount of time between the deposition of sample RESC2 (the earliest) and the deposition of sample RESC4 (the latest) is on the order of 365 days, olivine formed deep in the plumbing system and transported upwards by the magma would have already settled to greater depths before the later eruption of sample RESC4. Note that the settling rate is very dependent on the value used for viscosity, and this value varies significantly depending on many factors. For instance, the viscosity calculated from Bottinga & Weill (1972) is one order of magnitude higher than that predicted by the model of Giordano *et al.* (2008). Using the viscosity from Bottinga & Weill (1972) results in a settling time on the order of 10 years. On the other hand, using the viscosity calculated from Giordano & Dingwell (2003) results in a settling time on the order of tens of days.

The interpretation that earlier-formed phenocrysts are not included in the later eruptive products because these crystals were removed to form cumulates is supported by results from Orsi *et al.* (1999). These workers suggest that gabbroic bodies (representing the cumulates?) are present beneath Procida Island at depths from 2 to 10 km, based on 3-D modelling of residual aeromagnetic anomalies.

If settling of early and deeper-formed olivines occurred as described above, we would not expect to find Fo-rich olivine in the latest erupted sample (RESC4), but Fo-rich olivine does occur in this sample. Also, we might expect to see a positive correlation between CO₂ content of MI and Fo content of the host – again this correlation is not observed. However, we observe reverse and oscillatory zoning in some of the olivine phenocrysts which indicates open system processes, in agreement with recharge of deeper and more mafic magmas into the shallower reservoir to produce more Fo-rich olivine late in the eruptive history. In addition, the latest sample RESC4 (highest in the stratigraphy) has the highest ratio of zoned to unzoned olivine (see Table 2). One possible scenario that is consistent with the settling hypothesis is that more mafic melt was episodically injected at various times into the shallow magma chamber at 2-4 km and Fo-rich olivines grew in this more mafic melt before sample RESC4 was erupted.

Anomalous MI

In addition to the much more common (97 out of 109) “normal” MI described above, Sr-rich MI and enriched MI were also observed in the Solchiaro samples.

Sr-rich MI have been reported from many different geodynamic settings and they often represent a small proportion of all MI in the samples, as we observed at Solchiaro. In other studies, workers have interpreted Sr-rich MI to represent (i) mantle-derived melts

that originate from subducted gabbroic bodies, which have been recycled in a mantle plume (Sobolev *et al.*, 2000), (ii) mantle-derived melts produced by different melting fractions and different melting pressures in a mantle plume column (Gurenko & Chaussidon, 1995), (iii) pyroxenite-derived melts generated by intermediate to high degrees of partial melting at lower crust to upper mantle pressures (Schiano *et al.*, 2000), and (iv) dissolution-reaction-mixing (DRM) when a basaltic magma interacts with a preexisting plagioclase-bearing mush zone (Danyushevsky *et al.*, 2004). The Sr-rich MI reported in the literature are characterized by a positive Eu anomaly along with a negative Zr anomaly and a general depletion of most other trace elements, in particular of LILE (Gurenko & Chaussidon, 1995; Sobolev *et al.*, 2000; Schiano *et al.*, 2000; Kent *et al.*, 2002; Lassiter *et al.*, 2002; Danyushevsky *et al.*, 2004).

For Solchiaro samples, Sr-rich MI are also enriched in CaO and show strong negative anomalies for Nb, Zr, and Ti, and a positive anomaly for Eu (Fig. 5). These features suggest that plagioclase melting is involved in the source region for the Sr-rich MI. In contrast, Al₂O₃ is not as enriched as would be expected if plagioclase dissolution generated the Sr-rich melt, as has also been observed by Sobolev *et al.* (2000). The FeO (and MgO) content of the MI cannot be used to test whether or not plagioclase dissolution was involved in producing the Sr-rich melts because the FeO was assumed to be the same for all MI in this study to correct for Fe-loss (Danyushevsky *et al.*, 2000; Danyushevsky *et al.*, 2002a), and the MgO content of the melt is related to FeO through olivine equilibria.

Even though trace element patterns of Sr-rich MI from this study are similar to those of Sr-rich MI from other studies, they show large variation in their absolute abundances. For instance, the highest Sr concentration among studied MI is 1,808 ppm (RESC3-O22-MA, Table 4a), while the highest concentration from bulk rocks of the Solchiaro and Vivara eruptions from literature is 1007 ppm (sample APRO 33 from D'Antonio *et al.*, 1999). This concentration is an order of magnitude greater than that typically reported by other workers (Gurenko & Chaussidon, 1995; Sobolev *et al.*, 2000; Schiano *et al.*, 2000; Kent *et al.*, 2002; Lassiter *et al.*, 2002; Danyushevsky *et al.*, 2004). In contrast, the lowest Zr and Nb concentrations (RESC3-O22-MA, Table 4a) are less than those of primitive mantle (Sun & McDonough, 1989) and comparable to published values for Sr-rich MI from other studies. Sr-rich MI show a positive anomaly for most LILE, in addition to Sr and Eu, which is expressed as a “saw-tooth” pattern in the spider diagram (Fig. 5). The shallow crust in the area consists mainly of interlayered trachytic volcanites and marine siltstone, sandstone, and carbonate. Unless carbonates are assumed to be the contaminant, assimilation of this crustal material is not consistent with the strong depletion in most of the LILE elements of the Solchiaro MI. In addition, the low CO₂ contents of Sr-rich MI are not consistent with assimilation of carbonates.

Sobolev *et al.* (2000) argue that Al₂O₃ contents in Sr-rich MI are inconsistent with a plagioclase melt reaction. However, Danyushevsky *et al.* (2004) show that the Al₂O₃ concentrations in Sr-rich MI can be justified by the occurrence of spinel among the products of the dissolution reaction involving plagioclase (see reaction 1 in Danyushevsky *et al.*, 2004). This is consistent with petrographic observations in which Sr-rich MI are associated with Cr-poor/Al-rich spinel (Danyushevsky *et al.*, 2003). Three of the five Sr-rich MI from our study are associated with spinel, but this phase was not observed in the other two Sr-rich MI. However, if the spinel phase contained in MI is

relatively small and located along the MI wall normal to the plane of observation, it may be difficult to recognize this phase during petrographic analysis. Thus, our interpretation for the origin of Sr-rich melts at Solchiaro is that they are produced by plagioclase dissolution-reaction-mixing, as proposed by Danyushevsky *et al.* (2004). This interpretation is also in agreement with the Cl, CO₂ and S abundances in MI, which decrease with increasing Sr or CaO and increase with increasing concentration of most other elements, especially the LILE and some HFSE. Compared to the Cl, CO₂ and S, H₂O and F contents of Sr-rich MI do not correlate with other elements and concentrations are similar to those in “normal” MI (Fig. 7). In Sr-rich MI from Solchiaro, the combination of low Cl, CO₂ and S contents with high H₂O and F contents is not consistent with an origin of Sr-rich melt from mantle melting because these volatiles show a comparable degree of incompatibility during melting of mantle minerals. Although all volatiles are incompatible in plagioclase, H⁺ will diffuse rapidly from the Solchiaro melt into the melt generated by plagioclase melting (Watson, 1994). Importantly, the most depleted volatile in Sr-rich MI is CO₂, followed by S (with the exception of RESC3-O22-MA) and Cl (Fig. 7). Baker *et al.* (2005) reported that H₂O is the fastest diffusing volatile in silicate melts, CO₂ generally diffuses more slowly compared to H₂O, S diffuses as much as 3 orders of magnitude slower than H₂O in silicic melt, Cl diffuses at rates intermediate between those of H₂O and S, and F diffusion is not well understood. The results of Baker *et al.* (2005) are consistent with volatile concentrations observed in Sr-rich MI from this study, as the anomalous Sr-rich melts are not depleted in H₂O and F, but are depleted in all the other volatiles, with CO₂ and S being the most depleted (Fig. 7). Consequently, if the distribution of volatiles in Sr-rich MI is explained by diffusion processes in the Solchiaro melt, then results of this study suggest that F diffuses at rates comparable to those of H₂O in a melt of this composition.

The second type of anomalous MI observed in the Solchiaro samples is referred to as enriched MI. These MI are variably enriched in TiO₂, K₂O, F, Cl, P₂O₅, LILE, HFSE and REE relative to “normal” MI, and in other studies have been interpreted as (i) mantle-derived melts from a low degree of partial melting combined with different mineralogical assemblages along the mantle plume column (Gurenko & Chaussidon, 1995), (ii) assimilation of heterogeneous crustal material into the crystallizing magma (Kent *et al.*, 2002), and (iii) dissolution-reaction-mixing as proposed for Sr-rich MI (Danyushevsky *et al.*, 2004). In this study, the elements Ti, K, P, F, Cl, LILE, REE and HFSE show anomalous concentrations in the enriched MI, although not all enriched MI are enriched in all of these elements (Figs 5 and 7). The origin of this type of MI is more difficult to constrain compared to the Sr-rich MI because only some minor and trace element concentrations diverge significantly from the normal MI.

Some of the olivine in this study shows both strong reverse/oscillatory zoning and a large range in composition (from Fo₇₉ to Fo₉₀) which may indicate that some olivines were inherited from different magmas that subsequently mixed with the Solchiaro melt. Therefore, enriched MI may be inherited from magmas other than the one representing the Solchiaro magma. However, the observation that one enriched MI (RESC5-O23-MA) is hosted in an unzoned olivine phenocryst, combined with the fact that MI are rarely found at the interface between two zones in zoned olivine, suggests that not all enriched MI are contained in inherited olivines. The interpretation that the enriched MI are inherited from a different magma may be valid for some MI but not for all enriched MI.

An alternative explanation is that enriched MI may reflect dissolution-reaction-mixing processes involving the Solchiaro magma and crustal material containing apatite, Ti-magnetite, sanidine and clinopyroxene in the mush zone of a magma chamber, with a small proportion of solid phases involved in the reaction. Thus, MI enriched in TiO₂, P₂O₅ and F are linked to dissolution of apatite together with Ti-magnetite, MI enriched in K₂O and Ba (LILE) may reflect dissolution of sanidine while those enriched in REE and Hf are likely the product of dissolution of clinopyroxene. All of the phases mentioned above as possible sources of the anomalous elements in the enriched MI are detected in more evolved products from the PVD. Variability in both the amount and mineralogy of the crustal material involved could lead to large heterogeneities in the melt over relatively small distances.

If both types of anomalous MI are interpreted as products of dissolution-reaction-mixing (DRM) processes, MI compositions are consistent with Solchiaro magma migrating through a plumbing system consisting of interconnected chambers in which well-developed mush zones exist, as discussed by Danyushevsky *et al.* (2004). For instance, at greater depths the mush zones may be relatively primitive and rich in plagioclase, while at shallower depths mush zones may be more evolved in composition and thus rich in phases characteristic of more evolved PVD magmas, such as apatite, clinopyroxene, and sanidine. We note that sample RESC4 contains no "deep" olivine or CO₂-rich MI and is interpreted to have been erupted from a shallow depth, and we did not observe any Sr-rich MI in this sample.

In summary, the anomalous MI are not representative of the Solchiaro melt, but rather are the result of dissolution-reaction-mixing processes (Danyushevsky *et al.*, 2004) between the Solchiaro trachy-basalt melt and melts produced by dissolution of plagioclase and other minerals in the mush zone within the magma plumbing system.

7. Summary

Solchiaro is the latest erupted of five volcanoes that make up Procida Island within the Phlegrean Volcanic District (PVD) of southern Italy. The Solchiaro eruption occurred sometime between 19.6 and 14.1 ka, based on paleosols that underlie and overly the Solchiaro deposits (Alessio *et al.*, 1989). The Solchiaro eruption represents the least evolved composition found in the entire PVD. Solchiaro pre-eruptive melt compositions were determined by analyzing 109 MI hosted in olivine phenocrysts from 4 representative samples of the Solchiaro eruption. The samples were collected from different stratigraphic positions in order to better understand the temporal evolution of the Solchiaro magma during eruption. Most of the MI (referred to as "normal" MI) show trends for major, minor and trace element concentrations that are similar to bulk rock compositions reported in the literature. About 10% of the studied MI show compositions (anomalous MI) that vary considerably in abundances of one or more elements when compared to "normal" MI, and the anomalous MI do not follow the same trends shown by bulk rock compositions from the literature. We interpret these MI to have originated from dissolution-reaction-mixing processes in the mush zone of the Solchiaro magma body.

Considering only normal MI, volatile concentrations, especially CO₂, Cl and S, span a wide range, both in individual samples and between the 4 samples. The variation in

volatile concentrations is the result of melt entrapment under volatile-saturated conditions at different locations (different depths) and at different times (different crystal fraction) within the evolving magmatic system. The samples contain both bubble-free and bubble-bearing MI, and the bubble-free MI provide the most reliable information concerning the volatile evolution during eruption of the Solchiaro magma. Based on the correlation between CO₂ contents of MI and stratigraphic position, the Solchiaro melt was saturated in volatiles and started to crystallize at ≥ 8 km depth. This depth is consistent with a geophysical discontinuity at 7.5 km suggested by seismic reflection data in the CF volcanic field (Zollo *et al.*, 2008). The Solchiaro magma ascended through the crust and ponded at shallower levels (between 4 and 2 km), where extensive crystallization occurred that released volatiles from the volatile-saturated melt and triggered the eruption. The depth of magma ponding is in agreement with the depth proposed for a supercritical fluid-bearing rock layer beneath the PVD, based on geophysical data (Zollo *et al.*, 2008).

8. Acknowledgments

We thank Angelo Paone and Giuseppe Rolandi for help identifying eruptive units and collecting samples. Harvey E. Belkin and Clayton Loehn provided valuable assistance with EMP analysis, Rocky Severs provided advice on MI techniques, and Paola Petrosino provided information concerning the possible duration of the Solchiaro eruption and similarities to Capelinhos eruption in the Azores. Comments on an earlier version of this manuscript by Nicole Métrich, Marialuce Frezzotti, Roman Botcharnikov and Wendy Bohrson greatly improved the quality and clarity of the presentation. The research was partially funded by the International Doctorate Fellowship by the Italian Ministry of Research and University (MUR). This material is based upon work supported in part by the National Science Foundation under Grant no. EAR-0711333 to R.J.B. LVD acknowledges support of the Australian Research Council through funding to the Centre of Excellence in Ore Deposits (CODES).

9. References

- Alessio, M., Allegri, L., Azzi, C., Calderoni, G., Cortesi, C., Improta, S. & Petrone, V. (1989). ^{14}C tephrochronology with different fractions of Paleosol humic matter at Procida Island, Italy. *Radiocarbon* 31, 664-671.
- Almeev, R. R., Holtz, F., Koepke, J., Parat, F. & Botcharnikov, R. E. (2007). The effect of H_2O on olivine crystallization in MORB; experimental calibration at 200 MPa. *American Mineralogist* 92, 670-674.
- Anderson, A. T. (1976). Magma mixing; petrological process and volcanological tool. *Journal of Volcanology and Geothermal Research* 1, 3-33.
- Anderson, A. T., Davis, A. M. & Lu, F. (2000). Evolution of Bishop Tuff rhyolitic magma based on melt and magnetite inclusions and zoned phenocrysts. *Journal of Petrology* 41, 449-473.
- Anderson, A. T., Jr. & Brown, G. G. (1993). CO_2 contents and formation pressures of some Kilauean melt inclusions. *American Mineralogist* 78, 794-803.
- Arienzo, I., Moretti, R., Civetta, L., Orsi, G. & Papale, P. (2010). The feeding system of Agnano-Monte Spina eruption (Campi Flegrei, Italy): Dragging the past into present activity and future scenarios. *Chemical Geology* 270, 135-147.
- Baker, D. R., Freda, C., Brooker, R. A. & Scarlato, P. (2005). Volatile diffusion in silicate melts and its effects on melt inclusions. *Annals of Geophysics* 48, 699-717.
- Bartole, R. (1984). Tectonic structure of the Latian-Campanian shelf (Tyrrhenian Sea). *Bollettino di Oceanologia Teorica ed Applicata* 2, 197-230.
- Benjamin, E. R., Plank, T., Wade, J. A., Kelley, K. A., Hauri, E. H. & Alvarado, G. E. (2007). High water contents in basaltic magmas from Irazu Volcano, Costa Rica. *Journal of Volcanology and Geothermal Research* 168, 68-92.
- Blundy, J. & Cashman, K. (2008). Petrologic reconstruction of magmatic system variables and processes. *Reviews in Mineralogy and Geochemistry* 69, 179-239.
- Bodnar, R. J. & Student, J. J. (2006). Melt inclusions in plutonic rocks: Petrography and microthermometry. In *Melt Inclusions in Plutonic Rocks* (J. D. Webster, ed.) Mineralogical Association of Canada, Short Course 36, 1-26.
- Borisov, A. A. & Shapkin, A. I. (1990). A new empirical equation rating $\text{Fe}^{3+}/\text{Fe}^{2+}$ in magmas to their composition, oxygen fugacity, and temperature. *Geochemistry international* 27, 111-116.
- Bottinga, Y. & Richet, P. (1981). High-Pressure and Temperature Equation of State and Calculation of the Thermodynamic Properties of Gaseous Carbon-Dioxide. *American Journal of Science* 281, 615-660.
- Bottinga, Y. & Weill, D. F. (1972). The viscosity of magmatic silicate liquids; a model calculation. *American Journal of Science* 272, 438-475.
- Burnham, C. W. (1979). The importance of volatile constituents. In: Yoder, H. S., Jr. (ed.). *The evolution of igneous rocks*. Princeton: Princeton Univ. Press, 439-482.
- Cannatelli, C., Lima, A., Bodnar, R. J., De Vivo, B., Webster, J. D. & Fedele, L. (2007). Geochemistry of melt inclusions from the Fondo Riccio and Minopoli 1 eruptions at Campi Flegrei (Italy). *Chemical Geology* 237, 418-432.
- Cecchetti, A., Fulignati, P., Marianelli, P., Proto, N., Sbrana, A. (2001). The feeding system of Campi Flegrei. Insights from melt and fluid inclusions on Ignimbrite

- Campana, Solchiaro and Minopoli eruptions. GNV-INGV Meeting. Rome, Italy, 9-11 October, 2011, Abstract vol: 190-191
- Cecchetti, A., Marianelli, P., and Sbrana, A. (2005). Neapolitan active volcanoes: A study of the medium-high pressure feeding systems through melt inclusions. XVIII European Conference on Research on Fluid Inclusions. Siena, Italy, University of Siena.
- Cervantes, P. & Wallace, P. (2003). Magma degassing and basaltic eruption styles; a case study of approximately 2000 year BP Xitle Volcano in central Mexico. *Journal of Volcanology and Geothermal Research* 120, 249-270.
- Cervantes, P., Kamenetsky, V. & Wallace, P. (2002). Melt inclusion volatile contents, pressures of crystallization for hawaiian picrites, and the problem of shrinkage bubbles. Paper presented at the American Geophysical Union 2002, San Francisco, CA, US.
- Civetta, L., Orsi, G., Pappalardo, L., Fisher, R. V., Heiken, G. & Ort, M. (1997). Geochemical zoning, mingling, eruptive dynamics and depositional processes -- the campanian ignimbrite, Campi Flegrei caldera, Italy. *Journal of Volcanology and Geothermal Research* 75 (3-4):183-219.
- D'Antonio, M., Civetta, L. & Di Girolamo, P. (1999). Mantle source heterogeneity in the Campanian Region (South Italy) as inferred from geochemical and isotopic features of mafic volcanic rocks with shoshonitic affinity. *Mineralogy and Petrology* 67, 163-192.
- D'Argenio, B., Pescatore, T., Scandone, P. & Segre, B. (1973). Schema geologico dell'Appennino meridionale (Campania e Lucania). *Problemi Attuali di Scienza e Cultura*. Rome: Accademia Nazionale dei Lincei, 183, 49-81.
- Danyushevsky, L. V., Della Pasqua, F. N. & Sokolov, S. (2000). Re-equilibration of melt inclusions trapped by magnesian olivine phenocrysts from subduction-related magmas; petrological implications. *Contributions to Mineralogy and Petrology* 138, 68-83.
- Danyushevsky, L. V., Leslie, R. A. J., Crawford, A. J., Durance, P., Niu, Y., Herzberg, C. & Wilson, M. (2004). Melt inclusions in primitive olivine phenocrysts; the role of localized reaction processes in the origin of anomalous compositions. *Journal of Petrology* 45, 2531-2553.
- Danyushevsky, L. V., McNeill, A. W. & Sobolev, A. V. (2002a). Experimental and petrological studies of melt inclusions in phenocrysts from mantle-derived magmas: an overview of techniques, advantages and complications. *Chemical Geology* 183, 5-24.
- Danyushevsky, L. V., Perfit, M. R., Eggins, S. M. & Falloon, T. J. (2003). Crustal origin for coupled "ultra-depleted" and "plagioclase" signatures in MORB olivine-hosted melt inclusions; evidence from the Siqueiros transform fault, East Pacific Rise. *Contributions to Mineralogy and Petrology* 144, 619-637.
- Danyushevsky, L. V., Sobolev, A. V. & Falloon, T. J. (1995). North Tongan high-Ca boninite petrogenesis - the role of Samoan plume and subduction zone-transform fault transition. *Journal of Geodynamics* 20, 219-241.
- Danyushevsky, L. V., Sokolov, S. & Falloon, T. J. (2002b). Melt inclusions in olivine phenocrysts; using diffusive re-equilibration to determine the cooling history of a

- crystal, with implications for the origin of olivine-phyric volcanic rocks. *Journal of Petrology* 43, 1651-1671.
- De Astis, G., Piochi, M. & Pappalardo, L. (2004). Procida Volcanic History: new insights in the evolution of the Phlegraean Volcanic District (Campania, Italy). *Bulletin of Volcanology* 66, 622-641.
- De Vivo, B., & Bodnar, R. J. (2003). *Melt inclusions in volcanic systems*: Elsevier Sciences.
- De Vivo, B., Rolandi, G., Gans, P. B., Calvert, A., Bohron, W. A., Spera, F. J. & Belkin, H. E. (2001). New constraints on the pyroclastic eruptive history of the Campanian volcanic plain (Italy). *Mineralogy and Petrology* 73, 47-65.
- Di Girolamo, P., Ghiara, M. R., Lirer, Munno, R., Rolandi, G. & Stanzione, D. (1984). *Vulcanologia e petrologia dei Campi Flegreei*. *Volcanology and petrology of Phlegraean Fields*. *Bollettino della Società Geologica Italiana* 103, 349-413.
- Di Girolamo, P. & Stanzione, D. (1973). Lineamenti geologici e petrologici dell'isola di Procida. *Rendiconti della Società Italiana di Mineralogia e Petrologia* 29, 81-125.
- Esposito, R., Bodnar, R. J., Hunter, J. & De Vivo, B. (2010a). Do melt inclusions record the pre-eruptive volatile content of magmas? Paper presented at the PanAmerican Current Research on Fluid Inclusions (PACROFI-X) Las Vegas, Nevada, US, June 2010.
- Esposito, R., Fedele, L., Steele-MacInnis, M. & Bodnar, R. J. (2010b). Evolution of H₂O and CO₂ contents in silicate melt inclusions during post-entrapment crystallization. Paper presented at the Goldschmidt 2010, Knoxville, NC, US, 13-18 June 2010. Abstract vol: A272
- Falloon, T. J. & Danyushevsky, L. V. (2000). Melting of refractory mantle at 1.5, 2 and 2.5 GPa under anhydrous and H₂O-undersaturated conditions; implications for the petrogenesis of high-Ca boninites and the influence of subduction components on mantle melting. *Journal of Petrology*, 41, no.2, 257-283.
- Faure, F. & Schiano, P. (2005). Experimental investigation of equilibration conditions during forsterite growth and melt inclusion formation. *Earth and Planetary Science Letters* 236, 882-898.
- Finetti, I. & Morelli, C. (1974). Esplorazione sismica a riflessione dei Golfi di Napoli e Pozzuoli. *Bollettino di Geofisica Teorica ed Applicata* 16, 175-222.
- Ford, C. E., Russell, D. G., Craven, J. A. & Fisk, M. R. (1983). Olivine-liquid equilibria; temperature, pressure and composition dependence of the crystal/liquid cation partition coefficients for Mg, Fe²⁺, Ca and Mn. *Journal of Petrology* 24, 256-265.
- Frezzotti, M. L. (2001). Silicate-melt inclusions in magmatic rocks; applications to petrology. *Lithos* 55, 273-299.
- Giordano, D. & Dingwell, D. B. (2003). Non-Arrhenian multicomponent melt viscosity: a model. *Earth and Planetary Science Letters* 208, 337-349.
- Giordano, D., Russell, J. K. & Dingwell, D. B. (2008). Viscosity of magmatic liquids: A model. *Earth and Planetary Science Letters* 271, 123-134.
- Gurenko, A. A. & Chaussidon, M. (1995). Enriched and depleted primitive melts included in olivine from Icelandic tholeiites; origin by continuous melting of a single mantle column. *Geochimica et Cosmochimica Acta* 59, 2905-2917.

- Helo, C., Longpré, M. A., Shimizu, N., Clague, D. A. & Stix, J. (2011). Explosive eruptions at mid-ocean ridges driven by CO₂-rich magmas. *Nature Geoscience* 4, 260-263.
- Ippolito, F., Ortolani, F. & Russo, M. (1973). Struttura marginale tirrenica dell'Appennino Campano; reinterpretazione di dati di antiche ricerche di idrocarburi. *Memorie della Società Geologica Italiana* 12, 227-250.
- Johnson, E. R., Wallace, P. J., Cashman, K. V., Granados, H. D. & Kent, A. J. R. (2008). Magmatic volatile contents and degassing-induced crystallization at Volcan Jorullo, Mexico; implications for melt evolution and the plumbing systems of monogenetic volcanoes. *Earth and Planetary Science Letters* 269, 477-486.
- Kamenetsky, V., Metrich, N. & Cioni, R. (1995). Potassic primary melts of Vulcini (Roman Province); evidence from mineralogy and melt inclusions. *Contributions to Mineralogy and Petrology* 120, 186-196.
- Kawakami, Y., Yamamoto, J. & Kagi, H. (2003). Micro-Raman densimeter for CO₂ inclusions in mantle-derived minerals. *Applied Spectroscopy* 57, 1333-1339.
- Kent, A. J. R., Baker, J. A. & Wiedenbeck, M. (2002). Contamination and melt aggregation processes in continental flood basalts; constraints from melt inclusions in Oligocene basalts from Yemen. *Earth and Planetary Science Letters* 202, 577-594.
- Kent, A. J. R. (2008). Melt inclusions in basaltic and related volcanic rocks. *Reviews in Mineralogy and Geochemistry* 69, 273-331.
- Kress, V. C. & Ghiorso, M. S. (2004). Thermodynamic modeling of post-entrapment crystallization in igneous phases. *Journal of Volcanology and Geothermal Research* 137 (4):247-260. doi:DOI 10.1016/j.jvolgeores.2004.05.012.
- Lange, R. A. & Carmichael, I. S. E. (1987). Densities of Na₂O-K₂O-MgO-MgO-FeO-Fe₂O₃-Al₂O₃-TiO₂-SiO₂ liquids: New measurements and derived partial molar properties. *Geochimica et Cosmochimica Acta* 51, 2931-2946.
- Lassiter, J. C., Hauri, E. H., Nikogosian, I. K. & Barseczus, H. G. (2002). Chlorine-potassium variations in melt inclusions from Raivavae and Rapa, Austral Islands; constraints on chlorine recycling in the mantle and evidence for brine-induced melting of oceanic crust. *Earth and Planetary Science Letters* 202, 525-540.
- Le Bas, M. J., Le Maitre, R. W., Streckeisen, A. & Zanettin, B. A. (1986). Chemical classification of volcanic rocks based on the total alkali-silica diagram. *Journal of Petrology* 27, 745-750.
- Lirer, L., Rolandi, G. & Rubin, M. (1991). ¹⁴C age of the "Museum Breccia" (Campi Flegrei) and its relevance for the origin of the Campanian Ignimbrite. *Journal of Volcanology and Geothermal Research* 48, 223-227.
- Lowenstern, J. B. (1995). Applications of silicate-melt inclusions to the study of magmatic volatiles. *Short Course Handbook* 23, 71-99.
- Mangiacapra, A., Moretti, R., Rutherford, M., Civetta, L., Orsi, G. & Papale, P. (2008). The deep magmatic system of the Campi Flegrei caldera (Italy). *Geophysical Research Letter* 35, L21304.
- Marianelli, P., Sbrana, A. & Proto, M. (2006). Magma chamber of the Campi Flegrei supervolcano at the time of eruption of the Campanian Ignimbrite. *Geology* 34, 937-940.

- Medard, E. & Grove, T. L. (2008). The effect of H₂O on the olivine liquidus of basaltic melts; experiments and thermodynamic models. *Contributions to Mineralogy and Petrology* 155, 417-432.
- Métrich, N. & Clochiatti, R. (1996). Sulfur abundance and its speciation in oxidized alkaline melts. *Geochimica et Cosmochimica Acta* 60, 4151-4160.
- Métrich, N. & Wallace, P. J. (2008). Volatile abundances in basaltic magmas and their degassing paths tracked by melt inclusions. *Reviews in Mineralogy and Geochemistry* 69, 363-402.
- Moore, G. (2008). Interpreting H₂O and CO₂ contents in melt inclusions; constraints from solubility experiments and modeling. *Reviews in Mineralogy and Geochemistry* 69, 333-362.
- Mutchler, S. R., Fedele, L. & Bodnar, R. J. (2008). Appendix A5; Analysis Management System (AMS) for reduction of laser ablation ICP-MS data. In: Sylvester, P. J. (ed.) *Short Course Series - Mineralogical Association of Canada*. Quebec: Mineralogical Association of Canada, 40 318-327.
- Orsi, G., Patella, D., Piochi, M., Tramacere, A. (1999). Magnetic modeling of the phlegraean volcanic district with extension to the ponza archipelago, italy. *Journal of Volcanology and Geothermal Research* 91 (2-4):345-360.
- Papale, P., Moretti, R. & Barbato, D. (2006). The compositional dependence of the saturation surface of H₂O + CO₂ fluids in silicate melts. *Chemical Geology* 229, 78-95.
- Pearce, J.A. & Peate, D.W. (1995). Tectonic implications of the composition of volcanic arc magmas. In: *Annual Review of Earth and Planetary Sciences*, vol 23. pp 251-285.
- Peccerillo, A. (1999). Multiple mantle metasomatism in central-southern Italy; geochemical effects, timing and geodynamic implications. *Geology* 27, 315-318.
- Peccerillo, A. (2005). *Plio-quadernary volcanism in italy: Petrology, geochemistry, geodynamics*. Springer. Heidelberg, Germany.
- Perrotta, A., Scarpati, C., Luongo, G. & Morra, V. (2010). Stratigraphy and volcanological evolution of the southwestern sector of Campi Flegrei and Procida Island, Italy, *Stratigraphy and Geology of Volcanic Areas*. In: Groppelli, G. & Viereck-Goette, L. (eds.) *Stratigraphy and Geology of Volcanic Areas*. Special Paper 464, Milano, Italy: Geological Society of America, 171-191.
- Pescatore, T. & Rolandi, G. (1981). Preliminary observations of the stratigraphy of volcanoclastic deposits of the south-west sector of Phlegrean Fields (in italian). *Bollettino della Società Geologica Italiana* 100, 233-254.
- Portnyagin, M., Almeev, R., Matveev, S. & Holtz, F. (2008). Experimental evidence for rapid water exchange between melt inclusions in olivine and host magma. *Earth and Planetary Science Letters* 272, 541-552.
- Roach, A. L. (2005). *The evolution of silicic magmatism in the post-caldera volcanism of the Phlegrean Fields, Italy*. Ph.D. Thesis, Providence: Brown University.
- Roedder, E. (1979). Origin and significance of magmatic inclusions. *Bulletin de Mineralogie* 102, 487-510.
- Rolandi, G., Bellucci, F., Heizler, M. T., Belkin, H. E. & De Vivo, B. (2003). Tectonic controls on the genesis of ignimbrites from the Campanian Volcanic Zone, southern Italy. *Mineralogy and Petrology* 79, 3-31.

- Rosi, M., Sbrana, A. & Vezzoli, L. (1988). Correlazioni tefrostratigrafiche di alcuni livelli di Ischia, Procida e Campi Flegrei. *Memorie della Societa Geologica Italiana* 41, 1015-1027.
- Saito, G., Kazahaya, K., Shinohara, H., Stimac, J. & Kawanabe, Y. (2001). Variation of volatile concentration in a magma system of Satsuma-Iwojima Volcano deduced from melt inclusion analyses. *Journal of Volcanology and Geothermal Research* 108, 11-31.
- Schiano, P. (2003). Primitive mantle magmas recorded as silicate melt inclusions in igneous minerals. *Earth-Science Reviews* 63, 121-144.
- Schiano, P., Eiler, J. M., Hutcheon, I. D. & Stolper, E. M. (2000). Primitive CaO-rich, silica-undersaturated melts in island arcs; evidence for the involvement of clinopyroxene-rich lithologies in the petrogenesis of arc magmas. *Geochemistry, Geophysics, Geosystems* 1, doi: 10.1029/1999GC000032.
- Severs, M. J., Azbej, T., Thomas, J. B., Mandeville, C. W. & Bodnar, R. J. (2007). Experimental determination of H₂O loss from melt inclusions during laboratory heating: Evidence from Raman spectroscopy. *Chemical Geology* 237, 3-4.
- Signorelli, S., Vaggelli, G., Romano, C. & Carroll, M. R. (2001). Volatile element zonation in Campanian ignimbrite magmas (Phlegrean Fields, Italy); evidence from the study of glass inclusions and matrix glasses. *Contributions to Mineralogy and Petrology* 140, 543-553.
- Sobolev, A. V. (1996). Melt inclusions in minerals as a source of principal petrological information. *Petrology* 4, 209-220.
- Sobolev, A. V., Hofmann, A. W. & Nikogosian, I. K. (2000). Recycled oceanic crust observed in 'ghost plagioclase' within the source of Mauna Loa lavas. *Nature* 404, 986-990.
- Sobolev, A. V. & Shimizu, N. (1993). Ultra-depleted primary melt included in an olivine from the Mid-Atlantic Ridge. *Nature* 363, 151-154.
- Steele-MacInnis, M., Esposito, R. & Bodnar, R. J. (in press). Thermodynamic model for the effect of post-entrapment crystallization on the H₂O-CO₂ systematics of volatile saturated silicate melt inclusions. *Journal of Petrology*
- Streck, M. J. (2008). Mineral textures and zoning as evidence for open system processes. *Reviews in Mineralogy and Geochemistry* 69, 595-622.
- Student, J. J. & Bodnar, R. J. (2004). Silicate melt inclusions in porphyry copper deposits; identification and homogenization behavior. In: Kontak, D. J., Anderson, A. J. & Marshall, D. D. (eds.) *The Canadian Mineralogist*, vol.42, Part 5. Ottawa: Mineralogical Association of Canada, 1583-1599.
- Sun, S. S. (1980). Lead Isotopic Study of Young Volcanic-Rocks from Mid-Ocean Ridges, Ocean Islands and Island Arcs. *Philosophical Transactions of the Royal Society of London Series a-Mathematical Physical and Engineering Sciences* 297, 409-445.
- Sun, S. S. & McDonough, W. F. (1989). Chemical and isotopic systematics of oceanic basalts; implications for mantle composition and processes. *Geological Society Special Publications* 42, 313-345.
- Thomas, J. B. & Bodnar, R. J. (2002). A technique for mounting and polishing melt inclusions in small (>1 mm) crystals. *American Mineralogist* 87, 1505-1508.

- Tonarini, S., Leeman, W. P., Civetta, L., D'Antonio, M., Ferrara, G. & Necco, A. (2004). B/Nb and delta ¹¹B systematics in the Phlegrean volcanic district, Italy. *Journal of Volcanology and Geothermal Research* 133, 123-139.
- Toplis, M. J. (2005). The thermodynamics of iron and magnesium partitioning between olivine and liquid; criteria for assessing and predicting equilibrium in natural and experimental systems. *Contributions to Mineralogy and Petrology* 149, 22-39.
- Turco, E., Schettino, A., Pierantoni, P. P. & Santarelli, G. (2006). The Pleistocene extension of the Campania Plain in the framework of the southern Tyrrhenian tectonic evolution: morphotectonic analysis, kinematic model and implications for volcanism. In: De Vivo, B. (ed.) *Developments in Volcanology*: Elsevier, 27-51.
- Wade, J. A., Plank, T., Melson, W. G., Soto, G. J. & Hauri, E. H. (2006). The volatile content of magmas from Arenal Volcano, Costa Rica. *Journal of Volcanology and Geothermal Research* 157, 94-120.
- Wallace, P. J., Anderson, A. T., Jr. & Davis, A. M. (1999). Gradients in H₂O, CO₂, and exsolved gas in a large-volume silicic magma system; interpreting the record preserved in melt inclusions from the Bishop Tuff. *Journal of Geophysical Research* 104, 20,097-020,122.
- Watson, E. B. (1994). Diffusion in volatile-bearing magmas. *Reviews in Mineralogy* 30, 371-411.
- Webster, J. D., Raia, F., Tappen, C. & De Vivo, B. (2003). Pre-eruptive geochemistry of the ignimbrite-forming magmas of the Campanian Volcanic Zone, Southern Italy, determined from silicate melt inclusions. *Mineralogy and Petrology* 79, 99-125.
- Zollo, A., Maercklin, N., Vassallo, M., Dello Iacono, D., Virieux, J. & Gasparini, P. (2008). Seismic reflections reveal a massive melt layer feeding Campi Flegrei Caldera. *Geophysical Research Letters* 35, doi: 10.1029/2008GL034242.

10. Tables

Table 1. Pre-eruptive magma storage depths for PVD eruptions based on MI data.

Eruption	Pressure of formation Mpa	Magmatic depth (27 Mpa/km) km	Rock composition (TAS)	Reference
Campanian Ignimbrite	50-100	2_4	Trachy-phonolite	Signorelli et al. (2001)
Campanian Ignimbrite	40-150	1_6	Trachy-phonolite	Marianelli et al. (2006)
Solchiaro	200-800	7_30	trachybasalt	Cecchetti et al. (2001)
Solchiaro	200-400	7_15	trachybasalt	Cecchetti et al. (2005)
Minopoli 2			Latite	
Fondo Riccio	100-200	4_7	Latite	Mangiacapra et al. (2008)
Minopoli 2	50-200	2_7	Shoshonite	
Agnano-Monte Spina	20-50 and 250	1_2 and 9	Trachytic	Roach (2005)
Agnano-Monte Spina	108-211	4_8	Trachytic	Arienzo et al. (2010)
Solchiaro	20- \geq 210	1_ \geq 8	trachybasalt	This study

Table 2a. Petrographic information for MI from samples RESC2 and RESC3. All MI are hosted in olivine.

Sample RESC2

Inclusion ID	MI shape	MI dimensions (μm) ¹	Bubbles in MI	Crystals in MI ²	Fe/Mg zoning of host
RESC2-O22-MA	ellipsoidal	25	1	none	reverse
RESC2-O22-MB	spherical	40	none	none	reverse
RESC2-O22-MC	negative crystal	46 x 29	1	none	reverse
RESC2-O26-MF	ellipsoidal	50 x 30	none	none	none
RESC2-O22-ME	spherical	25	1	none	reverse
RESC2-O26-M1	ellipsoidal	65 x 90	1	chromite	none
RESC2-O26-M2	spherical	30	none	chromite	none
RESC2-O26-M3	ellipsoidal	159 x 102	1	none	none
RESC2-O26-M4	irregular	392 x 99	4	none	none
RESC2-O51-MA	spherical	32	1	none	none
RESC2-O52-MA	negative crystal	173 x 121	none	chromite	none

Sample RESC3

Inclusion ID	MI shape	MI dimensions (μm) ¹	Bubbles in MI	Crystal in MI ²	Fe/Mg zoning of host
RESC3-O1-MA	negative crystal	75 x 110	none	none	none
RESC3-O2-MA	spherical	80	1	chromite	oscillatory
RESC3-O3-MA	spherical	45	none	none	normal
RESC3-O4-MA	negative crystal	100 x 40	1	chromite	oscillatory
RESC3-O6-MA	negative crystal	25 x 35	none	chromite	normal
RESC3-O7-MA	spherical	150	none	chromite	oscillatory
RESC3-O9-MA	spherical	50	none	chromite	none
RESC3-O10-MA	ellipsoidal	50 x 40	none	none	none
RESC3-O10-MB	negative crystal	35 x 45	none	none	none
RESC3-O10-MC	ellipsoidal	80 x 50	1	none	none
RESC3-O10-MD	ellipsoidal	60 x 45	1	none	none
RESC3-O10-ME	spherical	100	3	none	none
RESC3-O11-MA	ellipsoidal	50 x 45	1	none	oscillatory
RESC3-O12-MB	negative crystal	130 x 100	1	none	none
RESC3-O13-MA	negative crystal	30 x 20	1	none	none
RESC3-O14-MA	negative crystal	85 x 95	1	chromite	reverse
RESC3-O15-MA	negative crystal	50 x 30	1	chromite	oscillatory
RESC3-O16-MA	negative crystal	50 x 35	none	chromite	oscillatory
RESC3-O16-MB	negative crystal	45 x 55	1	chromite	oscillatory
RESC3-O18-MA	negative crystal	45 x 55	none	none	none
RESC3-O20-MA	irregular	60 x 30	1	chromite	oscillatory
RESC3-O21-MA	negative crystal	35 x 45	1	chromite	none
RESC3-O21-MB	ellipsoidal	140 x 100	1	none	none
RESC3-O22-MA	spherical	80	none	none	none
RESC3-O22-MC	ellipsoidal	100 x 80	1	chromite	none
RESC3-O23-MA	irregular	105 x 115	none	none	patchy
RESC3-O23-MC	irregular	105 x 115	1	none	patchy
RESC3-O25-MC	ellipsoidal	30 x 50	1	none	direct
RESC3-O25-MD	ellipsoidal	30 x 50	1	chromite	direct
RESC3-O26-MA	ellipsoidal	20 x 40	none	none	oscillatory
RESC3-O26-MB	ellipsoidal	30 x 60	1	chromite	oscillatory
RESC3-O26-MC	ellipsoidal	50 x 65	1	none	oscillatory
RESC3-O26-MD	ellipsoidal	80 x 20	multiple	1	oscillatory
RESC3-O26-ME	ellipsoidal	30 x 40	1	none	oscillatory
RESC3-O27-MA	negative crystal	40 x 20	none	none	none
RESC3-O27-MB	negative crystal	60 x 30	none	none	none
RESC3-O28-MA	ellipsoidal	60 x 40	none	chromite	oscillatory
RESC3-O28-MB	irregular	80 x 40	none	chromite	oscillatory
RESC3-O29-MA	spherical	50	none	none	normal

¹ For spherical MI the diameter is listed; for all other MI the maximum and minimum dimensions are listed

² Crystals in MI are trapped solids and not daughter minerals

Table 2b. Petrographic information for MI from samples RESC4 and RESC5. All MI are hosted in olivine.

Sample RESC4					
Inclusion ID	MI shape	MI dimension (μm) ¹	Bubbles in MI	Crystal in MI ²	Fe/Mg zoning of host
RESC4-O2-MA	ellipsoidal	40 x 60	none	none	oscillatory
RESC4-O3-MA	spherical	23	none	chromite	oscillatory
RESC4-O4-MA	ellipsoidal	40 x 30	none	none	oscillatory
RESC4-O5-MA	spherical	60	1	chromite	none
RESC4-O5-MB	spherical	110	2	chromite	none
RESC4-O6-MA	spherical	25	none	none	normal
RESC4-O7-MA	ellipsoidal	50 x 100	none	none	none
RESC4-O9-MA	negative crystal	55 x 65	none	none	oscillatory
RESC4-O9-MB	ellipsoidal	20 x 50	none	chromite	oscillatory
RESC4-O9-MC	ellipsoidal	20 x 60	none	none	oscillatory
RESC4-O10-MA	ellipsoidal	120 x 70	none	none	oscillatory
RESC4-O11-MA	ellipsoidal	40 x 60	none	none	normal
RESC4-O11-MC	ellipsoidal	145 x 100	2	none	normal
RESC4-O12-MA	spherical	60	none	none	oscillatory
RESC4-O14-MA	negative crystal	70 x 50	none	none	oscillatory
RESC4-O14-MB	negative crystal	100 x 120	1	none	oscillatory
RESC4-O14-MC	ellipsoidal	35 x 20	none	none	oscillatory
RESC4-O15-MA	ellipsoidal	50 x 25	none	none	oscillatory
Sample RESC5					
Inclusion ID	MI shape	MI dimension (μm) ¹	Bubbles in MI	Crystal in MI ²	Fe/Mg zoning of host
RESC5-O1-MA	ellipsoidal	40 x 30	none	none	none
RESC5-O2-MA	irregular	135 x 120	7	none	none
RESC5-O3-MA	ellipsoidal	30 x 50	1	none	reverse
RESC5-O4-MA	negative crystal	55 x 65	1	none	none
RESC5-O5-MA	ellipsoidal	50 x 35	none	none	reverse
RESC5-O6-MA	spherical	80	none	none	none
RESC5-O7-MA	negative crystal	60 x 30	1	none	reverse
RESC5-O8-MA	ellipsoidal	40 x 70	1	chromite	normal
RESC5-O8-MB	spherical	120	1	diopside, chromite	normal
RESC5-O8-MC	spherical	130	1	chromite	normal
RESC5-O9-MA	spherical	50	1	none	oscillatory
RESC5-O10-MA	ellipsoidal	50	none	none	none
RESC5-O10-MD	ellipsoidal	40 x 90	none	chromite	none
RESC5-O11-MA	spherical	50	1	chromite	none
RESC5-O12-MA	spherical	50	1	chromite	oscillatory
RESC5-O13-MA	negative crystal	110 x 70	1	chromite	oscillatory
RESC5-O13-MC	negative crystal	140 x 80	1	none	oscillatory
RESC5-O13-MD	negative crystal	160 x 100	1	none	oscillatory
RESC5-O14-MB	spherical	130	1	chromite	none
RESC5-O15-MA	spherical	50	none	none	none
RESC5-O15-MB	spherical	400	1	chromite	none
RESC5-O16-MA	ellipsoidal	50 x 80	1	chromite	none
RESC5-O16-MB	ellipsoidal	100 x 75	1	chromite	none
RESC5-O17-MB	spherical	40	1	none	none
RESC5-O17-MC	spherical	200	1	chromite	none
RESC5-O17-MD	ellipsoidal	60 x 30	1	chromite	none
RESC5-O18-MA	negative crystal	180 x 120	none	none	none
RESC5-O18-MB	irregular	300 x 60	5	none	none
RESC5-O18-MC	spherical	35	1	none	none
RESC5-O18-MD	irregular	20 x 60	3	none	none
RESC5-O19-MC	spherical	90	1	none	normal
RESC5-O21-MA	spherical	40	none	none	oscillatory
RESC5-O21-MB	spherical	80	1	chromite	oscillatory
RESC5-O21-MC	ellipsoidal	120 x 60	7	chromite	oscillatory
RESC5-O21-ME	spherical	35	none	none	oscillatory
RESC5-O22-MA	negative crystal	80 x 50	none	chromite	none
RESC5-O23-MA	spherical	60	1	chromite	none
RESC5-O25-MA	spherical	40	1	none	oscillatory
RESC5-O25-MB	ellipsoidal	80 x 20	none	none	oscillatory
RESC5-O26-MA	ellipsoidal	80 x 60	none	chromite	oscillatory
RESC5-O27-MB	spherical	45	none	none	unknown
RESC5-O28-MB	spherical	80	none	none	none
RESC5-O30-MA	spherical	150	1	none	none

¹ For spherical MI the diameter is listed; for all other MI the maximum and minimum dimensions are listed

² Crystals in MI are trapped solids and not daughter minerals

Table 3. Representative EMP analysis of olivine from samples RESC3, RESC4 and RESC5.

Olivine ID	wt%						mole%
	SiO ₂	FeO	MnO	MgO	CaO	Tot	Fo
RESC2-O22-H1-core	38.63	16.75	0.21	44.31	0.21	100.1	82.08
RESC-2-O22-H1-rim	39.61	12.95	0.14	46.96	0.35	100.0	86.07
RE-SC2-O13-H1	39.01	13.19	0.26	47.28	0.26	100.0	85.94
RE.SC2.O8.H1	39.80	12.61	0.31	46.96	0.32	100.0	86.27
RESC3-O16-H1-core	39.67	12.19	0.23	47.57	0.33	100.0	86.85
RESC3-O16-H2-rim	38.51	19.16	0.30	41.87	0.30	100.1	78.99
RESC3-O22-H1-core	39.39	13.23	0.23	46.78	0.38	100.0	85.67
RESC3-O23-H2-core	38.94	17.46	0.26	43.14	0.29	100.1	80.95
RESC3-O23-H4-rim	39.68	13.23	0.15	46.58	0.36	100.0	85.71
RESC4-O7-H1-core	39.09	14.66	0.17	45.80	0.34	100.1	84.25
RESC4-O2-H1-core	38.98	15.75	0.24	44.79	0.31	100.1	82.97
RESC4-O3-H1-core	39.89	11.56	0.18	48.01	0.34	100.0	87.55
RESC4-O3-H3-rim	39.57	13.12	0.17	46.81	0.34	100.0	85.87
RESC5-O5-H1-core	39.41	12.51	0.17	47.61	0.32	100.0	86.63
RESC5-O5-H3-rim	40.21	10.69	0.10	48.68	0.26	99.9	88.63
RESC5-O8-H1-core	40.19	9.59	0.18	49.62	0.34	99.9	89.66
RESC5-O8-H3-rim	39.57	12.47	0.14	47.54	0.29	100.0	86.71

Table 4a. Representative major, minor and trace element and volatile content of MI from samples RESC2 and RESC3.

Sample MI ID type	uncorrected	corrected	uncorrected	corrected	uncorrected	corrected	uncorrected	corrected	uncorrected	corrected	uncorrected	corrected	uncorrected	corrected
	RESC2 O3.M1 Normal MI	RESC2 O3.M1 Normal MI	RESC2 O26.M1 Sr-rich MI	RESC2 O26.M1 Sr-rich MI	RESC3 O21-MB Normal MI	RESC3 O21-MB Normal MI	RESC3 O21-MA Sr-rich MI	RESC3 O21-MA Sr-rich MI	RESC3 O22-MC Normal MI	RESC3 O22-MC Normal MI	RESC3 O22-MA Sr-rich MI	RESC3 O22-MA Sr-rich MI	RESC3 O4-MA Enriched MI	RESC3 O4-MA Enriched MI
SiO ₂	47.88	49.89	47.05	49.05	49.77	51.94	47.21	50.47	48.28	51.03	47.94	50.71	46.72	50.17
TiO ₂	1.13	1.17	0.62	0.63	1.17	1.14	0.63	0.65	1.31	1.34	0.37	0.38	1.50	1.56
Al ₂ O ₃	16.86	17.44	17.03	17.20	16.91	16.53	16.58	16.93	15.62	15.92	16.62	16.89	16.41	17.02
Fe ₂ O ₃	8.86	1.11	7.35	1.12	5.72	1.11	6.98	1.12	6.85	1.11	6.83	1.11	7.75	1.12
FeO	7.01	7.01	7.04	7.04	7.01	7.01	7.02	7.02	7.02	7.00	7.01	7.01	7.05	7.05
MnO	0.19	0.20	0.14	0.14	0.13	0.13	0.11	0.11	0.12	0.12	0.12	0.12	0.12	0.12
MgO	4.86	6.16	5.83	7.58	4.16	7.16	4.62	7.22	4.92	6.86	5.29	7.45	3.81	6.27
CaO	9.14	9.46	13.71	13.85	8.34	8.15	12.57	12.84	11.22	11.44	13.23	13.45	9.15	9.49
Na ₂ O	3.1	3.21	1.91	1.93	2.89	2.83	2.31	2.37	2.67	2.72	2.15	2.18	2.68	2.77
K ₂ O	3.73	3.86	1.16	1.17	3.62	3.54	1.02	1.05	2.05	2.09	0.49	0.50	3.43	3.56
P ₂ O ₅	0.49	0.51	0.23	0.23	0.43	0.43	0.15	0.16	0.36	0.37	0.17	0.18	0.82	0.86
Fo		85		86		86		86		85		86		84
Mg#		62		66		64		63		66		65		61
Be	bdl	bdl	7.7	7.4	bdl	bdl	bdl	bdl	bdl	bdl	bdl	bdl	8.9	8.5
B	bdl	bdl	bdl	bdl	13.2	12.1	bdl	bdl	9.2	8.7	bdl	bdl	17.8	17
V	188	187	193	186	154	141	203	191	189	218	207	250	240	240
Rb	134	133	38.1	36.6	112	102	25.2	23.8	71.5	68.2	5.7	5.4	113	108
Sr	599	597	1309	1258	550	501	1181	1115	476	454	1906	1808	865	829
Y	17.5	17.5	16.5	15.9	17	15.1	14.5	13.7	19.4	18.5	18.3	17.3	23.8	22.9
Zr	97.1	96.8	33.9	32.6	105	95.7	29.6	27.9	102.7	97.9	7.6	7.2	208	199
Nb	18.4	18.3	5.9	5.6	22.5	20.5	5.9	5.5	14.2	13.5	0.7	0.7	55.2	53
Cs	5.6	5.6	8.37	8.1	4.2	3.8	2.6	2.4	4.	3.8	0.5	0.5	7.3	7
Ba	980	977	447	430	895	816	295	278	593	565	416	395	1328	1273
La	25.	24.9	10.5	10.1	26.8	24.5	9.1	8.6	16.9	16.1	5.6	5.3	45.26	43.4
Ce	53.6	53.4	19.9	19.1	56.5	51.5	17.8	16.8	35.1	33.5	8.7	8.2	85.8	82.3
Pr	5.6	5.5	2.3	2.2	6.2	5.7	1.9	1.8	4.5	4.3	1.	1	9.46	9.1
Nd	27.4	27.3	10	10	26.	23.7	8.4	7.9	20.9	19.9	5.6	5.3	42.4	40.6
Sm	5	5	2.4	2.3	4.9	4.5	2.4	2.3	4.8	4.5	1.	1	7.4	7.1
Eu	1.7	1.7	0.9	0.9	1.6	1.5	0.8	0.7	1.6	1.6	0.9	0.9	2.98	2.9
Gd	4.7	4.7	2.2	2.1	4.8	4.3	1.6	1.5	4.6	4.4	1.3	1.2	7.	6.7
Tb	0.7	0.7	0.4	0.3	0.6	0.6	0.4	0.4	0.7	0.6	0.3	0.2	0.9	0.9
Dy	3.2	3.2	2.9	2.8	3.6	3.3	4.	3.8	3.8	3.6	2.8	2.6	5.5	5.3
Yb	1.5	1.5	1.9	1.8	1.4	1.3	1.8	1.7	1.7	1.6	2.	1.9	2.2	2.1
Lu	bdl	bdl	bdl	bdl	bdl	bdl	bdl	bdl	bdl	bdl	bdl	bdl	bdl	bdl
Hf	2.8	2.8	1.3	1.2	2.4	2.2	bdl	bdl	2.6	2.4	bdl	bdl	5.1	4.9
Ta	0.8	0.8	bdl	bdl	1.	0.9	0.6	0.6	0.7	0.7	bdl	bdl	2.9	2.8
Pb	16.2	16.1	5.4	5.2	13.2	12.1	3.8	3.6	8.4	8	1.99	1.9	13.23	12.7
Th	6.2	6.2	1.8	1.8	6.1	5.6	2.	1.9	3.7	3.5	0.26	0.2	9.82	9.4
U	bdl	bdl	bdl	bdl	1.7	1.5	0.38	0.36	1.1	1.1	0.11	0.1	2.29	2.2
CO ₂	642	640	107	102	296	270	128	121	685	653	79	75	700	672
H ₂ O	1.29	1.29	1.10	1.06	1.30	1.18	1.40	1.32	1.21	1.15	1.14	1.09	1.32	1.27
F	1396	1391	1119	1076	1150	1048	1357	1280	991	944	1345	1276	1265	1213
S	1037	1034	293	282	980	893	309	292	1285	1224	35	33	1591	1526
Cl	1984	1978	746	717	1504	1371	323	305	1739	1656	93	88	1724	1653
X _{ol} %		0.9		3.9		9.0		5.9		4.7		5.2		4.5

Mg# = 100x(Mg/Mg + Fe²⁺); Fo = forsterite in mole % of olivine.

bdl = below detection limit.

X_{ol} = percentage of olivine crystallized on the wall of MI after trapping.

Major and minor elements and H₂O are in wt% all others in ppm.

Table 4b. Representative major, minor and trace element and volatile content of MI from samples RESC4 and RESC5.

Sample MI ID	uncorrected	corrected	uncorrected	corrected	uncorrected	corrected	uncorrected	corrected	uncorrected	corrected	uncorrected	corrected	uncorrected	corrected
	RESC4 O2-MA	RESC4 O2-MA	RESC4 O9-MA	RESC4 O9-MA	RESC4 O9-MD	RESC4 O9-MD	RESC5 O21-MA	RESC5 O21-MA	RESC5 O21-ME	RESC5 O21-ME	RESC5 O28-MA	RESC5 O28-MA	RESC5 O8-MA	RESC5 O8-MA
type	Normal MI	Normal MI	Normal MI	Normal MI	Enriched MI	Enriched MI	Normal MI	Normal MI	Normal MI	Normal MI	Sr-rich MI	Sr-rich MI	Enriched MI	Enriched MI
SiO ₂	48.16	49.81	47.36	49.48	47.85	49.53	48.51	50.59	48.81	50.89	47.70	49.27	47.67	48.44
TiO ₂	1.18	1.21	1.00	1.02	1.30	1.30	1.42	1.42	1.39	1.39	1.13	1.10	2.43	2.22
Al ₂ O ₃	17.48	17.97	17.56	17.86	18.22	18.15	16.91	16.85	16.63	16.63	17.25	16.73	14.83	13.56
Fe ₂ O ₃	8.14	1.11	7.86	1.11	7.72	1.11	7.93	1.11	7.87	1.11	6.00	7.01	4.83	1.11
FeO		7.01	7.00	7.00	7.01	7.01	7.01	7.01	7.02	7.02	7.01	7.01	7.01	7.00
MnO	0.18	0.19	0.18	0.18	0.20	0.20	0.11	0.11	0.07	0.07	0.12	0.12	0.14	0.13
MgO	4.89	5.63	4.24	6.06	3.76	6.07	3.26	6.23	3.53	6.25	4.76	7.44	5.97	9.97
CaO	9.28	9.54	10.83	11.02	10.57	10.53	11.50	11.46	11.43	11.43	11.54	11.19	12.81	11.71
Na ₂ O	2.52	2.59	2.26	2.30	2.38	2.37	2.60	2.60	2.63	2.63	2.79	2.71	2.36	2.16
K ₂ O	4.11	4.23	3.27	3.33	3.19	3.18	2.18	2.17	2.12	2.12	2.75	2.67	2.51	2.29
P ₂ O ₅	0.70	0.72	0.62	0.63	0.55	0.55	0.44	0.44	0.47	0.47	0.59	0.57	1.52	1.39
Fo		83		84		84		84		84		87		90
Mg#		64		65		64		62		64		65		66
Be	bdl	bdl	4.6	4.5	bdl	bdl	bdl	bdl	bdl	bdl	4	3.7	9	7.8
B	15.4	15.3	19.6	19	bdl	bdl	bdl	bdl	bdl	bdl	bdl	bdl	12.2	10.6
V	211	210	178	172	243	232	213	201	175	166	250	230	210	183
Rb	144	143	127	123	129	123	70.2	66.5	72.9	69.3	82.1	75.5	76.4	66.4
Sr	713.6	710	594	575	954.9	912	608	575	478.3	455	1135	1044	553	481
Y	16.2	16.1	17.2	16.7	24.1	23	26.7	25.3	21.10	20.1	19.6	18	23.4	20.4
Zr	111	110	110.4	107	149	142	124	117	105	99.8	109	101	161	140
Nb	20.6	20.5	17.5	16.9	21.4	20.4	19.2	18.2	14.5	13.8	21.6	19.9	14.5	12.6
Cs	10.7	10.6	6.2	6.0	634	606	n.a.	bdl	3.0	2.9	3.7	3.4	n.a.	bdl
Ba	1183	1176	953	924	1188	1135	724	685	571	542	951	874	820	713
La	29.8	29.6	25.4	24.7	33.4	31.9	18.8	17.8	17.7	16.8	28.5	26.2	25.5	22.2
Ce	64.2	63.8	53.2	51.6	72.6	69.3	50.	47.3	34.8	33.1	61.	56.1	57.7	50.2
Pr	7.5	7.5	6.3	6.1	8.9	8.5	6.9	6.6	4.3	4	7.4	6.8	7.6	6.6
Nd	31.	30.8	27.3	26.5	27.	25.8	35.2	33.3	20.2	19.2	33.2	30.5	32.6	28.4
Sm	6.3	6.3	5.5	5.3	13.9	13.2	13.1	12.4	4.5	4.3	4.6	4.2	7.	6.1
Eu	2.1	2.1	1.5	1.4	2.1	2	1.4	1.3	1.8	1.7	1.9	1.7	2.3	2
Gd	5.7	5.6	4.9	4.8	8.9	8.5	9.	8.5	6.9	6.6	4.8	4.4	6.	5.2
Tb	0.6	0.6	0.7	0.7	1.8	1.7	1.1	1.1	0.7	0.7	0.6	0.6	1.	0.9
Dy	3.5	3.5	3.5	3.4	bdl	bdl	4.9	4.6	4.3	4.1	3.5	3.2	5.4	4.7
Yb	1.5	1.4	1.4	1.4	2.8	2.6	2.1	2	2.	1.9	2.	1.8	2.3	2
Lu	bdl	bdl	0.6	0.6	bdl	bdl	0.3	0.3						
Hf	2.6	2.6	2.3	2.2	bdl	bdl	bdl	bdl	1.9	1.8	2.6	2.4	2.9	2.5
Ta	1.	1	0.8	0.8	1.7	1.6	0.4	0.4	0.8	0.8	1.2	1.1	0.7	0.6
Pb	16.3	16.3	15.	14.5	17.	16.2	9.9	9.4	8.9	8.5	9.5	8.7	10.	8.7
Th	6.8	6.8	6.1	5.9	8.7	8.3	4.4	4.2	4.2	4	5.1	4.7	4.6	4
U	2.4	2.4	2.1	2	2.3	2.2	1.9	1.8	1.	1	1.3	1.2	1.5	1.3
CO ₂	145	145	424	411	533	509	1185	1121	914	869	216	198	175	152
H ₂ O	1.10	1.09	1.26	1.22	1.44	1.38	1.33	1.26	1.33	1.26	1.37	1.26	1.47	1.28
F	1250	1243	1720	1668	1761	1682	1393	1318	1272	1208	1166	1072	1887	1641
S	1442	1434	1475	1430	1706	1629	1344	1272	1342	1276	987	907	793	690
Cl	2660	2646	2872	2784	3104	2964	1905	1803	1870	1778	1293	1188	1278	1112
X _{ol} %		0.8		3.4		4.9		6.0		5.5		8.1		13.6

Mg# = 100x(Mg/Mg + Fe²⁺); Fo = forsterite in mole % of olivine.

bdl = below detection limit. n.a. = not available.

X_{ol} = percentage of olivine crystallized on the wall of MI after trapping.

Major and minor elements and H₂O are in wt% all others in ppm.

Table 5. Parameters used to calculate total CO₂ contained in a bubble-bearing MI (RESC2-O26-M3).

	<i>parameter</i>	<i>measured value</i>
Raman spectrum	Peak 1 (cm ⁻¹)	1284.33
	Peak 2 (cm ⁻¹)	1387.21
	Δ (cm ⁻¹)	102.88
Vapor bubble	Vapor density (g/cm ³) ¹	1.67 x 10 ⁻¹
	Bubble diameter (cm)	4.00 x 10 ⁻³
	Vapor volume. (cm ³) ²	3.35 x 10 ⁻⁸
	CO ₂ mass (g)	5.60 x 10 ⁻⁹
Melt/Glass	Inclusion. diameter (cm)	1.50 x 10 ⁻²
	Inclusion volume (cm ³) ²	1.77 x 10 ⁻⁶
	Melt/Glass volume (cm ³) ³	1.73 x 10 ⁻⁶
	Melt/Glass density (g/cm ³)	2.75
	Melt/Glass mass (g)	4.77 x 10 ⁻⁶
	Inclusion mass ⁵ (g)	4.77 x 10 ⁻⁶
	Bubble volume percent	1.90%
CO ₂ contents	CO₂ melt (ppm)⁵	650
	CO₂ in the MI (melt + vapor) (ppm)	1822

The CO₂ density in the vapor bubble was determined from Raman spectroscopic analysis. It should be noted that the CO₂ concentration dissolved in the melt (glass) is only the 36% of the total CO₂ in the MI, and the bubble accounts for 64% of the total CO₂ in the MI (table modified from Steele-MacInnis et al., 2011).

¹ Estimated using the equation of Kawakami et al. (2003).

² Volumes estimated from the MI/bubble diameters assuming spherical geometry.

³ Melt or glass volume = inclusion volume – vapor volume

⁴ Inclusion mass = melt/glass mass + vapor mass

⁵ Measured using SIMS.

Table 6. Settling times calculated for an olivine phenocryst in the Solchiaro magma.

Olivine liquidus temperature (°C) ^a	1114
Pressure (Mpa)	100
Oxidation state	NNO
viscosity (kg/ms) ^b	36
density melt (kg/m ³) ^c	2651
density olivine (kg/m ³)	3300
olivine diameter (mm)	3
Velocity (m/sec) ^d	4.7E-04
Chamber thickness (km) ^e	2
sinking time (days)	262

^a= Calculated using Ford et al. (1983) and Falloon and Danyushevsky (2000)

^b= Calculated from the Giordano et al. (2008)

^c= Calculated from Lange & Carmichael (1987)

^d= from Stoke's equation

^e= from Fig. 9 of this study

11. Figures

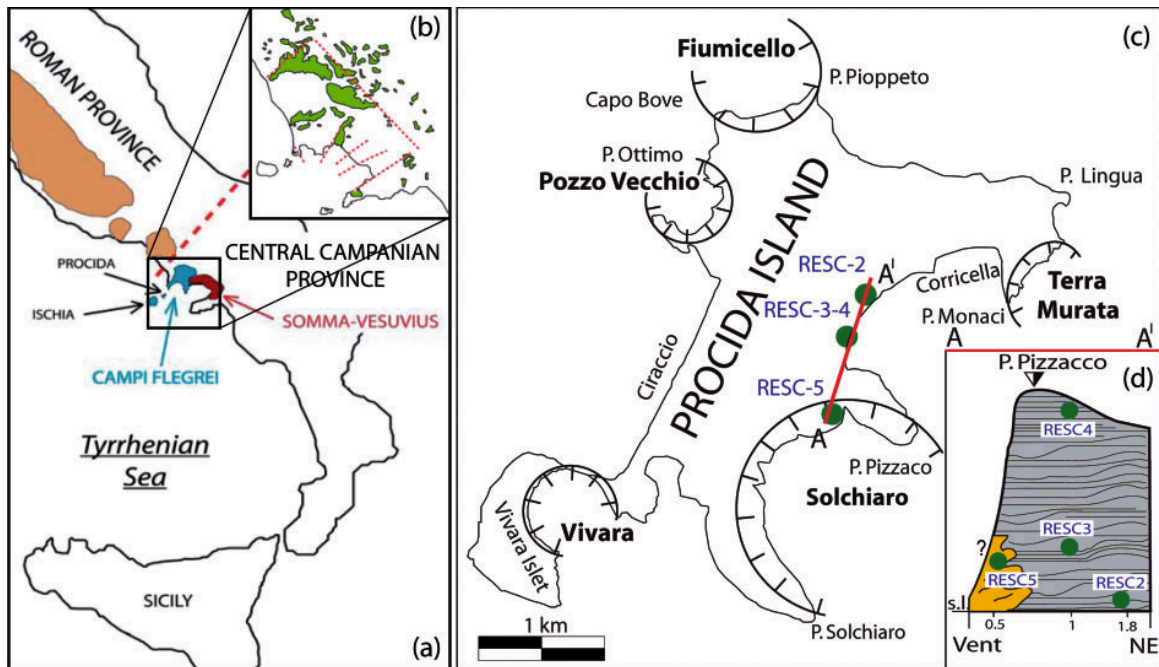


Fig. 1. a) Location of the Campi Flegrei area showing the distribution of volcanism in central-southern Italy (after Tonarini et al., 2004). The red dashed line represents the Ortona-Roccamonfina structural line separating the Roman magmatic province to the north and the Central Campanian magmatic province to the south. b) Map showing outcrops of the Campanian Ignimbrite (green areas) and the major faults in the Campanian Plain (red dotted lines) after De Vivo et al. (2001). c) Map of Procida Island showing the sample locations and the five volcanic vents that have been recognized on the island: Vivara, Terra Murata, Pozzo Vecchio, Fiumicello and Solchiaro (modified from De Astis et al., 2004). The green dots along the cross-section A-A' represent the sample locations shown in (d), with sample numbers listed beside each dot. d) Relative stratigraphic position of the samples in this study. The yellow area indicates the yellow tuff proximal facies and grey area represents the base surge deposits with both sand wave facies and plano-parallel facies. The chronostratigraphic correlation between sample RESC5 and the others is unknown.

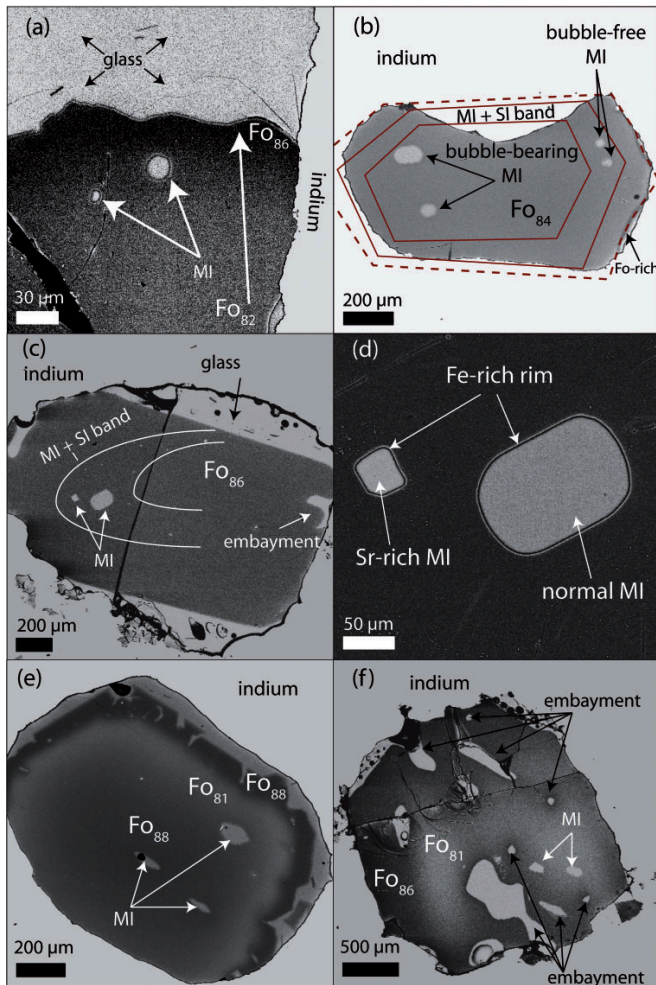


Fig. 2. Back-scattered electron images of olivine phenocrysts from the Solchiaro eruption. The light colored background on the right represents the indium in which the phenocrysts are mounted. A) Olivine (RESC2-O22) showing intense reverse zoning from Fo_{82} at the core to Fo_{86} at the rim. It should be noted that an Fe-rich rim is always present at the interface between olivine and glass. B) Olivine (RESC5-O21) showing 4 MI exposed at the surface. The dashed line is the crystal border (partially beneath the surface and covered by indium) and the two solid lines delimit the growth zone defined by MI and spinel inclusions (MI + SI; SI not exposed). Two bubble-free MI in the same growth zone (MIA) are exposed, as well as two bubble-bearing MI in the core of the crystal. A thin MgO-rich band in contact with the glass rim is visible on the right side of the image. C) Unzoned olivine (RESC3-O21) showing two MI and a band of MI plus spinel inclusions. D) Enlargement of the portion of the olivine in (C) that contains the one normal MI and one Sr-rich MI, both showing a rim of Fe-rich olivine at the olivine/MI interface. This feature has been interpreted to represent crystallization of olivine during quenching by Sobolev & Shimizu (1993). E) Olivine (RESC5-O13) showing oscillatory zoning and 3 MI exposed at the surface. Note the irregular olivine rim characteristic of dissolution/ recrystallization. F) Olivine (RESC3-O23) showing patchy zoning indicative of olivine re-equilibration with the surrounding melt. Note the presence of embayments (melt channels) that are surrounded by olivine with a composition of Fo_{86} . Two fully enclosed MI are exposed at the surface.

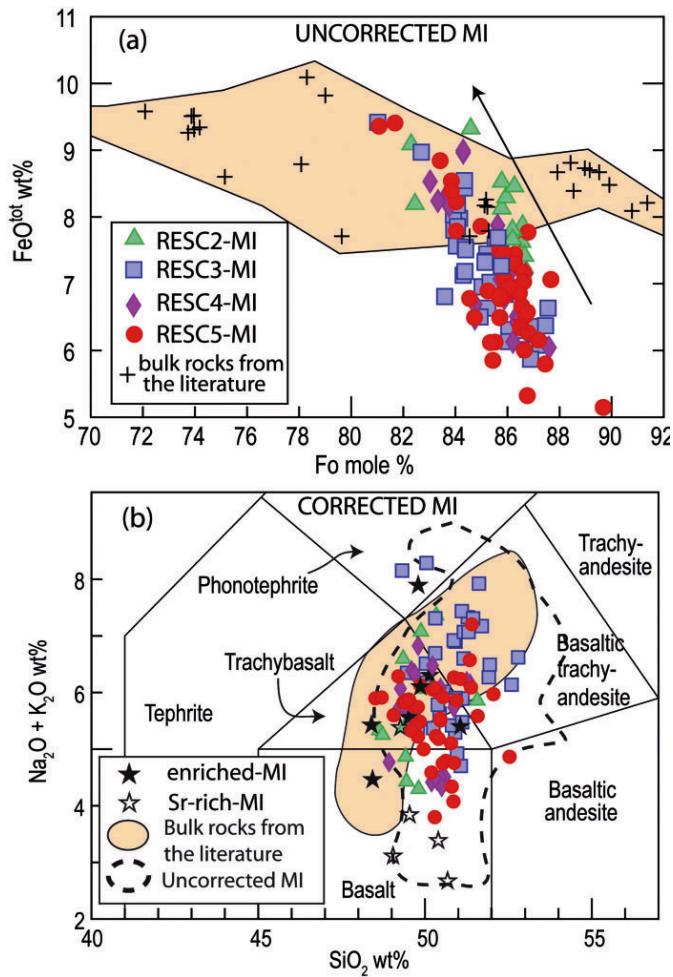


Fig. 3. Compositions of MI from Solchiaro. a) Fo mole % vs. uncorrected FeO^{tot} wt% of MI. The yellow background represents bulk rock compositions of Solchiaro scorias and lava lithics from the literature (Di Girolamo *et al.*, 1984; D'Antonio *et al.*, 1999; De Astis *et al.*, 2004). The bulk rock Fo mole% assumes that olivine was in equilibrium with the whole rock composition and was calculated using the equation of Ford *et al.* (1983) and assuming NNO oxidation state and f_{O_2} calculated using the equation of Borisov & Shapkin (1990). The arrow shows the trend in composition during crystallization assuming that all the MI had the same cooling rate, as suggested by Danyushevsky *et al.* (2002a). It should be noted that most of the MI show FeO depletion compared to bulk rock compositions. b) Rock type classification based on corrected MI compositions from Solchiaro (TAS diagram, Le Bas *et al.*, 1986). Also reported are the bulk rock compositions from the literature (yellow area; data from Di Girolamo *et al.*, 1984; D'Antonio *et al.* 1999; De Astis *et al.*, 2004) and the uncorrected MI field (field outlined by the dashed line). It should be noted that corrected and uncorrected MI compositions plot in the same fields. Most of the Sr-rich MI plot in the basalt field at lower alkalis relative to the other MI.

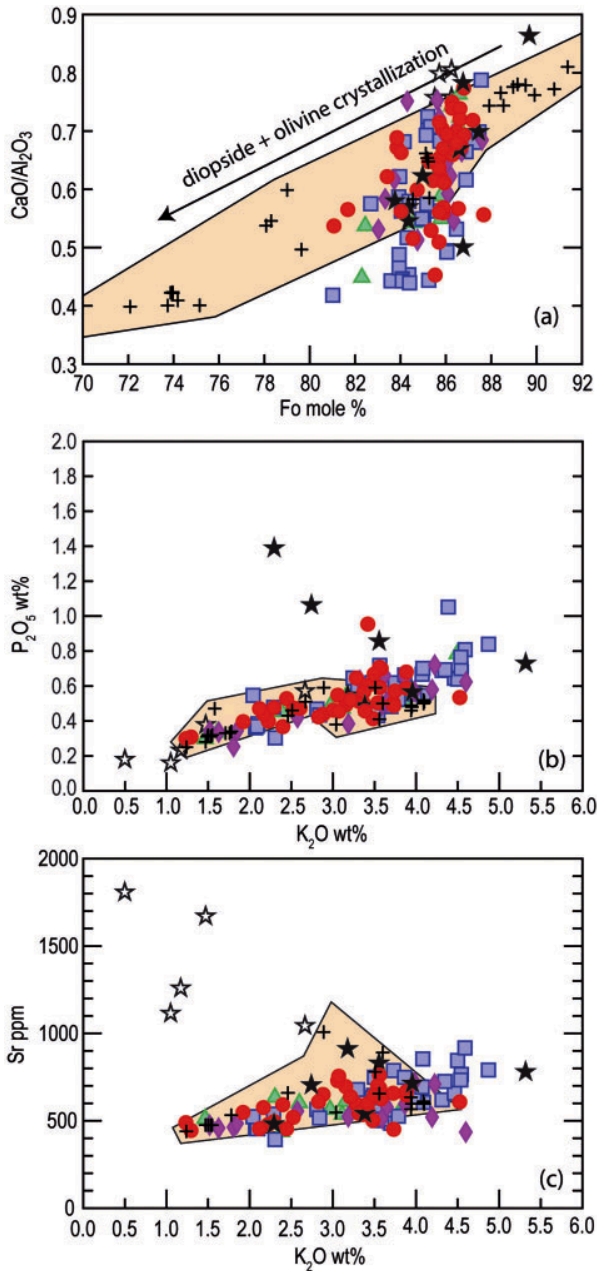


Fig. 4. Compositions of corrected MI. a) Fo mole % vs. CaO/Al₂O₃. Note that Sr-rich and enriched MI compositions are also shown. The arrow shows the trend in composition expected during crystallization of diopside and olivine. It should be noted that most of the normal and enriched MI plot within the compositional range for bulk rock, but that Sr-rich MI generally plot above (higher CaO/Al₂O₃) the bulk rock range. b) K₂O vs. P₂O₅. Note the larger range of MI composition relative to the bulk rocks from the literature (Di Girolamo *et al.*, 1984; D'Antonio *et al.*, 1999; De Astis *et al.*, 2004). Also, it is important to note that some of the enriched MI (black stars) plot far from the general trend. c) K₂O vs. Sr showing that Sr-rich MI plot outside of the trend of normal MI.

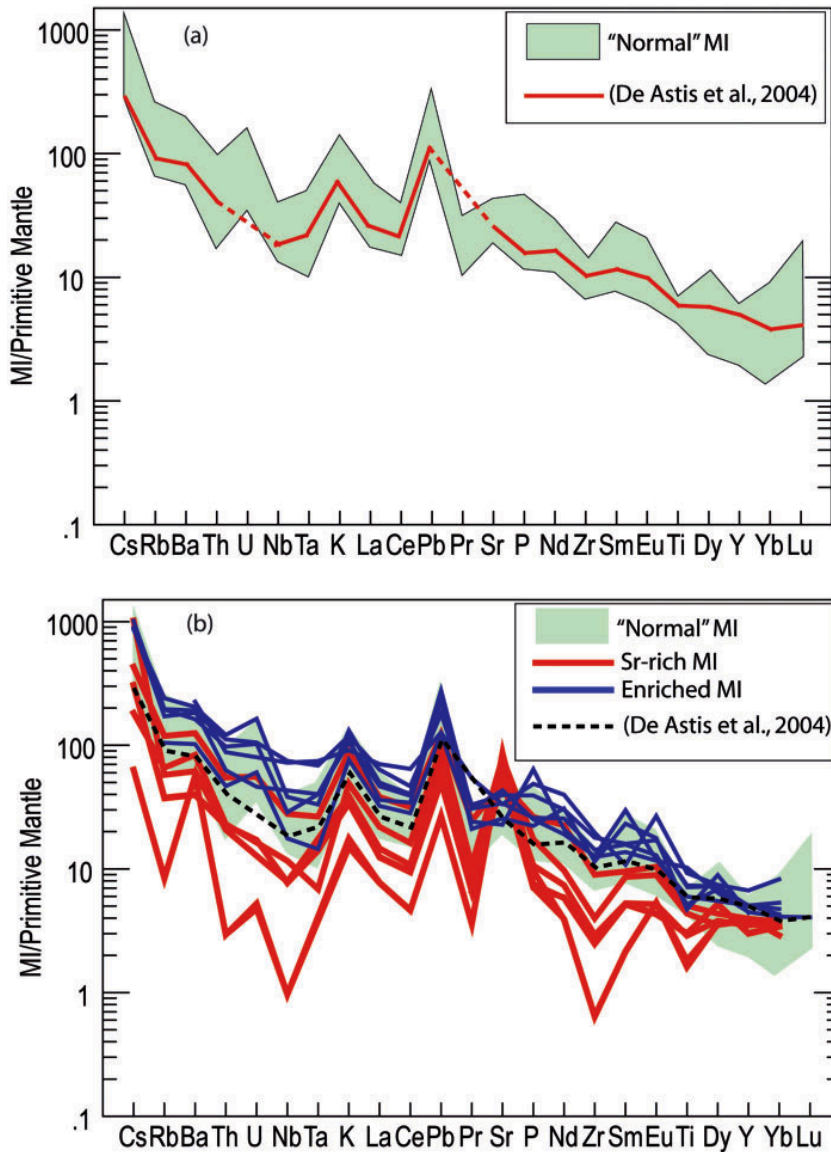


Fig. 5. Primitive mantle-normalized incompatible trace element abundances (Sun & McDonough, 1989) of MI from Solchiaro obtained in this study. a) Normal MI patterns compared to the most primitive bulk rock composition observed in the PVD from Solchiaro unit I (sample Pro 7/11 from De Astis *et al.*, 2004). Note that the normal MI distribution matches the bulk rock composition for Solchiaro Unit 1 from De Astis *et al.* (2004). b) Anomalous MI patterns compared with the normal MI pattern. Note the degree of depletion in some elements and the “saw-tooth” pattern displayed by Sr-rich MI (see text for discussion).

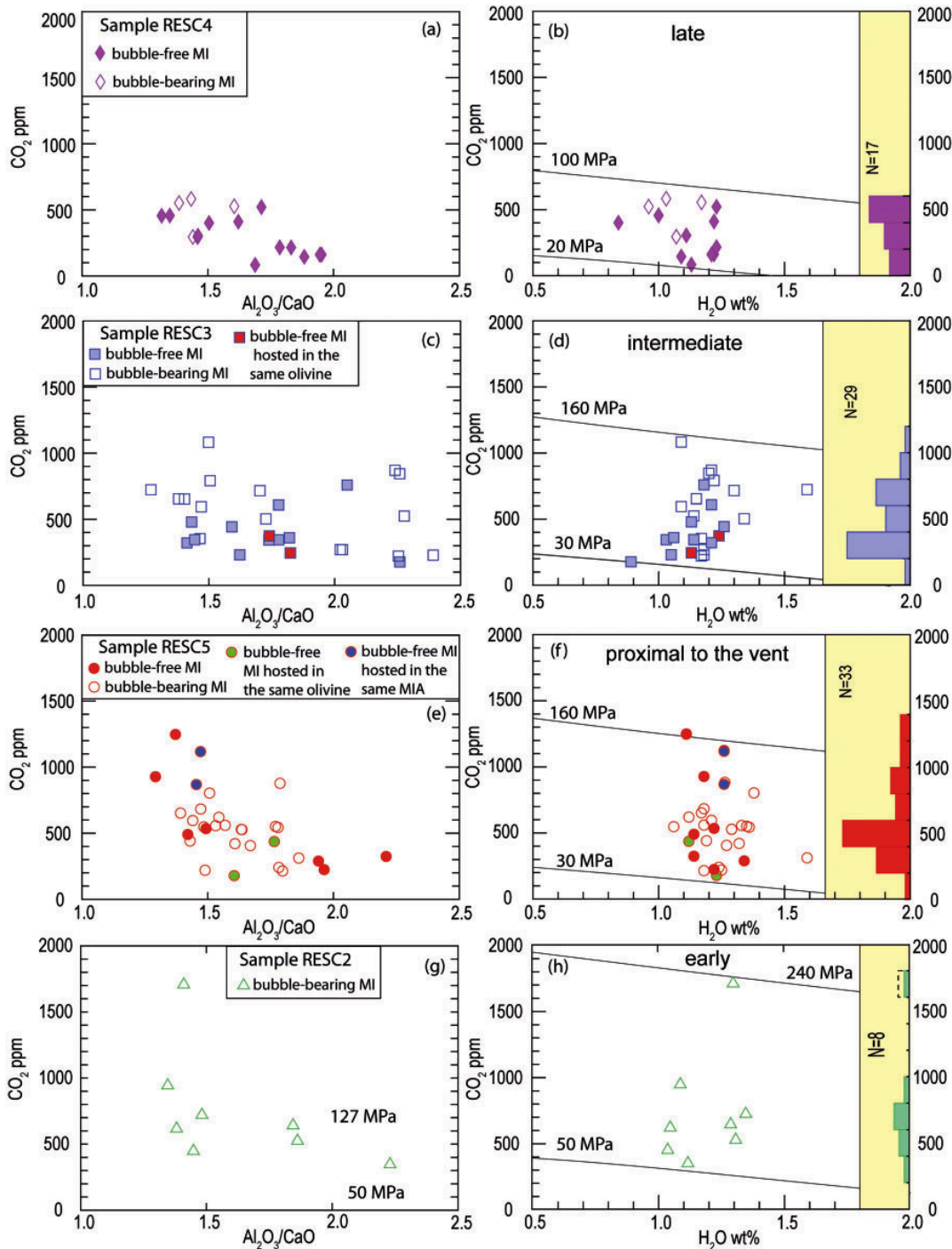


Fig. 6. Abundances of CO_2 vs. $\text{Al}_2\text{O}_3/\text{CaO}$ and CO_2 vs. H_2O of all studied MI, shown according to sample. Isobars (blue solid lines) were calculated using the model of Papale *et al.* (2006) assuming the average MI composition and $T=1200^\circ\text{C}$. Histograms along the right ordinate for each sample show the distribution in CO_2 . The dashed rectangle in the RESC2 histogram at ≈ 1800 ppm represents the estimated CO_2 content after adding back into the melt all of the CO_2 contained in the bubble of one bubble-bearing MI (see text and Table 5). It is important to note, especially for samples RESC2 and RESC4, the good correlation between fractionation and CO_2 concentrations.

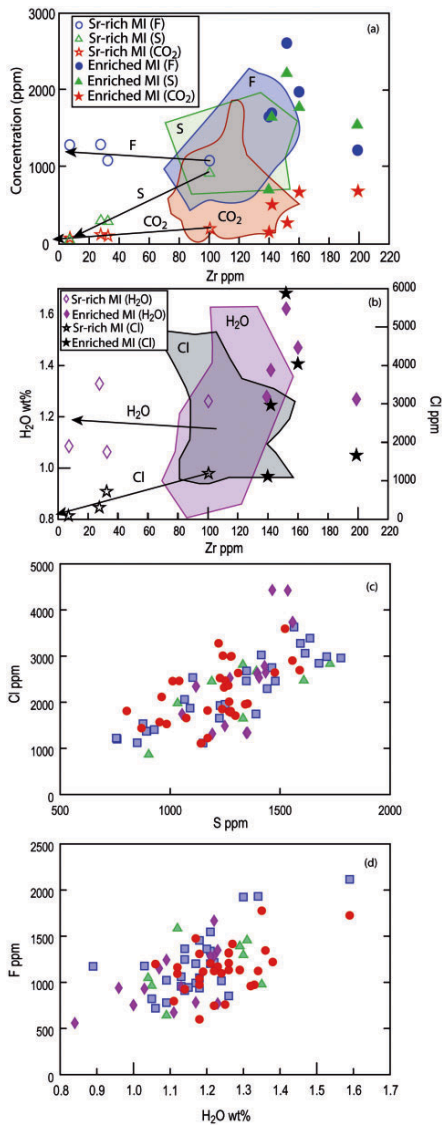


Fig.7. Compositions of anomalous MI hosted in olivine from Solchiaro compared to volatile abundances of normal MI. (a) Abundances of F (blue circles), S (green triangles) and CO₂ (red stars) vs. Zr concentration in anomalous MI. Open symbols are Sr-rich MI and filled symbols represent enriched MI (see text for definitions). Ranges in concentrations of F (blue field), S (green field), and CO₂ (red field) of “normal” MI are indicated by the colored areas. (b) Concentrations of H₂O (pink diamonds) and Cl (black stars) vs. Zr in anomalous MI. Open symbols are Sr-rich MI and filled symbols are enriched MI. Ranges in concentrations of H₂O (pink field) and Cl (grey field) of “normal” MI are shown by the colored areas. Arrows on (a) and (b) are “eyeball” fits through the data for the anomalous MI and suggest dilution of the normal Solchiaro melt by plagioclase. It should be noted that arrows corresponding to Cl, S, and CO₂ project through the origin and that H₂O and F abundances in anomalous MI are not depleted relative to the normal MI (see text for further discussion). (c) Abundances of Cl vs S concentration of normal MI, and (d) concentrations of F vs concentrations of H₂O. For panels (c) and (d), symbols are as in Fig. 3b.

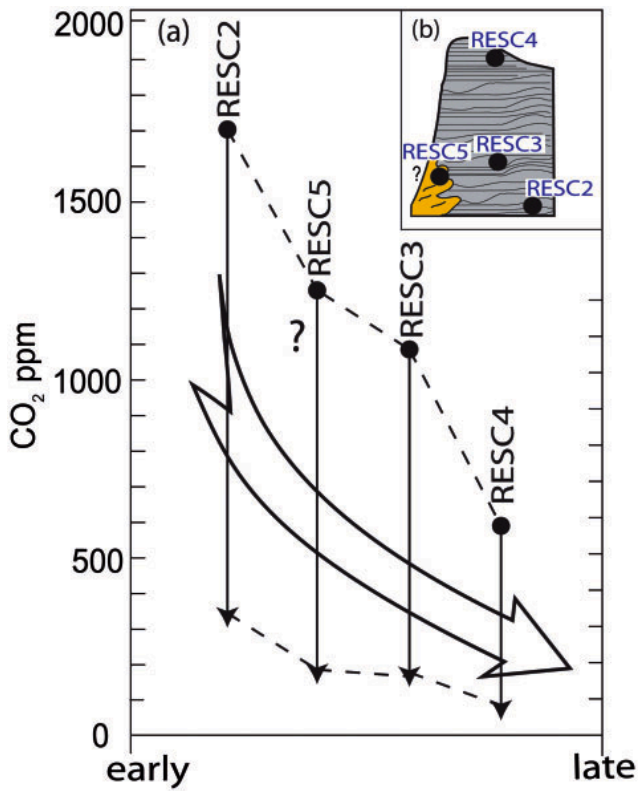


Fig. 8. a) Variation in CO₂ abundances with eruptive time in normal MI. b) Relative stratigraphic position of the Solchiaro samples. The question mark represents the unknown stratigraphic correlation between RESC5 and the other Solchiaro samples. Note that from the earlier to the later sample the CO₂ contents span a shorter range and the maximum and minimum CO₂ contents both decrease with time. The arrow shows the trend from early to late eruptions.

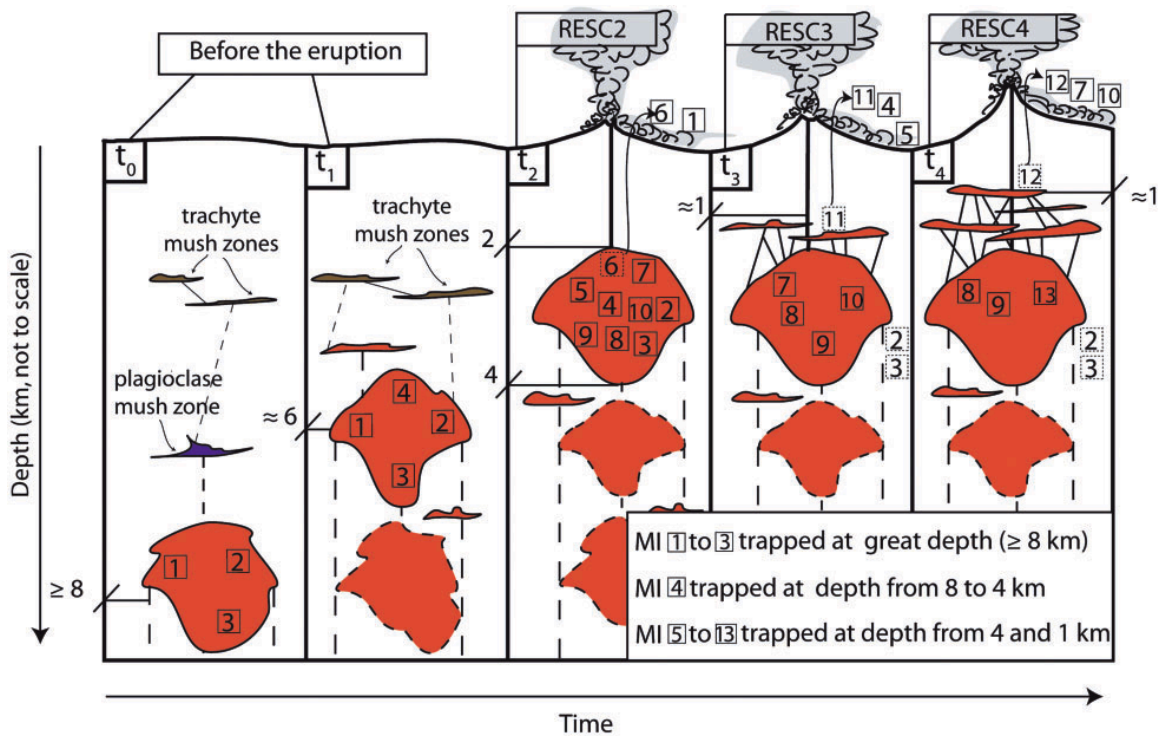


Fig. 9. Schematic representation of the dynamic evolution of the Solchiaro magmatic system showing where (when) in the overall evolution different MI were trapped and erupted to the surface. The numbered squares represent MI trapped in olivine phenocrysts. MI from 1 to 3 were trapped at depths of ≥ 8 km. MI 4 was trapped at a depth between 8 and 4 km, and MI 5 to 12 were trapped at depths between 4 and 1 km. The dashed squares represent MI (and host olivines) that were removed from the melt as the phenocrysts settled to form a cumulate (MI 2 and 3), or MI that were formed at shallow depth and ejected from the magma chamber shortly after they formed (MI 6, 11 and 12). The temporal evolution of the Solchiaro magma is summarized as follows: at t_0 , the volatile-saturated Solchiaro magma body started to crystallize at ≥ 8 km and began to ascend through the crust. The Solchiaro magma continuously crystallized during ascent, trapping MI along the way (t_1) until it ponded at 2 km depth, which represents the shallowest depth recorded by MI from sample RESC2 that erupted at time t_2 . Following the eruption of sample RESC2 at time t_2 , the magma body continued to ascend through the crust to a depth of about 1 km and sample RESC3 was erupted at time t_3 . At t_4 , the magma body ascended at shallower depth (< 1 km), and the latest sample (RESC4) was erupted.

CHAPTER 4

Esposito, R., Bodnar, R.J., Klebesz. R., Bartoli. O., Klyukin, Y.I., Moncada D. & Doherty A. L. (*accepted*). Application of the Linkam TS1400XY heating stage to melt inclusion studies. *Central European Journal of Geosciences*, Vol. 4(2), pg 208-218, DOI: 10.2478/s13533-011-0054-y.

Application of the Linkam TS1400XY heating stage to melt inclusion studies

R. Esposito^a, R. Klebesz^{a, b}, O. Bartoli^c, Y. I. Klyukin^d, D. Moncada^a, A. L. Doherty^{a, b, e} and R. J. Bodnar^a

^a Virginia Polytechnic Institute & State University, Department of Geosciences, Blacksburg, 24061, VA, USA

^b Università di Napoli Federico II, Dipartimento di Scienze della Terra, Naples, 80138, Italy

^c Università degli Studi di Parma, Dipartimento di Scienze della Terra, Parma, 43100, Italy

^d Institute of Geology and Geochemistry of Urals Branch, Russian Academy of Sciences, Yekaterinburg, Russia

^e Università degli Studi di Messina, Dipartimento degli Alimenti e dell'Ambiente, Messina, 98166, Italy

Abstract

Melt inclusions (MI) trapped in igneous phenocrysts provide one of the best tools available for characterizing magmatic processes. Some MI experience post-entrapment modifications, including crystallization of material on the walls, formation of a vapor bubble containing volatiles originally dissolved in the melt, or partial to complete crystallization of the melt. In these cases, laboratory heating may be necessary to return the MI to its original homogeneous melt state, followed by rapid quenching of the melt to produce a homogeneous glass phase, before microanalyses can be undertaken.

Here we describe a series of heating experiments that have been performed on crystallized MI hosted in olivine, clinopyroxene and quartz phenocrysts, using the Linkam TS1400XY microscope heating stage. During the experiments, we have recorded the melting behaviors of the MI up to a maximum temperature of 1360°C. In most of the experiments, the MI were homogenized completely (without crystals or bubbles) and remained homogeneous during quenching to room temperature. The resulting single phase MI contained a homogeneous glass phase. These tests demonstrate the applicability of the Linkam TS1400XY microscope heating stage to homogenize and quench MI to produce homogeneous glasses that can be analyzed with various techniques such as Electron Microprobe (EMP), Secondary Ion Mass Spectrometric (SIMS), Laser ablation Inductively Coupled Plasma Mass Spectrometry (LA ICP-MS), Raman spectroscopy, FTIR spectroscopy, etc.

During heating experiments, the optical quality varied greatly between samples and was a function of not only the temperature of observation, but also on the amount of matrix glass attached to the phenocryst, the presence of other MI in the sample which are connected to the outside of the crystal, and the existence of mineral inclusions in the host.

Key words: microscope heating stage, melt inclusion, microthermometry, volatiles

1. Introduction

Melt inclusions provide perhaps the most direct method to study magmatic processes and the evolution of magmatic systems (Metrich *et al.*, 2008, Sobolev *et al.*, 2011), and the number of publications that mention melt inclusions has increased dramatically in recent years (De Vivo, 2003). In fact, the only direct way to determine the volatile content of the melt in a magma body before an eruption is by measuring the volatile contents in MI. It is widely accepted that the concentration of volatiles (H₂O, CO₂, SO₂, etc.) in a magma chamber beneath a volcano determines the magnitude and style of the volcanic eruption, and many studies have focused on measurement of the volatiles in MI (Helo *et al.*, 2011, Metrich *et al.*, 2008). These analyses assume that the MI represents the quenched melt that was trapped at magmatic conditions and has undergone no changes during cooling. Depending on the MI pressure-temperature path before and during natural quenching (Danyushevsky *et al.*, 2002, Lowenstern, 1995, Roedder, 1979, Sobolev & Kostyuk, 1976), the MI may partially or totally crystallize, and/or some of the volatiles that were originally dissolved in the melt may exsolve during cooling to form a vapor bubble. Some volatiles may also diffuse out of the MI

following trapping, but this process is beyond the scope of this study and is not discussed further.

Depending on the type of information sought and the analytical technique to be used (e.g., electron microprobe analysis, EMO, or secondary ion mass spectrometry, SIMS), it may be necessary to re-homogenize the MI before analysis in order to obtain compositional data that are representative of the melt at the time of trapping. Various techniques have been used to successfully homogenize melt inclusions, including heating in one-atmosphere furnaces (Fedele *et al.*, 2003, Nielsen *et al.*, 1995, Sinton *et al.*, 1993, Student & Bodnar, 1999), heating in high-pressure (cold-seal or internally-heated) vessels (Anderson *et al.*, 2000, Skirius *et al.*, 1990, Student & Bodnar, 2004, Thomas *et al.*, 2003), heating in piston cylinder apparatus (Bartoli *et al.*, 2011, Cesare *et al.*, 2011, Ferrero *et al.*, in press), and heating in a microscope-mounted high temperature stage (Clocchiatti, 1975, Fedele *et al.*, 2003, Frezzotti, 1992, Lowenstern, 1994, Reyf, 1997, Sobolev & Kostyuk, 1976). Each of these techniques has advantages and disadvantages, as described by (Bodnar & Student, 2006, Student & Bodnar, 2004).

One of the major advantages of using a microscope-mounted heating stage to homogenize MI is that the MI can be observed continuously during heating from room temperature to homogenization. This approach allows information such as the temperature of first melting and the temperatures (and order) of disappearance of various phases to be observed and measured (Fig. 1 in (Student & Bodnar, 2004)), and prevents overheating of the MI because heating can be stopped at the moment of homogenization. Importantly, homogenization of the MI using a microscope mounted heating stage allows workers to determine if phases present after quenching represent phases that were still present at the highest temperature to which the MI were heated, or if they represent phases that nucleated from the melt during quenching. This information is critical to understanding whether or not the MI trapped a single melt phase, and if heating rates were sufficiently slow to maintain equilibrium between the phases in the MI, and if quenching rates were sufficiently fast to prevent new phases (crystals and vapor bubbles) from nucleating during cooling. As described in (Roedder, 1979, Schiano, 2003, Sobolev & Kostyuk, 1976), in order to rehomogenize the melt to obtain the original volatile content of MI, many researchers have used a heating stage with a rapid quenching system mounted on an optical microscope (e.g. the Vernadsky stage, (Sobolev *et al.*, 1980)). Some earlier high temperature stages, such as the Linkam TH1500 that was the precursor model to the stage described here, offered only a relatively slow cooling by turning off power to the heater. In this and similar stages, it was often not possible to quench the MI without significant crystallization on the walls, or without crystallizing daughter minerals or nucleating a vapor bubble in the inclusion.

In this study, several experiments have been performed using the new Linkam TS1400XY heating stage to assess its applicability for homogenizing MI, followed by quenching the homogeneous melt to a glass, and examine the optical viewing quality at elevated temperature. Samples studied are from the Toba Tuff eruption (Sumatra), from the Solchiaro eruption on the Island of Procida (Southern Italy), and from the Sarno eruption at Monte Somma-Vesuvius (Southern Italy). The geology and petrologic characteristics of the Toba Tuff (Beddoe-Stephens *et al.*, 1983, Chesner, 1998, Newman & Chesner, 1989), Solchiaro eruption (Esposito *et al.*, 2011 and references therein) and the Sarno eruption (Bertagnini *et al.*, 1998, Landi *et al.*, 1999) have been

described previously, and the interested reader is referred to these sources for additional information.

The three samples used for this study were gently crushed using a wooden pestle to avoid damaging phenocrysts and crystals were selected and mounted on glass bars and polished using the method described by (Thomas & Bodnar, 2002). Quartz phenocrysts were selected from pumice fragments of the Toba Tuff deposits, olivine and clinopyroxene phenocrysts were extracted from scoria ejected from the Solchiaro volcano, and finally clinopyroxene crystal were selected from nodules of the Sarno eruption. Only crystals containing partially or totally recrystallized MI were selected.

2. Description of the hardware and analytical conditions

The Linkam TS1400XY heating stage (Fig. 1a, c) consists of a platinum winding encased in ceramic (Fig. 1b) to produce a tube furnace that is large enough to accommodate 5 mm x 5 mm samples with a thickness of up to ≈ 0.5 mm. If inert gas is not circulated through the furnace during heating, the highest temperature achievable is 1400°C; however, we highly recommend that inert gas is circulated through the furnace during operation, especially for iron-bearing host phases, as described below.

The temperature inside the furnace of the Linkam TS1400XY stage is controlled by the T95-LinkPad system controller that includes a touch-screen controller, which can be operated with either a stylus or using one's fingers (Fig. 1d). With this digital controller, the temperature can be regulated manually, similar to other microscope-mounted heating stages, but can also be programmed before each experiment with a known and constant heating rate. Ramps can also be programmed, whereby the sample is held at a temperature for some period of time before heating is continued, as was described by (Student & Bodnar, 1999). During heating experiments, a constant flow of an inert gas is usually introduced into the heating stage to prevent oxidation of the analyzed sample (Bodnar & Student, 2006). If He is circulated through the furnace to avoid oxidation of the sample at high temperature, the highest temperature reached during heating experiments was 1260°C. If Ar is circulated through the stage instead of He, the highest temperature achieved during heating experiments was 1360°C. In this study, we used argon gas at a flow rate of $0.5 \pm 5\%$ liter/min to prevent oxidation. With these conditions, even though we programmed the stage to go to a temperature higher than 1360°C, the temperature "plateaued" at $\approx 1360^\circ\text{C}$. Before each experiment, the heating stage was calibrated using the melting temperatures of NaCl (801°C) and Au (1064.2°C). The difference between the known melting temperatures of the calibration standards and the measured temperature was always $< 10^\circ\text{C}$.

Samples are placed on a sapphire plate that is mechanically connected to a metal frame that allows the sample to be moved into and out of the furnace (see Fig. 1b). Once the sample is inserted into the ceramic tube furnace, the sapphire plate can be moved ≈ 6 mm in the X and Y directions to locate and monitor inclusions during heating. The earlier version of this stage, the Linkam TH1500, did not permit the sample to be moved in the X and Y directions after the lid was placed onto the stage. The Linkam TS1400XY heating stage is provided with a spring mechanism connected to the sapphire slide (Fig. 1a, 1c). The spring mechanism allows the user to remove the crystal from the ceramic furnace rapidly to quench the MI after homogenization is

achieved. When the sample is removed from the furnace using this technique, it is placed on top of a water cooled metallic platform that reduces the sample temperature to a few hundred degrees in a few seconds. The quench rate with the Linkam TS1400XY stage was determined to be $\approx 240^{\circ}\text{C/s}$ from 1400 to 800°C, and $\approx 230^{\circ}\text{C/s}$ from 1400 to 600°C, based on numerous quenching tests. This quench rate is slower than that reported for the Vernadsky stage (1-2 seconds to quench from as high as 1500°C to room temperature (Sobolev *et al.*, 1980)), but was fast enough to quench the MI tested in this study. The heating rates that can be accommodated by the Linkam TS1400XY range from 1 to 200°C/min.

Various workers use different heating rates and protocols (continuous versus stepped heating) to homogenize silicate melt inclusions, and it does not appear that any single rate or method is applicable to all MI in all different host phases. The method that is most appropriate for a given set of MI should be established based on kinetic experiments (Danyushevsky *et al.*, 2002) that consist of heating (followed by cooling) the same MI at different heating rates (from faster to slower), and recording the homogenization temperature for each heating rate. As reported in Fig. 2 by (Danyushevsky *et al.*, 2002), in kinetic experiments, the homogenization temperature decreases as the heating rate decreases until, eventually, the homogenization temperature approaches a constant value, even though the heating rate decreases. For each host phase, the “correct” heating rate is that which corresponds to the heating rate at which the homogenization temperature becomes constant. When faster heating rates are used, the recorded homogenization temperature will be higher compared to the homogenization temperature determined with slower heating rates. However, when slower heating rates are used, the likelihood that the MI composition will be modified by diffusion of components into or out of the MI increases (Bodnar & Student, 2006). A complete discussion of procedure to determine the “correct” heating rates and homogenization temperatures is beyond the scope of this study, and the reader is referred to (Danyushevsky *et al.*, 2002, Student & Bodnar, 1999). We did not perform kinetic experiments on the MI in this study because the goal of this study was not to determine the “correct” homogenization temperature but, rather, to examine the behavior of MI during heating to produce a homogeneous melt phase, and to determine if the homogenized MI could be quenched quickly enough to maintain a homogeneous melt (glass) to ambient conditions, without the formation of a vapor bubble or crystals. The heating schedules used for heating experiments on crystals from the samples studied are reported in Table 1. It should be noted that the heating rates used in this study (Table 1) are comparable to heating rates used by other workers (1 to 3 °C/min near the homogenization temperature in (Sobolev *et al.*, 1988, Student & Bodnar, 1999, Thomas *et al.*, 2003)). In some cases, after homogenization, the temperature was held constant for about 10 minutes to photograph the MI before quenching.

For the experiments described here, the Linkam TS1400XY was mounted on an Olympus BX60 petrographic microscope and 10X and 40X objective lenses were used for viewing and photographing the inclusions.

3. Results

In most of the experiments described here, it was possible to completely homogenize the MI and, importantly, to quench the melt to a homogeneous glass after homogenization (Figs. 2-5). A few of the MI could not be heated to homogenization either because the optics deteriorated before homogenization was achieved or, in one case, because the crystals began to fracture and break into smaller pieces owing to the high internal pressures generated in the volatile-rich MI during heating. For such samples, it is necessary to heat the MI in a pressurized vessel to eliminate or minimize decrepitation and/or leakage (Bodnar & Student, 2006, Severs *et al.*, 2007, Skirius *et al.*, 1990, Student & Bodnar, 2004).

In experiments performed on crystallized MI in quartz from the Toba Tuff in Sumatra, it was always possible completely homogenize and quench the MI to a bubble-free, homogeneous glass (Fig. 2). More importantly, during the heating experiment, the MI behavior was easy to monitor because the viewing optics remained very good up to the highest temperature required for homogenization ($< 1000^{\circ}\text{C}$) (Fig. 2). The behavior of the MI in quartz from the Toba Tuff is expected to be characteristic of MI in quartz from most environments, based on the cumulative experiences of the investigators in this study.

MI in olivine and clinopyroxene from the Solchiaro eruption on Procida Island (Southern Italy) commonly contain one or more solid phases as well as one or more vapor bubbles. These MI homogenized between 1060 and 1340°C . A range in temperatures could be related to several factors. It is well known that there is a positive correlation between the size of the MI and the temperature of homogenization, because the larger the inclusion the greater the energy necessary to melt the crystal around the MI [7]. However, in these experiments there was no correlation between the size of MI and the temperature of homogenization, suggesting that MI size was not responsible for this temperature range. Rather, the temperature range reflects differences in melt composition reflecting trapping at different times during evolution of the magma. Thus, more primitive MI entrapped in more primitive olivine/clinopyroxene show homogenization temperatures that are much higher than MI entrapped in more evolved phenocrysts (e.g., Fo-poor olivine) (Esposito *et al.*, 2011). Furthermore, phenocrysts may not be linked genetically and thus MI analyzed may have formed in totally different environments within the magma body, and/or at different times. For this study, petrographic analysis of the phenocrysts and MI was not conducted because the purpose of this study was not to determine a melt petrogenesis but, rather, to test applicability of the Linkam stage for homogenizing and quenching MI.

Some experiments on recrystallized MI from Solchiaro produced homogeneous glassy MI with no vapor bubble (Fig. 3) after quenching from high temperature (1060 to $\sim 1300^{\circ}\text{C}$). In a few experiments, the sample was heated to approximately 1340°C but complete homogenization was not achieved. During heating to that temperature, the field of view became progressively darker and a reddish glow developed, making it difficult to observe the behavior of the MI during continued heating. Darkening and development of the reddish glow generally became noticeable and caused the optics to degrade to the point where the MI could no longer be observed over a temperature range of about 50°C . At lower temperatures, the optics were generally excellent, with the quality of the optics depending mostly on two factors: the thickness of the

phenocryst and the relative area of the sample represented by solid and/or melt inclusions, with the optical quality being inversely related to the inclusion content. Also, the optics improved if the crystal was free of matrix glass. As previously noted by (Student & Bodnar, 2004), groundmass adhering to phenocrysts affects the optics because it consists of dark recrystallized glass that generally melts before the MI has completely homogenized and flows around the phenocryst (or through fractures in the phenocryst) causing the optics to deteriorate. In order to remove matrix glass from the crystals before heating experiments, some authors have suggested that the samples should be placed in concentrated hydrofluoric acid solution for several seconds (Anderson, 1991, Student & Bodnar, 2004), but this was not done for the phenocrysts studied here.

In some cases, the MI were heated to relatively high temperature and all of the solids in the MI melted, but the vapor bubble did not completely dissolve back into the melt before the optics deteriorated and it was no longer possible to observe the MI behavior. When the MI was quenched from a temperature slightly higher than that at which the MI could no longer be observed (*blind quenching*), the single bubble that (presumably) remained in the MI grew larger as the MI cooled due to the effect of the greater thermal contraction of the melt relative to the host (Fig. 4). Because the MI could not be observed to the point of complete vapor bubble disappearance, it is not clear if the bubble did indeed disappear but re-nucleated during cooling, or if the bubble never completely disappeared and simply grew larger during cooling. Moreover, the bubble in these MI may represent a trapped vapor bubble (i.e., the MI trapped a volatile-saturated melt plus a vapor bubble) and, thus, the bubble should not be expected to dissolve back into the melt. Another interpretation (especially for relatively larger MI) could be that the internal pressure in the MI is now less than the internal pressure at the moment of the entrapment owing to the compressibility of the host phase. Because the host phase is heated at one atmosphere pressure during the experiments, the confining pressure is lower than the pressure at which the phenocryst trapped the MI. Therefore, the volume of the host phase, and the "cavity" represented by the MI, is slightly greater than that at the time of trapping, resulting in lower internal pressure in the MI during laboratory heating and, concomitantly, lower volatile solubility in the melt phase. A final explanation for the fact that the bubble remained at the highest temperature to which the MI could be heated and observed is that the actual homogenization temperature is higher than this temperature. However, in our experiment, the latter interpretation is unlikely owing to the widespread melting of the host observed at these high temperatures (e.g., >1320°C).

In half of the experiments performed on clinopyroxene-hosted, recrystallized MI from nodules from the Sarno eruption of Monte Somma-Vesuvius (Southern Italy), it was possible to quench the MI to a homogeneous glass without re-nucleating vapor bubbles (Fig. 5). Similar to samples from Solchiaro, some of the MI could not be monitored completely up to the temperature of homogenization owing to the deterioration of the optics above a certain temperature. Crystals from the Sarno eruption are rich in solid and recrystallized MI. For this reason, the optics deteriorated at a lower temperature, compared to the experiments performed on olivines from Solchiaro, which contain relatively few melt and solid inclusions. For the Sarno

clinopyroxene-hosted MI, the optics remained relatively good up to $\approx 1260^\circ\text{C}$; above this temperature they deteriorated rapidly with further heating.

4. Discussion of advantages and limitations of the Linkam TS1400XY stage

The most important advantage of using a microscope-mounted heating stage (such as the Linkam TS1400XY) relative to one atmosphere furnaces and high pressure autoclaves is that the MI can be observed continuously during the heating/cooling experiments (Student & Bodnar, 2004). For example, the appearance/disappearance of a microscopically recognizable phase is possible during heating experiments using these types of devices, but is not possible when the MI is heated in a furnace. Also, the temperatures at which phase changes occur in the MI can be determined with better precision using a microscope-mounted heating stage, compared to a large volume furnace. As noted by (Student & Bodnar, 2004) the ability to monitor the behavior of MI from the Red Mountain, Arizona, porphyry copper deposit continuously during heating made it possible for those workers to determine that quartz, plagioclase and probably apatite were three minerals on the liquidus when the melt inclusions were trapped, and that the melt was H_2O -saturated. These workers were also able to distinguish between MI that trapped only a melt phase, and those that trapped melt \pm crystals \pm vapor, and to eliminate those MI that trapped multiple phases from any subsequent analyses.

Compared to some other microscope-mounted heating stages, the Linkam TS1400XY stage offers several advantages. Firstly, the Linkam TS1400XY heating stage is a "turn key" digitally controlled system (e.g., the T95-LinkPad; see Fig. 1d), while some other heating stages require the user to design and build a system to control and monitor the temperature. Thus, compared to some other commercially available stages, the Linkam system may be better for someone who does not have access to machining and/or electronics facilities. The digitally controlled system allows one to set heating/cooling cycles, which, as described above, can be used to establish heating rates to determine the "correct" temperature of homogenization. These cycles adopted during kinetic experiments are easier to perform when the heating rates are controlled electronically rather than manually. Secondly, we found it easier to load crystals into the furnace of the Linkam TS1400XY stage than it is to load crystals into the somewhat confined platinum furnace of the Vernadsky stage. Thirdly, the position of the crystal under the microscope can be moved during the heating experiment without the need to move the entire heating stage. In this way, more MI in a single grain can be monitored while viewing the sample at high magnification during heating experiments, by moving the crystal in X-Y space during heating and observation. Finally, in the Vernadsky stage the analyzed crystal is placed onto a metal frame and thus photography during the heating experiment may be compromised, while in the Linkam TS1400XY stage the analyzed crystal sits on a sapphire slide which is transparent to light, resulting in relatively good optics during most of the heating sequence.

As reported above, even though the quench rate with the Linkam TS1400XY stage is slower than that of the Vernadsky stage ($\approx 240^\circ\text{C/s}$ from 1400 to 800°C , and $\approx 230^\circ\text{C/s}$ from 1400 to 600°C), the quenching rate was fast enough to quench the MI tested in this study. The most significant limitation of the Linkam TS1400XY heating

stage identified in this study is the poor visibility that sometimes results during high temperature operation. This effect was not observed for MI hosted in quartz, but was only observed with olivine and pyroxene-hosted MI that require higher temperatures to achieve homogenization. In our experiments involving olivine from Solchiaro, the optics degraded to the point where the MI were not recognizable at a temperature around 1340°C. For experiments on clinopyroxene from the Sarno eruption, the visibility deteriorated to the point that it was not possible to observe the behavior of MI at a temperature around 1260°C. In most cases, the deterioration in the optics was manifested by the sample becoming darker and with a reddish glow that increased in intensity as the temperature increased. The deterioration in optical quality during heating MI in olivine and clinopyroxene is influenced by (1) the presence of matrix glass adhering to the phenocryst, (2) the presence of MI connected (open) to the crystal surface, because they may “boil” during heating, releasing melt to the outside of the crystal, and (3) the high abundance of solid/melt inclusions in the sample. In addition, we noticed that the optics improved as the sample became thinner. Our observations suggest that during heating the infrared energy ("light") generated by the hot furnace ceramic is reflected in all directions, leading to deterioration in the optics during high temperature experiments, and the presence of matrix glass, solid and melt inclusions in the sample, and melt on the exterior of the crystal all serve to enhance this reflection. If a microscope-mounted digital camera is used during heating experiments, the visibility may be improved. Also, the optical issue may be solved in the future by using a confocal method of observation (e.g., spinning disc or laser confocal; V. Kamp, personal communication). In addition, it should be emphasized that the degradation of the optics at a high temperature is not unique to the Linkam TS1400XY heating stage, but also occurs with the Vernadsky stage (and probably with other high temperature microscope stages). The effect is less significant in the Vernadsky stage because of the smaller size of the furnace and because the sample is not encased (or surrounded) by ceramic material.

In summary, the following suggestions can be adopted in order to improve the optical quality during heating experiments using the Linkam TS1400XY. First of all, as much of the matrix glass as possible should be removed from the crystals before heating experiments are conducted (e.g., using concentrated hydrofluoric acid solution as suggested by (Anderson, 1991, Student & Bodnar, 2004)). Secondly, the host crystals should be as thin as possible because, as explained above, less material reflects less light (infrared energy) generated in the furnace at high temperature. Thirdly, a microscope-mounted digital camera should be used to improve the visibility, especially at high temperature when it becomes difficult to make any observation looking through the microscope lens. Finally, the optics may be improved by using a different optical imaging technique, such as confocal spinning disk or a confocal laser scanning microscope.

5. Summary

Tests confirm that the Linkam TS1400XY heating stage is capable of heating MI to homogenization and quenching to produce a homogenous glass. This method produces glassy MI that can be analyzed using various microanalytical techniques that require a

single, homogeneous phase for quantitative analysis to determine the compositions (especially the volatile contents) of the pre-eruptive melt. Experiments performed on recrystallized MI that homogenize at less than $\sim 1100^{\circ}\text{C}$ are optimal for observing the heating/cooling behavior of MI. Thus, for felsic melts and most intermediate composition melts, optical conditions during heating/cooling experiments are generally quite good. For mafic melt compositions, or samples with crystals that are rich in matrix glass, or contain opened MI or mineral inclusions, the optical quality may deteriorate to the point where the inclusion is no longer visible during heating experiments, and cannot be observed to complete homogenization.

6. Acknowledgements

We would like to thank the Linkam Group for providing the opportunity to test the functions of the Linkam TS1400XY heating stage, in particular Jeff D. McGinn and Vincent Kamp. We also thank Matthew Steele-MacInnis and Pilar Lecumberri Sanchez for discussions on the topic and editorial assistance. This material is based upon work supported by the National Science Foundation under grant no. EAR-1019770.

7. References

- Anderson, A. T., Davis, A. M. & Lu, F. (2000). Evolution of Bishop Tuff rhyolitic magma based on melt and magnetite inclusions and zoned phenocrysts. *Journal of Petrology* 41, 449-473.
- Anderson, A. T., Jr. (1991). Hourglass inclusions; theory and application to the Bishop rhyolitic tuff. *American Mineralogist* 76, 530-547.
- Bartoli, O., Cesare, B., Poli, S., Bodnar, R. J., Frezzotti, M. L., Acosta-Vigil, A. & Meli, S. (2011). Melting in the deep crust: message from melt inclusions in peritectic garnet from migmatites. *Mineralogical Magazine* 75, 495.
- Beddoe-Stephens, B., Aspden, J. A. & Shepherd, T. J. (1983). Glass inclusions and melt compositions of the Toba Tuffs, northern Sumatra. *Contributions to Mineralogy and Petrology* 83, 278-287.
- Bertagnini, A., Landi, P., Rosi, M. & Vigliargio, A. (1998). The Pomici di Base plinian eruption of Somma-Vesuvius. *Journal of Volcanology and Geothermal Research* 83, 219-239.
- Bodnar, R. J. & Student, J. J. (2006). Melt inclusions in plutonic rocks: Petrography and microthermometry. *Melt Inclusions in Plutonic Rocks* 36, 1-25.
- Cesare, B., Acosta-Vigil, A., Ferrero, S. & Bartoli, O. (2011). Melt inclusions in migmatites and granulites. *Journal of the Virtual Explorer* 40.
- Chesner, C. A. (1998). Petrogenesis of the Toba Tuffs, Sumatra, Indonesia. *Journal of Petrology* 39, 397-438.
- Clocchiatti, R. (1975). Les inclusions vitreuses des cristaux de quartz; Etude optique, thermo-optique et chimique; Applications geologiques. Vitreous inclusions in quartz crystals; optical, thermo-optical and chemical studies; geologic applications. *Memoires de la Societe Geologique de France*, no 122.
- Danyushevsky, L. V., McNeill, A. W. & Sobolev, A. V. (2002). Experimental and petrological studies of melt inclusions in phenocrysts from mantle-derived

- magmas: an overview of techniques, advantages and complications. *Chemical Geology* 183, 5-24.
- De Vivo, B., and Bodnar, R.J., (2003). Melt inclusions in volcanic systems.
- Esposito, R., Bodnar, R. J., Danyushevsky, L., De Vivo, B., Fedele, L., Hunter, J., Lima, A. & Shimizu, N. (2011). Volatile Evolution of Magma Associated with the Solchiaro Eruption in the Phlegrean Volcanic District (Italy). *Journal of Petrology* 52, 2431-2460.
- Fedele, L., Bodnar, R. J., DeVivo, B. & Tracy, R. (2003). Melt inclusion geochemistry and computer modeling of trachyte petrogenesis at Ponza, Italy. *Chemical Geology* 194, 81-104.
- Ferrero, S., Bartoli, O., Cesare, B., Salvioli-Mariani, E., Acosta-Vigil, A., Cavallo, A., Groppo, C. & Battiston, S. (in press). Microstructures of melt inclusions in anatectic metasedimentary rocks. *Journal of Metamorphic Geology*.
- Frezzotti, M. L. (1992). Magmatic immiscibility and fluid phase evolution in the Mount Genis granite (southeastern Sardinia, Italy). *Geochimica et Cosmochimica Acta* 56, 21-33.
- Helo, C., Longpre, M. A., Shimizu, N., Clague, D. A. & Stix, J. (2011). Explosive eruptions at mid-ocean ridges driven by CO₂-rich magmas. *Nature Geoscience* 4, 260-263.
- Landi, P., Bertagnini, A. & Rosi, M. (1999). Chemical zoning and crystallization mechanisms in the magma chamber of the Pomici di Base plinian eruption of Somma-Vesuvius (Italy). *Contributions to Mineralogy and Petrology* 135, 179-197.
- Lowenstern, J. B. (1994). Dissolved Volatile Concentrations in an Ore-Forming Magma. *Geology* 22, 893-896.
- Lowenstern, J. B. (1995). Applications of silicate-melt inclusions to the study of magmatic volatiles. *Short Course Handbook* 23, 71-99.
- Metrich, N., Wallace, P. J., Putirka, K. D. & Tepley, F. J., III. (2008). Volatile abundances in basaltic magmas and their degassing paths tracked by melt inclusions. *Reviews in Mineralogy and Geochemistry* 69, 363-402.
- Newman, S. & Chesner, C. (1989). Volatile compositions of glass inclusions from the 75Ka Toba Tuff, Sumatra. *Geological Society of America, 1989 annual meeting* 21, 271.
- Nielsen, R. L., Crum, J., Bourgeois, R., Hascall, K., Forsythe, L. M., Fisk, M. R. & Christie, D. M. (1995). Melt inclusions in high-An plagioclase from the Gorda Ridge: an example of the local diversity of MORB parent magmas. *Contributions to Mineralogy and Petrology* 122, 34-50.
- Reyf, F. G. (1997). Direct evolution of W-rich brines from crystallizing melt within the Mariktikan granite pluton, west Transbaikalia. *Mineralium Deposita* 32, 475-490.
- Roedder, E. (1979). Origin and significance of magmatic inclusions. *Bulletin de Mineralogie* 102, 487-510.
- Schiano, P. (2003). Primitive mantle magmas recorded as silicate melt inclusions in igneous minerals. *Earth-Science Reviews* 63, 121-144.

- Severs, M. J., Azbej, T., Thomas, J. B., Mandeville, C. W. & Bodnar, R. J. (2007). Experimental determination of H₂O loss from melt inclusions during laboratory heating: Evidence from Raman spectroscopy. *Chemical Geology* 237, 358-371.
- Sinton, C. W., Christie, D. M., Coombs, V. L., Nielsen, R. L. & Fisk, M. R. (1993). Near-primary melt inclusions in anorthite phenocrysts from the Galapagos Platform. *Earth and Planetary Science Letters* 119, 527-537.
- Skirius, C. M., Peterson, J. W. & Anderson, A. T. (1990). Homogenizing Rhyolitic Glass Inclusions from the Bishop Tuff. *American Mineralogist* 75, 1381-1398.
- Sobolev, A. V., Danyushevsky, L. V., Dmitriev, L. V. & Sushchevskaya, N. M. (1988). High-Alumina Magnesium Tholeiite as One of Primary Melts of Basalts of the Mid-Oceanic Ridges. *Geokhimiya*, 1522-1528.
- Sobolev, A. V., Dmitriev, L. V., Barsukov, V. L., Nevsorov, V. N. & Slutsky, A. B. (1980). The formation conditions of the high magnesium olivines from the monomineralic fraction of Luna 24 regolith. *Proceedings of the Lunar and Planetary Science Conference* 11, 105-116.
- Sobolev, A. V., Hofmann, A. W., Jochum, K. P., Kuzmin, D. V. & Stoll, B. (2011). A young source for the Hawaiian plume. *Nature* 476, 434-437.
- Sobolev, A. V. & Kostyuk, V. P. (1976). Magmatic crystallization based on study of melt inclusions. *Fluid inclusion research* 9, 182-253.
- Student, J. J. & Bodnar, R. J. (1999). Synthetic Fluid Inclusions XIV: Coexisting Silicate Melt and Aqueous Fluid Inclusions in the Haplogranite–H₂O–NaCl–KCl System. *Journal of Petrology* 40, 1509-1525.
- Student, J. J. & Bodnar, R. J. (2004). Silicate melt inclusions in porphyry copper deposits: Identification and homogenization behavior. *Canadian Mineralogist* 42, 1583-1599.
- Thomas, J. B. & Bodnar, R. J. (2002). A technique for mounting and polishing melt inclusions in small (>1 mm) crystals. *American Mineralogist* 87, 1505-1508.
- Thomas, J. B., Bodnar, R. J., Shimizu, N. & Chesner, C. A. (2003). Melt Inclusions in Zircon. *Reviews in Mineralogy and Geochemistry* 53, 63-87.

8. Tables

Table 1. Heating schedule used for heating experiments on crystals from the Solchiaro, Sarno and Toba Tuff eruptions.

Temperature °C	Heating rate °C/min	sample
25 - 900	100	Solchiaro and Sarno
900 - 1000	50	Solchiaro and Sarno
1000 - 1100	25	Solchiaro and Sarno
1100 - 1200	10	Solchiaro and Sarno
1200 - 1360	5	Solchiaro and Sarno
25 - 600	100	Toba Tuff
600 - 700	50	Toba Tuff
700 - 800	25	Toba Tuff
800 - 850	10	Toba Tuff
850 - 1000	5	Toba Tuff

9. Figures

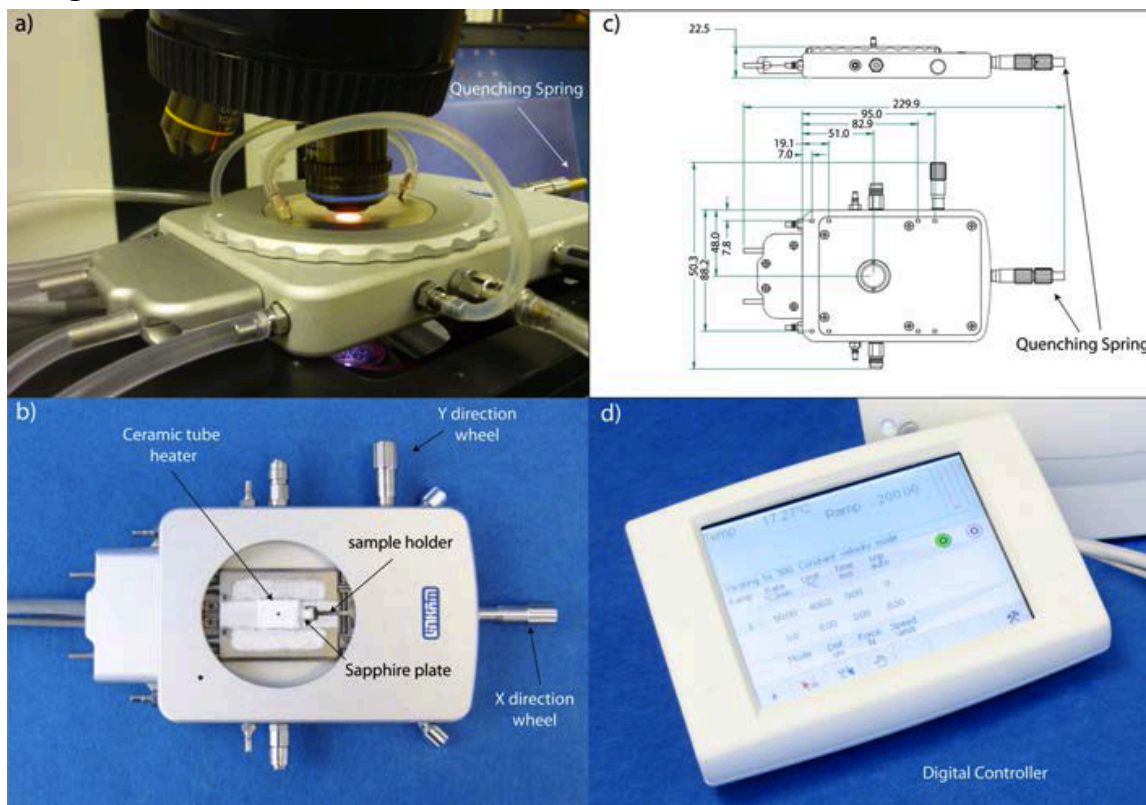


Fig. 1. The Linkam TS1400XY heating stage. 1a) The Linkam TS1400XY stage mounted on a microscope during a heating experiment, with the temperature at $\approx 1350^{\circ}\text{C}$. The quenching spring is on the right side of the heating stage as indicated by the arrow. The bright spot immediately beneath the objective lens is the reddish glow from the furnace at this high temperature. 1b) The Linkam TS1400XY with the lid opened. It is possible to observe the ceramic furnace, the sapphire plate with the metallic frame, and the XY control wheels. This photo is modified from: http://www.mccronemicroscopes.com/store/catalog.asp?item=356&category_id=48. 1c) Technical drawing of the Linkam TS1400XY heating stage. All the measurements reported are in mm. Important to note is the quenching spring connected to the X-direction wheel (courtesy of V. Kamp). 1d) T95-LinkPad system controller. Additional technical information and images are available at the Linkam website (<http://www.linkam.co.uk/>).

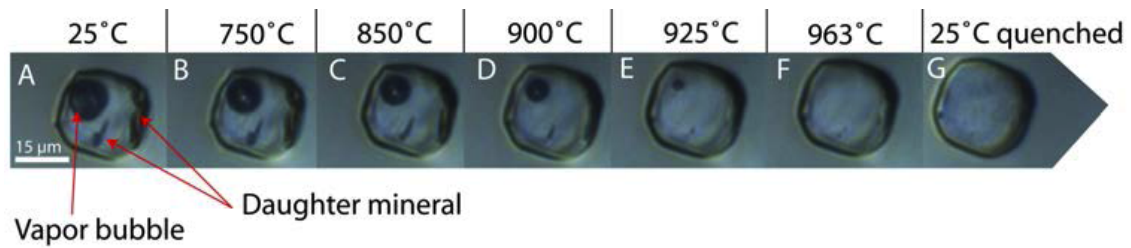


Fig. 2. Heating experiment performed on quartz phenocryst from the Toba Tuff eruption in Sumatra. The MI is around 15 μm in diameter and has a sub-rectangular shape. A) At room temperature (25°C), the MI contains one vapor bubble and three unidentified daughter crystals. From B to F) From 750°C to 925 °C the volumes of the vapor bubble and of the three daughter crystals progressively decrease as these phases dissolve back into the melt. G) At 963°C the MI consists of only a homogeneous silicate melt phase. H) The MI at ambient conditions after quenching from \approx 963°C to produce a homogenous glass.

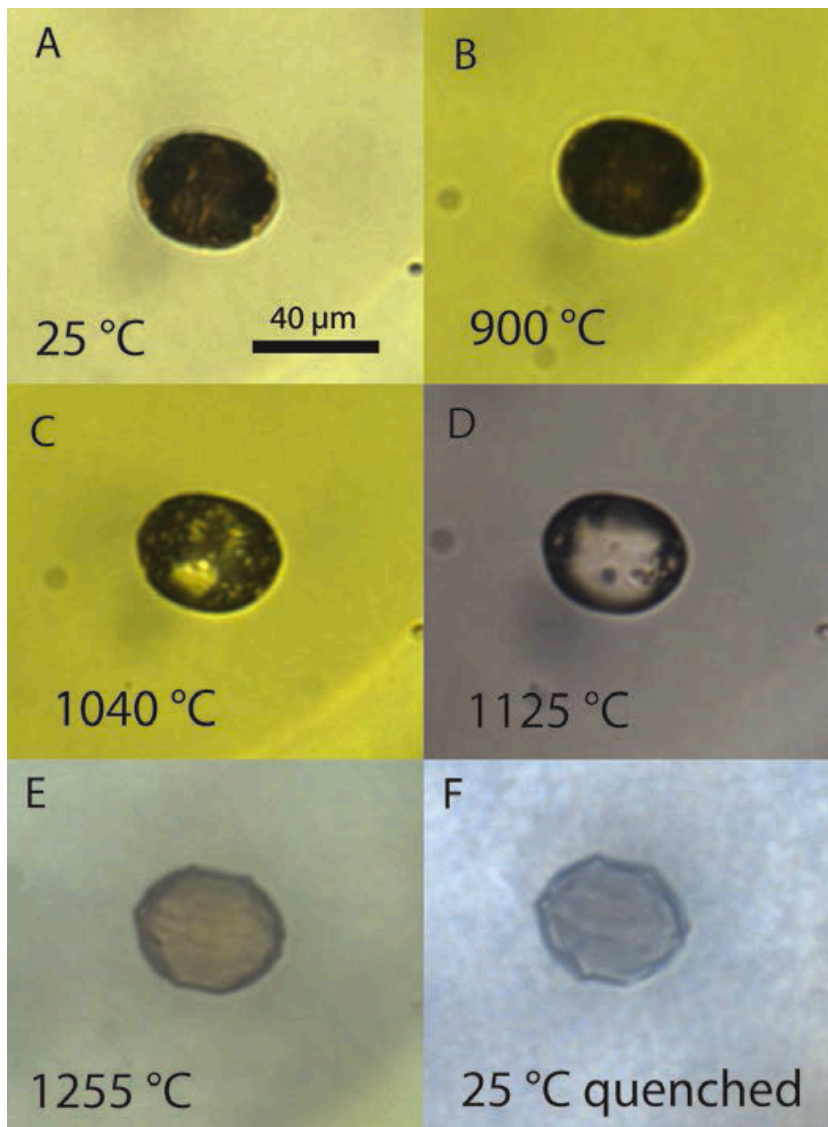


Fig. 3. Heating experiment performed on MI in an olivine phenocryst from scoriae of the Solchiaro eruption of the Phlegrean Volcanic District (PVD) in Southern Italy. The MI has an ellipsoidal shape. A) At room temperature (25°C), the MI is partially recrystallized and nearly opaque. Some daughter crystals are visible at the olivine host – melt inclusion interface. B) At 900°C, daughter crystals at the olivine/inclusion interface are smaller relative to those at room temperature. C) At 1040°C it is possible to observe some vapor bubbles, solid and melt phases. D) At 1125°C most of the melt inclusion consists of a silicate melt phase. E) At 1255°C the MI is completely homogenized and contains only a melt phase. Note that at this temperature the MI assumes a negative crystal shape. Also, the "wrinkles" at the melt/crystal interface may indicate that the MI was overheated and that the host phase has begun to melt. F) After quenching from > 1260°C to ambient temperature the MI contains a homogenous glass. During the quenching, some crystallization of olivine at the olivine/glass interface may have occurred.

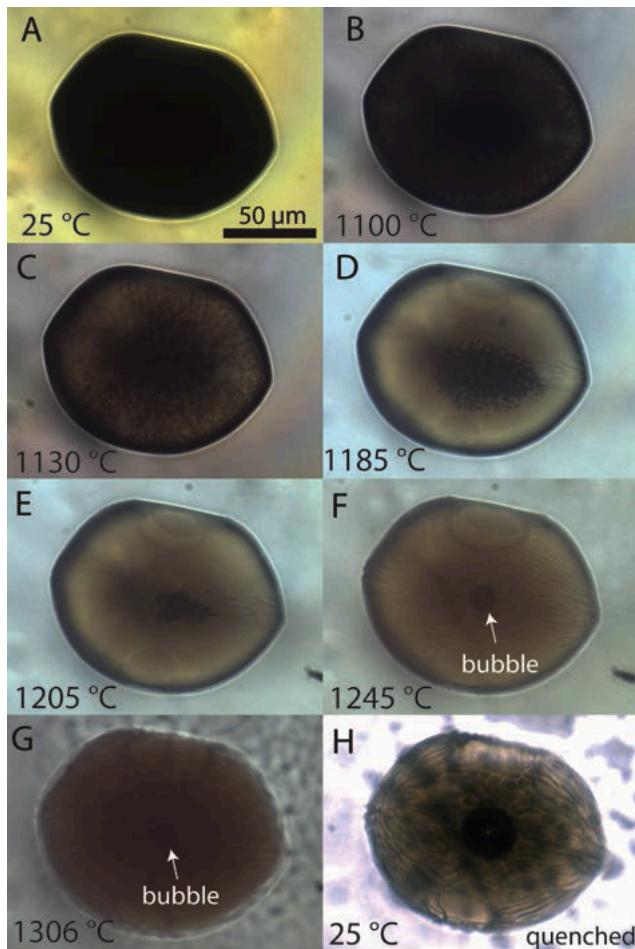


Fig. 4. Heating experiment performed on MI contained in an olivine phenocryst from scoriae of the Solchiaro eruption of the Phlegrean Volcanic District (PVD) in Southern Italy. The MI has a sub-negative crystal shape with smooth olivine/inclusion interface. A) At room temperature (25°C), the MI is totally crystallized and may be mis-identified as an opaque solid inclusion (e.g., spinel) during petrographic examination. There are no features visible to suggest that this is a melt inclusion. B) At 1110°C a melt phase can be observed near the olivine/MI interface. The inner part of the MI remains dark. C) As the temperature increases (e.g., 1130°C), the melt region expands toward the center of the MI. D) At 1185°C the black spots in the interior of the MI appear to assemble to form larger vapor bubbles. The MI tends to a more negative crystal shape as the temperature increases. E) At 1205°C a few vapor bubbles are observed and most of the MI consists of silicate melt. F) At 1245°C the MI consists of silicate melt and a single vapor bubble in the center of the MI. G) During heating from 1300 to 1340°C the bubble does not dissolve into the melt and the bubble size does not change. At 1340°C the MI was no longer visible as the field of view became dark and with a reddish glow. H) After quenching from 1340°C to room temperature, the MI contains a homogenous glass plus a vapor bubble that is likely of primary origin. Note the difference between the MI before the experiment and after quenching. The glass composition can be analyzed for major, trace and volatile elements, while the bubble can be analyzed for volatiles using Raman spectrometry.



Fig.5. Heating experiment performed on a melt inclusion in clinopyroxene from a nodule from the Sarno eruption at Mt Somma-Vesuvius in Southern Italy. The Sarno eruption is considered to be the largest volume eruption in the history of Somma-Vesuvius (Bertagnini *et al.*, 1998). A) At room temperature (25°C), the MI is partially crystallized. Some daughter crystals or vapor bubbles are visible. B) At 1170 °C the size of the daughter crystals/vapor bubbles has decreased significantly. C) At 1200°C MI contains only silicate melt. F) After quenching from 1200°C to room temperature, the MI contains a homogenous glass.